Safety of Light Water Reactor Fuel with Silicon Carbide Cladding

by

Youho Lee

B.S. in Nuclear and Quantum Engineering, Korea Advanced Institute of Science and Technology, 2009
M.S. in Nuclear Science and Engineering, Massachusetts Institute of Technology, 2011

Submitted to the Department of Nuclear Science and Engineering
in Partial Fulfillment of the Requirement for the Degree of

Doctor of Philosophy in Nuclear Science and Engineering

At the

MASSACHUSETTS INSTITUTE of TECHNOLOGY

September 2013

Signature of Author: _____
Department of Nuclear Science and Engineering
August 19, 2013

Certified By: _____
Mujid S. Kazimi, Ph.D.
TEPCO Professor of Nuclear Engineering
Thesis Supervisor

Certified By: _____
Thomas J. McKrell, Ph.D.
Research Scientist
Thesis Reader

Certified By: _____
Ronald G. Ballinger, Ph.D.
Professor
Thesis Reader

Accepted By: _____
Mujid S. Kazimi, Ph.D.
TEPCO Professor of Nuclear Engineering
Chairman, Committee on Graduate Students

Safety of Light Water Reactor Fuel with Silicon Carbide Cladding

by

Youho Lee

Submitted to the Department of Nuclear Science and Engineering
on August 19, 2013 in Partial Fulfillment of the
Requirement for the Degree of Doctor of Philosophy in
Nuclear Science and Engineering

ABSTRACT

Structural aspects of the performance of light water reactor (LWR) fuel rod with triplex silicon carbide (SiC) cladding – an emerging option to replace the zirconium alloy cladding – are assessed. Its behavior under accident conditions is examined with an integrated approach of experiments, modeling, and simulation. High temperature (1100°C~1500°C) steam oxidation experiments demonstrated that the oxidation of monolithic SiC is about three orders of magnitude slower than that of zirconium alloys, and with a weaker impact on mechanical strength. This, along with the presence of the environmental barrier coating around the load carrying intermediate layer of SiC fiber composite, diminishes the importance of oxidation for cladding failure mechanisms.

Thermal shock experiments showed strength retention for both α-SiC and β-SiC, as well as Al_2O_3 samples quenched from temperatures up to 1260°C in saturated water. The initial heat transfer upon the solid – fluid contact in the quenching transient is found to be a controlling factor in the potential for brittle fracture. This implies that SiC would not fail by thermal shock induced fracture during the reflood phase of a loss of coolant accident, which includes fuel-cladding quenching by emergency coolant at saturation conditions.

A thermo-mechanical model for stress distribution and Weibull statistical fracture of laminated SiC cladding during normal and accident conditions is developed. It is coupled to fuel rod performance code FRAPCON-3.4 (modified here for SiC) and RELAP-5 (to determine coolant conditions). It is concluded that a PWR fuel rod with SiC cladding can extend the fuel residence time in the core, while keeping the internal pressure level within the safety assurance limit during steady-state and loss of coolant accidents. Peak burnup of 93 MWD/kgU (10% central void in fuel pellets) at 74 months of in-core residence time is found achievable with conventional PWR fuel rod design, but with an extended plenum length (70 cm). An easier to manufacture, 30% larger SiC cladding thickness requires an improved thermal conductivity of the composite layer to reduce thermal stress levels under steady-state operation to avoid failure at the same burnup. A larger Weibull modulus of the SiC cladding improves chances of avoiding brittle failure.

Thesis Supervisor: Mujid S. Kazimi

Title: TEPCO Professor of Nuclear Engineering and Professor of Mechanical Engineering

ACKNOWLEDGEMENTS

I would like to thank my advisor Professor Kazimi with my deepest respect for his guidance and opportunities he has given to me. In addition to the depth and the breadth of knowledge, I also learned his attitudes towards research and people. Without his support and wisdom, this work would have not been possible.

I would like to thank Dr. McKrell for his guidance. His experience and help have pervaded every corner of the experimental work of this study, and I very much enjoyed working and learning from him. I would like to thank Professor Ballinger for having provided me with enriching comments. I appreciate Professor Buongiorno for having taken my spontaneous questions and served on the thesis committee. I am very grateful for Professor Li for having provided me with indispensable insights in understanding mechanical behavior of materials. He always willingly taught me essential insights and framework that I cannot easily find from written literatures. I would like to thank Dr. Bernard for being a great mentor throughout my graduate life and for encouragement to study fundamentals of the nuclear engineering discipline. I am also grateful for Professor Forsberg and Professor Driscoll for their guidance in early years of my graduate studies.

I have been benefited by diverse expertises existing in the Advanced Fuels and Fuel Cycle Group of the Department. Especially, I would like to express my sincere thanks to Aline Montecot, Yann Song, Chao Yue, Ramsey Arnold, and Michael Pantano for being great helpers/collaborators in the oxidation experiment. I would like to thank Dr. Carpenter for his cordial sharing of experience and knowledge on SiC cladding. I learned a lot from conversations I had with him. I would like to thank Dr. Shirvan for helping me run RELAP, transfer SIMULATE results, and being a good mentor as a senior. I am very grateful for Peter Stahle for helping me conduct destructive material tests, which ran very smoothly thanks to his unfathomable hands-on experience.

I would like to thank Professor Hee Cheon No of KAIST, for his solid training and education throughout my undergraduate time at KAIST. Four years of research experience under his supervision in KAIST served as an invaluable asset to my graduate studies. I would like to also express my sincere gratitude for Professor Jeong Ik Lee of KAIST for being a great mentor.

I appreciate financial support from CANES of the Department of Nuclear Science and Engineering, INL Academic Center of Excellence at MIT, AREVA Fellowship in Nuclear Energy Technology at MIT, and the Korean Government Scholarship through Korea Institute of Energy Technology Evaluation and Planning for the first two years of my study in the U.S.

TABLE of CONTENTS

LIST of FIGURES

LIST of TABLES

NOMENCLATURE

ASTM	American Society for Testing and Materials
BOL	Beginning-of-Life
BWR	Boiling Water Reactor
CEA	French Alternative Energies and Atomic Energy Commision
CFR	Code of Federal Regulation
CTP	Ceramic Tubular Products
CVD	Chemical Vapor Deposition
CVI	Chemical Vapor Infilteration
DAS	Data Acquisition System
DBA	Design Basis Accident
DPA	Displacement Per Atom
EBC	Environmental Barrier Coating
ECCS	Emergency Core Cooling System
ECR	Equivalent Cladding Reacted
EDS	Energy Dispersive Spectroscopy
EOL	End-of-Life
FDM	Finite Difference Method
HNLS	Hi-Nicalon™ Type-S
HTR	High Temperature Reactor
IAEA	International Atomic Energy Agency
ID	Inner Diameter
KAERI	Korea Atomic Energy Research Institute
LOCA	Loss of Coolant Accident
LWR	Light Water Reactor
MIT	Massachusetts Institute of Technology
MITR	MIT Nuclear Research Reactor
MOL	Middle-of-Life
NEA	Nuclear Energy Agency
NRC	Nuclear Regulator Commision
OD	Outer Diameter
OECD	Organisation for Economic Co-operation and Development
ORNL	Oakridge National Laboratory
PCMI	Pellet-Cladding Mechanical Interaction
PNNL	Pacific Northwest National Laboratory
PWR	Pressurized Water Reactor
SEM	Scanning Electorn Microscopy
TMI	Threee Mile Island
US	United States
Zircaloy	Zirconium Based Alloy
Zr-4	Zircaloy-4

Chapter 1

Introduction

1.1 Role of Light Water Reactor Cladding

Nuclear fuel rod cladding plays two roles that bear critical importance to both safety and operation of a nuclear power plant. First, it is an element in the concept of Defense-in-Depth that encapsulates the fuel pellet, made of UO_2 and fission by-products, to prevent the release of radioactivity. Second, it transfers heat generated from the fuel pellet to the coolant. These unique roles of the fuel cladding have resulted in rigorous requirements for its performance under the most challenging environment in a nuclear power plant: to maintain its integrity during exposure to the high temperature, stresses, radiation, and chemical attacks while maintaining a reasonable level of thermal conductivity. Very little is expected from fuel pellet integrity in terms of radioactivity containment, as they are allowed to crack and undergo significant micro-structure deformations with high burnup under increasingly aggressive operating conditions. Nevertheless, a fuel rod is regarded intact as long as its encapsulating cladding maintains its integrity. Hence, it is the integrity of fuel rod cladding that ensures safety of the nuclear fuel rod, upon which safety of the nuclear power plant is centered.

1.2 Limitations of the Current Zirconium-Based Alloy Cladding

Zirconium–based alloy (Zircaloy) was first deployed as a Light Water Reactor (LWR) cladding material in 1940s in naval reactors in U.S as a replacement for stainless steel (Carpenter, 2010). Zircaloy was selected due to its advantageous properties over stainless steel in a number of respects on both operations and safety, including lower neutron absorption, and higher tolerance to chloride stress corrosion cracking, especially in Boiling Water Reactors (BWRs) (Carpenter, 2010), (Locke, 1975). During the 1960s, most civil LWRs started to adopt Zircaloy cladding and finished switching to Zircaloy clad fuel in the mid-1970s while the last use of the stainless steel clad was terminated in the U.S at the Haddam Neck power plant in the 1990s (DOE, 1994), (Carpenter, 2010).

Zircaloy has remained the fuel cladding of choice for LWRs. It proved its reliability under normal operating conditions with increasing industrial experience and research to find ideal manufacturing

technologies and material compositions despite some initial problems surrounding immature quality control processes.

1.2.1 Limitations of Zircaloy Cladding on Steady-State Operation

In recent years, however, Zircaloy has suffered from problems during steady-state operations at very high burnup especially due to its embrittlement. Zircaloy embrittlement occurs even under steady-state operations because of radiation damage and chemical interactions with the coolant. Today, limitations imposed by the zirconium based alloy embrittlement on steady-state operation are being recognized with serious attentions due to the increasing number of fuel failures. This increase originates from operating fuel rods in increasingly aggressive environments in pursuit of enhancing productivity and efficiency of LWRs, such as longer fuel residence time, and higher power level. Also, reactor water chemistry modifications for the purpose of protecting other plant materials have increased cladding corrosion and hydriding (Yang, 2006). This is seen particularly in increasing grid fretting failures in recent trends in US PWR failures as shown in Figure 1-1.

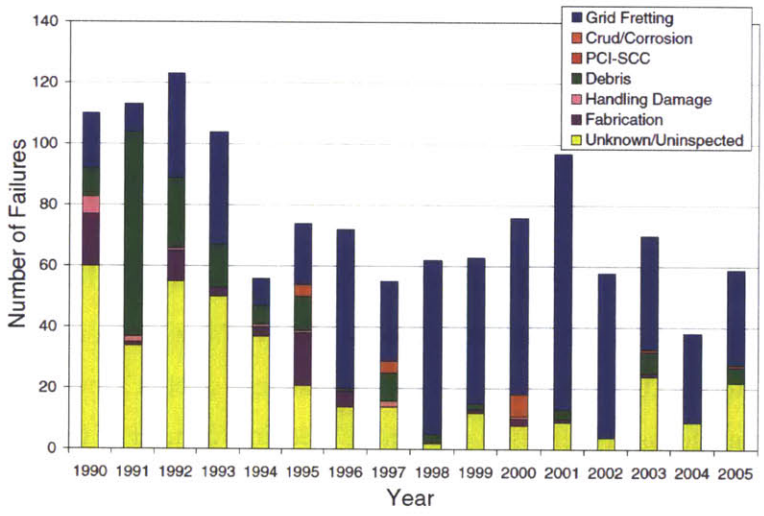

Figure 1-1 Trend in US PWR Failure Root Causes (Yang, 2006)

Solutions for these increases in failures are being found for most cases with accumulation of experiences. However, it has become clear that a more robust fuel cladding would allow for increasing power uprates and productivity of LWRs by safely allowing more aggressive operating conditions. However, this is not what is happening today; recognized limitations surrounding the cladding embrittlement have become a shackle for further advancements with LWRs both on productivity and safety. In particular, embrittlement of the cladding and the resulting uncertainty on its performance in postulated accidents conditions as well

as steady-state operations in terms of pellet cladding mechanical interaction (PCMI), excessive fuel rod stresses, hydrogen pickup and corrosion has resulted in regulatory limits on fuel rod discharge burnup to be 62 MWD/kgU average for the peak fuel rod[1] (NRC, 2000), (Carpenter, 2010). This burnup limit was not regarded seriously in the past when LWRs had to lower burnups ranging between 35 and 40 MWD/kgU for PWRs and around 30 MWD/kgU for BWRs (Olander, 2001). Today, however, the current burnup limit of 62 MWD/kgU is now actually a limiting value as commercial LWRs are operating at right below the limit as shown in Figure 1-2.

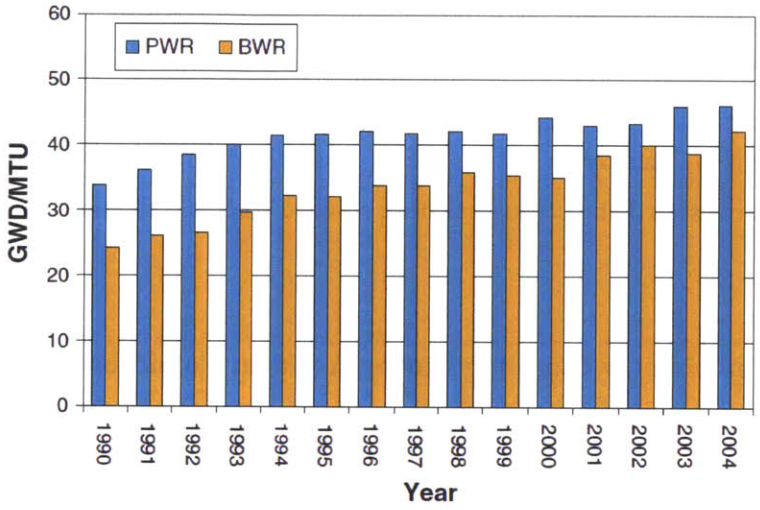

Figure 1-2 Average Discharge Burnup in U.S (Yang, 2006)

A reason for the continually increasing burnup is rooted in economic pressure of cost competitiveness with other technologies. A study in year 2001 states as follows:

"Recent economic pressure from gas-fired electricity production has forced nuclear utilities to demand more of the fuel: average burnups approaching 60MWD/kg for PWRs and 50MWD/kg for BWRs; linear heat rating increases of 10±15% for PWRs; and operating cycles of 1.5±2years (Olander, 2001)*"*

The motivation for increasing the burnup limit through the use of advanced cladding material may not be primarily viewed as an attempt to cut the levelized fuel cycle cost. A study on very high burnup LWR fuels found that fuel cycle costs may not necessarily decrease with burnup increase beyond the current practice although it unambiguously decreased with increasing burnup up to the current level (NEA, 2006).

[1] LWR burnup limits are not set by uranium enrichment. A recent study conducted by Nuclear Energy Agency (NEA) at Organization for Economic Co-Operation and Development (OECD) shows that an initial enrichment of U-235 between 8 and 9 % would be enough for an LWR to achieve average discharge burnups of 100 MWD/kgU or more. This will still ensure a margin to the 20% highly-enriched uranium (HEU) threshold set by International Atomic Energy Agency (IAEA) (NEA, 2006).

Considering, that fuel cost is only around 20% of the total cost of a nuclear power plant, the overall economic incentive coming from reduction in fuel costs by higher burnup fuels may not be significant, if there is any. Nevertheless, there exist clear incentives for higher burnup fuels in other reasons - operational and design flexibilities, reduction in volume of discharged fuels, and improved safety margins, which may help answer the question of whether the historic trend of burnup evolutions will to continue (NEA, 2006).

Although the material of choice for the cladding has been a Zircaloy for decades, the gradual attainment of higher burnup and power uprating have been possible due to overarching advancements in reactor engineering including optimizing Zircaloy material compositions through improved fuel behavior understanding, advanced fuel manufacturing capabilities, and accumulations of operational experiences. However, the limitations of Zircaloy on today's fuel & reactor performance are being felt differently from the past, indicating a clear sign that a ceiling has been reached leaving little room for further improvement.

1.2.2 Limitations of Zircaloy Cladding During Accident Conditions

Limitations of Zircaloy cladding become even more evident under accident conditions. Current LWRs are designed to ensure compliance with safety-related regulatory criteria specified for accident situations such as a loss of coolant accident (LOCA). Such criteria are usually established on the basis of the performance of the fuel rod under accident conditions, as it is the primary source of radioactivity and nuclear energy (Chung, 2005), (Lee, 2013).The current U.S NRC criteria for emergency core cooling systems for design-based LOCAs of LWRs are stated in the Code of Federal Regulation, Title 10, Part 50.46, "Acceptance Criteria for Emergency Core Cooling Systems (ECCS) for Light-Water Nuclear Reactors" (10 CFR 50.46) as follows (NRC, 2013):

"(1) Peak cladding temperature. The calculated maximum fuel element cladding temperature shall not exceed 2200° F (1204°C).

(2) Maximum cladding oxidation. The calculated total oxidation of the cladding shall nowhere exceed 0.17 times the total cladding thickness before oxidation. As used in this subparagraph total oxidation means the total thickness of cladding metal that would be locally converted to oxide if all the oxygen absorbed by and reacted with the cladding locally were converted to stoichiometric zirconium dioxide. If cladding rupture is calculated to occur, the inside surfaces of the cladding shall be included in the oxidation, beginning at the calculated time of rupture. Cladding thickness before oxidation means the radial distance from inside to outside the cladding, after any calculated rupture or swelling has occurred

but before significant oxidation. Where the calculated conditions of transient pressure and temperature lead to a prediction of cladding swelling, with or without cladding rupture, the unoxidized cladding thickness shall be defined as the cladding cross-sectional area, taken at a horizontal plane at the elevation of the rupture, if it occurs, or at the elevation of the highest cladding temperature if no rupture is calculated to occur, divided by the average circumference at that elevation. For ruptured cladding the circumference does not include the rupture opening.

(3) Maximum hydrogen generation. The calculated total amount of hydrogen generated from the chemical reaction of the cladding with water or steam shall not exceed 0.01 times the hypothetical amount that would be generated if all of the metal in the cladding cylinders surrounding the fuel, excluding the cladding surrounding the plenum volume, were to react.

(4) Coolable geometry. Calculated changes in core geometry shall be such that the core remains amenable to cooling.

(5) Long-term cooling. After any calculated successful initial operation of the ECCS, the calculated core temperature shall be maintained at an acceptably low value and decay heat shall be removed for the extended period of time required by the long-lived radioactivity remaining in the core."

Each of these five categories is closely aligned with behavior of Zircaloy cladding during postulated LOCAs, indicating that the integrity of Zircaloy cladding dictates the safety of the fuel rod under the accident conditions. In recent years, these limitations of Zircaloy cladding are being viewed with more caution with increasing demand for enhanced safety. Today, the U.S NRC is modifying 10CFR50.46 to reflect the fact that the current limits of maximum cladding temperature and maximum oxidation are not conservative for high burnup cladding (NRC, 2007), (NRC, 2008). In particular, hydrogen embrittlement of Zircaloy cladding is significantly exacerbated with burnup. The new rule is focusing on maintaining appropriate ductility as the unit of measure to determine survivability during the quench process and any other unforeseeable event with a particular attention to high burnup fuel.

Although Zircaloy exhibits marginal performance in terms of safety during postulated design basis accidents (DBAs) in accordance with the current ECCS rule, its limits prescribed in 10 CFR 50.46 become serious safety issues as an accident starts to depart from postulated scenarios beyond the design basis. In particular, temperature rise with an onset of unexpected deterioration in heat removal from fuel rods beyond the design basis will cause serious material degradation of Zircaloy cladding even at temperatures below the melting point (1760°C); at around 900°C, ballooning and bursting of Zircaloy cladding begins to manifest itself due to reduced mechanical strength which leads to release of radioactive

fission products. Above 1250°C, rapid oxidation of Zircaloy with steam occurs that accelerates cladding heating with localized core damage to reach extended and/or complete core damage, given continuing loss of heat removal.

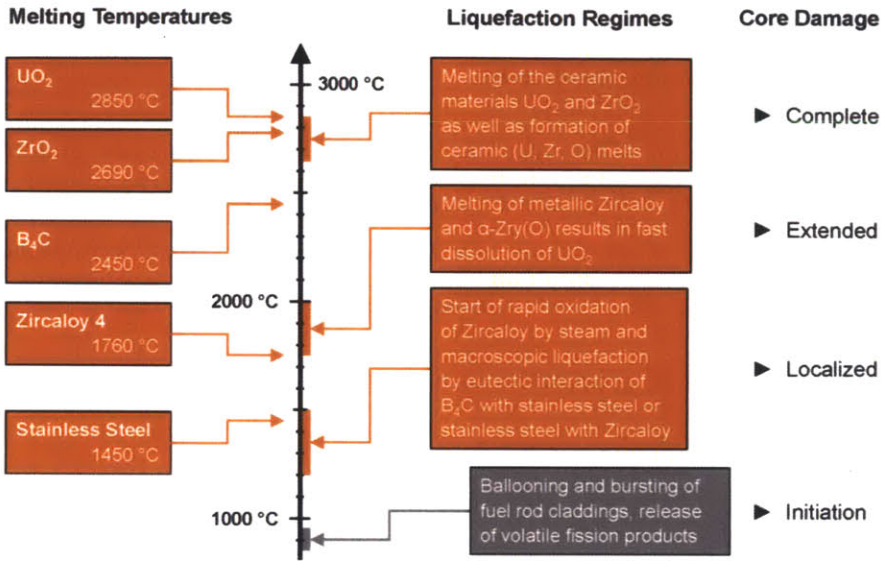

Figure 1-3 Core Materials Degradation Temperature Regime (Arnold, 2011)

Zircaloy cladding integrity is further challenged during a LOCA by thermal shock by the injection of cold emergency reflooding water. Formation of brittle phases including the Zircaloy oxide layer (ZrO_2) and oxygen-saturated α-phase Zircaloy substrate as a result of high temperature steam oxidation promotes brittle fracture when they are quenched in cooling water (Chung, 2005), (Hobson & Rittenhouse, 1972). Essentially, the current criteria of fuel rod safety during postulated LOCAs (NRC, 2013) proscribe the brittle fracture of zirclaoy cladding upon quenching during refloods.

In addition, the hydrogen, that is generated as a result of the rapid oxidation of Zircaloy with steam, can cause a detonation or deflagration if certain conditions are met in terms of relative air, hydrogen, and water vapor contents. The concern for hydrogen generation with Zircaloy-steam reaction during LOCA has emerged as a serious technical issue experienced in real accidents since the Three Mile Island (TMI) accident in 1979. At TMI-2, a large quantity of hydrogen was generated as a result of Zircaloy-steam reaction during LOCA (Henrie, 1987). The produced hydrogen accumulated in the upper dome of the reactor vessel and difficulty occurred when removing the produced hydrogen using a recombiner and, arguably, by venting to the atmosphere (Henrie, 1982). In the Fukushima accidents in 2011, the hydrogen generated from the Zircaloy-steam reaction made the consequences of the accidents much worse.

Extensive hydrogen explosions destroyed the reactor containment as well as damaging the vessel, leading to unconstrained release of radioactivity to the environment. The Fukushima accidents have sparked rethought about the use of Zircaloy cladding with an emphasis on hydrogen generation via high temperature steam oxidation.

Today, LWRs are facing fundamental challenges with the current fuel cladding material for further improvements in both safety and productivity, given that these recently revisited technical issues in accidents and operation are fundamentally rooted in the inherent material characteristics of Zircaloy itself. Under this situation, very little can be expected from adjustments of operating conditions or minor improvements in cladding material quality. The nuclear community is calling for a more fundamental solution.

1.3 Philosophy of Accident-Tolerant Nuclear Fuel

In the past, advanced LWR nuclear fuel developments tended to be primarily driven by interest in operational productivity, given that no major accidents whose consequences were severely exacerbated by fuel-tolerance had taken place before the Fukushima accidents in 2011. With the occurrence of the disastrous hydrogen explosions in the Fukushima accidents, recognized limitations of LWR fuel performance began to be considered from the view point of nuclear safety.

LWR safety has been historically addressed in one dimensional frame; safety assurance principles have predominantly relied upon safety assurance systems which are not the subject of accidents. These safety assurance systems include ECCS, hydrogen recombiner, and even actions of human intervention. The safety assurance mechanisms are usually further fostered by redundancy. Extensive studies and improvements have been made to safety assurance systems to lower the risk of accidents. This one dimensional approach for nuclear safety by leveraging redundant safety assurance systems had been believed to be ultimately reliable until recently. The recent accidents, including Fukushima and TMI, revealed that the one-dimensional reliance on safety assurance systems can actually leave the reactor essentially unprotected when the safety assurance systems fail. Despite extremely low probability of failures of redundant safety assurance systems, failures did happen. This occurs when a serial alignment of multiple holes in the postulated assumptions and neglected cause of dangers takes place - the profound limitation in the current safety assurance mechanism. Ideally, a brute-force way of assuring safety is to make nuclear fuel - the source of heat and radiation –more robust under accidents.

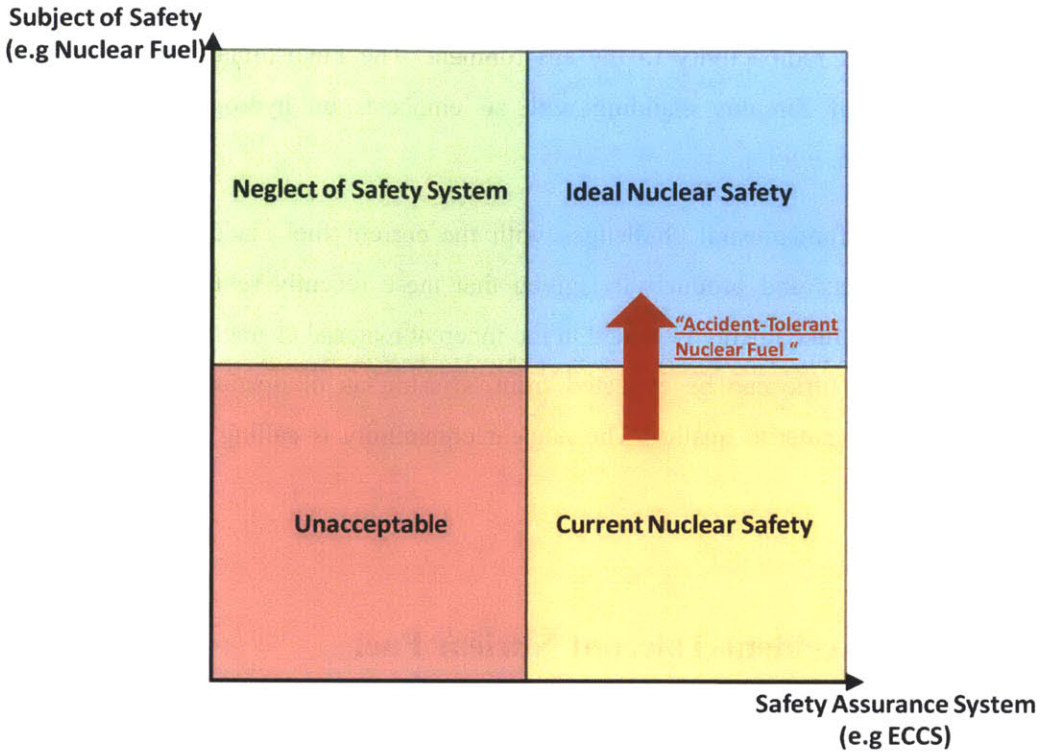

Figure 1-4 Nuclear Safety Assurance Principles and Role of Accident-Tolerant Nuclear Fuel

This study proposes to make the nuclear fuel, the subject of accident (a major component in an accident), as a new axis on the current nuclear safety assurance efforts, in a sense that its performance during accidents is regarded with highlighted attention equal to that given to safety assurance systems, as illustrated in Figure 1-4. It is a multi-dimensional safety assurance principle that covers the subject of accidents as well as safety systems. The proposed approach implies considering accident-tolerance of nuclear fuel as equally/or more important a criterion as its performance during steady-state operations. Developing LWR fuel rods of enhanced accident-tolerance without sacrificing their operational performance will significantly lower the risk of accidents for both DBAs and severe accidents. Enhanced accident-tolerance of nuclear fuel will expand the range of manageable accidents with the current safety assurance systems, and even address accidents that are currently regarded as severe accidents.

1.4 Silicon Carbide Cladding as a Solution

Understanding that zirconium-based cladding has become an impediment for further advancement of LWR fuel, this study investigates Silicon Carbide (SiC) as a replacement for the current zirconium-based

cladding for LWRs, as an effort to make LWR fuel more accident-tolerant. The preferred composition of the SiC cladding is a SiC monolith laminated with a SiC/SiC composite structure as shown in Figure 1-5 (Stempien, 2011)

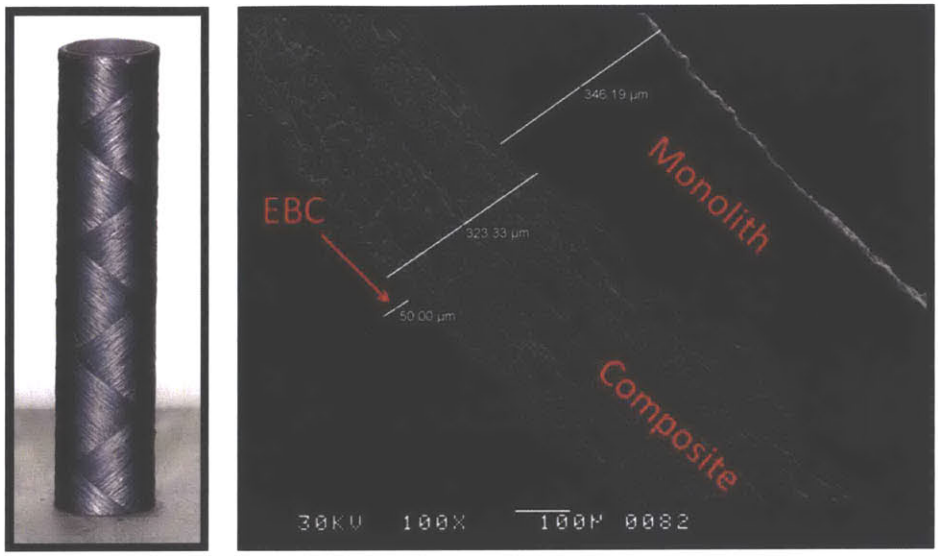

Figure 1-5 Laminated Layers of SiC Monolith/SiC Composite Cladding (Stempien, 2011)

The innermost layer is made of monolithic SiC to serve as a primary structure for fission gas retention. The monolith is surrounded by a SiC/SiC composite layer, which is composed of wound reinforced silicon carbide fibers, as shown in Figure 1-6 (Snead, 2004).

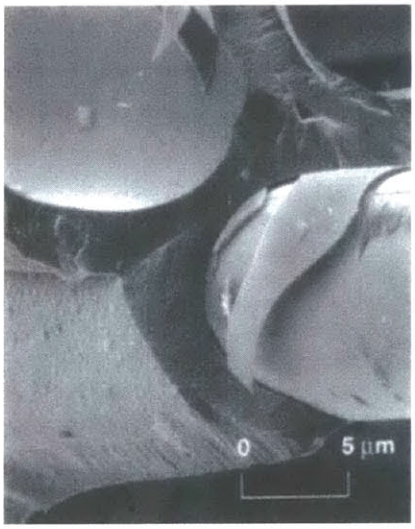

Figure 1-6 Magnified View of SiC Fiber Composite Structure (Snead, 2004)

SiC fiber composite, characterized with roughly an order of magnitude higher fracture toughness (25-30 MPa $m^{1/2}$) than the monolith (2.5-3MPa $m^{1/2}$), gives the brittle ceramic cladding an extra capability to arrest propagating cracks (Snead, 2004). In addition, interfacial frictions between the fiber and the ceramic matrix render pseudo-plasticity that functions as a structural ductility (Katoh, 2007), (Nozawa, 2011), (Nozawa, 2012). The outermost surface of the SiC cladding is deposited with environmental barrier coating (EBC) to avoid corrugated textures of composite, which might promote reactions in SiC strands. This preliminary SiC monolith/SiC-SiC composite cladding design is based on judgement of anticipated in-service behavior. Final designs would have to be based on actual test and performance data.

SiC is a well-known high temperature refractory material. Its melting temperature is 2730°C, roughly 1000°C higher than the melting point of Zircaloy-4 cladding (1760°C). While strength of Zircaloy decreases about 2% for every 10°C above 300°C, and the elastic modulus 1% for every 10°C (Carpenter, 2010), CVD SiC exhibited no significant degradation of strength up to 1500°C, and even an increase above 1100°C with approximately a maximum 10% degradation of elastic modulus at 1500°C (Snead, 2007). SiC is regarded as a more chemically stable material than Zircaloy because in general covalently bonded ceramic atomic structures are less reactive than metallic bonded materials. Also, SiC is physically stable at high temperatures and under irradiation, as demonstared in its use as a pressure boundary in TRISO particles in gas cooled reactors and as a potential fusion reactor blanket material. Details of material property dependence on temperature and irradiation will be addressed in the fuel modeling discussions below. The discussed properties are favorable aspects of SiC over zirconium alloy from a safety point of view. During operations, SiC cladding may be more transparent to neutrons/ or equally transparent than zirconium-alloy cladding.

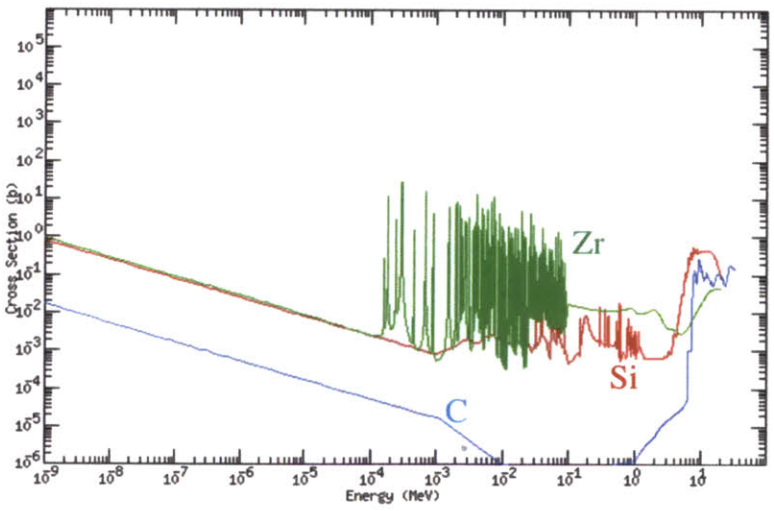

Figure 1-7 Total Absorption Cross Sections for Zirconium (Zr), Silicon (Si), and Carbon (C) (KAERI)

Figure 1-7 shows that the absorption cross sections for silicon and carbide show that silicon and carbon present smaller total absorption cross section than zirconium (Zr) except for fast neutrons. However, SiC is a brittle ceramic material and has a lower thermal conductivity than Zircaloy, particularly after irradiation. Thus, its use in reactors should be subject to a careful evaluation that evaluates probable failure modes as well. Use of silicon carbide cladding may present increasing safety margins by leveraging favorable structural tolerance at high temperatures while imposing new failure modes associated with brittle fractures.

1.5 Previous and On-going Studies on SiC Cladding for LWRs

Consideration of using SiC cladding for LWR fuel rods has been drawing international attention, particularly since the Fukushima accidents in 2010. Today, several research agencies over the world are investigating different aspects of the use of SiC cladding for LWRs. Extensive SiC data can be found from past studies primarily conducted for TRISO fuel applications in high temperature gas cooled reactors (HTRs) and many of them are applicable for LWRs. This section summarizes key results of investigating SiC as cladding material for LWRs.

1.5.1 SiC Properties for Nuclear Fuel Studies

In the early stage of advanced fuel development, a priority is placed on attaining relevant fuel performance related material properties. Extensive experience and studies conducted with SiC in TRISO particles can be readily used for LWR fuel performance. A widely used summary of fuel performance relevant properties of SiC is work published by Snead et. al (Snead, 2007), which can be used to obtain properties for monolithic SiC. For SiC-SiC fiber-reinforced composite, studies conducted in consideration of fusion applications can be utilized (Katoh, 2007), (Nozawa, 2011), (Nozawa, 2012), (Katoh, 2011), (Katoh, 2010).

1.5.2 SiC Cladding Irradiation

The thermal neutron spectrum in LWRs, when coupled with LWR water chemistry, may lead to different behavior of SiC from what was observed in HTR environments. Carpenter investigated performance of SiC-cladding (monolith and SiC monolith/SiC composite) under a neutron-radiation field similar to that

of typical light water reactors using the MIT Nuclear Reactor (MITR-II) (Carpenter, 2010). In his study, post-irradiation examination found some SiC specimens had acceptably low irradiation-enhanced corrosion rates and predictable swelling behavior. However, other specimens did not fare as well and showed excessive corrosion and cracking. He concluded that the performance of the SiC cladding will depend on appropriate selection of manufacturing techniques. This can be interpreted as a "not-negative" statement of SiC cladding performance as manufacturing techniques can be developed to address the need of cladding performance. If the source of poor performance can be identified then, assuring that it is manufacturing related, the process can be adjusted.

As a continuing effort on SiC irradiation, Stempien assessed the behavior of Triplex SiC fuel cladding designs tested under simulated PWR conditions (Stempien, 2011). In his study, mechanical testing revealed significant a strength reduction in the Triplex samples due to irradiation-induced point defects, corrosive pitting of the monolith, and possible differences in the behavior of the Triplex components. Some manufacturing abnormalities were also discovered which could have compromised strength. In his study thermal diffusivity measurements of the Triplex material showed substantial decreases with irradiation (saturating at about 1 displacement per atom, dpa) due to the accumulation of phonon-scattering defects and corrosion of SiC. Measured saturated thermal conductivity of Triplex SiC after irradiation was lower (~4.8W/m-k) than the monolith conductivity (~10-20 W/m-k) because the thermal conductivity of fiber composite is lower than that of the monolith. Also, carbon coated SiC fibers behave differently from matrix SiC under irradiation fields in terms of swelling, and thermal expansion etc, causing voided sites which aggravate thermal conductivity decrease in the fiber composite SiC.

Although the SiC irradiation experiments conducted at MITR-II simulate irradiation effects with LWR water chemistry, they have limited capabilities in exploring high burnup effects on SiC cladding as their irradiation doses were limited to around 1 dpa. This implies that material behavior and properties that do not saturate within 1dpa are subject to uncertainties. For this concern, extensive SiC irradiation experimental data obtained in consideration of HTR and fusion reactor applications can be useful if effects of LWR water chemistry on SiC cladding can be separately understood. In particular, radiation damage that SiC in TRISO would receive in an HTR will be roughly the same level with LWR conditions (<50 dpa) as they depend on thermal neutrons as illustrated in Figure 1-8 (Yvon, 2009).

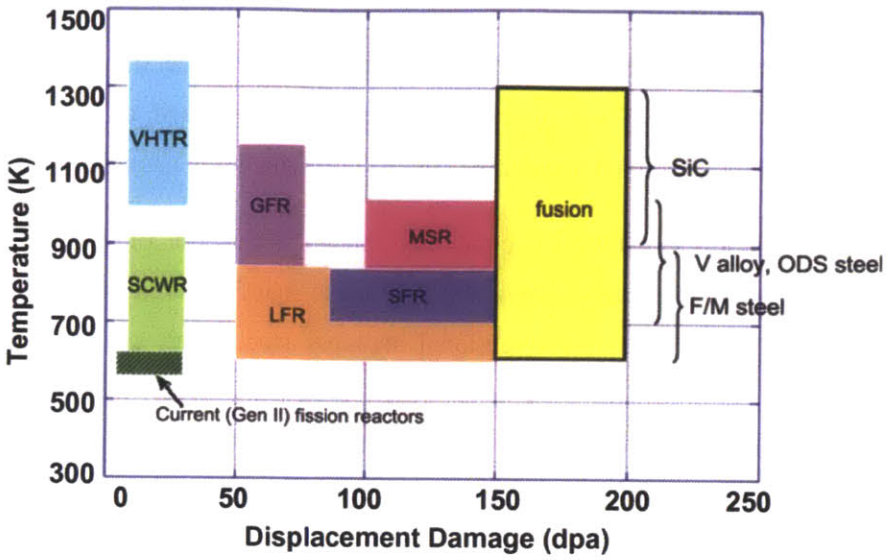

Figure 1-8 Operating Temperature and Radiation Damage for Different Reactor Systems (Yvon, 2009)

"Handbook of SiC properties for fuel performance modeling" summarized by Snead.et al (Snead, 2007) is a widely used text that includes relevant SiC properties for fuel modeling. The paper shows that a high purity CVD SiC exhibits irradiation tolerant strength with evidence of even strengthening effects at 573-1273K, possibly due to irradiation-induced modifications in the flaw characteristics, surface changes, and relaxations of manufacturing induced stresses. In that work, it is stated

"The strength of SiC depends significantly on stoichiometry under neutron irradiation. Both the sintered SiC and the reaction bonded SiC forms exhibit significant deterioration in strength by neutron irradiation. The presence of impurities such as sintering additives for sintered SiC and excess Si for reaction bonded SiC, which typically segregate to grain boundaries, have a significant influence on strength under neutron irradiation. For the case of sintered SiC with boron compounds as sintering additives, the reaction of ^{10}B (n,a)^{7}Li causes the accumulation of helium bubbles near the grain boundaries under neutron irradiation. In contrast, anisotropic swelling between Si and SiC for reaction bonded SiC causes disruption at the grain boundary, severely reducing the strength".

This finding is consistent with Carpenter's observations - the performance of the SiC cladding will depend on appropriate selection of manufacturing techniques.

1.5.3 SiC Cladding Oxidation

Extensive SiC oxidation studies have been conducted related to high temperature refractory applications such as gas combustion engines. These investigations will be discussed to help understand steam oxidation with SiC under loss of coolant accidents (LOCAs) presented in Chapter 2 and Chapter 3.

Oak Ridge National Laboratory (ORNL) conducted steam oxidation of SiC in LWR accident environments (Terrani, 2012). This study shows that SiC offers significant reduction in oxidation rates in comparison with zirconium alloys and conventional stainless steels with system pressure dependent material loss. However, the SiC/SiC composite experienced substantial strength degradation with oxidation, because steam ingress between fibers (PyC layer) quickly degraded the material, implying that the integrity of SiC/SiC composite is governed by the CVI overcoat & EBC. Indeed, strength of fiber composite SiC has been shown to be subject to degradations with oxidation by several studies conducted in the past (Filipuzzi, 1994), (Ogbuji, 1998), (Gilme, 1998), (Yin, 2001). The strength degradations of SiC composite occurs primarily by degradation of the carbon coating of the SiC fiber, which provides interfacial friction with the SiC matrix. In the early phase of oxidation of the thin carbon interface, silica (SiO_2) quickly fills the pores created by loss of carbon. In this case, material strength degradation is limited as filling silica provides the material with a self-healing character. However, extended oxidation time leads to local stress concentrations from the SiC/SiO_2 conversion that fills the gap between matrix and fibers, leads to substantial strength degradation (Gilme, 1998). Oxidation of the carbon interface of fiber-reinforced SiC composite was observed to be evident at 700°C without the presence of coating material and even more substantial weight loss of the material occurred at temperatures beyond 1250°C due to decomposition of the ternary SiC_xO_y phase present in Nicalon fibers (Filipuzzi, 1994). From these studies, one can infer that unless properly coated, fiber-reinforced SiC composite SiC cladding has a possibility of introducing more problems than the structural benefits it brings at high temperature. CVD coating of the fiber composite is a commercially available option to prevent oxidants from gaining access to the SiC fibers of the composite. A few α-phase SiC samples were oxidized with steam at 1200°C under a laminar flow condition at MIT and the results showed orders of magnitudes slower oxidation rate for α-SiC in comparison with Zircaloy-4 (Arnold, 2011). Similar results were also obtained by Ceramic Tubular Products (CTP) with various types of SiCs (Feinroth, 2012).

For oxidation of SiC under steady-state conditions, an experiment was conducted in 290°C water with sintered SiC (mainly α-SiC) under varying pH levels (Hirayama, 1989). The study showed non-negligible material loss from sintered SiC with increasing pH and dissolved oxygen concentration. A comprehensive study for steady-state SiC oxidation in LWR conditions can be found in Carpenter's work (Carpenter, 2010). In his experiment, α-SiC, β-SiC, and Triplex SiC were exposed to typical LWR neutron spectrum,

the same coolant temperature range, and flow velocities for up to several months – a completely realistic set of SiC cladding oxidation conditions under steady state. The results of the experiment show significant variations between different types of SiC. Some SiC samples were found to be almost dissolved in water whereas high quality SiC, in terms of impurity and stoichiometric balance, showed negligible oxidation reaction. Again, this observation shows the importance of SiC manufacturing technologies for SiC cladding in LWRs.

1.5.4 SiC Cladding Neutronics Core Design

It is hoped that SiC cladding can substitute for the zirconium-based material with minimal changes in the current core design of LWRs. A neutronic core design study was conducted by Dobisesky et.al (Dobisesky, 2011) with UO_2 fuel and SiC cladding in a standard Westinnghouse 4-loop PWR using the Studsvik Core Management System code (CASMO-4E, CMS-Link, and SIMULATE-3). Results show that a reactor core with SiC cladding could achieve the desired operating cycle lengths and target values for reactor physics parameters limited by NRC rules, with the maximum average discharge burnup of 80MWd/kgU. A similar core design study is currently being investigated with a thicker cladding size and various fuel types & designs (Bloore, 2013).

1.5.5 Fuel Performance with SiC Cladding

Steady-state fuel performance was investigated using U.S NRC's fuel performance code FRAPCON-3.3, modified for use with SiC cladding by Carpenter et.al (Carpenter, 2010). This study showed extended gap closure time and about 200°C higher fuel center line temperature for fuel rods with SiC cladding. The study proposed having a central void in fuel pellets or different fuel designs with better heat transfer features to minimize the temperature penalty. Westinghouse is investigating use of uranium-nitride based fuels with SiC cladding for LWRs due to its high thermal conductivity and high density (Lahoda, 2012). ORNL and Korea Atomic Energy Research Institute are jointly studying to apply fully ceramic micro encapsulated ceramic fuels in either SiC or stainless steel cladding for LWRs (Snead, 2012), (Lee Won Jae, 2013), (Lim, 2013). General Atomics (GA) is studying fuel rod behavior of SiC clad fuel pin in LWR using the FEMAXI code updated with SiC properties (Choi, 2013). MIT is investigating different fuel types and designs with FRAPCON-3.4 including a UO_2-BeO mixture pellet with SiC cladding for its high thermal conductivity (Kazimi, 2013).

1.5.6 End-cap Joining of SiC Cladding

Joining SiC cladding end-caps has been one of the main material issues with the concept. Three SiC/SiC bonding methods (six samples total) were irradiated in the MITR-II to 0.2 dpa, and five of the six samples failed. SEM analysis indicated radiation induced degradation of the bond material. Dimensional and volume measurements identified the anisotropic swelling of the two SiC specimens in each bond sample, which would have caused shear stresses on the bonds, contributing to their failure (Stempien, 2011). General Atomics developed high purity β-SiC joints for LWR cladding by hybrid CVI (Chemical Vapor Infiltration) preceramic polymer which combines polymer and CVI (Khalifa, 2012). This technology has a potential for overcoming problems in current SiC joining technologies – glass ceramic joints, NITE SiC, diffusion bonding with metal insert, and brazing. These technologies may pose structural issues under LWR environments due to residual amorphous structure, radiation damage due to impurities, multiphase metallic composition and the presence of elemental free silicons. Nevertheless, the strength of the hybrid CVI preceramic polymer must be improved beyond the current level (10~20MPa in shear strength) for use in LWR fuel rod applications. It is worth noting that bonding SiC/SiC is a proven technology. Yet, further development should be addressed in terms of its tolerance under LWR operating conditions with irradiation damage. Laser-weld of SiC (Knorr, 2008)and brazing weld method (Chaumat, 2006) has been used by industry in applications of SiC material in high temperature and in highly corrosive environment, including heat exchangers. Snead et. al (Snead, 2013) reported irradiation tolerant SiC/SiC joining for fusion reactor structural and fission clad application that exhibits a shear strength of ~350 MPa on average under 500°C for 3.0 – 3.4 dpa. This is a very positive result and further investigations are needed to characterize the statistical strength distribution of the joint.

1.5.7 Other On-Going Studies on SiC Cladding for LWRs

Feinroth investigated mechanical shock resistance of SiC cladding (Feinroth, 2013). His results show that the fiber architecture has been improved, and a crack inhibiting barrier between the composite layer and the monolith layer can provide sufficient mechanical shock resistance. The French Alternative Energies and Atomic Energy Commission (CEA) recently extended their SiC composite research programs to PWR cladding applications (Brossard, 2012). Their research focus consists of fabrication, leak-tightness (micro-cracking, and welding), mechanical resistance, and material compatibility (fuel, and coolant). Also, AREVA is participating in SiC cladding projects with CEA (Strumpell, 2012).

In addition, research activities are being conducted by a number of other major research institutions over the world to evaluate SiC's preliminary characteristics as cladding material for LWRs. Yet, quantification of its key performance parameters as well as feasibility have not been addressed systematically.

1.6 Thesis Objectives

A systematic approach to safety assessment of SiC cladding for LWRs is timely. An in depth safety assessments of SiC cladding fuel and reactor behavior during steady-state and accident situations remain essentially unexplored. The objective of this thesis can be abbreviated in one sentence as follows:

"Quantitatively assess performance of LWR fuel rod with SiC cladding in terms of its safety and evaluate its feasibility".

Such an assessment should examine service of the cladding material in the unique operating environment of LWRs. To systematically achieve the goal, the scope of the work is divided into two steps:

(1) Quantify and formulate physical mechanisms of key safety-related phenomena affecting the SiC cladding through experiments and modeling. In this study, the following were focused on: (a) SiC-steam oxidation during loss of coolant accidents and (b) SiC brittle fracture under tensile stresses upon fuel pressurization and post-LOCA quenching as two pivotal physical mechanisms to understand safety, operation, and feasibility of use of SiC cladding for LWR fuel rods.

(2) Analyze fuel rod behavior with SiC cladding through simulations during steady and accident conditions using experimental data and models developed in (1). Identify design strategies of SiC cladding to maximize its performance in terms of safety and operation.

This study takes a holistic approach that connects experiment, modeling, and simulations. Explanations of specific approaches are discussed in each chapter.

1.7 Thesis Organizations

The organization of the thesis is made to reflect information flow and contents illustrated in Figure 1-9.

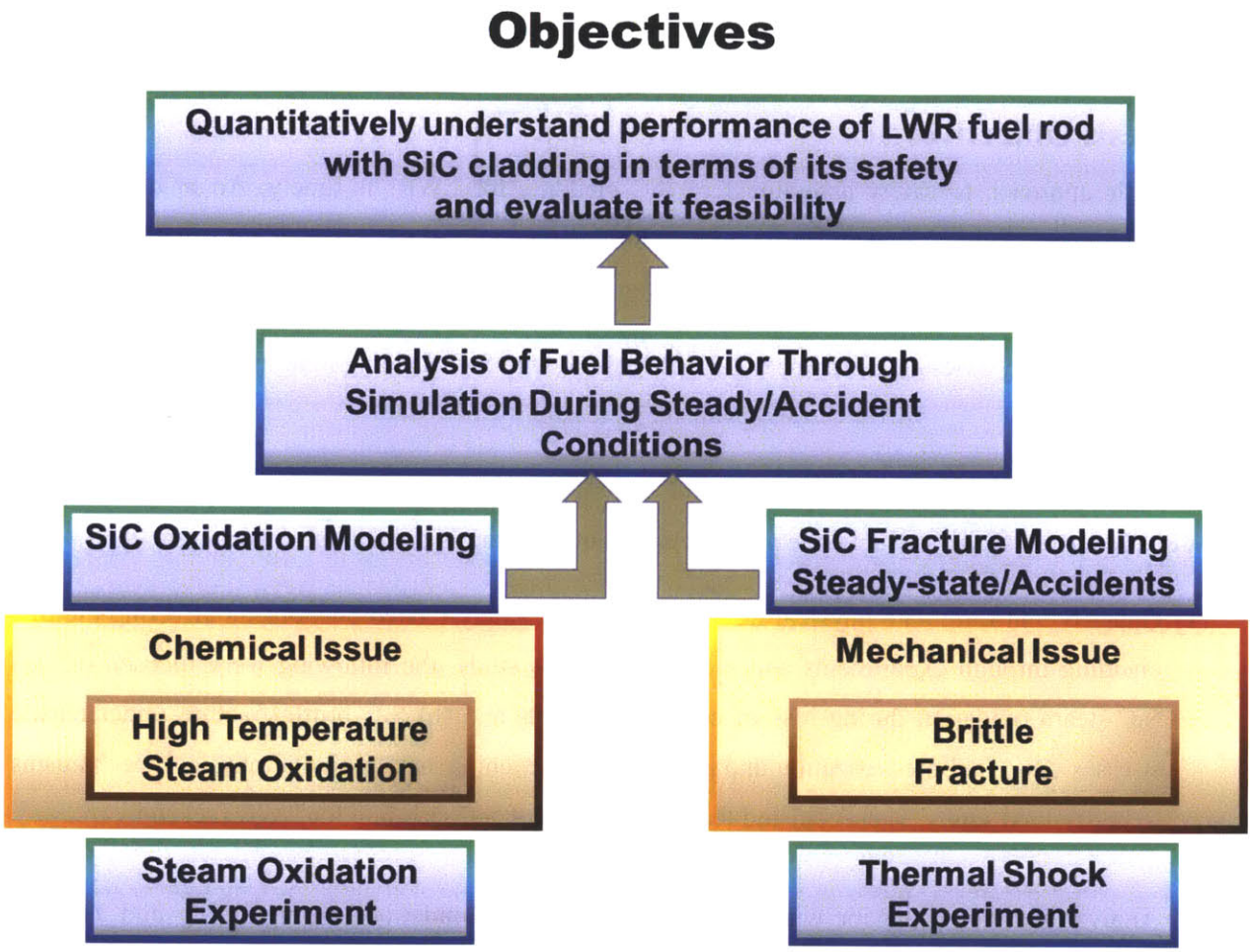

Figure 1-9 Schematic of Contents of the Thesis

Chapter 2 – SiC Cladding steam oxidation I: Experiment

This chapter discusses procedures, and results of SiC steam oxidation experiments. The experiments investigated SiC weight loss rates, material microstructure changes with scanning electron microscopy (SEM), and effects on material strength by destructive tests of material to high temperature steam.

Chapter 3 – SiC Cladding steam oxidation II: Theories and Models

This chapter identifies and discusses factors that affect SiC weight loss rates under steam environment based on the experimental data developed in Chapter 2. Development of correlations for SiC weight loss as a function of the relevant factors is discussed. The developed correlations capture unique chemical and mass-transfer effects seen in the steam environment. Further, the use of developed correlations as well as their implications for designing SiC cladding is discussed.

Chapter 4 – Brittle Fracture of SiC Cladding I: Statistical Fracture Model

This chapter explores the development of a SiC cladding statistical fracture model with Weibull statistics under tensile loading conditions. Implications of the developed statistical model on SiC cladding failure modes under steady-state and accident conditions are discussed.

Chapter 5 – Brittle Fracture of SiC Cladding II: Thermal Shock Experiments

Procedures and results of thermal shock experiments of SiC cladding under a prototypic LOCA reflood phase are discussed. The investigation covers strength changes of quenched SiCs, material microstructure analysis with SEM, and high speed video camera observation of heat transfer modes during the quenching moments.

Chapter 6 – Brittle Fracture of SiC Cladding III: Thermal Shock Fracture - Theories and Models

This chapter discusses thermal shock fracture theories to explore the potential microstructure and heat transfer origins of SiC thermal shock fractures observed in Chapter 5. SiC thermal shock fracture models are developed to be used in simulations of LWR fuel rods of SiC cladding during LOCA in Chapter 7.

Chapter 7 – Simulation of Light Water Reactor Fuel With SiC Cladding

This chapter discusses fuel rod simulations of SiC cladding with conventional fuel rod simulation codes modified for use with SiC cladding, a developed transient thermo-mechanical code, and obtained experimental data from previous chapters and models. Steady-state fuel rod behavior with SiC clad was

investigated using FRAPCON-3.4 modified with SiC cladding properties, with a feed of fuel pin power history from a previously conducted SiC fuel core optimization study and the developed statistical SiC failure models under tensile stresses in Chapter 4. Also, RELAP-5 was run with SiC cladding properties during a simulated large break LOCA for generating thermal hydraulic inputs in a limiting accident scenario. A transient thermo-mechanical code that runs with inputs from (a) burnup initialized parameters from FRAPCON-3.4 SiC, (b) thermal hydraulic conditions during accidents from RELAP, and (c) developed models for SiC strength failure modes under tensile stresses in Chapter 4 was developed. Safe operation envelopes and limits were explored with conservatively varying nuclear fuel rod designs with SiC cladding.

Chapter 8 – Summary of Conclusions, and Recommendation for Future Work

Design implications and strategies for LWR fuel rods fabricated using SiC cladding are summarized with the goal of maximizing its safety margin and operational benefits. Characteristics of SiC cladding performance in terms of its operation and safety are evaluated in comparison with the current zirconium alloy cladding. Key future studies are discussed.

Chapter 2

SiC Cladding Steam Oxidation I: Experiment

2.1 Introduction

This chapter presents and discusses experimental work that was conducted to study SiC oxidation during LOCA conditions. Current light water reactors (LWRs) are designed to ensure compliance with safety-related regulatory criteria specified for accident situations such as loss of coolant accident. Such criteria are usually established on the basis of the performance of the fuel rod under accident conditions as it is the primary source of radioactivity and heat. The current regulations impose criteria for the performance of zirconium alloy clad fuel rods. The current U.S NRC LOCA criteria stated in the Code of Federal Regulation, Title 10, Part 50.46, "Acceptance Criteria for Emergency Core Cooling Systems (ECCS) for Light-Water Nuclear Power Reactors" (10CFR50.46) consists of five separate limits or requirements as stated in section 1.2.2.

Although the specific safety criteria listed above are subject to changes resulting from the SiC fuel design and the potential changes this brings to reactor operation (e.g high fuel burn-up and longer fuel cycle), the principles of LWR safety during LOCA conditions underlying the current criteria would still apply to the new cladding material.

It is worth noting how pervasive were the effects of cladding oxidation in the establishment of the current U.S NRC LOCA criteria. Indeed, the fundamental mechanism of cladding embrittlement of Zircaloy during LOCA conditions is due to micro-structural modification of the cladding due to oxidation (Parker, 1965). That is, the oxidized cladding cross section exhibits an oxide layer, an oxygen-stabilized alpha-phase layer, and a region of prior beta-phase. Importantly, oxidation of Zircaloy above the alpha-to-beta transformation temperature results in inherently brittle phases for the regions affected by oxygen. Hence, ductility of Zircaloy cladding is significantly impaired with oxidation and embrittlement can lead to cladding fragmentation during the quenching phase in a LOCA. The ability of the cladding to withstand the thermal shock stresses during the reflood phase of LOCA is closely related to the degree of oxidation reaction (Chung, 2005), (OECD/NEA, 2009). The current allowable peak cladding temperature (1204°C) and the maximum oxidation (17% Equivalent Cladding Reacted (ECR)) criteria were chosen in such a

context – these limits are adequate to ensure survival of the cladding under the thermal shock during reflood phase of LOCA (Hobson & Rittenhouse, 1972), (Hobson, 1972). The maximum hydrogen generation limit is also affected by cladding oxidation. The coolable geometry criterion predominantly concerns the change in coolant channel geometry due to potential blockages through brittle cladding failure or super-plastic deformation. Cladding brittle failure is predominantly caused by lower ductility as a result of oxidation during LOCA. The long-term cooling criterion is also affected by cladding oxidation as the oxide layer formed on the cladding surface lowers the cladding thermal conductance.

From the above it is evident that cladding oxidation is a key performance metric, which significantly affects almost every aspect of the current LOCA criteria established for Zircaloy cladding. Thus assessment of oxidation performance of a new cladding candidate is an indispensable step to understand its safety performance in comparison with the current Zircaloy cladding, as well as development of new safety criteria for SiC in a LOCA scenario. The objective of this study is to (1) experimentally explore phenomenological aspects of silicon carbide (SiC) cladding oxidation behavior under conditions representative of a LOCA and (2) assess its ramifications on reactor safety by identifying key phenomena and safety criteria for the SiC cladding.

2.2 SiC Oxidation Mechanism

At high temperature, SiC reacts with water vapor. The reaction of SiC with water vapor can be categorized into the following two reactions.

$$SiC\ (s) + 3H_2O\ (g) = SiO_2\ (s) + CO\ (g) + 3H_2\ (g) \quad (2\text{-}1)$$

$$SiC\ (s) + 2H_2O\ (g) = SiO\ (g) + CO\ (g) + 2H_2\ (g) \quad (2\text{-}2)$$

Reaction (2-1) is termed "passive oxidation" and leads to the formation of a protective silica (SiO_2) scale on the silicon carbide. When the environment contains low oxidant pressures such that SiO_2 cannot form, the SiC reaction with water vapor proceeds along reaction (2-2). This type of behavior is termed "active oxidation" (Singhal(A), 1976).

The criteria for the transition to active oxidation are discussed in several studies (Opila, 1995), (Wagner, 1958), (Singhal(A), 1976). The "active oxidation" occurs when water vapor partial pressure is far below atmospheric ($\sim 10^{-4}$atm). Therefore, most engineering applications undergo reaction (2-1), "passive oxidation". Use of SiC cladding for LWR nuclear power generation is not an exception, and in this study, SiC undergoes passive oxidation when in contact with the low pressure and high temperature steam.

The silica scale (SiO_2) formed on SiC may simultaneously volatilize by forming a silicon hydroxide or silicon oxyhydroxide species. Some possible volatilization reactions are (Opila, 1997)

$$SiO_2 + H_2O\,(g) = SiO(OH)_2\,(g) \quad (2\text{-}3)$$

$$SiO_2 + 2H_2O\,(g) = Si(OH)_4\,(g) \quad (2\text{-}4)$$

$$2SiO_2 + 3H_2O\,(g) = Si_2O(OH)_6\,(g) \quad (2\text{-}5)$$

The kinetics of the oxidation reaction are described by the parabolic rate constant of oxide formation, Kp, whereas the kinetics of the volatilization reactions are described by the linear rate constant for oxide volatilization, K_l (Opila, 1997) as illustrated in Figure 2-1.

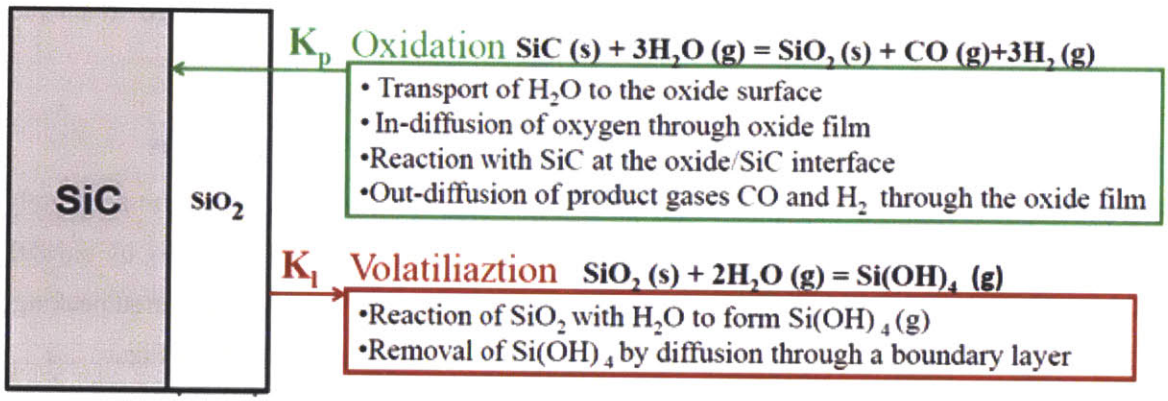

Figure 2-1 Schematic of SiC Oxidation Mechanism[2]

These simultaneous reactions, one forming SiO_2 and the other removing SiO_2, are described by paralinear kinetics developed by Tedmon, Jr (Tedmon, 1966) and given in Eq.(2-6)

$$\frac{dx}{dt} = \frac{K_p}{2x} - K_l \quad (2\text{-}6)$$

At steady state, in which these reactions occur at the same rate, if it is achieved, the oxide found on the surface would have a constant thickness (x) with time (t), and the recession of the underlying material occurs at a linear rate. The oxide scale thickness parabolically grows until it reaches the limiting value $K_p/2K_l$. The SiC recession rate, hence weight loss, closely follows a linear behavior as the oxide thickness gets closer to its limiting value. The linear SiC recession rate, once observed, is practically the same as the SiO_2 volatilization rate.

[2] Volatilization reaction is regarded as a surface reaction, hence diffusion of oxidants into silica is omitted

Modeling of the parabolic rate constant, K_p, has been well achieved by previous research of oxidation of silicon (Si) (Deal, 1965), and in an associated study of SiC by Song.et.al (Song, 2004). In essence, the key step for modeling of K_p is the calculation of the diffusion coefficient of the oxidant species in the oxide scale. Generally, studies of SiC oxidation have used the Chapman-Enskog theory (Geiger, 1973) to predict the diffusion coefficient. Understanding of the linear volatilization, K_l, is at an immature state. However, it is believed that the thickness of the fluid boundary layer on the material surface most strongly affects the volatilization rate of SiO_2, making the SiC recession dependent on flow characteristics. This is because the reaction rate is affected by the outward diffusion of volatile products through the fluid boundary layer. Modeling volatilization of SiO_2 has been restrictively conducted in previous studies, on the assumption of an infinite-flat surface for the SiC sample and other assumptions (Opila, Smialek, 1999) not relevant to nuclear fuel rods. Details of volatilization modeling will be discussed in chapter 3.

2.3 SiC Oxidation Under Beyond Design Based LOCA Conditions

For SiC oxidation studies, it is important to design an experimental facility that stimulates accurately the LWR accident environment. Usually the LOCA accidents involve loss of cooling ability by partially or completely uncovering the fuel rods. Hence, a simple, yet representative, partially uncovered peaking fuel rod was modeled to assess flow characteristics relevant to SiC oxidation as illustrated in Figure 2-2.

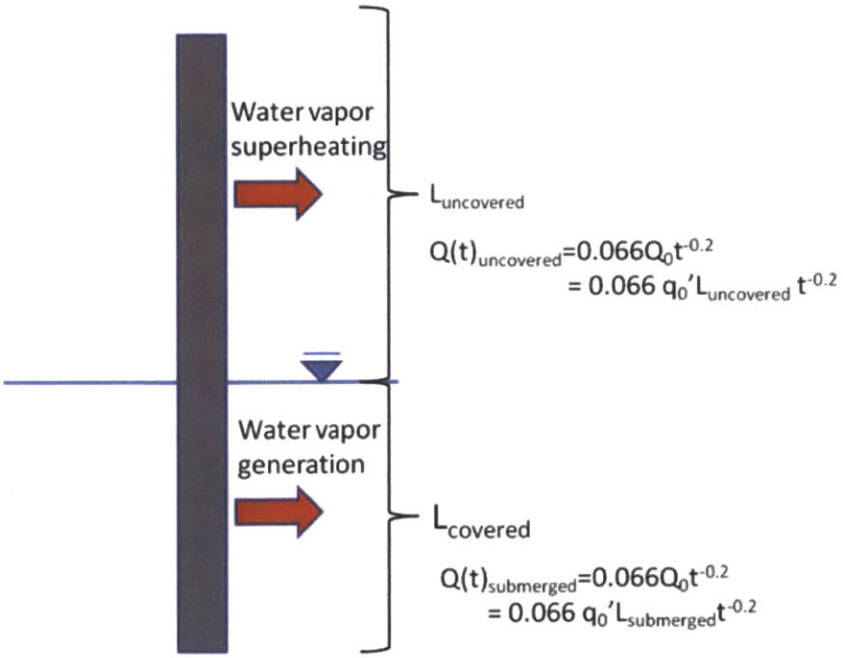

Figure 2-2 Schematic of an Uncovered Fuel Rod

The fuel pin with the highest heat generation rate (peak pin) in the 3411 MW(th) Sequoyah Westinghouse Pressurized Water Reactor (PWR) (Todreas, 2012) is modeled here. The reactor fuel rod design parameters used are shown in Table 2-1.

Table 2-1 Fuel Rod Parameters for 3411MW(th) Sequoyah Westinghouse Pressurized Water Reactor

Core Average Linear Fuel Pin Power	17.86 kW/m
Radial Peaking Factor	1.55
Axial and Local Peaking Factor	1.3
Active Fuel Length	3.658m
Fuel Outer Diameter	9.5mm
Fuel Rod Pitch	12.60mm

The fuel rod is assumed to be partially submerged, for variable fractions of the rod length, while generating decay heat at the rate of $P/Po=0.066t^{-0.2}$ (Todreas, 2012), where Po is the initial pin power and t in seconds.

The system pressure was assumed to be atmospheric after the blow down phase. The fraction of the fuel rod submerged contributes to the generation of steam while the pool of the water is at saturation and atmospheric pressure. The uncovered length of the fuel rod superheats the steam flowing from below. This scenario is shown in Figure 2-2. The situation is assumed to be a quasi-static process, with a fixed uncovered length. The decay heat is taken to be generated uniformly over the axial length of the fuel rod. Importantly, it is assumed that such a state, where the fuel rod being uncovered at atmospheric pressure, is reached 20 seconds after reactor shutdown, as the typical blow-down period of a large break (LB) LOCA is the initial 20 seconds of the accident (Hewitt, 2000). The following equations were solved for "t" ranging from 20 seconds to 72 hours. The use of 72 hours was based on the recently published U.S NRC's near-term task force recommendations[3] after review of insights from the Fukushima accident (NRC, 2011). Steam flow rate $\dot{m}_{steam}$ was generated at the saturated condition at atmospheric pressure by the decay heat of the submerged fraction of the rod.

[3] The near-term task force states *"Initiate rulemaking to revise 10 CFR 50.63 to require each operating and new reactor licensee to (1) establish a minimum coping time of 8 hours for a loss of all ac power, (2) establish the equipment, procedures, and training necessary to implement an "extended loss of all ac" coping time of 72 hours for core and spent fuel pool cooling and for reactor coolant system and primary containment integrity as needed, ...*(continue)", The development of 72 hours of oxidation performance of SiC cladding is useful or potentially required information for its safety assessment and licensing.

$$\dot{m}_{steam}(t) = \frac{\dot{Q}_{submerged}}{h_{fg}} = \frac{0.066 q_0{}' L_{submerged} t^{-0.2}}{h_{fg}} \tag{2-7}$$

where $\dot{Q}_{submerged}$ is heat generation of the submerged portion of the fuel rod, h_{fg} is heat of vaporization, $q_0{}'$ is initial linear pin power and $L_{submerged}$ is the submerged length of the fuel rod. The steam then flows upwards where it gets superheated along the uncovered fraction of the fuel rod by the decay heat of the rod. The exit steam enthalpy was calculated as follows.

$$h_{out}(t) = \frac{\dot{Q}_{uncovered}}{\dot{m}_{steam}} + h_g = \frac{0.066 q_0{}' L_{uncovered} t^{-0.2}}{h_{fg}} + h_g \tag{2-8}$$

where h_{out} is outlet steam enthalpy, $\dot{Q}_{uncovered}$ is heat generation of the uncovered portion of the fuel rod, $L_{uncovered}$ is uncovered length of the fuel rod and h_g is saturated steam enthalpy. Knowing the operating pressure and enthalpy, h_{out}, the exit steam temperature T_{out} can be obtained using steam tables

$$T_{out} = f(P, h_{out}) \tag{2-9}$$

Peak cladding surface temperature, $T_{peak,clad,}$ occurs at the exit since uniform decay heat generation rate in a fuel rod was assumed:

$$T_{peak,clad}(t) = \frac{q''}{h} + T_{out} = \frac{q_0{}' t^{-0.2}}{\pi D h} + T_{out} \tag{2-10}$$

where q'' is heat flux, h is heat transfer coefficient and D is fuel rod diameter.

A heat transfer coefficient, h in Eq. (2-10), of a constant value was used for fully developed laminar flow parallel to an array of circular tubes when the Reynolds (Re) number was smaller than 2300 (Todreas, 2012). For pitch/diameter ratio 1.326 for the PWR subchannel, the Nusselt number was found to be (Kakac, 1987)

$$Nu \approx 8 \tag{2-11}$$

Gnielinski's correlation (Gnielinski, 1986) was used for the transition region 2300<Re<5000. Heat transfer coefficients were multiplied by a correction factor (>1) that captures the rod bundle effect (Todreas, 2012)

$$Nu = \frac{\frac{f}{8}(Re - 1000)Pr}{1 + 12.7(Pr^{\frac{2}{3}} - 1)\sqrt{\frac{f}{8}}} \tag{2-12}$$

where Nu is the Nusselt number, Re is the Reynolds number, Pr is the Prandtl number and f is the Moody friction factor expressed by

$$f = \left(\frac{1}{1.8logRe - 1.5}\right)^2 \tag{2-13}$$

The Nusselt number for a circular tube in Eq.(2-12) is multiplied by a correction factor given by (Todreas, 2012)

$$\psi = 1 + 9.9120Re^{-0.1}Pr^{0.4}(1 - 2.0043e^{-B}) \tag{2-14}$$

where the Reynolds number (Re) is based on the equivalent hydraulic diameter (De) and velocity characteristic of the subchannels surrounding the subject fuel rod. The exponent B is given by

$$B = \frac{D_e}{D} \tag{2-15}$$

Using the above methodology, Figure 2-3 and Figure 2-4 show the fuel temperatures as a function of the submerged fraction of fuel length for various post LBLOCA times.

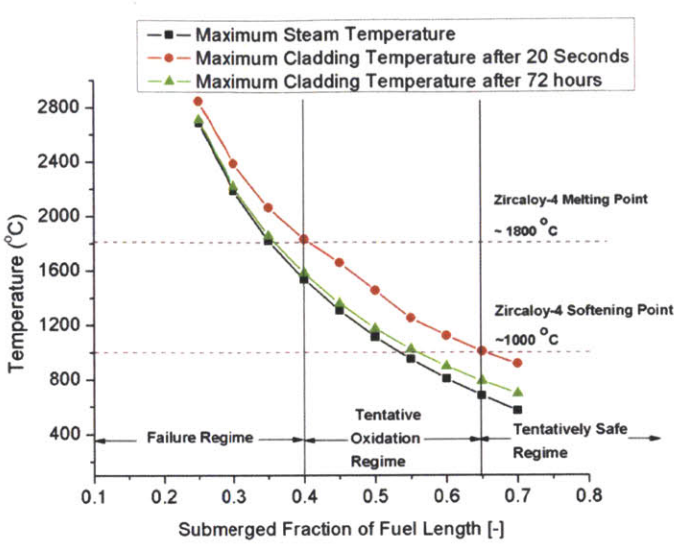

Figure 2-3 Oxidation Regime for Zircaloy-4[4]

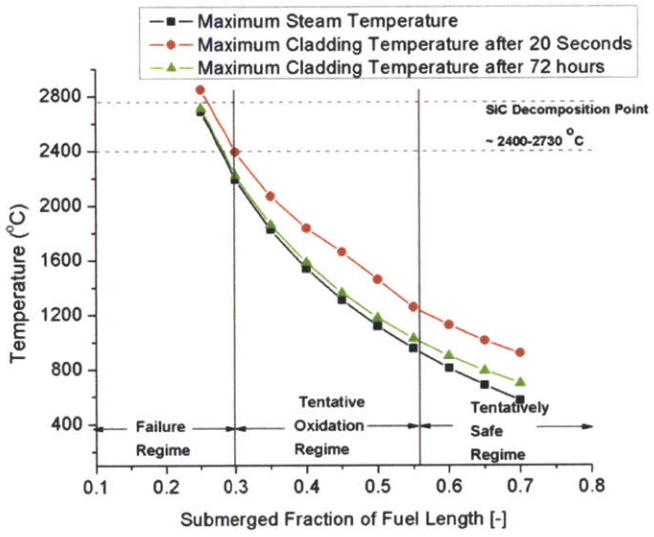

Figure 2-4 Oxidation Regime for SiC

[4] Clad ballooning and burst effects of Zircaloy are not explicitly modeled in the analysis. Clad ballooning and partial burst effects are typically considered negligible in thermal hydraulics analysis as long as the original subchannel geometry is not significantly altered. These effects are considered in the regime defined as tentative oxidation regime, which is between the melting and cladding softening point defined in Fig.3. Core reflood conditions such as flow rate and water level vary based on detailed accident scenarios. Thermal hydraulics analysis used here is a rather generic approach, which models and illustrates thermal hydraulics conditions at a certain water level during beyond design basis accidents.

Each line in Figure 2-3 and Figure 2-4 represents the maximum steam temperature and maximum cladding temperature at 20 seconds and at 72 hours, respectively. As shown by Eq. (2-8) and Eq. (2-9), the steam temperature is independent of time as its equilibrium value is used. These cladding temperatures monotonically decrease with increasing submerged fraction of fuel length as the water vapor mass flow rate experiences shorter rod fuel length. Different cladding safety limits are applied for Zircaloy-4 and SiC. For Zircaloy-4, cladding softening starts to occur as the temperature exceeds roughly 1000°C, which causes cladding breach and the release of fission gases. As illustrated in Figure 2-3, the model predicts that 65% of the fuel rod axial length must be submerged to avoid cladding softening of Zircaloy-4. Submergence of the fuel rod above the 65% limit is regarded tentatively as safe. The melting temperature of the Zr-4 cladding is around 1800°C and this temperature limit is violated when the submergence level is below 40%. The safe temperature of 1204 °C to avoid auto-catalytic Zr-4 oxidation requires limiting the uncovering of the fuel to less than 55% of its length. Considering the prescribed temperature behavior and limits, submerged fuel length percentages between 40% and 65% represents the region where oxidation of Zr-4 can introduce significant safety issues with simultaneous cladding softening.

A similar analysis is shown for the SiC cladding in Figure 2-4. SiC can reach its higher decomposition temperature (2400~2730°C) with no appreciable softening (Snead, 2007). This higher decomposition temperature implies 10% reduction in the required minimum submerged fraction of fuel rod length compared to Zr-4. That is 30% for SiC compared to 40% for Zircaloy-4. At a submerged fuel rod fraction greater than 55% the fuel is regarded as tentatively safe as the cladding temperature does not exceed 1204 °C. The temperature limit of 1204°C has been established by the U.S NRC for Zircaloy. In this study, the significant oxidation regime for SiC is defined as the region where the SiC cladding temperature is between 1204 °C and the decomposition temperature. If the use of SiC eliminates the safety concerns associated with oxidation at 1204°C, it can fully leverage the benefit of the higher cladding decomposition temperature and allow the fuel rod up to 35% reduction in required submerged fraction of fuel rod compared to that of Zircaloy-4.

Currently, the oxidation behavior of SiC under the conditions of a LOCA is unknown. Given the significance of the oxidation/volatilization kinetics in the safety analysis detailed above, here we report on experimental activities to determine them. The flow characteristics of the steam are very important to the volatilization kinetics, therefore Figure 2-5 shows the flow characteristics for the tentative oxidation regime defined in Figure 2-4. Steam flow becomes progressively laminarized with decreasing decay power of the fuel pin.

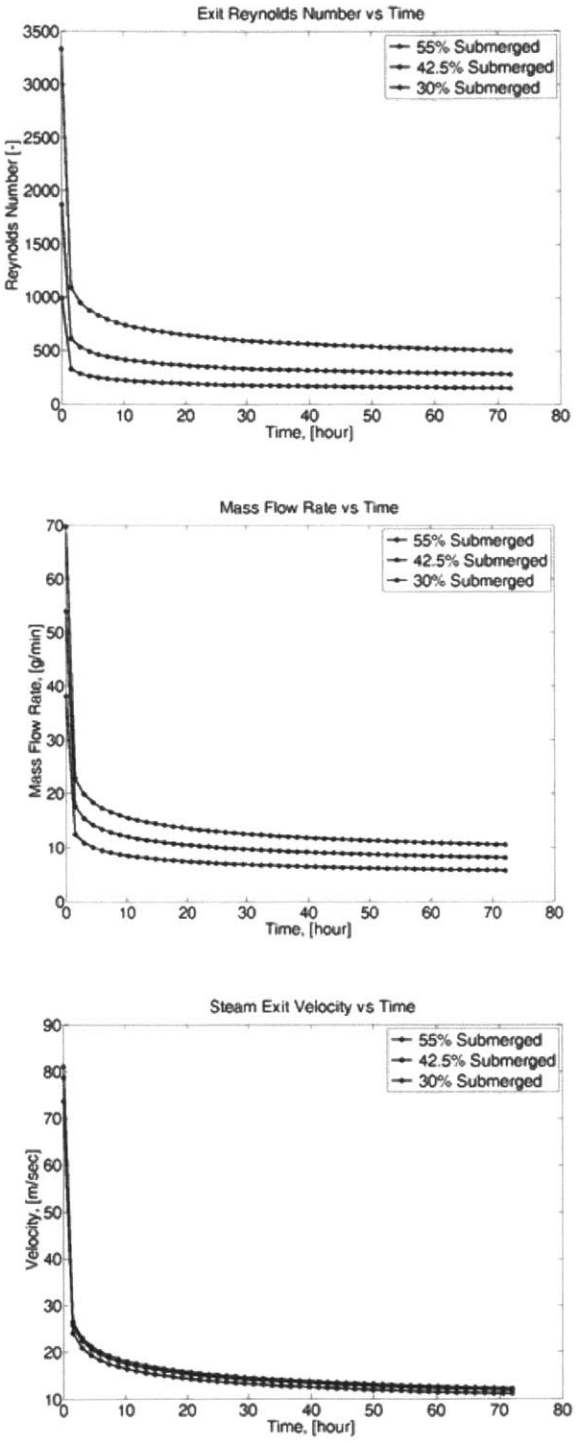

Figure 2-5 Flow Characteristics of the Tentative Oxidation Regime for SiC: Reynolds Number, Subchannel Water Vapor Mass Flow Rate, and Velocity

2.4 SiC Oxidation Experimental Procedure

2.4.1 Tested SiC Specimens

The material used in this experimental study was monolithic tubular pressureless-sintered α-SiC and CVD β-SiC. Two different manufacturer's monolithic α-SiC tubular samples were tested. The density of one of the SiC sample was 2.95g/cc and was obtained from Ceramic Tubular Products (CTP). These tubes samples were obtained by CTP from Saint-Gobain,Inc. The other sample was directly obtained from Saint-Gobain, Inc.; its density was 3.05g/cc, and its trade name is SE type Hexoloy. Dimensions of the samples were also slightly different. The CTP samples had dimensions of 12.6mm outer diameter (OD), thickness of 0.93mm, and height of 13.0mm. The Saint-Gobain samples had dimensions of 14.0mm OD, thickness of 1.56mm, and height of 13.0mm. High purity CVD β-SiCs samples were obtained from Bomas (Somerville, MA). Its density is 3.21g/cc and is in a bar shape (ASTM C 1161 size: 25mm x 2mm x 1.5mm). Samples were ultrasonically cleaned with detergent added to water, deionized (DI) water, acetone, and methanol prior to furnace exposures.

2.4.2 Oxidation Facility

A schematic of the oxidation apparatus is shown in Figure 2-6. This apparatus was designed to expose SiC samples to water vapor (H_2O) at a temperature up to 1500°C for up to 72 hours. Tubular SiC specimens were drilled in their side surfaces and pinned by 0.15875 cm (1/16'') OD alumina rod. A cleaned, preweighed tubular SiC sample was suspended by an alumina rod inserted in drilled holes on the material surface in the middle of the heating section of the sample furnace in the quartz tube (inner diameter of 1.9cm). It is worth noting that impurities from alumina tubes have been shown to affect the oxidation results of SiC, especially in water vapor (Opila, 1994). The alumina rod that was used to hold SiC samples was made to assure that its overlapping length with the SiC sample height is minimal to minimize possible contaminations. CVD β-SiC specimens were vertically held in the middle of the sample furnace heating section inside the quartz tube by K-type thermocouple wire winding roughly the top 10% of the vertical length of the bar. The wired portion of the specimen was cut after the test to exclude the covered area from the analysis.

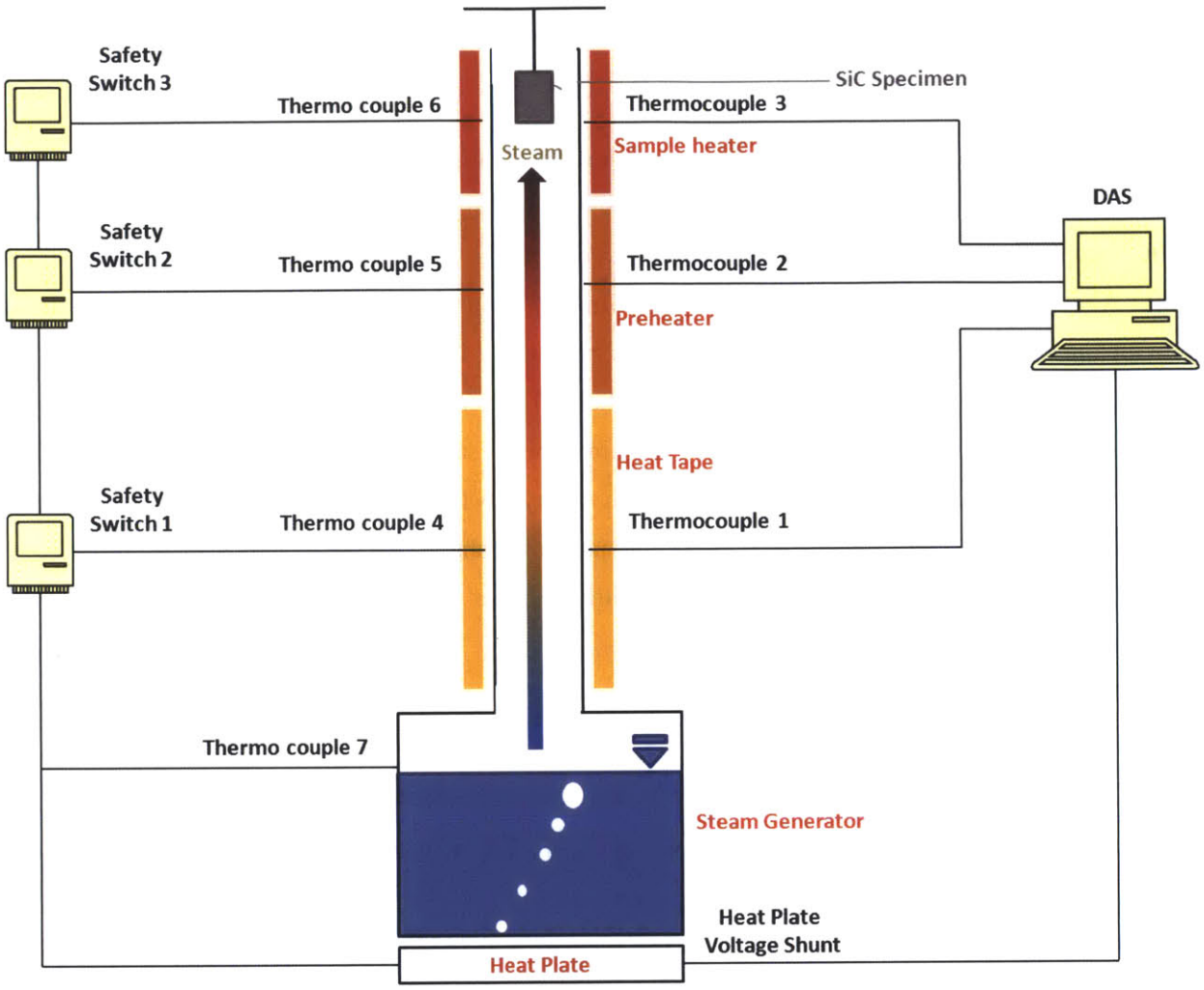

Figure 2-6 Schematic of the Steam-Oxidation Facility

Three heated sections were employed outside the quartz tube along the flow channel to heat the water vapor as illustrated in Figure 2-6. The heat tape serves a role of heating the water vapor from its initial formation temperature (~100°C) up to 750°C. The preheater and sample furnace then further heated the water vapor up to 1200°C and 1500°C, respectively. The sample furnace uses molybdenum disilicide ($MoSi_2$) heating coils of maximum power of 1200 watts. Each heating region was equipped with a thermocouple placed at the outer surface of the quartz tube for acquisition with a data acquisition system (DAS). K-type thermocouples were used for the preheater and heat tape region while a B-type thermocouple was used in the sample furnace for higher temperature measurements. All the heaters and heat plate for steam generation are manipulated by independent controllers for power control. A series electric circuit was built with additional thermocouples in the heating stages and steam generator for safety of unmanned operation of the facility (Arnold, 2011). For that, safety switches connected in series shuts down the facility upon a violation of temperature limits in any of the three heating stages and steam

generator. The steam generator was 75.7 quart in size and steam flow rate was measured by dividing the mass deficit of the contained water by the steam generation time. Constant steam flow rate was validated for different steam generator water levels. A pressure-relief valve was installed on the steam generator lid for safety concern. A photograph of the steam-oxidation facility in operation is shown in Figure 2-7. Figure 2-8 and Figure 2-9 show how the sample holder is used to a hold tubular SiC specimen in the facility.

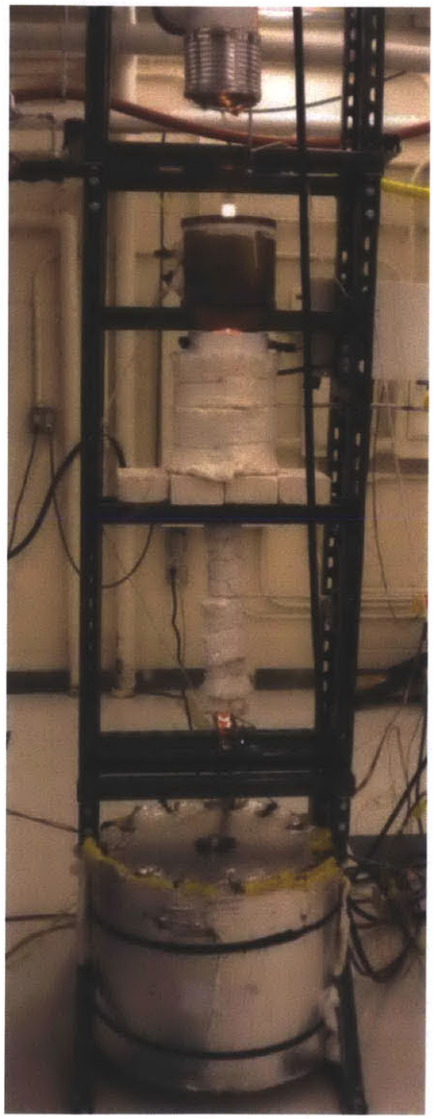

Figure 2-7 Steam-Oxidation Facility in Operation

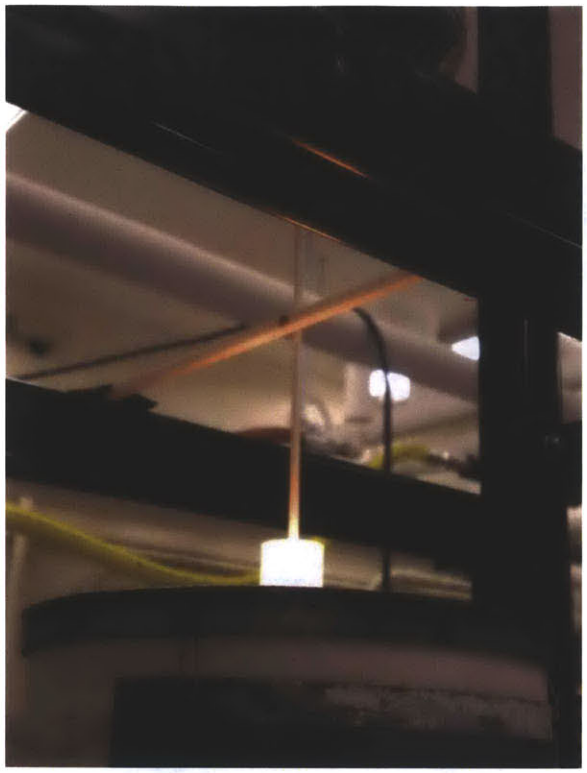

Figure 2-8 Photo of Sample Holder in Operation

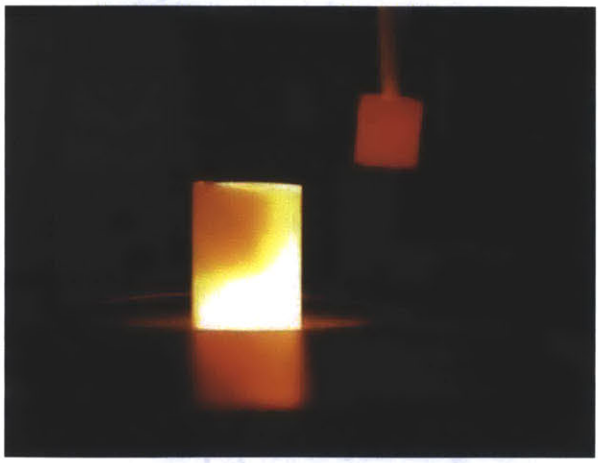

Figure 2-9 Photo of SiC Sample Suspended with Sample Holder by Pin (Being Discharged from the Facility)

2.4.3 Experiment Operating Conditions and Facility Verification

A test was run to verify that the temperature measured by the furnace thermocouple was representative of the sample temperature. To accomplish this, a thermocouple was attached to a sample surface using a refractory cement to compare the temperature at the sample surface with the temperature measured by the thermocouples at the exterior of the quartz tube and steam temperature that was measured by a bare thermocouple at the sample location. Roughly, the temperature difference observed between the sample and the steam was within 10°C when the steam temperature measurement was around 1200°C. Hence, in this study, for each test, steam temperature at the sample location was reported by a bare thermocouple inserted inside the quartz tube as it was found to be representative of the sample temperature.

Additional validation of the facility was performed by testing Zircaloy-4 tube samples. Figure 2-10 shows the strong agreement between the Zircaloy-4 data obtained with this facility (Arnold, 2011) and existing correlations that served as the basis for the U.S NRC licensing (Schanz, 2004).

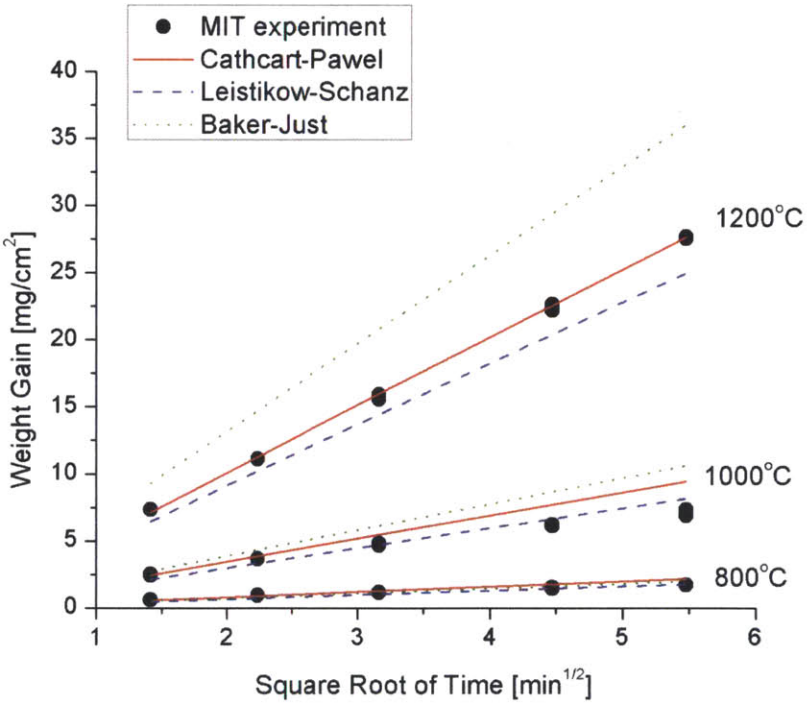

Figure 2-10 Comparison of Zircaloy-4 Oxidation Experimental Results Produced by the Steam-Oxidation Facility of This Study with Existing Correlations

Oxidation tests were conducted for different time intervals – primarily 8, 16, 24, 48 and 72 hours. A different sample was used for each time interval. Sample weights were measured before and after the tests. For each time interval, at least two duplicating tests were made for a consistency check. The experimental

environment of the facility is compared with that of the accident scenarios discussed in the prescribed model in Table 2-2.

Table 2-2 Oxidation Environment of Accident Conditions and the MIT Experiment[5]

	Accident Model		MIT Experiment
	Short-term (< 5hours)	**Long-term (5-72 hours)**	
SiC Geometry	Subchannel		Tubular
Hydraulic Diameter	1.18 cm		1.9 cm
Reynolds Number	400-3500	200-1000	40-500
Maximum Steam Velocity	20-80 m/sec	10- 20 m/sec	0.8 m/sec – 10 m/sec
Steam Flow Rate[6]	10-70 g/min	5 -20g/min	2-16g/min
Temperature	1200 – 1400°C		1100 – 1500°C
Heated Length of SiC	1.6 – 2.6m		No heat flux at the SiC sample surface
Flow Regime	Developing and fully developed regimes		Developing regime
Ri (Gr/Re^2)	10E-5	10E-4	10E-2 ~ 10E-1

As shown in Figure 2-5, the flow characteristics during accident conditions in the prescribed model can be distinctively divided into two different regimes with respect to time. For the short-term (< 5 hour), steam flow is in transition between laminar and turbulent. The flow becomes laminarized with increasing time due to decreasing flow rate with decaying heat generation rate.

The Grashof (Gr) number divided by the square of Reynolds number is termed the Richardson number (Ri), which is a measure of the ratio of buoyancy driven convection and forced convection of the flow. If Ri is substantially smaller than unity (Ri<< 1), then the flow is dominantly forced convection. Water vapor flow for both accident conditions and the experiments can be regarded as forced convection. The SiC material used in the experiment is not subject to surface heat flux whereas the actual SiC in service for fuel cladding is. When the heat flux at a surface is large enough to induce buoyancy driven momentum comparable to that of forced convection, the boundary layer near the surface may be re-

[5] Ri number in the experiment was evaluated based on the heat flux at the quartz tube wall surrounded by the heater. The Reynolds number and steam velocity of the experiment were evaluated at 1200 °C.

[6] Steam flow rates of the accident model was obtained for a subchannel

laminarized as it deviates from the forced convection only case. However, it is seen from the Richardson number that such a heat flux effect on material transfer is negligible as the buoyancy effect is small. Hence, the flow environment of the MIT experiment is representative of that of the accident scenario except for the early phase of the prescribed model where the flow rate is higher. It is worth noting that the term early phase is based on the fact that such a state, where the fuel rod is submerged in stagnant water upon a loss of coolant flow, is reached after 20 seconds from the time of initiation of a LBLOCA. This is a conservative assumption; as a realistic accident scenario deviates from such conservative cases, the experiment becomes more representative in long term accident time periods. However, the experiments were conducted with SiC samples in tubular shapes. Such a difference in the geometry between the subchannel and the tubular shapes introduces an irreconcilable limitation for the experimental data in the development of the oxidation model. This will be addressed in detail in Chapter 3.

2.5 Experimental Results

2.5.1 SiC Material Loss Rates

Exposure of the α-phase SiC at steam-oxidizing environment resulted in a linear weight loss of the materials for both CTP α-SiC and Saint-Gobain Hexoloy α-SiC as summarized in Table 2-3, and Table 2-4 The Linearity of weight loss was found by plotting the data with respect to time shown in Figure 2-11, and Figure 2-12[7]. Weight loss of CVD β-SiC is shown in Table 2-5, and additional data is being obtained.

Table 2-3 Weight Loss of CTP Pressureless Sintered α-SiC

Temperature	Flow Rates	Time and Average Weight Loss per Area				Average Weight Loss Rate ± 95% confidence (mg/cm^2 hr)
1140°C	2.4g/min	Time	8 hours	24 hours	48 hours	$-(12.3\pm2.5)\times10^{-3}$
		Weight Loss (mg/cm^2)	-0.183	-0.388	-0.547	
				-0.319	-0.560	
1140°C	7.9g/min	Time	8 hours	24 hours		$-(29.0\pm11.0)\times10^{-3}$
		Weight Loss (mg/cm^2)	-0.340	-0.814		
			-0.210	-0.550		
1500°C	16.0g/min	Time	8 hours			-
		Weight Loss (mg/cm^2)	-0.240			
			-0.250			

[7] ±95% confidence bands reported in Table 2-1 are intentionally omitted in Figure 2-12 for clearity of the graph.

Table 2-4 Weight Loss of Pressureless Sintered Saint-Gobain α-SiC

Temperature	Flow Rates	Time and Average Weight Loss per Area						Average Weight Loss Rate ± 95% confidence (mg/cm^2 hr)
1140°C	2.4g/min	Time	24 hours	48 hours				$-(10.0\pm2.8)\times10^{-3}$
		Weight Loss (mg/cm^2)	-0.185	-0.578				
			-0.291	-0.386				
1140°C	7.9g/min	Time	8 hours	16 hours	24 hours	48 hours		$-(17.6\pm1.0)\times10^{-3}$
		Weight Loss (mg/cm^2)	-0.256	-0.412	-0.530	-0.813	-0.611	
			-0.224	-0.369	-0.457	-0.929		
1140°C	16.0g/min	Time	8 hours	16 hours	24 hours	48 hours		$-(19.2\pm0.8)\times10^{-3}$
		Weight Loss (mg/cm^2)	-0.196	-0.306	-0.503	-0.882		
			-0.165	-0.321	-0.486	-0.919		
1230 °C	17.9g/min	Time	6.5 hours	8 hours	16 hours	24 hours	48 hours	$-(37.0\pm2.6)\times10^{-3}$
		Weight Loss (mg/cm^2)	-0.173	-0.335	-0.507	-0.702	-1.740	
				-0.353	-0.715	-0.954	-1.855	
1280 °C	2.4g/min	Time	8 hours	16 hours	24 hours	48 hours	72 hours	$-(17.1\pm1.0)\times10^{-3}$
		Weight Loss (mg/cm^2)	-0.075	-0.231	-0.357	-0.872	-1.267	
			-0.065	-0.218	-0.323	-0.877	-1.213	
1280 °C	7.6g/min	Time	8 hours	16 hours	24 hours	48 hours		$-(57.7\pm5.3)\times10^{-3}$
		Weight Loss (mg/cm^2)	-0.374	-0.837	-1.222	-2.703	-3.098	
			-0.422	-0.823	-1.308	-3.210	-2.260	
1280 °C	18g/min	Time	16 hours	24 hours	42.6 hours	48 hours		$-(79.1\pm15.4)\times10^{-3}$
		Weight Loss (mg/cm^2)	-1.609	-2.659	-2.828	-3.710		
			-1.212	-2.087				
1320 °C	7.1g/min	Time	48 hours					-
		Weight Loss (mg/cm^2)	-2.618	-2.119				
			-2.163					
1320 °C	16.2g/min1	Time	48 hours					-
		Weight Loss (mg/cm^2)	-3.225					
			-3.075					
1390 °C	8.0g/min	Time	8 hours	16 hours	24 hours	48 hours		$-(97.3\pm4.9)\times10^{-3}$
		Weight Loss (mg/cm^2)	-0.707	-1.353	-2.150	-4.671		
			-0.886	-1.599	-2.708	-4.630		
1500 °C	2.1g/min	Time	8 hours	16 hours	24 hours	48 hours		$-(22.7\pm1.7)\times10^{-3}$
		Weight Loss (mg/cm^2)	-0.093	-0.357	-0.502	-1.135		
			-0.130	-0.368	-0.535			

Table 2-5 Weight Loss of CVD β-SiC

Temperature	Flow Rates	Time and Average Weight Loss per Area				Average Weight Loss Rate ± 95% confidence (mg/cm^2 hr)
1155°C	6.4g/min	Time	8 hours	24 hours	48 hours	-
		Weight Loss (mg/cm^2)	-	-	-0.609	

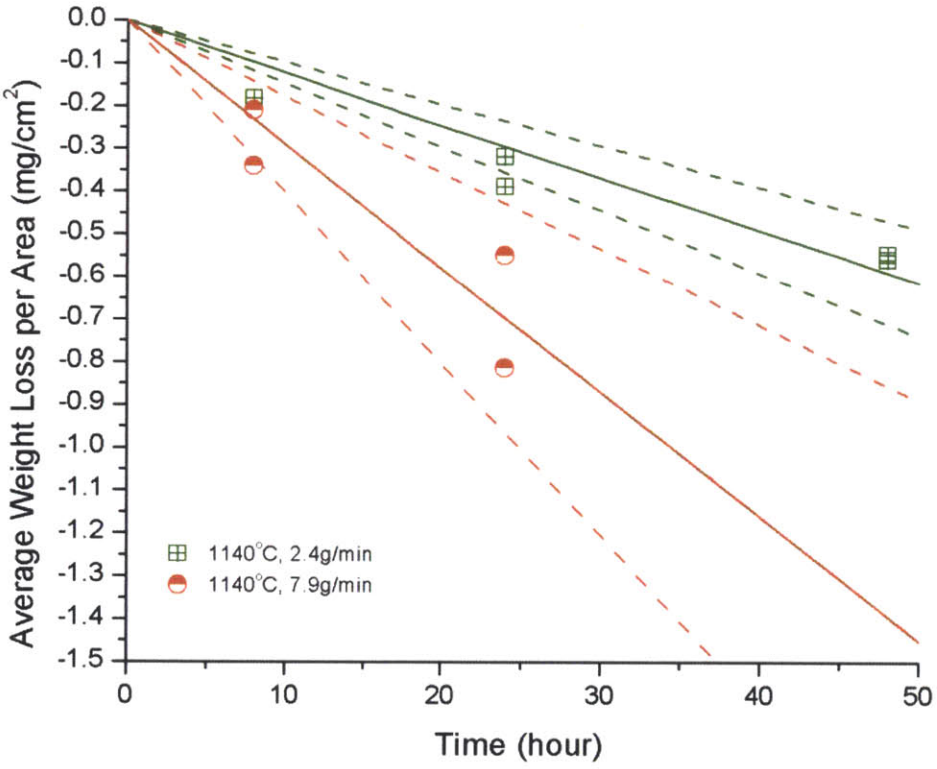

Figure 2-11 Average Weight Loss per Area of CTP α-SiC
(with ± 95% confidence bands with dashed lines)

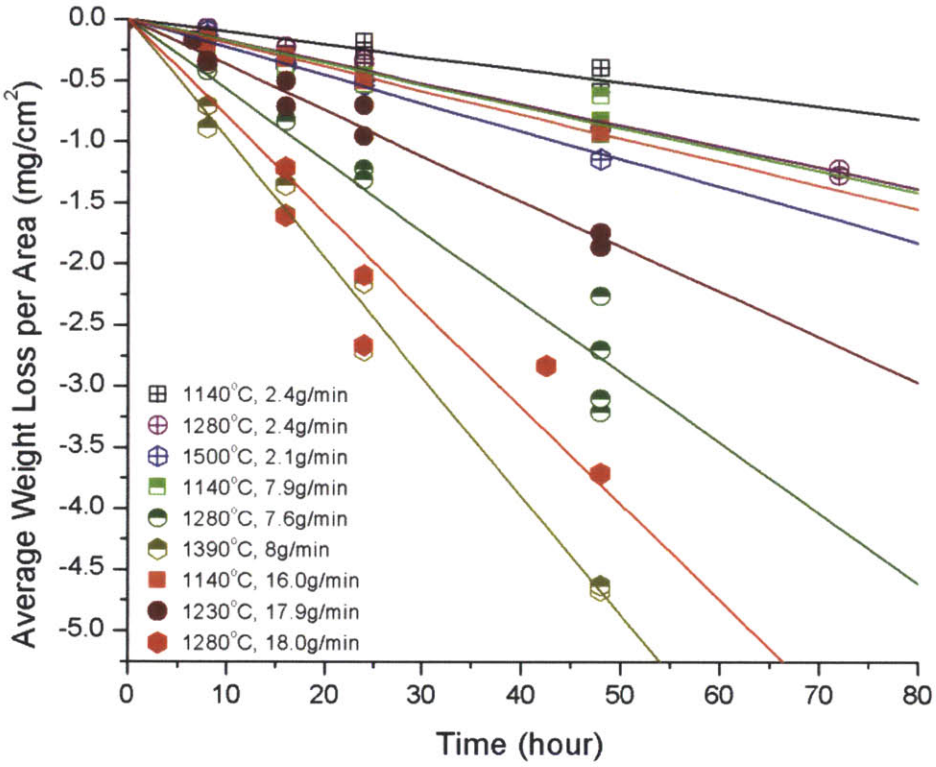

Figure 2-12 Average Weight Loss per Area for Saint Gobain α-SiC

For both types of SiC, increased flow rates resulted in faster weight loss rates. This implies that SiC volatilization is dependent on the flow characteristics, for instance mass flux, velocity or Reynolds number. Indeed this trend of SiC weight loss has been commonly observed in most experimental studies conducted at appreciable steam flow rates (Opila, 2003). Discussion of the flow dependent behavior of SiC weight loss is provided in detail in Chapter 3. The reported SiC weight loss rates were different for the two types of α-SiC, although it is difficult to tell which type is more susceptible to weight loss. CVD β-SiC demonstrated similar weight loss rate with Saint-Gobain α-SiC under similar oxidizing environment (0.609 mg/cm^2 in 1155°C, 6.4g/min for β-SiC, and average of 0.784mg/cm^2 in 1140°C, 7.9g/min for Saint-Gobain α-SiC) as shown in Table 2-5, and Table 2-4 respectively. A difference in weight loss rate can be expected as stochiometry, porosity, density, and surface characteristics of SiC samples reflect different manufacturing conditions. This may cause a difference in the growth of the oxide layer. Increasing temperature causes higher weight loss rates. This is because the higher temperature increases chemical reaction kinetics for both the oxide layer formation and volatilization and it also

affects the fluid properties including the diffusion coefficients (Opila, 2003). The equilibrium thickness of the oxide layer depends on the temperature sensitivity of the volatilization process versus the oxide layer formation process. Two independently controlled factors – temperature and flow rates – resulted in different material weight loss in the experiment. Sensitivity of SiC material loss to each factor can be found in Figure 2-13.

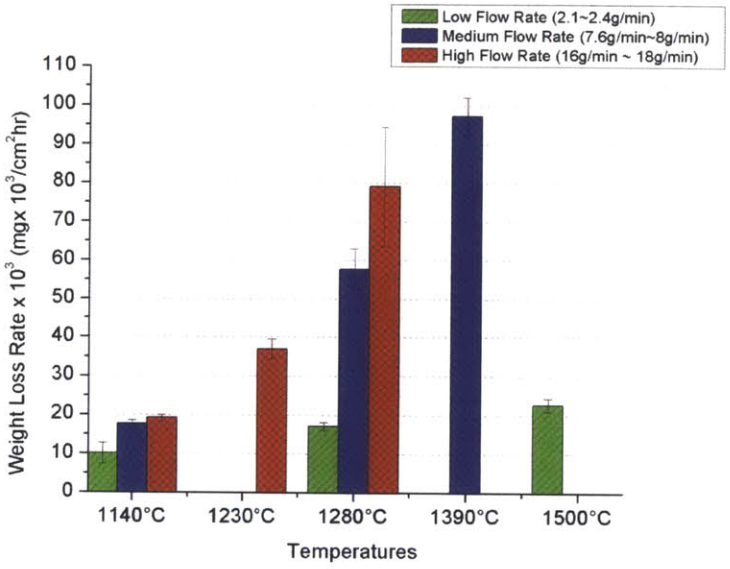

Figure 2-13 Weight Loss Rate for Sain-Gobain α-SiC

Figure 2-13 shows that at a higher temperature the material loss rates are more sensitive to flow rate than at lower temperature; in that, material loss becomes more sensitively dependent on temperature at a higher flow rate. This is because at a lower flow rate, out-ward diffusion of viscous silicate gases of the reaction products in the boundary layer to the bulk fluid become a reaction rate-limiting step – faster reaction rate at a higher temperature is not fully utilized because mass transfer limits the rate the overall volatilization process. On the other hand, at a higher flow rate, the thinner boundary layer at the specimen surface allows faster mass transfer, so the temperature-dependent volatilization reaction rate predominantly affects the rate of the overall volatilization process – reaction of $SiO_2 + H_2O$ in Eq.(2-1), Eq. (2-2) and Eq. (2-3) are not hampered by mass transfer. Depending on the relative magnitudes of the flow rate and temperature, the dominance of the interplay between the two factors can significantly vary with two extremes - one being temperature-limited (flow rate insensitive) and the other being mass transfer-limited (temperature insensitive).

2.5.2 Microstructure Analysis of Oxidized SiC

(A) Visual and Optical-microscopy Examination

Oxidation slightly darkens the surface color of the SiC specimens as shown in Figure 2-14. Overall, no significant alteration in sample's visually distinguishable characteristics was observed other than the darkening. In addition, no pre & post dimensional differences were seen.

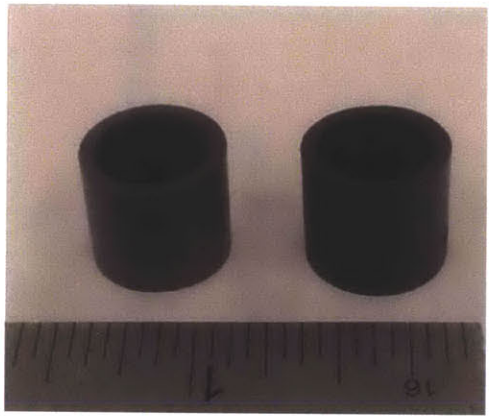

Figure 2-14 Saint-Gobain α-SiC Specimens: As-received (Left) and Oxidized (Right)

SiC specimens further were prepared by several steps for optical microscopy and scanning electron microscopy analysis. First, SiC specimens were mounted by castable mounting technology in epoxy (Buehler Epoxicure) which is chemically stable and has a hardness that ensures uniformly flat surface level with SiC when grinded and polished. The top and bottom surfaces were ground with 70μm and 30μm diamond grinding disks (Buehler Apex Diamond Grinding Disks), successively. Then, lapping was performed on specimen's cross-sectional surfaces to remove existing irregularities and scratches after the grinding process with 15, 9, 6, and 3μm particles (Allied High Tech Products lapping disks). As the last step to obtain a well-prepared flat surface, chemo-mechanical polishing was used with 0.06μm grains of silica (SiO_2) suspended in a basic (pH ≈ 10) solution (Buehler MasterMet) scattered into a synthetic cloth. Finally, cross sections of the SiC specimens were etched with Murakami solution made of 3g of sodium hydroxide (NaOH) and 30 g of potassium hexacyanoferrate III ($K_3[Fe(CN)_6]$) diluted into 60mL of distilled water. The etching solution preferentially attacked grain boundaries as shown by comparing

Figure 2-15 and Figure 2-16. Figure 2-16 also shows structures of linked grain networks of individual grains (~5μm), which may give an idea of pre-existing flaw sizes for SiC brittle fracture analysis.

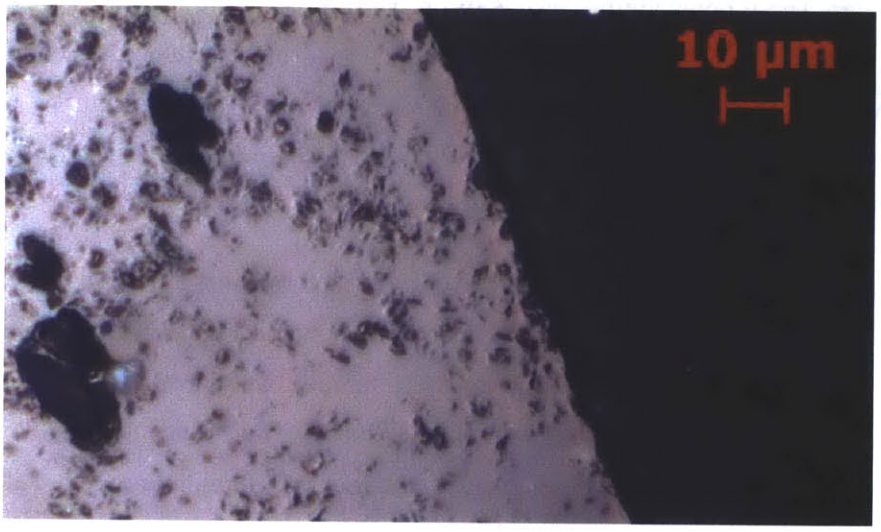

Figure 2-15 Typical Image of α-SiC Specimen before Etching (Mounting, Grinding, Lapping and Polishing were conducted on the Specimen)

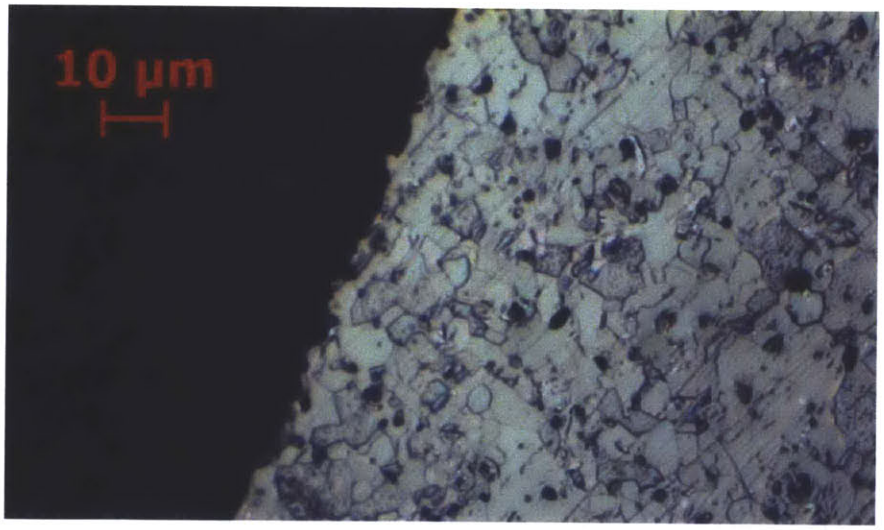

Figure 2-16 Typical Image of α-SiC Specimen after Etching

(B) Scanning Electron Microscopy (SEM) Analysis

Further, microstructural analysis was conducted using a SEM. Figure 2-17 and Figure 2-18 show images of cross section and side surfaces of as-received α-SiC. Considerable porosity was observed in sample cross section images. These pores are the results of pressureless sintering process. Pores are found to be distributed uniformly and they stimulate non-uniform local oxidation. In the cross section images, grain sizes were observed to be between 5 and 10μm, which are in agreement with the current understanding of grain sizes of typical sintered α-SiC (Munro (A), 1997). The as-received α-SiC in Figure 2-18 shows surface with uniform surface grain sizes of 5~10 μm.

In this study, formation of cracks, pits, and holes on SiO_2 scale formed on the SiC surface was commonly observed with oxidized specimens in various conditions as shown in Figure 2-19. Such cracks and holes in the oxide layer were also observed with high-pressure furnace experiments with CVD SiC at 1200°C, at 10 atm,15% H_2O with flow rate of 0.05cm/sec (Opila, 2003). The surface morphology found after 48 hours of exposure in 1500°C, 2.1g/min is remarkably similar to SiO_2 morphology found after 100 hours of oxidation under 1.4cm/sec of flow rate with 50% H_2O/ 50% O_2 at 1400°C shown in Figure 2-21 (Opila, 1997). Cracks in the SiO_2 scale are known to be primarily caused by β-to-α transformation of cristobalite on cooling. Thick porous oxide scales were also observed to develop with presence of H_2O vapor under a thin dense vitreous SiO_2 layer (Tortorelli, 2003) as shown in Figure 2-22.

A number of explanations exist on the formation of bubbles/pores observed in SiO_2 scale. Opila's study explains that high pressure of oxidizing species increases the parabolic oxidation rate, which increases the rate of production of gaseous oxidation products in Eq. (2-1), SiC (s) + $3H_2O$ (g) = SiO_2 (s) + CO (g) + $3H_2$ (g). Thus, increased production of these gaseous reaction products generates observed porosity in the oxide layer. A previous study showed that the amount of pores in the SiO_2 scale increases with steam pressure (P_{H2O}) with H_2O/O_2 mixture as shown in Figure 2-20 (Opila, 1999). In that study, parabolic oxidation, hence generation of gaseous reaction products, was found to be roughly two orders of magnitudes higher with with oxidation in H_2O than in O_2 primarily because the higher solubility of H_2O, than O_2, causes higher (~10 times) permeability. This explains the observed increase of porosity with H_2O partial pressure. Other studies explained the same phenomenon differently – the increase in parabolic oxidation rate with H_2O is a result of water-vapor induced modification of the atomic structure of SiO_2 reflected in the decrease of viscosity and density (Cappelen, 1981), (Irene, 1997), (Narushima, 1990). Other explanations for bubbles/pores generation also exist. Some studies found that the spherulitic features found on SiO_2 scales are material characteristics of cristobalite formation (Narushima, 1989), (Narushima, 1990), (Ogbuji, 1981) - Even existence of a small amount of water vapor is known to

accelerate the crystallization of amorphous SiO_2 (Wagstaff, 1966). Some studies reported that the pits and cracks in the spherulitic features of SiO_2 scale are caused by grain-boundary diffusion of oxidants through cristobalite, which assures significantly faster diffusion than intra-grain diffusion (Narushima, 1990). Presence of impurities is also known to attribute crystallization of amorphous SiO_2, which helps the bubble/pores to form (Luthra, 1991).

Tortorelli's work (Tortorelli, 2003) examined differences in morphologies between SiO_2 scales grown in sintered α-SiC (Hexoloy, SA) and CVD-SiC as shown in Figure 2-22. The sintered α-SiC was found to have a greater amount of and finer pores than CVD-SiC. Reasons for this may pertain to effects of impurities and sintering aids present in sintered α-SiC (Costello, 1981), (Costello, 1986), (Singhal (B), 1976), surface roughness that manifests on α-SiC, and preferential oxidation of non-stoichiometric excessive carbon in sintered α-SiC (Mieskowski, 1984), (Luthra, 1991), (Tortorelli, 2003).

These explanations of pore generation mechanisms are not mutually exclusive but they all probably have simultaneously contributed to an explanation of porous SiO_2 scale formation. As such, observed bubbles/pores are results of the grain-boundary diffusion of oxidants and product gases in cristobalite SiO_2 layer that results in progressive formation of amorphous SiO_2 with increasing presence of H_2O, impurities, and temperature.

Existence of pores and cracks in SiO_2 scale implies a departure from the parabolic growth of the oxide scale with respect to time. In that, gaseous transport of oxidants and reaction products occur through interconnected pores and cracks which is much faster than the solid-state transport; oxide scale growth rate is no longer controlled by solid-state transport of gaseous species. The oxide layer growth is now determined by either solid-state gaseous species transport through the dense vitreous layer, if there is any, or reaction rate of $SiC \rightarrow SiO_2$. With these rate controlling mechanisms without the function of protective SiO_2 scale, oxidation kinetics and corresponding oxide scale growth are linear, instead of parabolic. As evidence, a linear behavior in oxide growth was observed with presumably porous SiO_2 scale formed in the wet oxidation in the relatively long initial period (Narushima, 1990). This linear behavior supports the observation that the formed oxide scale is no longer protective. One should be careful in understanding what is meant by net weight loss of SiC when both oxidation and SiO_2 volatilization take place with a porous SiO_2 formation; smaller overall weight loss may imply an increase in SiC oxidation for relatively comparable SiO_2 volatilization rates. Faster oxidation of SiC into SiO_2 through non-protective oxide scale increases weight-gain term due to gain of O_2 in SiO_2 scale, while the weight-loss term – volatilization of SiO_2– remains relatively the same; this may result in the smaller weight loss despite of the faster oxidation process. Therefore, simply comparing weight losses of SiC specimens

under oxidizing/volatilizing conditions without knowing micro-structure of SiO_2 scale must be carefully addressed for some applications. Therefore, a more accurate weight loss assessment must be obtained by microstructure analysis of the samples.

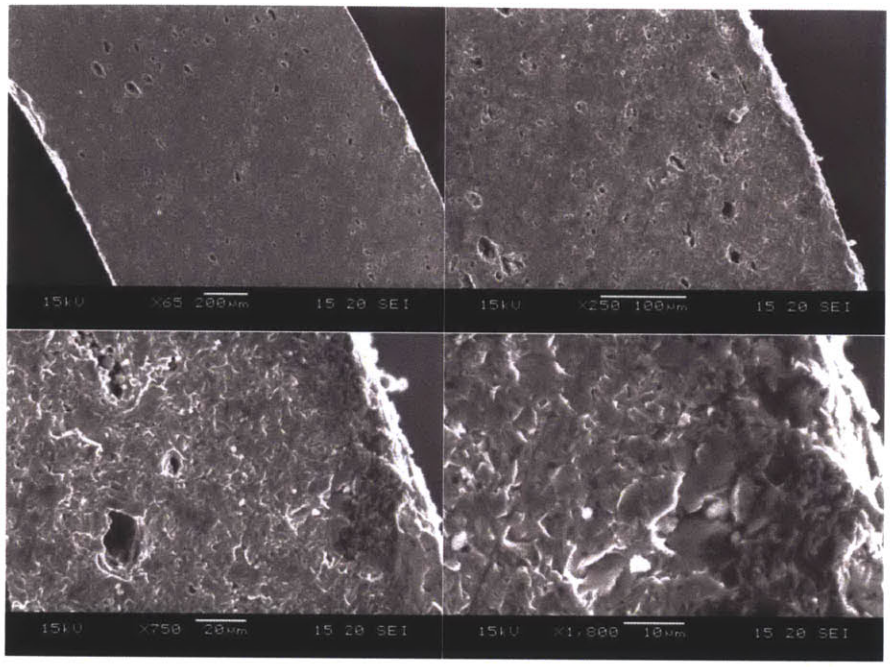

Figure 2-17 Cross Section of As-Received Tubular Saint-Gobain α-SiC

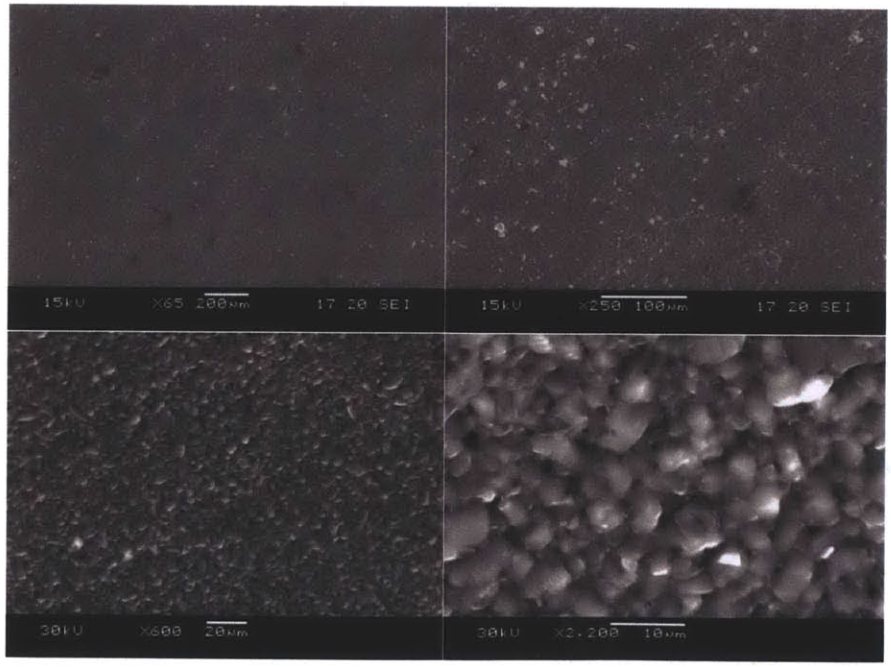

Figure 2-18 Side Surface of As-Received Tubular Saint-Gobain α-SiC

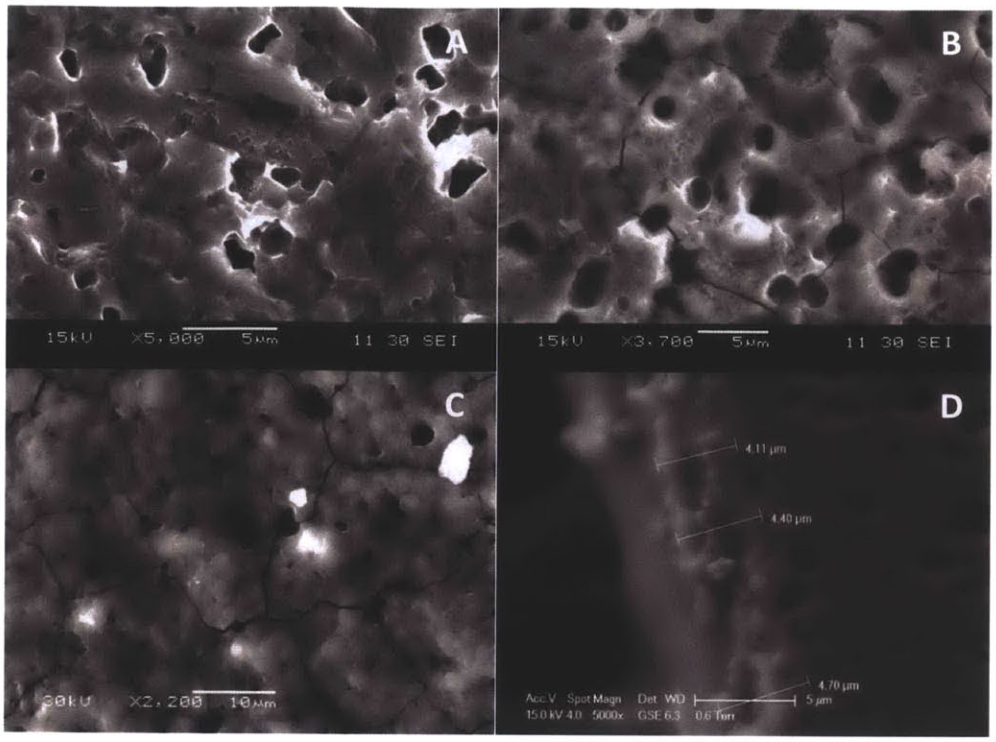

Figure 2-19 Oxide Scale Formed on the Surface of α-SiC: A - Side surface after 16 hours of exposure in 1140°C, 16.0g/min, B - Side surface after 48 hours of exposure in 1140°C, 2.4g/min, C, D- Side and Cross Section after 48 hours of exposure in 1500°C, 2.1g/min, respectively

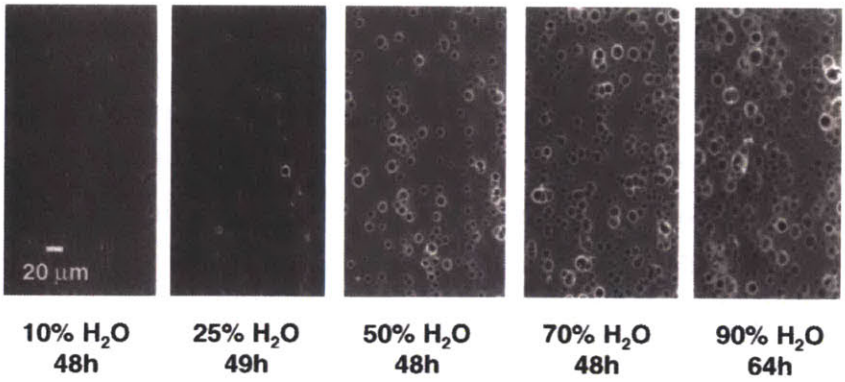

Figure 2-20 Amorphous SiO_2 Scale Morphology Formed on CVD SiC at 1200°C at times of ~48 hours, as a function of P_{H2O} (Opila E. J, 1999)

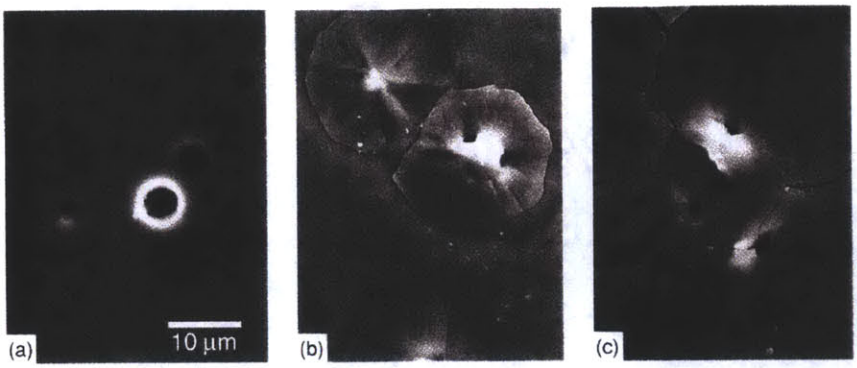

Figure 2-21 Oxide Layer Surface Morphology of CVD SiC Oxidized in 50% H_2O/50% O_2 for 100hours at 1.4cm/sec of flow rate as function of temperature: (a) 1200°C, (b) 1300°C, and (c) 1400°C (Opila, 1997)

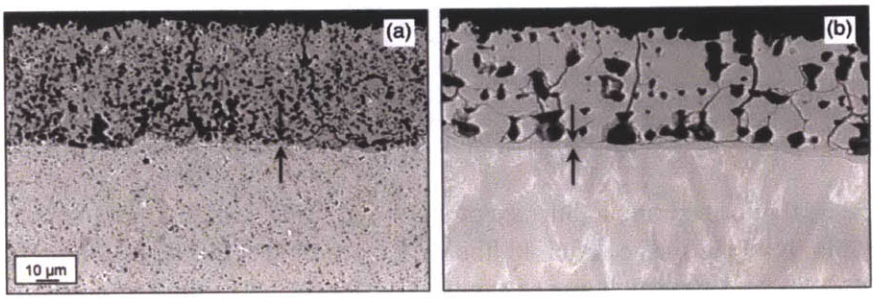

Figure 2-22 SiO_2 Scales Formed on (a) Sintered SiC and (b) CVD-SiC after Exposure at 1200°C, 3cm/min flow rate of air + 15% H_2O. Arrows denote underlying dense vitreous SiO_2 layer (Tortorelli, 2003)

Time-dependent oxide scale morphologies were investigated by comparing three different SiO_2 morphologies taken at different exposure times (8, 16, 24 and 48 hours) under identical oxidizing conditions (1280°C, 7.6g/min of H_2O), Figure 2-23 through Figure 2-30. Figure 2-23 shows formation of bubbles on the SiO_2 scale in the relatively early phase of oxidation. These bubbles are clearly different from typical pores and pits observed at relatively longer time as shown in Figure 2-19. In addition, the surface of the SiO_2 scale seems significantly smoother than the surfaces observed after a relatively longer time. Surface crack-blunting may be expected with the presence of a smooth SiO_2 overcoat in the long time period. Figure 2-24 and Figure 2-25 show the surfaces of a α-SiC specimen after 16 hours of exposure time and Figure 2-26 and Figure 2-27 show the surface of a α-SiC specimen after 24 hours of exposure, both in 1280°C, 7.6g/min of H_2O. The entire side surfaces of the oxidized surfaces exhibit evidence of oxidation characterized with pores, pits, and surface level irregularities that tend to manifest near the periphery of the material. The amount of porosity formed on SiO_2 scales on side surfaces the

specimens increases progressively with time as shown in bottom-right figures shown in Figure 2-25 and Figure 2-27. This observation may be a result of extended inter-granular diffusion of gaseous species that yields increasing sites for pore development. Figure 2-29 shows oxidized surface morphologies quite different from SiO_2 scales observed in previous time steps (16 and 24 hours). Although progressively increased pore densities were still found on the sample side surface of 48 hours of exposures time, cracks that arise from cooling of cristobalite was absent as shown in Figure 2-29. This may be due to stabilized thickness of SiO_2 grown on α-SiC surface or/and preferential volatilization of cracked region of SiO_2 or/and spallation of oxide layer during handling the sample or cooling processes. These key features on time evolution of SiO_2 scale formation – transition from bubble to pore/pits and crack, and further transformation into crack-free SiO_2 – is summarized in Figure 2-30.

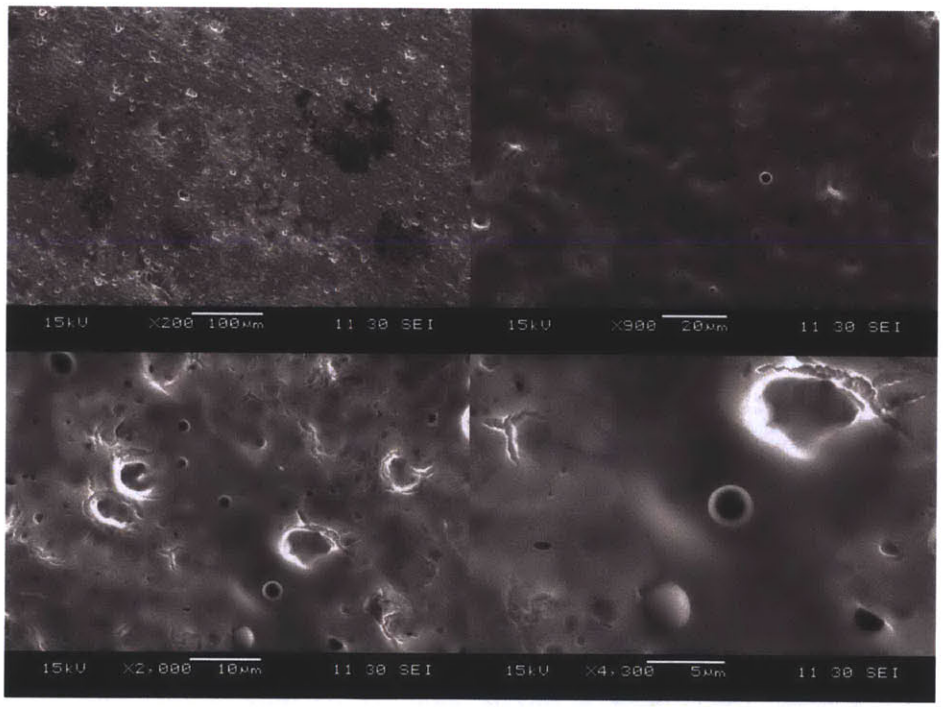

Figure 2-23 Side Surface of Oxidized SiC Specimen after 8 hours in 1280°C with 7.6g/min of H_2O Flow Rate

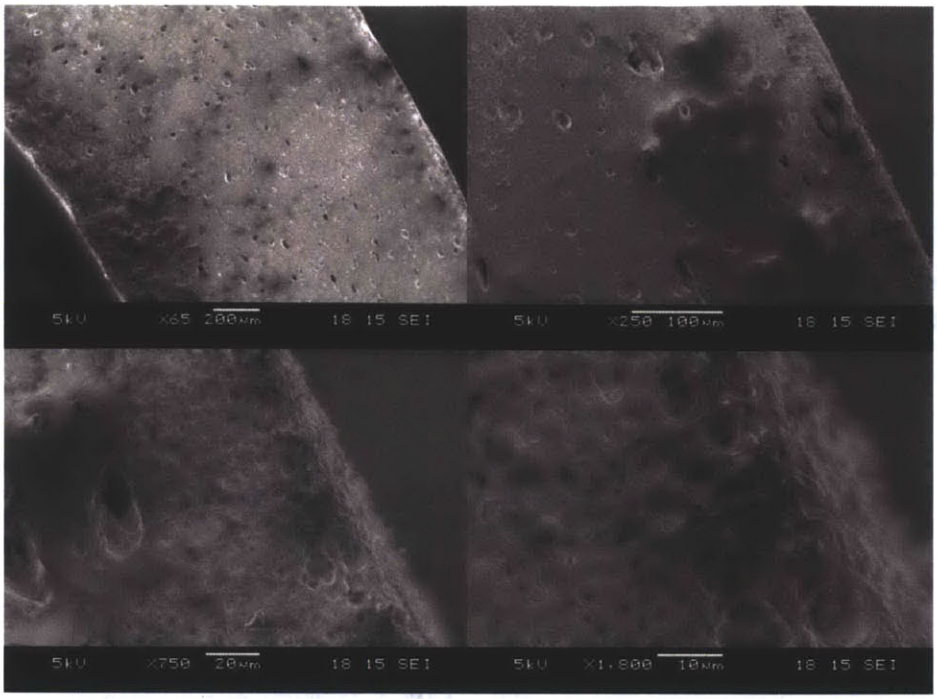

Figure 2-24 Cross Section of Oxidized SiC Specimen after 16 hours in 1280°C with 7.6g/min of H_2O Flow Rate

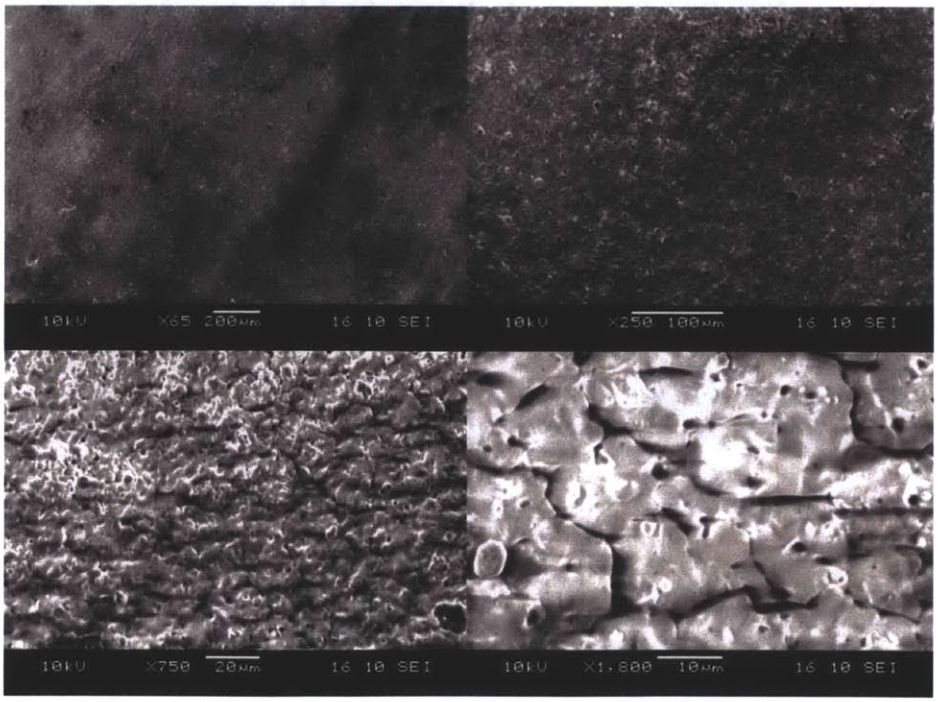

Figure 2-25 Side Surface of Oxidized SiC Specimen after 16 hours in 1280°C with 7.6g/min of H_2O Flow Rate

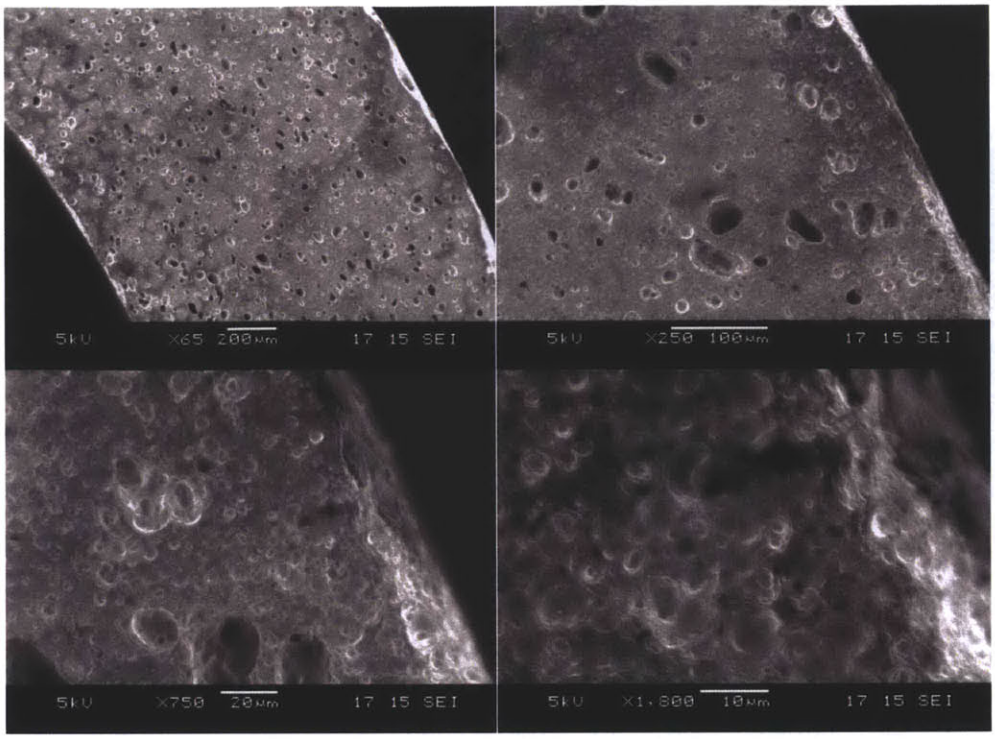

Figure 2-26 Cross Section of Oxidized SiC Specimen after 24 hours in 1280°C with 7.6g/min of H_2O Flow Rate

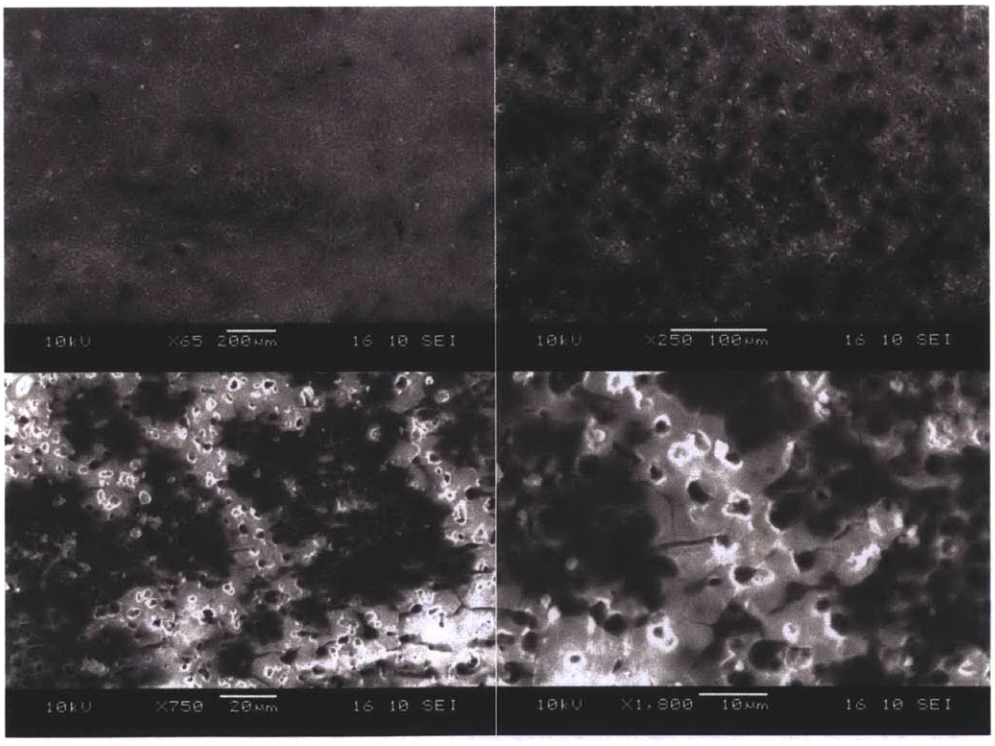

Figure 2-27 Side Surface of Oxidized SiC Specimen after 24 hours in 1280°C with 7.6g/min of H_2O Flow Rate

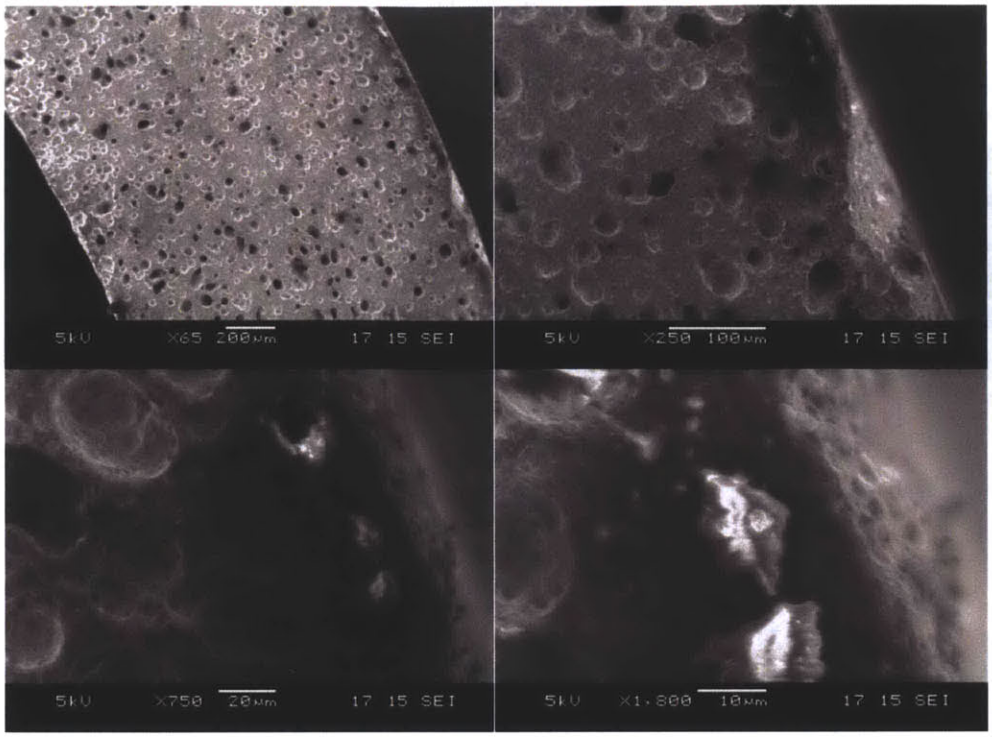

Figure 2-28 Cross Section of Oxidized SiC Specimen after 48 hours in 1280°C with 7.6g/min of H_2O Flow Rate

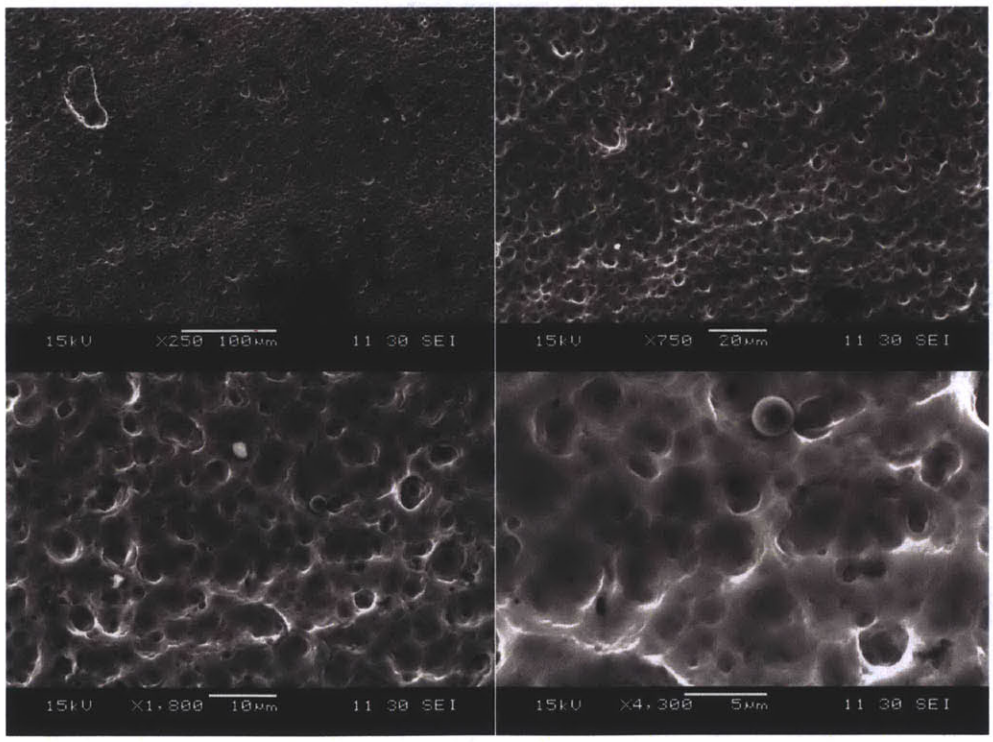

Figure 2-29 Side Surface of Oxidized SiC Specimen after 48 hours in 1280°C with 7.6g/min of H_2O Flow Rate

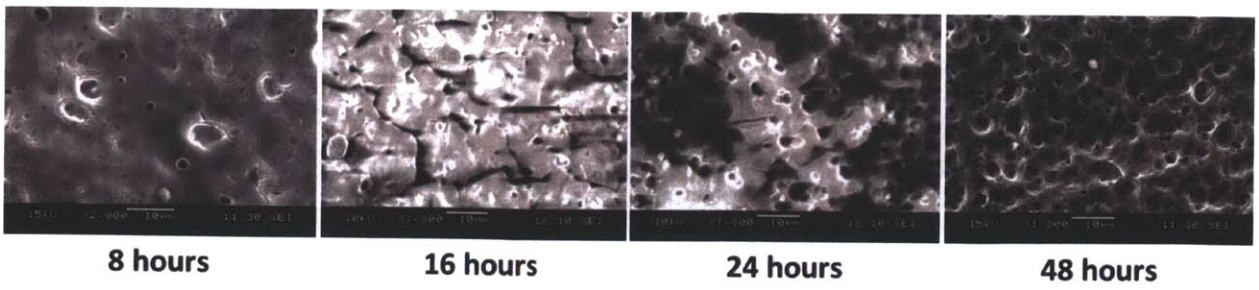

Figure 2-30 Some Key Features of Time Evolution of SiO_2 Scale Formed on the Surface in 1280°C with 7.6g/min of H_2O: Bubbles + Surface Smoothing SiO_2→ Crack/Pits/Pores SiO_2→ Crack Free SiO_2

The surface morphology of CVD β-SiC was observed to exhibit different characteristics from sintered α-SiC after exposure in an oxidation/volatilization environment. Figure 2-31 shows that the oxidized CVD β-SiC is characterized by spherulitic features on the SiO_2 surface. In addition, the formation of cracks after oxidation was not observed.

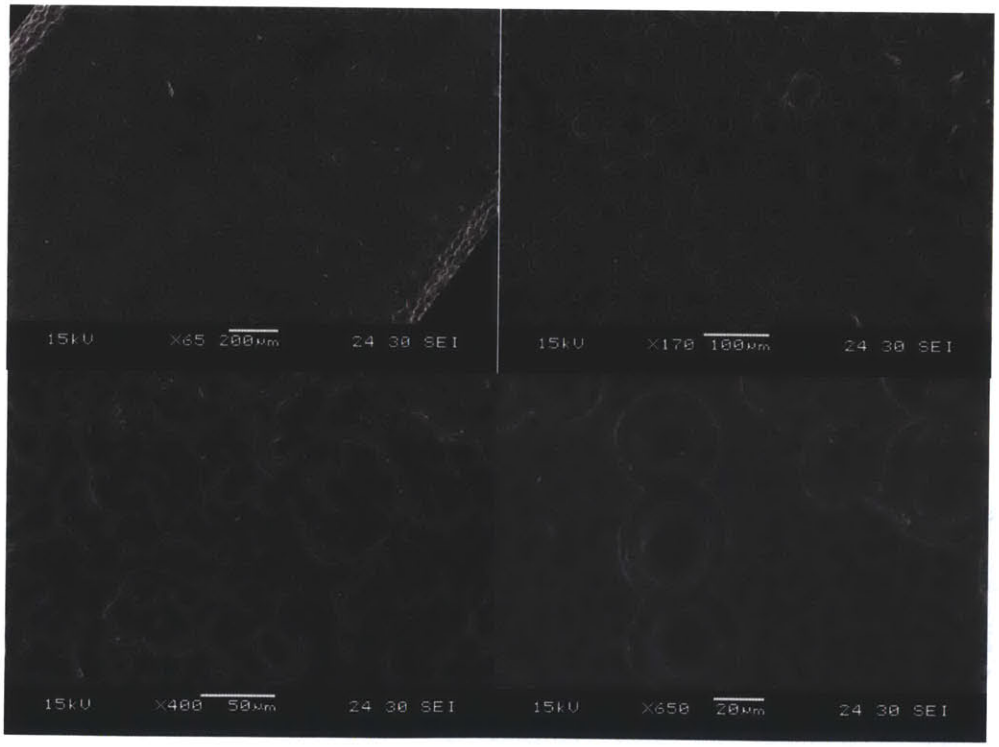

Figure 2-31 Side Surface Morphology of CVD β-SiC after 48 hours of exposure in 1155°C, 6.4g/min of H_2O Flow Rate

SiO_2 surface morphologies are known to change with exposure time in oxidizing environments (Tortorelli, 2003). As discussed earlier, the time evolution of oxide scale morphology may be regarded as a potential source of uncertainty in modeling/predicting SiC conversion into SiO_2. Different pore networks and cracks[8] alter the paths for gaseous species transport. Nevertheless, the influence of time evolution of SiO_2 pore and crack characteristics on oxidation kinetics may be negligible, except for the early phase of the oxidation or the extended time where oxide spallation can occur. Short circuit paths for gaseous species transports through the SiO_2 provided by initial development of pores may be sufficient for the reaction rate to become independent of the solid-state diffusion rate of gaseous species. Once the SiO_2 scale loses its protective function with a minimum number of pore formations in the early phase of oxidation, the presence of SiO_2 may no longer affect the overall oxidation reaction kinetics. Hence, the time scale of the application of interest may matter. For applications with long time periods of SiC oxidation that generates pores in the resulting SiO_2 scale, time evolution of SiO_2 is likely to be negligible because gaseous species transport through the porous oxide scale may saturate well in advance of early formations of pores in the scale. However, for applications with short time periods, early morphological changes of SiO_2 may significantly alter gaseous species transport rates during the time scale of interest. As far as SiC cladding oxidation under accident conditions is concerned, it is a bit tricky to draw conclusions concerning the effects of time evolution of oxide scale morphologies on SiC conversion into SiO_2 in the time scale of interest (~72 hours) with existing experimental data. In general, however, the effects of time evolution of SiO_2 morphology can be ignored as long as material weight loss exhibits linear behavior with time. Without any protective function carried out by the oxide scale, parabolic SiO_2 growth would have broken down and, linear growth of the oxide scale with respect to time will have occurred. Oxide scale growth rate with constant oxide layer growth can be re-written by changing the oxide growth term in Eq.(2-6) as follows

$$\frac{dx}{dt} = K_o - K_l \tag{2-16}$$

where K_o is linear oxide layer growth coefficient and K_l is linear volatilization coefficient, and $\frac{dx}{dt}$ is the time derivative of oxide scale thickness. Eq.(2-16) shows that once the oxide scale is formed ($\frac{dx}{dt} > 0$) it grows indefinitely with constant rate ($K_o - K_l$).

[8] Presence of cracks may not be as significant as pores under oxidizing environments – most observed cracks on SiO_2 scales are due to cooling of cristobalite after oxidation.

Energy dispersive spectroscopy (EDS) analysis was conducted to further investigate the distributions of elements in oxidized SiC. As shown in Figure 2-32, increasing signal intensity for silicon (Si) with simultaneously decreasing signal for oxygen (O) near the oxidized surface implies presence of SiO_2 scale. A similar result was found in a previous work that used energy dispersive X-ray spectroscopy (EDX) analysis to identify SiO_2 (Chu, 2004). Irregularities of SiO_2 morphologies formed on sintered α-SiC are shown by different distributions in signal intensities at different locations on the same specimen as shown in Figure 2-32.

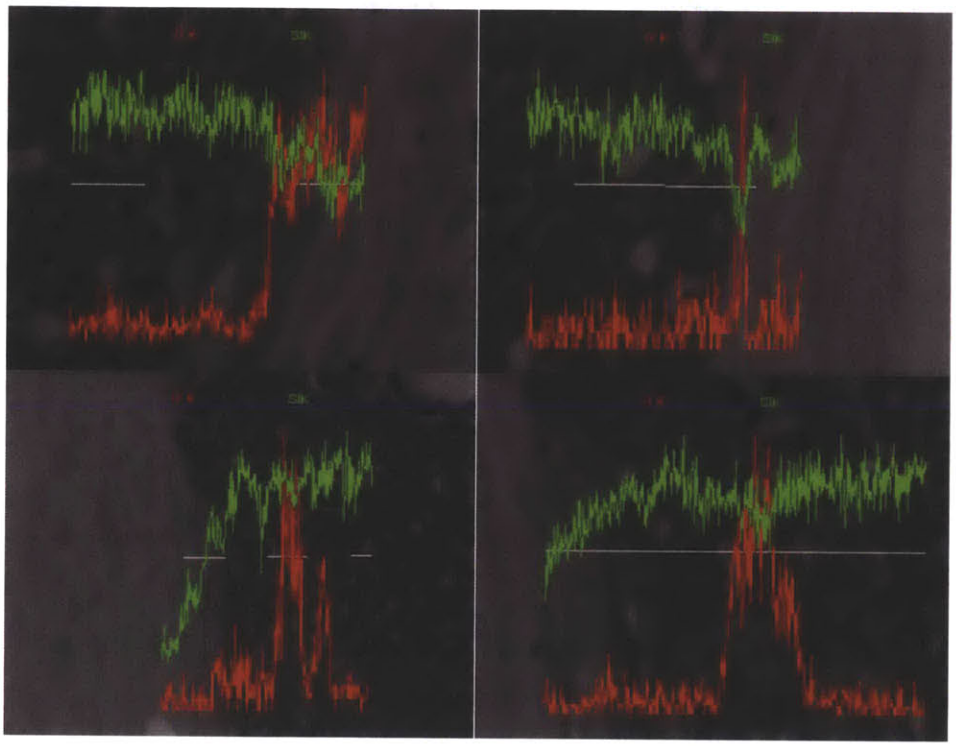

Figure 2-32 Energy Dispersive Spectroscopy (EDS) Analysis of Periphery of Oxidized SiC Cross Sections after 48 hours of exposure in 1340°C, with ~7.1g/min of H_2O[9]

[9] This sample's data is not included in neither Table 2-3 nor Table **2-4** as the sample's weight changes were not measured

2.5.3 Effects of Oxidation on SiC Strength

From an engineering perspective, SiC strength after oxidation is an important parameter for fuel rod safety and design. Strength of tubular α-SiC was measured by destructive burst tests. Polyurethane plugs (10 mm in O.D, 82A in durometer hardness), allowing approximately 0.44mm of clearance between the plug and the inner wall of SiC specimen, were inserted in tubular SiC specimens as shown in Figure 2-33

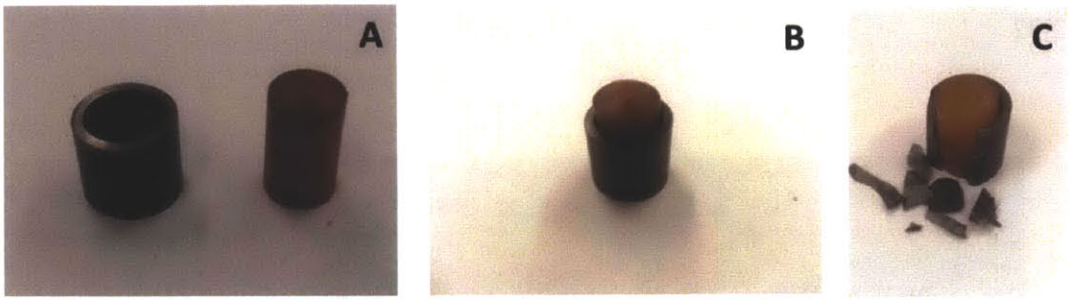

Figure 2-33 Polyurethane Plug and SiC Specimen for Destructive Strength Tests:
(A)- α-SiC and Polyurethane plug, (B)- Polyurethane plug inserted in the specimen, and (C)-Bursted specimen

The inserted poly urethane is compressively loaded and expanded in the radial direction, exerting tensile loads on the SiC tube walls, as illustrated in the schematic diagram in Figure 2-34. This loading scheme simulates internal pressurization of tubular SiC. The height of the polyurethane plug was carefully cut to make sure that the volume of polyurethane rod is the same as the internal hollow volume of the SiC tube. This method of determining polyurethane rod height was found after several trials to minimize discontinuity in stresses on SiC tube samples and to prevent the polyurethane plug from barreling out when compressed. Figure 2-35 shows a SiC tubes under loading with the facility.

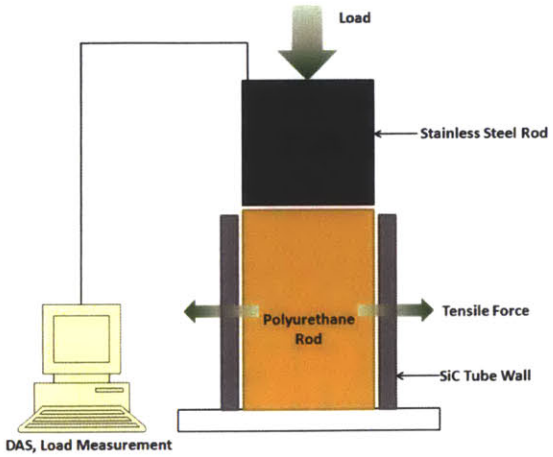

Figure 2-34 Schematic of Loading Method with Burst Test Facility

Figure 2-35 Picture of the Burst Experiment Facility when Loaded with a SiC Sample

During an experiment, the load gradually increases in a slow manner with compression of the polyurethane rod before contacting the sample wall – once contact is established, the load sharply increases as it starts to strain the material, as can be seen in Figure 2-36.

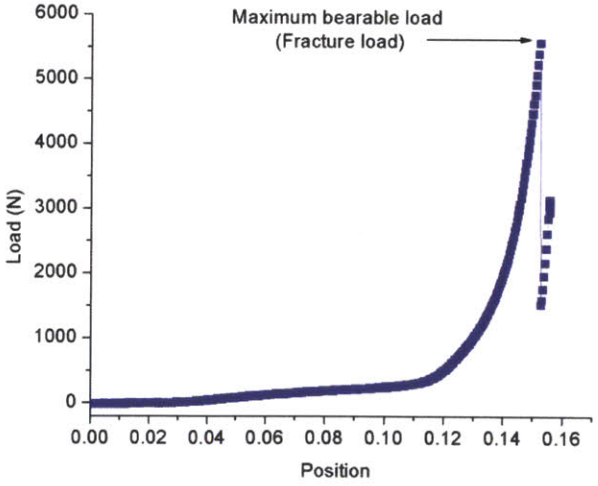

Figure 2-36 Typical Loading Curve for Burst Tests with Tubular α-SiC

Fracture of SiC specimen suddenly drops the load and the experiment is terminated. Recorded maximum bearable load (fracture load) is slightly overestimated because of initial loads for polyurethane

compression before it touches the wall. Nevertheless, this overestimation was a small portion of the fracture load (~5%) because most of the load is due to the SiC elastic response.

Oxidized α-SiC samples were drilled with two 0.15875 (1/16'') cm in O.D holes in the top portion of the side surface for sample holding in the oxidation facility, as discussed in section 2.4. Pre-existing drilled holes in a material lowers the material strength. Hence, the as-received SiC samples were also drilled with the same holes at the same locations in the sample for fair comparisons of material strength measurements. Fracture load (F_f) indicated in Figure 2-36 is divided by ID area of the internal hollow to yield the internal pressure (P_f) as follows

$$P_f = \frac{F_f}{\pi {r_p}^2} \tag{2-17}$$

where r_p is the radius of the internal polyurethane plug[10]. The thin-shell approach was used to calculate fracture hoop stress ($\sigma_{\theta,f}$) from the obtained P_f, given that the wall thickness of the tubular SiC is roughly 10% (~11.8% with Saint-Gobain α-SiC) of the tube diameter with the following equation.

$$\sigma_{\theta,f} = \frac{P_f r_m}{t_{thick}} \tag{2-18}$$

where r_m is the radius of the tubular SiC measured from the center of its wall thickness, and t_{thick} is the wall thickness.

Five as-received and twenty-one oxidized Saint-Gobain α-SiC specimens underwent destructive burst tests. Measured fracture hoop stresses are plotted as a function of weight loss per area of the oxidized sample in Figure 2-37. The presence of the drilled holes on the top of the sample surface reduced its average as-received strengths from 181 MPa[11] to 112 MPa. Introduction of drilled holes may have further dispersed the strength distributions of tested SiC specimens. The standard deviation of drilled as-received SiC specimens is 34 MPa with 5 measurements whereas that of undrilled specimens is 22 MPa with 10 measurements. Hence, wide bands of measured highest and lowest strengths shown in Figure 2-37, may be in part due to presence of the drilled holes. Generally speaking, effects of oxidation on α-SiC material strength are small in the tested conditions; as (1) their average strength, 102 MPa, is close to the average strength of as-received materials, 112MPa (2) extremes of oxidized strengths are still enveloped by the highest and lowest strengths of as- received materials, and (3) hardly any obvious trend is noticeable in

[10] Note that $r_p \approx r_i$ (=5.44 mm)
[11] Average strength of 10 undrilled as-received α-SiC specimens that were bursted in the same facility

terms of strengths of material with respect to weight losses (exposure times), and oxidation condition. This explanation may held true for all the observations made in this study except for the test condition of 1500°C with steam flow rate of 2.1g/min where the thickest oxide scale growth is expected due to low volatilization rate with relatively slower flow rate and high oxidation rates with high temperature.

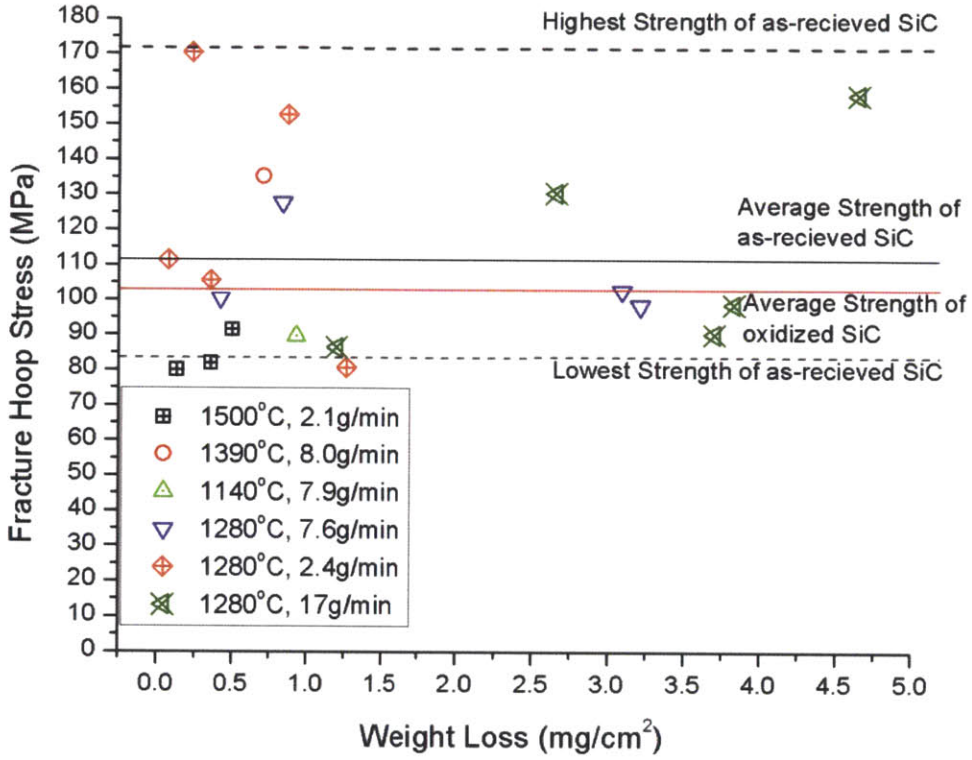

Figure 2-37 Fracture Hoop Stresses of As-Received Saint-Gobain α-SiC Specimens and Oxidized α-SiC Specimens (both with identical drilled holes) after Exposure to Oxidizing Conditions

Many studies have been conducted to assess effects of corrosion on the strength of SiC. Kim (Kim, 1990) investigated the effects of the corrosion-affected material surface modification on flexural strength of SiC and Si_3N_4. This study observed that the room temperature flexural strength of sintered α-SiC was reduced by surface defects formed by oxidation. The strength of the material was reduced by up to 50% when exposed for 10 hours at 1400°C to H_2-H_2O atmospheres. Formation of large pits and flaws during exposure were found to be responsible for this decrease in strength. On the other hand, the strength increased or was unaffected when a thin SiO_2 layer was formed on the surface. The higher strength is believed to be the result of crack blunting due to the formation of SiO_2 at the crack tips; the tip of an originally sharp crack is rounded during oxidation thereby arresting its propagation. Similar increases in

the strength of SiC by crack blunting via oxidation were previously observed (Kim, 1990), (Easler, 1981). Under the additional influence of an applied load during oxidation, material weakening was observed (Easler, 1981) and the most obvious mechanism for this is subcritical crack growth under the stress fields.

In addition to the surface modification due to oxide scale formation, changes of material phase underneath the oxide layer due to oxygen diffusion is of interest in understanding strength change. Minford (Minford, 1983) investigated oxygen penetration profiles into SiC samples (sintered α- SiC, hot-pressed SiC (~1.0% oxygen), and CVD SiC after oxidation at temperature between 1200°C – 1400°C. In the sintered α-SiC the oxygen penetration profile extended to a depth of ~15μm. CVD material showed a much sharper profile with little or no oxygen penetration, and penetration at the levels measured for the hot pressed SiC was masked by high background concentration. The study suggested that the oxygen penetration into the substrate material during oxidation involves accelerated diffusion with impurities at grain boundaries. Samples with detectable oxygen penetration exhibited basically similar behavior to what was observed in surface modification experiments – crack blunting versus strength degradation depending on the degree of oxygen penetration. It was believed that oxidized grain boundaries provide a low resistance path for slow crack growth for samples that exhibited strength degradation. Other studies (Tressler, 1990) found that strength degradation of SiC generally results from direct attack of the grain boundary phases, with pitting and bubble generation generally observed when a condensed silica scale is formed. Formation of subscale ternary crystalline phases has not been generally observed (Tressler, 1990).

Key characteristics of SiC oxidation under LOCA conditions were identified in this study - slow recession of the material and relatively thin oxide scale with volatilization imply that substantial degradation of mechanical strength due to surface impairment discussed in past studies (Kim, 1990), (Easler, 1981) is unlikely. There are even possibilities for a favorable crack blunting mechanism to take place. For tested sintered α-SiC specimens, pore clusters inside the material may practically serve as pre-existing cracks for fracture. In such a case, material's strength may not be sensitive to surface oxidation. In that regard, if there is any, oxidation effects on material strength may be more evident with CVD-SiC, because fracture would be initiated from the surface. Use of well prepared "Clean" CVD β-phase SiC for LWR cladding would minimize possible strength degradation due to discussed oxygen diffusion (Minford, 1983), (Tressler, 1990). These insights about the weaker interplay between SiC oxidation and mechanical property could imply a diminished importance of cladding oxidation in fuel rod safety during LOCA conditions compared to Zircaloy cladding.

2.6 Conclusion

The oxidation behavior of SiC and zirconium-based alloy claddings are vastly different; weight losses were observed for SiC while weight gains were found for Zr-4. This is because of the chemical stability of the oxide scales. Silica, SiO_2, undergoes a volatilization reaction with water vapor (H_2O), which involves outward diffusion of product species through a fluid boundary layer formed on the material surface. This mechanism is absent in Zircaloy oxidation, as zirconium oxide (ZrO_2) remains essentially inert in terms of chemical reactions with water vapor (Arnold, 2011). Therefore, oxidation of SiC eventually leads to material loss through SiO_2 volatilization, while oxidation of Zr-4 results in weight addition through capturing of oxygen atoms. Weight loss of Zircaloy with oxidation occasionally occurs through the oxide layer spallation.

The volatilization process introduces a key difference between SiC and Zircaloy oxidation – dependence on water vapor flow rate. The products of volatilization must be removed from the reaction sites in order for the reaction to proceed forward, and the effect of the fluid boundary layer on the material controls this process. Volatilization product species diffuse outward through the boundary layer formed on the material surface. Generally, the thicknesses of the boundary layers of fluids decrease with increasing flow rates, resulting in a shorter diffusion path. Therefore, the observed trend of increasing weight loss rate with increasing flow rate is a new observation made due to the volatilization reaction, which was not observed for Zr-4 oxidation. Material loss rates tend to become more sensitively dependent on flow rates at higher temperatures because SiO_2 volatilization is likely to be limited by material transport rates through fluid boundary layers.

The SiC steam oxidation investigation was conducted under pure steam environment, which will serve as conservative ceiling of the actual incore oxidation behavior during LOCA. This is because the oxidation reaction rate is at least 10 times higher with wet oxygen (H_2O) than with dry oxygen (O_2) due to a higher molecular concentration of wet oxygen at the same pressure (Opila,1994). Also, volatilization of the oxide layer with the formation of the hydroxyls in the presence of H_2O makes the oxide layer thinner, increasing the overall oxidation reaction rate. Hence, pure steam oxidation experiments without a carrier gas, conducted in this study, serve as a conservative experiment of SiC cladding oxidation.

SiC and Zr-4 oxidation rates can be quantitatively compared by using a metric termed equivalent cladding reacted (ECR), which is used by the U.S NRC LOCA criteria 10CFR50.46. ECR is defined to be the ratio of the reacted cladding thickness to initial cladding thickness. ECR of SiC was obtained based on the assumption that the thickness of the oxide layer formed on the surface is negligible compared to the

thickness of the cladding. Comparisons of oxidation rates between Zr-4 and SiC obtained in the same facility used in this study is presented in Table 2-6.

Table 2-6 Equivalent Cladding Reacted (ECR) of SiC vs. Zr-4 at 1200°C and 1140°C, respectively[12]

	Zr-4	α-SiC
Key Oxidation Mechanism	Diffusion controlled	Volatilization enhanced
Temperature Range of Concern	Serious safety concern at T>1204°C and even during normal operating conditions of LWRs	Unidentified
ECR per minute	1% at 1200°C with 3g/min of H_2O flow rates (5000)	0.0002% at 1140°C with 2.4g/min of H_2O flow rates (1)

* Numbers in the parenthesis () show relative material consumption rates

The oxidation of SiC is three orders of magnitude slower than Zr-4. Indeed, SiC oxidation has a few features that accelerate its reaction with oxidants; (1) Thinning of the protective silica layer with volatilization that leads to shorter solid-state diffusion paths for gaseous species, and (2) morphological degradation of the protective silica layer with observed formation of bubbles/pores and cracks that essentially allows 'instantaneous transport" of gaseous species through the oxide scale. Nevertheless, thanks to the bonding nature of the ceramic material, SiC demonstrates substantially slower conversion of its material in severe environments than zirconium-based alloys. This significantly slower reaction of SiC-H_2O with minimal influence on its mechanical strength may serve as a critical advantage of the use of SiC as a cladding material for LWRs over the current Zircaloy cladding. A temperature range of concern in terms of fuel rod safety with respect to oxidation could not be identified with SiC cladding below 1500°C, whereas ~1204°C serves as a regulatory limit for zirconium-based alloys in LOCA. In-depth discussion of SiC cladding oxidation design/operation implications of LOCA conditions and modeling the SiC material loss/recession for fuel rod simulation continues in the next chapter, Chapter 3.

[12] Comparison of the oxidation rates of SiC and Zircaloy near 1200°C is important because they can be used to discuss possibility of going beyond the current U.S NRC temperature limit (1204 °C).

Chapter 3

SiC Cladding Steam Oxidation II: Theories and Models

3.1 Introduction

This chapter is focused on theoretical studies for the development of SiC weight loss models as a continuing discussion of SiC cladding oxidation. Fuel rod design and reactor operation implications are drawn later in the chapter.

Volatilization of SiO_2 with reactions (2-3), (2-4),and (2-5) was observed through the weight loss of SiC in several past studies (Opila, 1997), (Robinson, 1999), (Opila, Smialek, 1999), (Opila, 2003). Studies (Opila, 1994), (Opila, 1999), (Tortorelli, 2003) , (Narushima, 1990) that were conducted with either stagnant oxidizing fluid or fluid with very slow velocity showed that volatilization did not occur - but a weight gain of the sample was observed through gain of oxygen.

It is generally understood that there is a threshold flow rate (or velocity) of the oxidizing species for SiO_2 volatilization to occur. Beyond the threshold velocity, higher velocity increases SiO_2 volatilization rates, resulting in faster material loss. In order for SiO_2 volatilization to continue, its silicate reaction products $SiO(OH)_2$, $Si(OH)_4$, or $Si_2O(OH)_6$ must be continually removed from the reaction sites – otherwise, the reaction stops upon reaching the thermodynamic equilibrium. Note that reaction product species are produced at the oxidized surface where fluid movements are stagnant under the boundary layer. Here, the term boundary layer follows the generic meaning, the distance from the surface where fluid velocity reaches 99% of the bulk fluid velocity. The species are transported towards the bulk fluid by gaseous-state molecular diffusion inside the boundary layer. The associated mass transport phenomena should be seen in such a way that lowers product species concentrations at the surface reaction sites. Species molecular diffusion in the boundary layer allows the volatilization reaction to proceed. Higher liquid velocities form thinner fluid boundary layers at the material surface which permit more rapid material transfer of product species to depart the reaction site. The diffusion rate is much slower in viscous silicate fluids than in aqueous fluids, so that there is more of tendency for the reaction process to be controlled by material-transfer phenomena rather than interface reactions (Kingery, 1976). Hence, appropriate modeling

of mass-transfer phenomena in the boundary layer is an essential requirement as is modeling of the solid/fluid interface reaction kinetics.

Depending on relative magnitudes in rates between weight gain from SiC to SiO_2 conversion and weight loss due to SiO_2 volatilization, the material's net weight change behavior varies significantly. Case (A) in Figure 3-1 illustrates oxidizing conditions with non/or negligible flow rates where no significant SiO_2 volatilization takes place. The dashed red line is weight gain with SiC $\rightarrow$ SiO_2 conversion ($\Delta m_{oxidation}$) and the dashed green line is weight loss with SiO_2 volatilization ($-\Delta m_{volatilization}$). The solid navy line is the measured net weight change of the material given by summation of weight gain and weight loss ($\Delta m_{net}=\Delta m_{oxidation}-\Delta m_{volatilization}$). In case (A), SiO_2 scale grows parabolically or perhaps linearly with presence of pores/cracks formed on the SiO_2 scale until it spalls. This behavior was commonly observed in many experiments including SiC oxidation processes developed in consideration of electronic applications, such as semi-conductors. Case (B) in Figure 3-1 illustrates conditions with comparable weight loss rate in volatilization and weight gain rate in Oxidation. Initial slight increase in the sample weight is observed due to fast growth of an oxide layer. The SiO_2 scale thickness parabolically grows until it reaches the limiting value $K_p/2K_l$ where reactions forming the oxide scale occur at the same rate as the reaction removing it. Once this steady-state is reached, the oxide at the surface has a constant thickness with time and the recession of the underlying material occurs at a linear rate. The material recession rate, hence weight loss, starts to closely follow a linear behavior as the oxide thickness gets closer to its limiting value. The linear SiC recession rate, once observed, is the same as the SiO_2 volatilization rate. The same holds for material weight change; material weight change rate is the same as linear weight loss rate found by SiO_2 volatilization rate. An example of the SiC oxidation behavior of case (B) is an experiment in 50%H_2O/50%O_2 gas mixture flowing at 1.4cm/sec (Opila, 1997). Case (C) shown in Figure 3-1 is an extension of case (B). With higher velocities, only linear weight loss was seen because the initial presumable non-linear behavior of material weight change due to early oxide formation is practically negligible and masked out by precisions in measurement systems. In this case, enhanced volatilization maintains a thinner steady-state oxide scale. Material weight loss rate is the same as SiO_2 volatilization rate. An example of the SiC oxidation behavior of case (C) is SiC exposure under a high-pressure burner rig of 1200°C - 1400°C fuel mixtures flowing 10 and 27 m/sec (Robinson, 1999). Case (D) in Figure 3-1 takes place with unusually high SiO_2 volatilization rates. It illustrates the situation where volatilization reaction is so fast that it removes SiO_2 scale as it forms. This situation cannot be modeled by paralinear oxidation in Eq.(2-6). The instantaneous removal of SiO_2 upon formation sets material weight loss rate to be the instantaneous rate of SiC $\rightarrow SiO_2$ conversion at zero oxide layer thickness ($x\rightarrow 0$). In Figure 3-1, case (D), the material weight loss rate is shown as a straight solid navy line that is

tangential to the fictitious reversed parabolic growth curve for SiO_2 growth. An example of the SiC oxidation behavior of case (D) can be found by complete removal of oxide scale formed on Si_3N_4 in a pressurized turbine with 1066 °C -1260°C steam flow at 573m/sec (Opila, 2003).

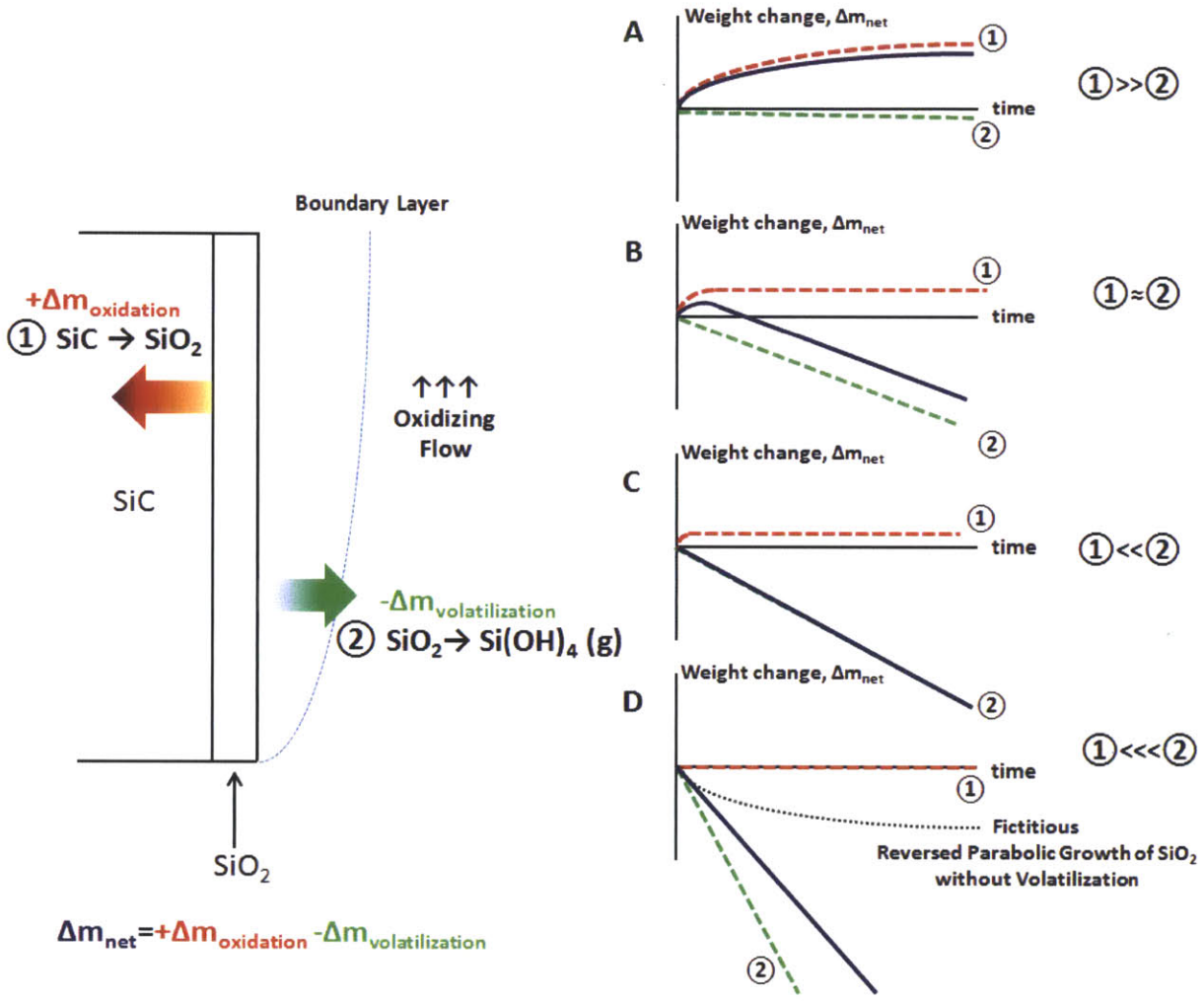

Figure 3-1 Four Possible Behavior Modes of SiC Weight Change in Different Oxidizing Environments: (A) Negligible volatilization, (B) Comparable Weight Loss Rate in Volatilization and Weight Gain Rate in Oxidation, (C) Clearly Higher Weight Loss Rate in Volatilization than Weight Gain Rate in Oxidations, and (D) Overwhelmingly Higher Volatilization Rate than Oxidation Rate

For the experimental results of this study, the presence of oxide scales and sensitive temperature dependent linear material losses extrapolated through the origin imply case (C) behavior. Hence, the observed material loss rates of SiCs with steam reaction under LOCA conditions can be modeled/and predicted by volatilization of SiO_2 scale.

3.2 Limitations of Previous SiO_2 Volatilization Correlations

The most widely used model for SiO_2 volatilization rate under an oxidizing environment is the correlation developed by Opila (Opila, 1997), (Robinson & Smialek, 1999), (Opila, Smialek, 1999). The correlation was developed by applying a heat and mass transfer analogy to a Nusselt number correlation for heat transfer. After the application of the analogy, the empirical correlation for the mass flux of volatile species was found to be

$$J\left[\frac{mg}{cm^2 hr}\right] = 0.664 Re^{1/2} Sc^{1/3} \frac{D_{diff}\rho_v}{L} \tag{3-1}$$

where J is the mass flux, Re is the Reynolds number, Sc is the Schmidt number, D_{diff} is the inter-diffusion coefficient of the volatile species in the fluid boundary layer, ρ_v is the concentration of the volatile species at the sold/gas interface, and L is the characteristic length of the tested specimen parallel to the direction of the gas flow. Eq.(3-1) was further manipulated to be expressed in terms of pressure, velocity, and temperature and the resulting correlation form is as follows

$$J\left[\frac{mg}{cm^2 hr}\right] = C exp(-\Delta G_0/RT) P^a v^b \tag{3-2}$$

where C, E, a, and b (~0.5)[13] are fitting parameters that are obtained from experimental data. This correlation form is analytically developed with the following assumptions – laminar flow, forced convection, external horizontal flat surface, and spatially constant velocity identical to the bulk fluid in the boundary layer. P is pressure, R is the gas-constant, T is temperature in kelvin, and v is bulk velocity of flow.

One noticeable step that led to Eq. (3-2) was expressing the non-dimensional numbers Re, and Sc and physical parameters D and in terms of functional dependencies imbedded in T, P, and v. In the course of such a simplifying step, all the constants ended up being lumped in the constant C in Eq.(3-2). Such a simplification of the correlation is essential in terms of making the correlation useable because the

[13] Power on the velocity term was intentionally fixed to be 0.5 for the lean-burn case in a burner-rig experiment. This is based on the rationale that the analytical dependency on velocity imbedded in the Re term in Eq.(3-1) is 0.5±0.16. For the rich-burn case, the power velocity term was found to be 0.69±0.32 (Opila, Smialek, Robinson, Fox, & Jacobson, 1999)

evaluation of the non-dimensional numbers Re, and Sc and D_{diff} for a complex gas mixture (e.g $4H_2 \cdot 12H_2O \cdot 10CO \cdot 7CO_2 \cdot 67N_2$ for a typical fuel-rich combustion mixture (Fox, 2000)) of interest, including lean-burn and rich-burn environments, is overwhelmingly complex.

The result of the simplification inevitably imposed several limitations on validity of the correlation form. The dimensional information imbedded in the Reynolds number (e.g, x in $\frac{\rho v x}{\mu}$ for 1-D flat plate) was lost. Also, the temperature dependencies of material properties in Re, Sc and in D and ρ_v were neglected in the course of the correlation simplification. As a result, the temperature dependent behavior captured by the exponential term in Eq.(3-2) shows the combined temperature dependency of the chemical reaction rate and fluid property changes. Hence, the activation energy of the interface chemical reaction, ΔG_0, obtained as a fitting factor is misleading as it includes the effect of the temperature dependency of the fluid properties. For wide ranges of temperatures encountered in the experiments, properties of a gas mixture undergo non-negligible changes, leading to a larger discrepancy between the true activation energy and the activation energy found in the correlation. In addition, the correlation form in Eq.(3-2) is somewhat misleading in its use of velocity as a parameter that describes how fast the fluid moves. Indeed, the use of mass-flux G, ($Re = \frac{GD}{\mu}$), would have made the correlation more universal for different sizes of geometry. In summary, the limitations of the previous correlation arises from basically two origins: (1) The unavoidable requirement for simplification of the correlation due to the complex gas-mixture of combustion related applications, and (2) The choice of the Nusselt number correlation form for the heat-mass transfer analogy. As for the first item, a volatilization correlation for a LWR fuel rod of SiC cladding during LOCA does not have to be oversimplified with the discussed simplifications, because the oxidizing flow is predominantly H_2O. For the second item, the choice of the Nusselt number correlation form that best captures the fluid velocity profile near the volatilizing surface is a key component to a more physically valid correlation. Recognizing these principles, in this study, new volatilization correlations for SiC cladding for LOCA conditions in LWRs were developed.

3.3 Development of SiO_2 Volatilization Correlation Forms in H_2O

The non-dimensional governing equations for continuity, momentum, energy, and concentration (species) are indicated in Eq.(3-3)-(3-6), respectively for incompressible flow with negligible viscous energy dissipation in a conduit (Schlichting, 2000).

$$\nabla^* \cdot u^* = 0 \tag{3-3}$$

$$\frac{\partial u^*}{\partial t} + u^* \cdot \nabla^* u^* = -\nabla^* P^* + \frac{1}{Re}\nabla^{*2} u^* + \frac{Gr_q}{Re^2} T^* \tag{3-4}$$

$$\frac{\partial T^*}{\partial t^*} + u^* \cdot \nabla^* T^* = \frac{1}{RePr}\nabla^{*2} T^* \tag{3-5}$$

$$\frac{\partial C^*}{\partial t^*} + u^* \cdot \nabla^* C^* = \frac{1}{ReSc}\nabla^{*2} C^* \tag{3-6}$$

Where the non-dimensional parameters are (in Cartesian coordinates), $t^* = \frac{t}{(D/U_b)}$, $x^* = \frac{x}{D}$, $y^* = \frac{y}{D}$, $z^* = \frac{z}{D}$, ${u_x}^* = \frac{u_x}{u_b}$, ${u_y}^* = \frac{u_y}{u_b}$, ${u_z}^* = \frac{u_z}{u_b}$, $P^* = \frac{P}{(\rho_0/{u_b}^2)}$, $T^* = \frac{k(T-T_0)}{{q_w}''D}$, $C^* = \frac{D_{diff}(C-C_0)}{JD}$, $Re = \frac{\rho_0 U_b D}{\mu}$, ${Gr_q}^* = \frac{g\beta {q_w}'' D^4}{k\nu^2}$, and $\rho^* = \frac{\rho}{\rho_0}$.

There are two important things to note in Eq.(3-3) to Eq.(3-6). In Eq. (3-4), the buoyancy force due to concentration difference is neglected because it is regarded as being very small compared to the buoyancy force induced by the temperature difference due to the wall heat flux. The resulting governing non-dimensional number that represents the buoyancy effect is therefore $\frac{Gr_q}{Re^2}$, which is the leading coefficient of the non-dimensional temperature T^*. As mentioned in chapter 2, $\frac{Gr_q}{Re^2}$ is negligibly small (<<1) in both the LWR LOCA case and the experimental environment, which makes the flow characteristics essentially identical to forced convection.

The Nusselt (Nu) number and Sherwood (Sh) number are equal to the dimensionless temperature gradient and concentration gradient at the surface and they are expressed as follows (Incropera, 2007),

$$Nu \equiv \frac{hD}{k} = +\frac{\partial T^*}{\partial y^*}\bigg|_{y^*=0} = f(x^*, z^*, Re, Pr) \tag{3-7}$$

$$Sh \equiv \frac{K_{mat}D}{D_{diff}} = +\frac{\partial C^*}{\partial y^*}\bigg|_{y^*=0} = g(x^*, z^*, Re, Pc) \tag{3-8}$$

The heat and mass transfer analogy holds when the functional form of f and g are the same. In the case of incompressible forced flow, the continuity and momentum equations provide input to the energy and mass equations except for some degree of mutual coupling through temperature dependent properties. That is, the continuity and momentum equations (Eq.(3-3) and Eq.(3-4), respectively) are solved for the velocity field without information from the energy and mass equations (Eq.(3-5) and Eq.(3-6), respectively). In contrast, through the appearance of the velocity fields (u^*) in the equations, the temperature (T^*) and species concentration fields (C^*) are coupled to the velocity fields while they are not affected by each other. With this one-sided coupling, functional forms for Nusselt number, f and Sherwood number, g in Eq.(3-7) and Eq.(3-8) are normally the same; this is termed the heat and mass transfer analogy [14]. Hence, from this understanding, a strategy for the volatilization correlation development in this study is to use the heat and mass transfer analogy to model material transport in the boundary layer from a functional form of a relevant heat transfer correlation.

The previous SiO_2 correlations made a choice of the analytically developed Nusselt number correlation for the 1-D infinite plane based on the rationale that their test sample geometry is in a simple planar coupon shape (Opila, 1997), (Robinson, 1999), (Opila, Smialek, 1999), (Opila, 2004). However, the true velocity fields near the volatilizing surface are likely to be dictated by the geometry of the fluid conduit channel. Hence, for most of the SiC oxidation experiments where samples are located inside a cylindrical conduit, the Nusselt number correlation for a pipe flow is recommended. Similarly, the coolant velocity field inside the subchannel of the LWR core is better represented by a pipe flow than the infinite plane case. Therefore, in this study, the following analytically developed heat transfer coefficient correlations

[14] Heat and mass transfer analogy breaks down with flows with non-negligible value of $\frac{Gr_q}{Re^2}$, such as natural circulation, because of the mutual coupling of the energy and momentum equations (Eq.(3-4) and Eq.(3-5), respectively). Also, the validity of heat and mass transfer analogy may become weaker in a system with wide range of temperature variations because the mutual indirect-coupling between the energy and momentum equations become more significant through temperature dependence of fluid properties.

for a developing laminar flow in a conduit for the combined velocity and thermal entry length (Incropera, 2007) was chosen for heat and mass transfer analogy

$$\overline{Nu}_D = 1.86\left(\frac{Re_D Pr}{L/D}\right)^{1/3}\left(\frac{\mu}{\mu_s}\right)^{0.14} \tag{3-9}$$

where $\overline{Nu}_D$ is the average Nusselt number over the length L from the entrance, Re_D is the Reynolds number in a conduit, Pr is Prandtl number, L is the length of interest along the flow direction, D is diameter, μ is bulk fluid viscosity, and μ_s is fluid viscosity at the surface. Eq.(3-9) is the Sieder and Tate correlation and is recommended for use when $0.6 \lesssim Pr \lesssim 5$, given that $\overline{Nu}_D \geq 3.66$. All properties appearing in Eq.(3-9) should be evaluated at the average bulk fluid temperature in the system of interest.

Eq.(3-9) was modified to the mass transfer equation by the employment of heat and mass transfer analogy as follows

$$\overline{Sh}_D = 1.86\left(\frac{Re_D Sc}{L/D}\right)^{1/3}\left(\frac{\mu}{\mu_s}\right)^{0.14} \tag{3-10}$$

Assuming the concentrations of volatile silicate species are very dilute in the bulk fluid ($\rho_v|_{bulk} \approx 0$), mass flux of volatile species, J, at the surface is given by

$$J\left[\frac{mg}{cm^2 hr}\right] = \left(\frac{D_{diff}\rho_v}{D}\right)\overline{Sh}_D \tag{3-11}$$

where D_{diff} is the diffusion coefficient of the volatile species in the boundary layer, D is conduit diameter, ρ_v is the density of volatile species at the surface. It is important to note that the density of volatile species in the fluid boundary layer is predominantly determined by the reaction of silica with water in an equilibrium state. Thus, before any volatile species diffuses out through the boundary layer, the silica scale reacts with water to produce volatile products inside the boundary layer. Assuming that SiC oxidation and volatilization processes are quasi-static processes, in that every snap shot of the process is in equilibrium in terms of temperature and concentration, the equilibrium pressure of $Si(OH)_4$, $P(Si(OH)_4)$ of the volatilization reaction $SiO_2 + 2H_2O$ (g) = $Si(OH)_4$ (g) at the surface SiO_2 (reaction site) can be expressed as follows

$$K_{eq} = \frac{P(Si(OH)_4)}{P(H_2O)^2} \tag{3-12}$$

where K_{eq} is the equilibrium reaction constant, and $P(H_2O)$ is the pressure of H_2O, which can be given by the system pressure in the 100% H_2O case. The diffusion coefficient, D_{diff}, is inversely proportional to the operating steam pressure and density of volatile species, ρ_v is proportional to the partial pressure of the species in the boundary layer. The general temperature dependence is obtained from the equilibrium constants, K_{eq} of the pertinent reactions with the following relationship after combining the Gibbs-Helmholz equation and the Van't Hoff equation

$$K_{eq} = exp\left(-\frac{\Delta G_0}{RT}\right) = \exp\left(-\frac{\Delta H_r^0}{RT} + \frac{\Delta S_r^0}{R}\right) = A_0 \exp\left(-\frac{\Delta H_r^0}{RT}\right) \tag{3-13}$$

where ΔG_0 is the standard Gibbs energy change of the reaction, ΔH_r^0 is the standard enthalpy change, and ΔS_r^0 is the standard entropy change. With the assumption that ΔH_r^0 and ΔS_r^0 are constant over the temperature range of interest, temperature dependency of equilibrium constant K_{eq}, is obtained by finding ΔH_r^0 and the pre-exponential factor $A_0 (= \exp\left(\frac{\Delta S_r^0}{R}\right))$ by fitting experimental data point (Hashimoto, 1992). Now, Eq. (3-11) can be expressed with measurable parameters as follows

$$J\left[\frac{mg}{cm^2 hr}\right] = Aexp\left(-\frac{\Delta H_r^0}{RT}\right) P^a Sh \tag{3-14}$$

where the power exponent, a, on the pressure term, P, contains information about types of volatilization reactions including product species and stoichiometry. The form of Eq.(3-14) is in the same form as Opila's correlations (Opila, 1997), (Opila, Smialek, 1999). The main difference comes from the choice of Sherwood number, Sh and retention of non-dimensional numbers that contain the physical aspects of mass transfer phenomena. In this study, the Sherwood number correlation relevant to developing laminar flow in a pipe shown in Eq.(3-10) was chosen to best model material transfer in the conducted experiments. Hence, Eq.(3-14) is now expressed as follows

$$J\left[\frac{mg}{cm^2 hr}\right] = A\, exp\left(-\frac{\Delta H_r^0}{RT}\right)\left(\frac{Re_D Sc}{L/D}\right)^b P^a \tag{3-15}$$

where A, a, and b are fitting parameters that can be found from fitting experimental data. The fitting coefficient, b, in Eq.(3-15)[15] determines the velocity dependence of material loss rate. The original Nusselt number correlations uses 1/3 for the parameter 'b' in Eq.(3-15).

A different correlation form is developed with an insight of the species molar flux based on species balance at the steady equilibrium state. The following relation decomposes inward flux of H_2O molecules ($J_{H_2O,mole}$) into H_2O molecules for oxidation at SiC-SiO_2 interface and H_2O molecules for volatilization

$$J_{H_2O,mole} = J_{H_2O,oxidation} + J_{H_2O,volatilization} = XR_{oxidation} + YR_{volatilization} \tag{3-16}$$

where $R_{oxidation}$ is reaction rate of oxidation and $R_{volatilization}$ is reaction rate of volatilization in terms of moles and, X and Y are constants determined by the stoichiometry of each reaction.

The inward molar flux of H_2O, $J_{H_2O,mole}$, can be seen as material transport phenomena driven by the concentration difference of the species

$$J_{H_2O,mole} = K_{mole}\left(C_{H_2O,bulk} - C_{H_2O,surface}\right) \tag{3-17}$$

where K_{mole} mole-based mass transfer rate of H_2O species, and $C_{H_2O,bulk}$ and $C_{H_2O,surface}$ are molar concentration of H_2O in bulk flow and at the surface, respectively.

$R_{oxidation}$ and $R_{volatilization}$ can be replaced by $K_{oxidation}\left[C_{H_2O,interface}\right]^m$ and $K_{volatilization}\left[C_{H_2O,wall}\right]^n$, respectively,

$$K_{mole}\left(C_{H_2O,bulk} - C_{H_2O,wall}\right) = XK_{oxidation}\left[C_{H_2O,interface}\right]^m + YK_{volatilization}\left[C_{H_2O,wall}\right]^n \tag{3-18}$$

where $K_{oxidation}$ is the Arrhenius rate of oxidation reaction at SiC-SiO_2 reaction, $K_{volatilization}$ is the Arrenius rate of volatilization reaction at SiO_2 surface, and m and n are factors that power concentration dependencies on oxidation and volatilization reaction rates, respectively. m and n are determined by stoichiometry of the reactions. Once the oxide thickness reaches a steady-state constant, the following relation holds with zero 'net change' in SiO_2 mass.

$$K_{oxidation}\left[C_{H_2O,interface}\right]^m - K_{volatilization}\left[C_{H_2O,wall}\right]^n = 0 \tag{3-19}$$

---

[15] $\left(\frac{\mu}{\mu_s}\right)^{0.14}$ term is assumed to be unity with $\mu_s \approx \mu$. Its influence on transport phenomena is in general not significant.

With Eq.(3-19), the right hand side of Eq.(3-18) can be simplified at steady state to

$$XK_{oxidation}\left[C_{H_2O,interface}\right]^m + YK_{volatilization}\left[C_{H_2O,wall}\right]^n = (X+Y)K_{volatilization}\left[C_{H_2O,wall}\right]^n \quad (3\text{-}20)$$

Hence the outward flux of the volatilized species can be found by a constant, C, multiplied by the inward molecular flux of H_2O

$$\therefore J_{volatilzation,mole} = K_{volatilization}\left[C_{H_2O,wall}\right]^n = \lambda J_{H_2O,mole} \quad (3\text{-}21)$$

where λ is given by $1/(X+Y)$.

Given the relations above, the following relation holds

$$CK_{mole}\left(C_{H_2O,bulk} - C_{H_2O,wall}\right) = K_{volatilization}\left[C_{H_2O,wall}\right]^n = J_{volatilzation,mole} \quad (3\text{-}22)$$

$\left[C_{H_2O,wall}\right]^n$ can be approximated by some constant ξ times $\left[C_{H_2O,wall}\right]$, resulting in the following relation

$$J_{volatilzation,mole} = \frac{C_{H_2O,bulk}}{\frac{1}{\lambda K_{mole}} + \frac{1}{\xi K_{volatilization}}} \quad (3\text{-}23)$$

The term $\frac{1}{\lambda K_{mole}} + \frac{1}{\xi K_{volatilization}}$ acts as the resistance against the volatilization process. If , $\lambda K_{mole} \gg \xi K_{volatilization}$, where material transfer coefficient is much greater than the chemical reaction rate constant, $J_{volatilzation,mole} \approx \xi K_{volatilization} C_{H_2O,bulk}$, essentially making the volatilization process reaction-rate limited and independent of the flow characteristics. On the other hand, if $\xi K_{volatilization} \gg \lambda K_{mole}$, $J_{volatilzation,mole} \approx \lambda K_{mole} C_{H_2O,bulk}$, where the volatilization process is material transfer limited. The Sherwood (Sh) number is related to the mass transfer coefficient as follows

$$K_{mole} = \frac{Sh\, D_{diff}}{D} \quad (3\text{-}24)$$

where D_{diff} is the diffusion coefficient, and D is a diameter of conduit.

The volatilization reaction rate kinetics $K_{volatilization}$ is expressed in the Arrhenius form as a function of temperature. Siedel-Tate Sherwood correlation in Eq.(3-10) was chosen to obtain the value of K_{mole}

appearing in Eq.(3-23). Concentration of H_2O species in the bulk coolant increases with pressure and inversely to temperature following ideal gas law, $C_{H_2O,bulk} \sim \frac{P}{T}$ and gaseous species diffusion coefficient D_{diff} is ~$T^{1.5}$ by the Chapman-Enskog theory[16]. Now, with these relations, Eq.(3-23) is expressed in a correlation form at a fixed pressure with the fitting constants $\gamma, b, \varphi, and\ E$ in Eq.(3-25).

$$J[\frac{mg}{cm^2 hr}] = \frac{1}{T\left[\frac{\gamma L^b D^{1-b}}{(Re_D Sc)^b T^{1.5}} + \varphi exp(\frac{E}{RT})\right]} \tag{3-25}$$

The fitting parameter, E in Eq.(3-25) represents activation energy for the kinetics of the volatilization reaction. Note that the correlation form in Eq.(3-25) may possibly be overly complex to capture pressured dependence. The primary reason for it is that the following step $\left[C_{H_2O,wall}\right]^n \sim \xi\left[C_{H_2O,wall}\right]$ in derivation of the correlation template in Eq.(3-23) makes pressure affect the pre-exponential factor $\varphi\ (= \xi A')$[17] in the volatilization reaction kinetics. Table 3-1 summarizes the developed correlation forms for SiC oxidation in the developing laminar flow of H_2O in a tube

[16] D_{diff} ~$T^{1.5}$ is based on the explicit temperature dependence appearing in Chapman-Enskog diffusion theory. Indeed, we checked that the consideration of additional temperature dependence on collision integral term obtained by Lennard-Jones potential slightly increases the temperature dependence to be $T^{1.7}$ by approximating with SiF_4-H_2O case. Because temperature sensitivity imbedded in the collision integral term depends on types of volatile species, this study uses $T^{1.5}$ as a reference case for the correlation development

[17] A' is an arbitrary constant, and $\xi = \left[C_{H_2O,wall}\right]^{n-1}$

Table 3-1 Summary of SiC Weight Loss Correlation Forms in Developing Laminar Flow of H_2O in Tube

	Correlation Form A	Correlation Form B
$J\left[\frac{mg}{cm^2hr}\right]$	$A\,exp\left(-\frac{\Delta H_r^0}{RT}\right)\left(\frac{Re_D Sc}{L/D}\right)^b P^a$	$\frac{1}{T\left[\frac{\gamma L^b D^{1-b}}{(Re_D Sc)^b T^{1.5}} + \varphi exp(\frac{ER}{T})\right]}$
Fitting Parameters	A, ΔH_r^0, b, and a	b, γ, φ, and E
Theoretical velocity factor	b~0.33	-

Note that the velocity field of laminar flow is significantly affected by the geometry of the flow path. Theses heat and mass transfer correlations are unique to different geometries. This implies that for the volatilization in a laminar flow, no volatilization correlation developed in an experiment can exactly predict what is going to happen in an assembly subchannel, unless the experiment was conducted with the same geometry of the LWR subchannel. Nevertheless, a reasonable choice of Sherwood number correlation for velocity fields of interest could contribute to minimizing the error between experiment based predictions and applications of interest. Extension of the developed correlations to the actual fuel rod will be discussed in following discussions

3.4 Fitting SiO_2 Volatilization Correlations to Experimental Data

3.4.1 Thermochemical Data of Si-hydroxide Gas Molecules with H_2O

Development of correlations for SiC weight losses should take into account existing thermochemical data of a mixture of Si-hydroxide gas molecules with H_2O. Hashimoto (Hashimoto, 1992) experimentally obtained the equilibrium constant for the chemical reaction, Eq. (2-4), $SiO_2(s) + 2H_2O\,(g) \leftrightarrows Si(OH)_4$ as follows,

$$log_{10}K_{eq,Si(OH)_4} = -(0.2963 \pm 0.0087) \times 10^4 \left(\frac{1}{T}\right) + (-3.4563 \pm 0.0545) \quad (3\text{-}26)$$

The standard enthalpy change ΔH_r^0 = 56.7±1.7 J/mol K is obtained from this relation, hence the $K_{eq,Si(OH)_4}$ follows

$$K_{eq,Si(OH)_4} \sim exp\left(-\frac{\Delta H_r^0 (= 56.7 kJ/mol)}{RT}\right) \tag{3-27}$$

The thermo-chemical data for $SiO_2(s) + 2H_2O\ (g) \leftrightarrows Si(OH)_4$ reaction is pertinent for this study and LBLOCA conditions because $Si(OH)_4$ is found to be the primary volatile species in water for temperatures between 1100°C and 1500°C (Hashimoto, 1992), demonstrating a square dependence on the amount with the water-vapor partial pressure measured by mass spectrometry.

3.4.2 Reynolds Number Calculation for the Correlation Development

In the experiments conducted in this study, steam flow separation between the internal and external areas of the tubular SiC specimen (see Figure 3-2) occurs as it passes by the sample.

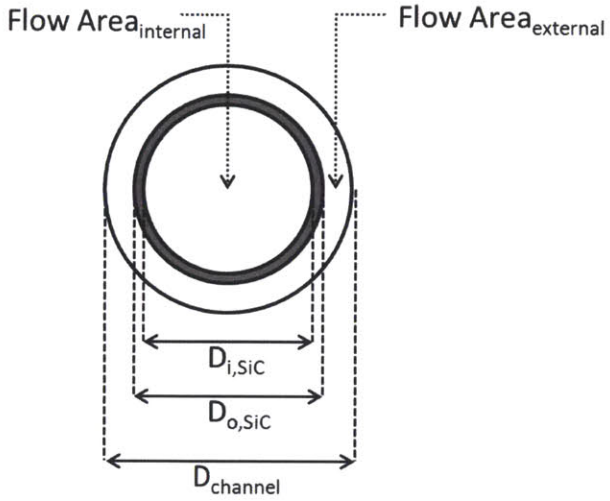

Figure 3-2 View of Tubular SiC Specimen Placed in Quartz Tube

Flow separation occurs in a way that the total of the two flows match the mass balance and differential pressures as shown in Eq.(3-28) and (3-29)

$$\dot{m}_{steam} = G_i A_i + G_e A_e \tag{3-28}$$

$$\Delta P_{intneral} = \Delta P_{external}$$
$$\rightarrow \frac{f_i L}{2D_{e,i}\rho} {G_i}^2 = \frac{f_e L}{2D_{e,e}\rho} {G_e}^2 \tag{3-29}$$

Where, G is the mass flux of steam, A is the flow area of steam, f is the friction factor, L is the length of the tubular SiC specimen, D_e is the equivalent diameter, and ρ is the density. Subscripts i, and e denote internal, and external regions, respectively. For laminar flow, the friction factor $f \sim C/Re$, where C is a constant. We can estimate the flow split by assuming that the temperature of steam is uniform in the flow areas, then Eq.(3-28) and (3-29) can be simultaneously solved, yielding

$$\frac{G_i}{G_e} = \frac{{D_{e,i}}^2}{{D_{e,e}}^2} \tag{3-30}$$

We are interested in a representative Reynolds number that captures the boundary layer development that occurs in both the internal and external surfaces of the tubular SiC specimen. Hence, in this study, a representative Reynolds number for tubular SiC specimens was calculated by surface-area-weighted average as shown in Eq. (3-31)

$$Re_{representative} = \frac{Re_i \pi D_{i,SiC} L + Re_e \pi D_{o,SiC} L}{\pi D_{i,SiC} L + \pi D_{o,SiC} L} \tag{3-31}$$

where $Re_i \left(= \frac{G_i D_{e,i}}{\mu}\right)$ is the Reynolds number for the internal surface of tubular SiC specimen and $Re_e \left(= \frac{G_e D_{e,e}}{\mu}\right)$ is the Reynolds number for the external surface of the tubular SiC specimen. $D_{i,SiC}$ and $D_{o,SiC}$ are the internal diameter and external diameter of a SiC specimen, as shown in Figure 3-2.

3.4.3 Development of Correlation A

The pressure dependence of SiC in the weight loss correlation was not necessary, as the H_2O pressure was fixed at 1 atm. Correlation A in Table 3-1, $A\, exp\left(-\frac{\Delta H_r^0}{RT}\right)\left(\frac{Re_D Sc}{L/D}\right)^b$ was fitted with the experimental data after linearization of the form as follows

$$\ln J = lnA - \frac{\Delta H_r^0}{RT} + b\, ln\left(\frac{Re_D Sc}{L/D}\right) \tag{3-32}$$

The weight loss rates of Saint-Gobain α-SiC shown in

Table **2-4** were used for material loss rates J in Eq.(3-32). Fitting was conducted with four different constraints: (1) no constraints (best-fitting), (2) fixed enthalpy change with Hashimoto's result, (3) fixed

flow rate dependence with Sieder-Tate correlation, and (4) both fixed enthalpy change and flow rate dependence. The results are summarized in Table 3-2.

Table 3-2 Summary of Correlation A (A, A-1, A-2, A-3) with Different Constraints

	Fitting Constraints	Correlations	Fitting Statistics
Correlation A (3-33)	None (Best-Fitting)	$J[\frac{mg}{cm^2hr}] = 3.826\, exp\left(-\frac{102.8\, kJ/mol}{RT}\right)\left(\frac{Re_D Sc}{L/D}\right)^{0.68}$	$R^2_{adj} = 0.71$
Correlation A-1 (3-34)	$\Delta H_r^0 = 56.7 kJ/mol$ (Hashimoto, 1992)	$J[\frac{mg}{cm^2hr}] = 0.174\, exp\left(-\frac{56.7 kJ/mol}{RT}\right)\left(\frac{Re_D Sc}{L/D}\right)^{0.56}$	$R^2_{adj} = 0.63$
Correlation A-2 (3-35)	b=0.33 (Sieder and Tate)	$J[\frac{mg}{cm^2hr}] = 4.463 exp\left(-\frac{83.6 kJ/mol}{RT}\right)\left(\frac{Re_D Sc}{L/D}\right)^{0.33}$	$R^2_{adj} = 0.60$
Correlation A-3 (3-36)	$\Delta H_r^0 = 56.7 kJ/mol$ (Hashimoto, 1992) b=0.33 (Sieder and Tate)	$J[\frac{mg}{cm^2hr}] = 0.537 exp\left(-\frac{56.7 kJ/mol}{RT}\right)\left(\frac{Re_D Sc}{L/D}\right)^{0.33}$	$R^2_{adj} = 0.60$

Correlation A without a fitting constraint gives statistically the best fitting with the experimental data in comparison with constrained correlations. Note that the velocity dependence is found to be 0.68, far greater than the theoretical estimation, 0.33 for developing laminar flow. This may imply that the flow dependence is thought to be somewhere between the expected laminar flow behavior (0.33) and expected turbulence (0.8) behavior. This flow dependence is in a good agreement with the general understanding of flow dependence found by past studies. Robinson's study on SiC weight losses in a burner rig with fuel gases yielded $\sim v^{0.69}$ and $\sim v^{0.5}$ dependence for fuel rich, and fuel lean cases, respectively (Robinson, 1999). The series of Opila's studies on SiC material loss rates found that the velocity dependence follows $\sim v^{0.5}$ for laminar flow and $\sim v^{0.8}$ for turbulence flow (Opila, 2004). A study on SiO_2 volatilization from silicon nitride also demonstrated $\sim v^{0.5}$ dependence (Sudhir, 2006). It was believed that $\sim v^{0.5}$ dependence comes from velocity dependence of the Reynolds number in the Nusselt number correlation for developing laminar flow in an infinite external horizontal surface. This explanation may be erroneous; tested specimen geometries are all different in the experiments of $\sim v^{0.5}$ dependence with radical departure from ideal infinite horizontal surface. Instead, what those experiments have in common is that they all used circular flow channels. Hence, it would be reasonable to think that the observed $\sim v^{0.5}$ flow dependence on SiC weight loss may pertain to velocity & concentration fields uniquely developed in a circular flow channel with significant variations in flow conditions upon interaction of the specimen along its path –

which might have caused a departure from ideal laminar behavior (~0.33). Unlike laminar flow, mass transfer in turbulent flow is not as sensitive to detailed geometry of flow channel & specimen geometries. Hence, the theoretical flow dependence, $\sim v^{0.8}$, is expected as observed by past experiments (Opila, 2004). The standard enthalpy change, ΔH_r^0, $102.8\,kJ/mol$ that gives the best fit with the experimental data exceed the value of $\Delta H_r^0 (= 56.7 kJ/mol)$ found by Hashimoto (Hashimoto, 1992). Robinson's study reported $108 kJ/mol$ for the fuel-lean case and 159kJ/mol for the fuel-rich case (Robinson, 1999). These values, however, contain a temperature dependence of flow properties as well, whereas ΔH_r^0 found in this study is separated from temperature dependence of flow properties by retention of mass-transfer relevant non-dimensional parameters.

Fixing $\Delta H_r^0 = 56.7 \text{kJ/mol}$ in the reaction standard enthalpy yielded a flow dependence of $\left(\frac{Re_D Sc}{L/D}\right)^{0.56}$ in Correlation A-1 (3-34), and fixing flow dependence $\left(\frac{Re_D Sc}{L/D}\right)^{0.33}$ lowered the standard enthalpy change to $\Delta H_r^0 = 83.6 \text{kJ/mol}$ in Correlation A. Fitting experimental data is still possible by fixing both ΔH_r^0 and the flow rate dependence found from other studies at the expense of predictability. For each correlation in Table 3-2, experimental data on material loss rates (J) in Table 2-4 was divided by the obtained correlations namely, $G_{fit} \left(= A \exp\left(-\frac{\Delta H_r^0}{RT}\right)\left(\frac{Re_D Sc}{L/D}\right)^b\right)$ to assess accuracy in predictability. The ideal case would yield J/G = 1, indicating a perfect agreement between the experimental data and the calculated value. Results of J/G (experimental data/calculated value) for the four different correlations are shown in Figure 3-3. It can be seen in Figure 3-3 that predictability tends to be slightly sacrificed with fitting constraints with increasing departure from unity. As the fitting statistics in Table 3-2show, correlation-A without a fixed fitting constraint gives the best prediction on average as seen by least scatters around unity. Correlation A-1 is the next best fit.

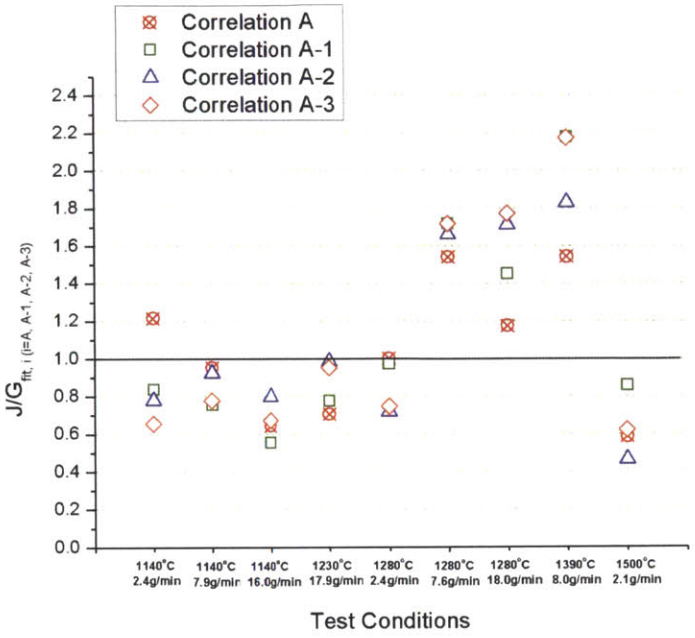

Figure 3-3 Experimental Data for SiC Weight Loss Rate (J)/Calculated Weight Loss Rate (G) for Four Different Correlations

Predictability of each correlation can be further investigated by separating the mass transfer effects and chemical equilibrium. The correlation form A enables addressing each effect by dividing the experimental data by the term corresponding to either mass transfer, $\left(\frac{Re_D Sc}{L/D}\right)^b$ or chemical equilibrium, $exp\left(-\frac{\Delta H_r^0}{RT}\right)$. Figure 3-4 shows predictability of the developed correlations for SiO_2 volatilization reaction equilibrium constant by eliminating the mass transfer effects through $J/\left(\frac{Re_D Sc}{L/D}\right)^a$. Correlation A with $\Delta H_r^0 = 102.8\ kJ/mol$ exhibits arguably the best agreement with the experimental data for obtained mass-transfer eliminated material loss rate $J/\left(\frac{Re_D Sc}{L/D}\right)^a$. Predictability of the calculation becomes weaker at high temperatures >1600K as higher importance was given to predictability at lower temperatures in fitting the experimental data, since the number of the available experimental data at temperature T < 1600K exceeds the number at T >1600K . This explains the observed tendency for decreasing predictability with high temperature of the calculations in Figure 3-3. Such an asymmetry in the number of experiments in terms of test conditions contributes to biased accuracy of the model for particular test conditions. Material transfer effects, however, do not contribute to the biased accuracy of the model as each set of three experiments was conducted uniformly over the entire range of tested $\left(\frac{Re_D Sc}{L/D}\right)$. This can be seen in Figure 3-5, showing volatile species material transfer dependent behavior of SiC material loss rate. Chemical

equilibrium effects are eliminated in the observed SiC material loss rates by dividing the observed material loss rates (J) by the temperature dependent reaction equilibrium, $exp\left(-\frac{\Delta H_r^0}{RT}\right)$.

Seeking the best fitting factor for a given constraint on either ΔH_r^0 or b in the regression processes still gives an acceptable agreement with the experimental data in comparison with the unconstrained correlation A-1; their effects on fitting statistics in Table 3-2 and the accuracy shown in Figure 3-3, Figure 3-4, and Figure 3-5 are still acceptable. Also, correlation-A does not give the most accurate fitting result over the entire test conditions – its virtue over the other ones only comes from its marginally better predictability in an average sense. These discussions leave the correlation development still open to further investigation with increasing number of available experimental data. Indeed, this kind of limited confidence in the fitting parameters is common to past studies on material loss of SiC in oxidizing environments, and to even general mass transfer –related studies, because of limited availability of data[18]. Nevertheless, Correlation A is the most representative of the experimental data among all correlations. The behavior of correlation A as a function of temperature and steam mass flux is shown in Figure 3-6.

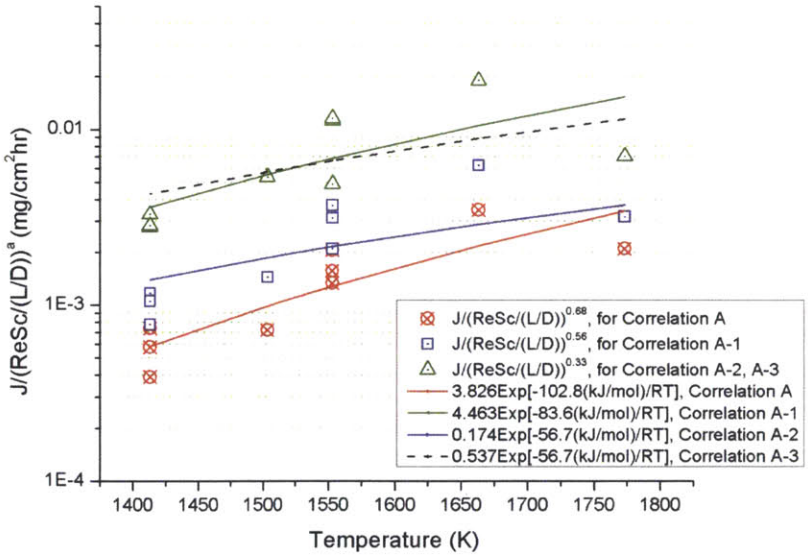

Figure 3-4 SiO_2 Volatilization Reaction Equilibrium Dependent Behavior of SiC Material Loss Rate: Points – Experimental Data with Tubular α-SiC, Lines – Calculation

[18] In general, the development of mass transfer a correlations requires exceeding amount time and resources compared to those of heat transfer.

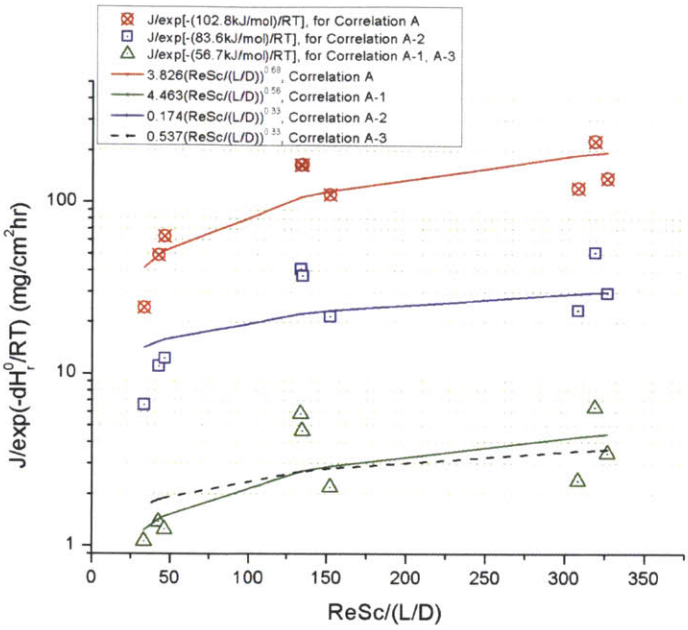

Figure 3-5 Volatile Species Material Transfer Dependent Behavior of SiC Material Loss Rate: Points – Experimental Data with Tubular α-SiC, Lines – Calculation

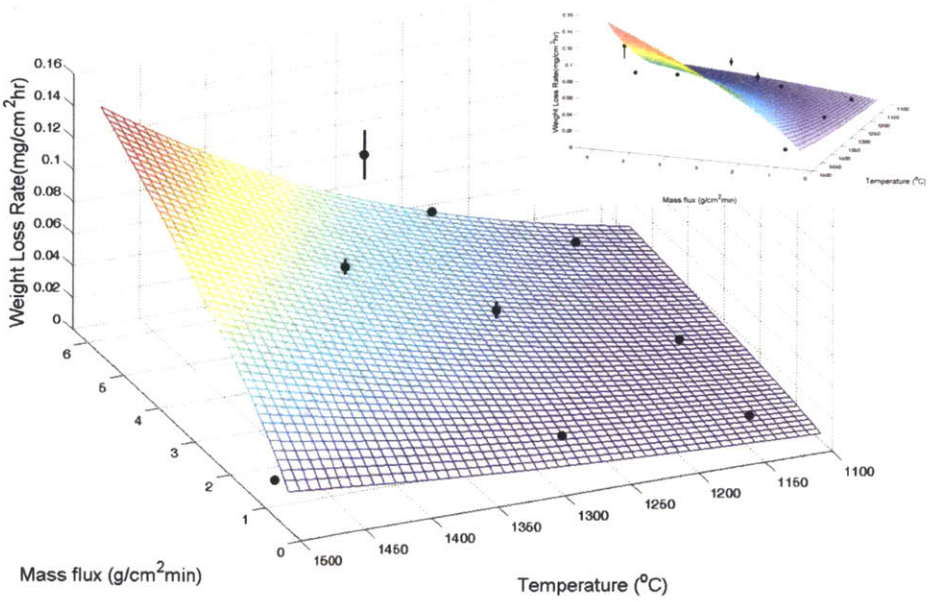

Figure 3-6 α-SiC Weight Loss Rate as a Function of Temperature and Steam Mass Flux at 1 atm, given by Correlation A, fitted Against Experimental Data Shown as Black Dots

For Correlation A, ΔH_r^0 is $102.8 \pm 33.8\, kJ/mol$ and mass transfer dependence varies as $\left(\frac{Re_D Sc}{L/D}\right)^{0.68\pm0.18}$ for a 80% confidence. Figure 3-7 shows the prediction by correlation-A of volatilization rate of α-SiC with ranges of $\Delta H_r^0 = 102.8 \pm 33.8\, kJ/mol$, and $\left(\frac{Re_D Sc}{L/D}\right)^{0.68\pm0.18}$. It can be seen that the error variance of $\pm\Delta H_r^0 (= \pm 33.8\, kJ/mol)$ may have been overestimated as their prediction gives an order of magnitude difference from experimental data for the range of reasonable mass transfer dependence $\left(\frac{Re_D Sc}{L/D}\right)^{0.68\pm0.18}$. Figure 3-8 shows that the experimental results are well bounded by $\left(\frac{Re_D Sc}{L/D}\right)^{0.68\pm0.18}$ when $\Delta H_r^0 = 102.8\, kJ/mol$. This again demonstrates that the mass transfer dependence of SiC material loss rates is bounded by ideal laminar flow and fully turbulent flow behavior.

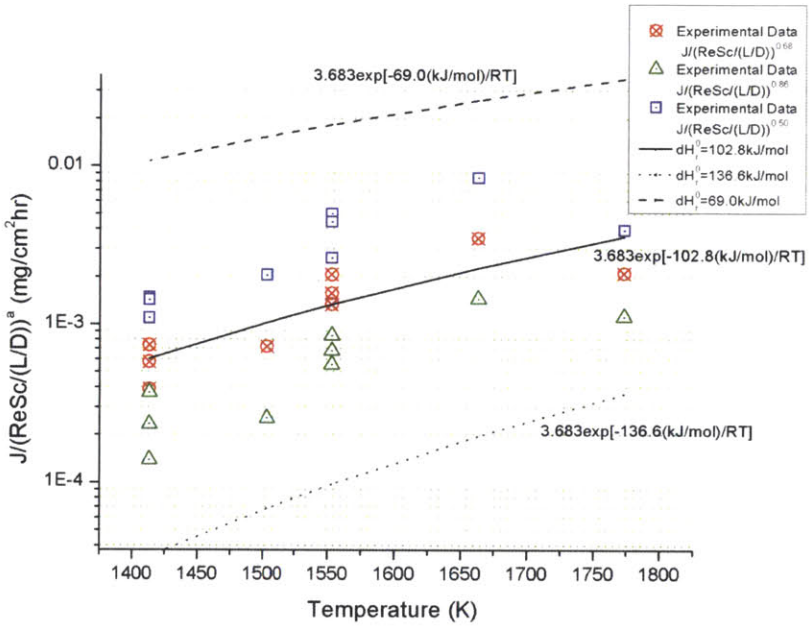

Figure 3-7 Prediction by Correlation-A of Volatilization Reaction rate of α-SiC at equilibrium: $\Delta H_r^0 = \mathbf{102.8 \pm 33.8\, kJ/mol}$, and $\left(\frac{Re_D Sc}{L/D}\right)^{0.68\pm0.18}$

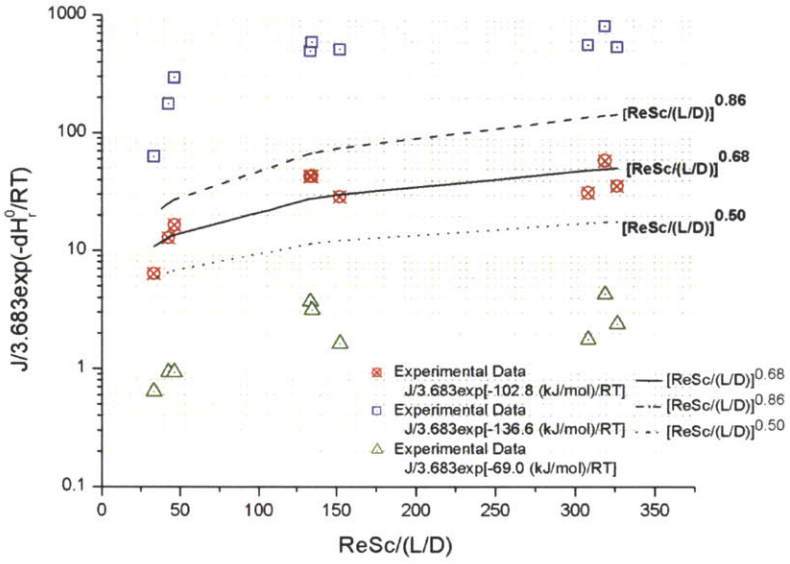

Figure 3-8 Prediction by Correlation-A of Volatile Species Material Transfer Dependence of α-SiC Material Loss Rates: $\Delta H_r^0 = 102.8 \pm 33.8\ kJ/mol$, and $\left(\frac{Re_D Sc}{L/D}\right)^{0.68\pm0.18}$

3.4.4 Development of Correlation B

Non-linear surface fitting of the correlation form B in Table 3-1 resulted in

$$J[\frac{mg}{cm^2 hr}] = \frac{1}{\mathrm{T}\left[\frac{45.43\times10^6 \mathrm{L}^{1.46}\mathrm{D}^{-0.46}}{(\mathrm{Re_D Sc})^{1.46}\,\mathrm{T}^{1.5}} + 7.8\times10^{-11}\exp(\frac{3427.9(\frac{\mathrm{J}}{\mathrm{mol}})}{\mathrm{RT}})\right]} \tag{3-37}$$

Prediction of correlation B in Eq.(3-37) is shown in Figure 3-9 as a function temperature and mass flux of steam.

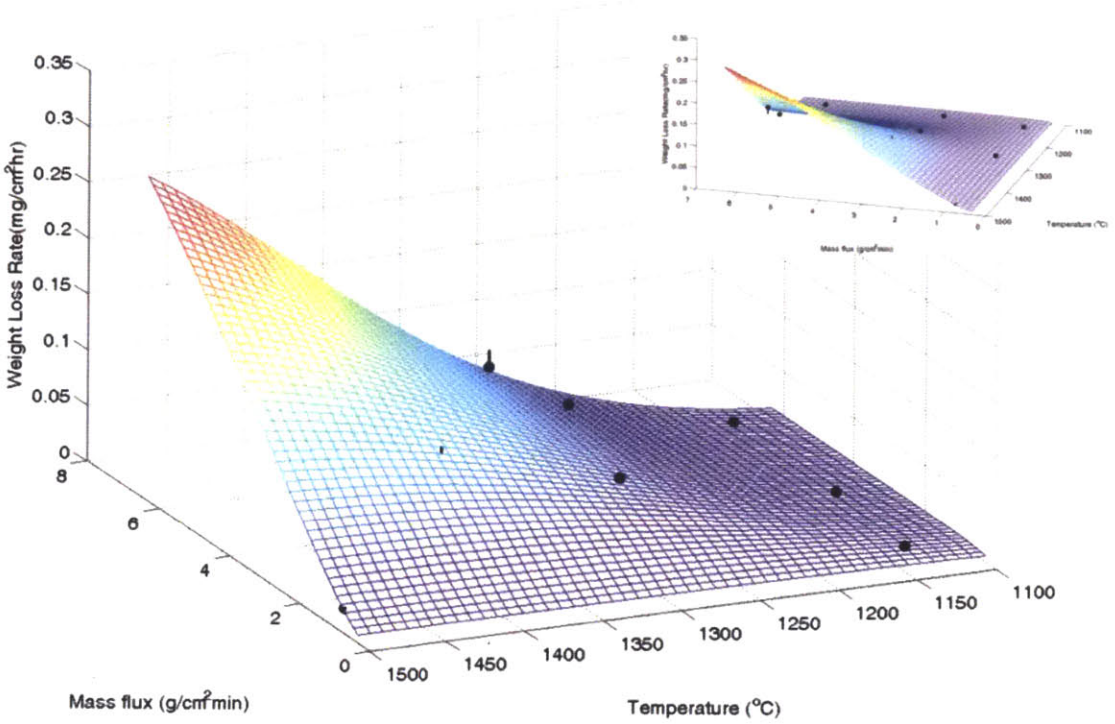

Figure 3-9 α-SiC Weight Loss Rate as a Function of Temperature and Steam Mass Flux at 1 atm, given by Correlation B, fitted Against Experimental Data Shown as Black Dots

Correlation-B gives a more accurate prediction of the experimental data than correlation-A. Its prediction is within ± 30% of the experimental data as can be seen in Figure 3-10. In addition, its accuracy is not particularly biased toward certain experimental conditions. This seemingly enhanced accuracy of correlation B pertains to non-linearity of the correlation form, which facilitates capturing more detailed behavior of 'a weight loss rate surface' in the fitting process. Fitting the experimental data yields activation energy, E, of 3.428 kJ/mol for the volatilization reaction kinetics.

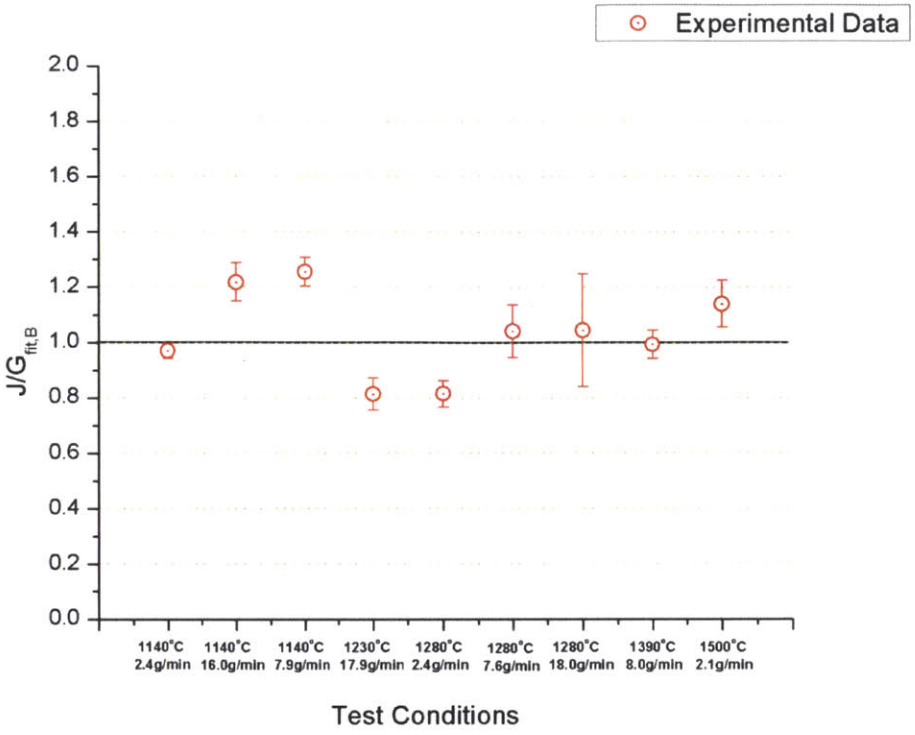

Figure 3-10 Experimental Data for SiC Weight Loss Rate (J)/Calculated Weight Loss Rate ($G_{fit,B}$) by Correlation B

A virtue of correlation B is that it enables evaluating of the magnitude of each reaction controlling resistance in terms of its contribution to the overall weight loss rates. Correlation B shown in Eq. (3-37) can be expressed as follows

$$J\left[\frac{mg}{cm^2 hr}\right] = \frac{1}{R_{total}} = \frac{1}{R_{mass\ transfer} + R_{reaction}} \tag{3-38}$$

where we defined a mass transfer resistance $R_{mass\ transfer} = \frac{T45.43\times10^{6}L^{1.46}D^{-0.46}}{(Re_D Sc)^{1.46}\,T^{1.5}}$ and a reaction resistance $R_{Reaction} = 7.8\times10^{-11}T\exp(\frac{3427.9(\frac{J}{mol})}{RT})$. By comparing them, we can assess the relative importance of volatile species mass transfer rate, and reaction rate in the overall kinetics. If $R_{mass\ transfer} \gg R_{reaction}$, then, $R_{total} \approx R_{mass\ transfer}$, demonstrating that the overall kinetics is controlled by the rate of mass transfer. Each resistance was normalized by the total resistance R_{total}, giving normalized resistances $R'_{mass\ transfer}$, and $R'_{reaction}$ ($R'_{mass\ transfer} + R'_{reaction}$ =1). Figure 3-11 shows the relative magnitudes of each resistance for the tested conditions.

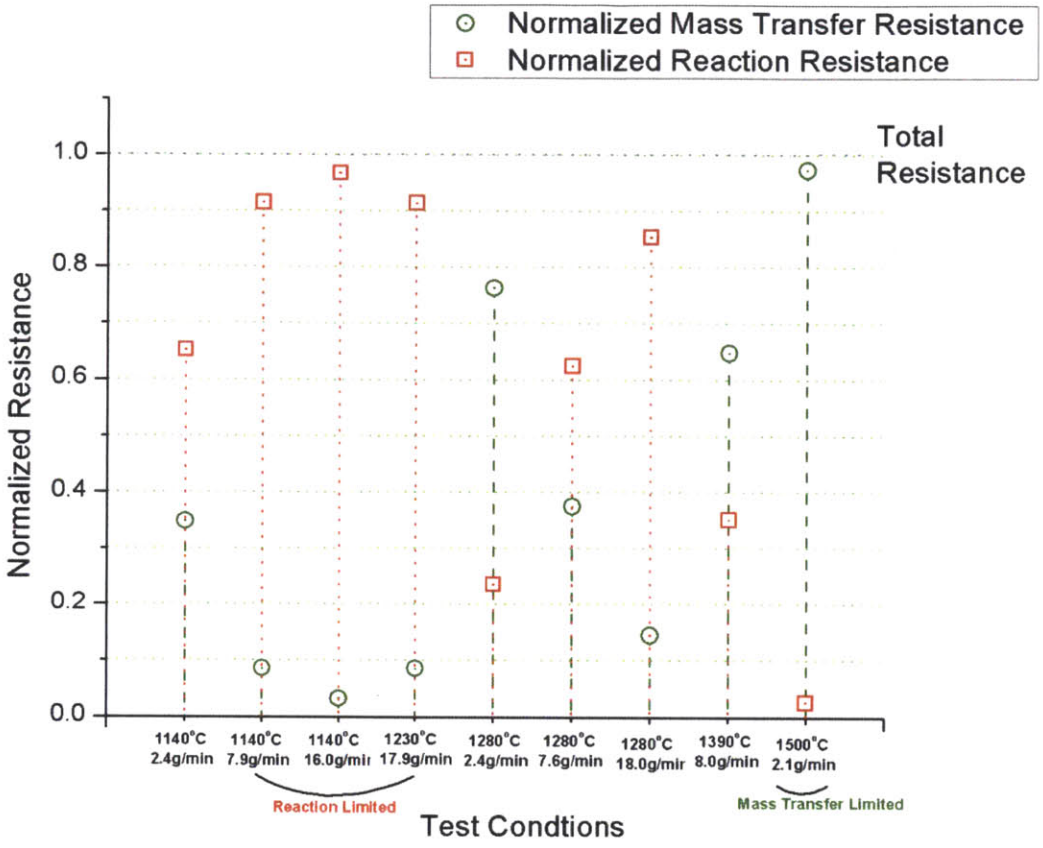

Figure 3-11 Contribution of Mass Transfer and Reaction Rate in the Overall SiO_2 Volatilization Kinetics for Tested Conditions

For test conditions of 1140°C & 7.9g/min, 1140°C & 16.0g/min, and 1230°C & 17.9g/min i.e. relatively low temperature and high flow rates, the overall kinetics are dominated by reaction resistance. This means that the overall material loss kinetics is suppressed by the slow volatilization reaction rate. On the other hand, for the test condition 1500°C & 2.1g/min – relatively high temperature and low flow rate, the overall kinetics is limited by mass transfer process of volatilization reaction products in the boundary layer. For these extreme conditions, the overall kinetics tends to be solely controlled by either temperature or oxidant flow rates. This explains the observed behavior of relative insensitivity of SiC material loss rate to steam flow rates with decreasing temperatures, shown in Figure 2-13. Conversely, sensitivity of SiC material loss rate to steam flow rate would increase with increasing steam temperature. For the other test conditions shown in Figure 3-11, the calculation demonstrates comparable resistances of mass transfer and chemical reaction, which is consistent with the experimental results.

3.5 Comparison with Past Studies and Validation of Developed Correlations

This study includes the use of Reynolds number (Re) to capture flow rate dependence of mass transfer effects on the SiO_2 volatilization mechanism, because it is fundamentally responsible for flow rate dependence of a mass transfer phenomenon. However, most studies have been using velocity to model flow rate effects of volatilization mechanisms. Use of velocity may be only understandable for oxidizing fluids whose compositions are so complex that evaluation of Reynolds number is overwhelmingly complicated. This would mean that for oxidizing fluids such as steam, and simple gas mixtures (e.g H_2O – O_2), the use of velocity instead of Reynolds number would inappropriately over simplify physical phenomena that may result in giving up generality of the model. Information of system size is an example; knowing temperature and velocity is not enough to generalize a mass transfer model to the same condition of a different system size. Therefore, a prediction of SiC weight loss rates in a different system is essentially impossible with a model that does not use the Reynolds number. Sudhir and Raj (Sudhir, 2006) corrected the SiC material loss correlations found by Robinson and Smialek (Robinson, 1999) for fuel lean conditions to H_2O conditions as follows

$$J\left[\frac{\text{mg}}{\text{cm}^2\text{hr}}\right] = 130.6\, exp\left(-\frac{-108kJ/mol}{RT}\right) P_{H_2O} P_{total}^{-0.5} v^{-0.5} \tag{3-39}$$

Depending on the system size and geometry of the experiment for which the correlation in Eq.(3-39) was developed, its prediction can vary by a factor of a constant while retaining the shape of the function. Knowing this, predictions of correlation A, correlation B and Sudhir and Raj's correlation are compared as a function of mass flux and temperature as shown in Figure 3-12. It can be seen that Sudhir and Raj's correlation gives remarkably similar prediction with the two correlations developed in this study despite of lack of system size correction. Reasons for this can be found from (1) similar functional dependence of T and flow rate as ($\Delta H_r^0 = -102.8\ kJ/mol$ for correlation A vs. $\Delta H_r^0 = -108\, kJ/mol$ for Sudhir and Raj's , and $v^{-0.68}$ for correlation A vs. $v^{-0.50}$ for Sudhir and Raj's), and (2) similar scale for facility and tested material sizes in terms of their dimensional order (~cm).

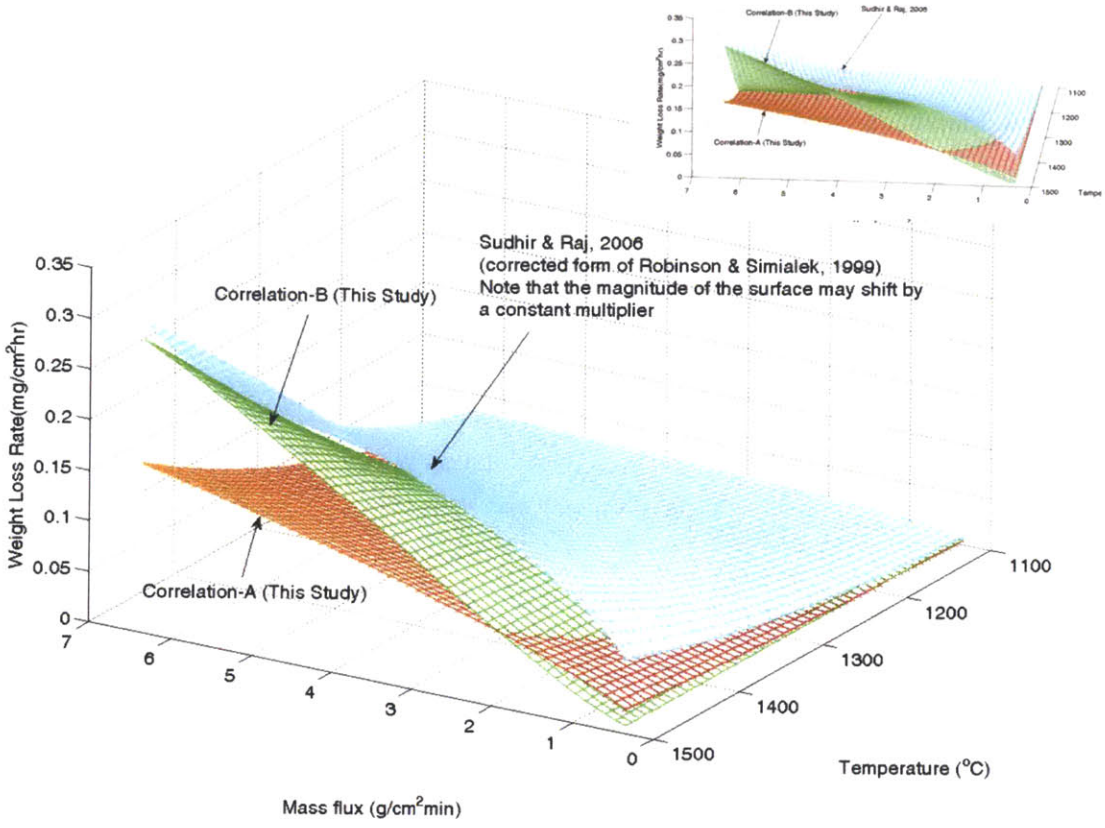

Figure 3-12 Comparisons of SiC Weight Loss Correlations

Most past studies used coupon shaped specimens placed inside a conduit. In those cases, one has to be careful about the choice of the Reynolds number expression to describe the situation. Most past studies calculated the Reynolds number ($Re_x = \rho v x/\mu$) of the SiC volatilization process by assuming the coupon specimen as a semi-infinite plate in an open environment. This assumption would be valid only if the boundary layer thickness on the specimen is so thin that it is not really affected by the conduit wall; so that the sample sees infinite distances into the bulk coolant. On the other hand, the boundary layer developed on a SiC specimen can be seen as an internally developing fluid upon perturbation. In that case, the Reynolds number ($Re_D = \rho v D_e/\mu$) should be calculated for internal flow with the equivalent diameter D_e would represent the boundary layer transport phenomena more accurately. Hence, an educated choice of Reynolds number expression that is representative of mass transfer phenomena of interest is essential for a model to become widely applicable and to minimize errors.

In this study, experiments and model developments were primarily conducted with consideration of developing fluids in a conduit. Hence, the developed correlations require information about conduit

geometry (Diameter, and Length) as well as mass flow rate and temperature. Despite limited available resources for a proper validation of the developed correlations, independent experiments conducted by Markham.et.al (Markham, 2012) for sintered α-SiC (22.35x12.07x9.53mm) in 100% H_2O at 1200°C and 1400°C in a tube of 6.4 cm I.D were compared to the calculated weight losses of correlation A and correlation B. Markham's study finds that the velocity of steam flow is about ~1m/sec. Reynolds number (Re_D) was calculated based on the size of the diameter of the test section, 6.4cm. The results are summarized in Table 3-3.

Table 3-3 Prediction of SiC Weight Loss Rates for α-SiC in 100% H_2O at 1atm

	Experiments of Markham.et.al			Prediction of This Study	
	Temperature (°C)	Velocity (m/sec)	Linear Weight Loss Rate (mg/cm^2sec)	Calculated Linear Rate Correlation A (mg/cm^2sec)	Calculated Linear Rate Correlation B (mg/cm^2sec)
Experiment 1	1200	~1m/sec	-0.022 -0.026	-0.083	-0.030
Experiment 2	1400	~1m/sec	-0.075 -0.092	-0.194	-0.114

Correlation B gives noticeably more accurate prediction for the experimental data. Prediction of correlation A did not give as accurate results as correlation B, resulting in significant differences. Note that these calculations are based on the Reynolds number of steam in the working section. This may imply that the boundary layer development on the plate shape sample in this experiment can be seen as a small perturbation of the boundary layer formation dictated by the flow characteristic in the conduit. More available experimental data for tubular SiC specimens would be helpful to further validate the models developed in this study.

3.6 Implications to Cladding Design: Required Thickness for Environmental Barrier Coating

In this work, experimental and theoretical discussions for monolithic SiC are presented. However, the actual SiC cladding designs are envisioned to be more complex. For example, the triplex design utilizes three layers of SiC in different forms. The inner most layer is a monolithic SiC tube and it functions as the

primary barrier to fission product release while providing most of the strength to the cladding tube. The middle layer is a SiC fiber-SiC matrix composite. Characterized by higher fracture toughness, and lower stiffness than the monolith, the SiC fiber-matrix composite provides protection to the monolith from mechanical damage, and pseudo-ductility for a graceful failure mode. The outer layer of the triplex cladding is an environmental barrier coating (EBC) deposited onto the composite and intended to avoid the corrugated textures of fibers from chemical reactions. The EBC is necessary because the SiC/SiC fiber composite exhibits considerable strength degradation in an oxidizing environment due to the reactivity of the carbon interphase (Filipuzzi, 1994), (Yin, 2001), (Ogbuji, 1998). Presence of a certain thickness of the EBC in the form of a monolith can protect the SiC fiber-matrix composite from mechanical degradation due to interaction with the coolant.

This study can be used to estimate the required thickness of the EBC coating from an oxidation in high temperature steam point of view. Currently, β-phase SiC is considered as the material of choice for the monolith part due to its isotropic behavior and high irradiation stability. This study showed comparable weight loss rates between sintered α-SiC and β-SiC (0.609 mg/cm^2 in 1155°C, 6.4g/min for β-SiC, and average of 0.784mg/cm^2 in 1140°C, 7.9g/min for α-SiC). A previous study (Tortorelli, 2003) conducted with a mixture of water vapor and air at 1MPa found that the material recession rate of CVD β-phase SiC is similar to that of sintered α-phase SiC (0.06μm/h for CVD β-SiC and 0.04-0.08 μm/h for sintered α-phase SiC). This study and some past studies discussed in section 2.5.2 found that there was a distinct difference in oxide morphology among oxidized CVD β-SiC and sintered α-phase SiC. This reflects the microstructural and impurity difference between the two types of SiC in the evolution of porosity in the cristobalite formed on the respective materials. Despite the difference in the oxide layer morphology, the similar weight loss rates can be expected if the effective outer surface areas for volatilization reaction and degree of protection of oxide layer for $SiC \rightarrow SiO_2$ conversion are similar. The fact, the EBC can be machined allows creation of a more uniform texture than the outer surface of the composite, which varies depending on the diameter of the fibers, tow size, winding technique, and extent of matrix infiltration (Carpenter, 2010).

The tentative minimum required EBC thicknesses were conservatively calculated by dividing the SiC weight loss rates predicted by the models developed in this study by SiC density (3.05g/cm^3). As suggested by NRC's recommendation after the Fukushima accidents (NRC, 2011), the required thicknesses were calculated based on 72 hours of oxidation duration. The results are plotted in Figure 3-13.

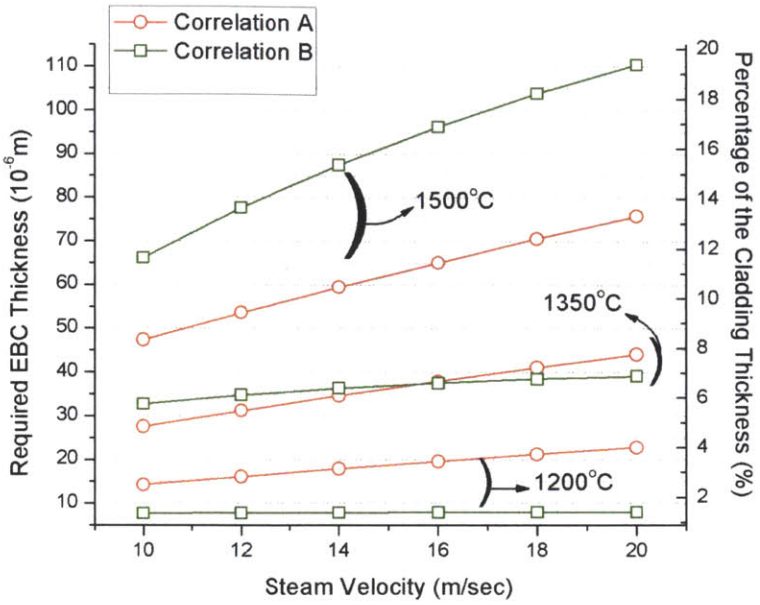

Figure 3-13 Required Thickness of Environmental Barrier Coating (EBC) for Silicon Carbide Cladding in LWRs in Loss of Coolant Accident Conditions for 72 hours of tolerance

As shown in Figure 2-5, the tentative oxidation regimes relevant to SiC oxidation with partial uncovering of fuel rods leads to 10 ~ 20 m/sec of steam flow rate in a sub channel. In this analysis, fixed temperatures ranging from 1200°C to 1500°C were investigated for the required thickness calculations. The results in Figure 3-13 show that the required thickness varies significantly depending on the regulatory requirements and expectations. For instance, if accident tolerance of SiC cladding is expected beyond 1500°C, the least EBC thicknesses between 45 ~ 110 μm is recommended to maintain 72 hours of separation of carbon coated fibers from any contact with steam. In this case, with EBC thicknesses more than 10% of the overall cladding thickness, it may start to influence the stress distribution of the cladding. If SiC cladding is expected to maintain its integrity from chemical reactions with steam between the current temperatures limit (1204°C for zirconium based alloy cladding) and 1350°C, an EBC thickness of 45 μm would suffice to assure no reaction between the carbon coated fiber and H_2O.

Note that the thickness determining criterion – no contact of composite fiber with H_2O – may be overly conservative as the composite can still maintain some/or most of its integrity when the carbon interphase is being consumed. Additional studies on LOCA steam oxidation studies at the most aggressive, yet relevant oxidizing environment, with understanding of time-dependent SiC composite strength

degradation in oxidizing environment, would be a valuable resource to determine the most reasonable EBC thicknesses.

3.7 Conclusion

In the history of cladding development projects in LWR, the attempt to use SiC definitely stands out in the sense that it is a radically different material (ceramic) from stainless steel, and zirconium-based alloys. At this stage, our understanding of SiC failure modes during its service as LWR cladding is in its infancy. Failure mechanisms of the cladding have to be identified in order to quantitatively assess the safety of a potential cladding candidate. As an attempt to identify key failure modes of SiC cladding in LWR, this study has demonstrated significantly slower (three orders of magnitudes) oxidation rate in comparison with Zircaloy cladding at ~1200°C (1200°C for Zr-4, and 1140°C for SiC). New experimental data was obtained with temperature, velocity, and geometry applicable to LWR LOCA conditions. Two SiC material loss correlations were developed, demonstrating acceptable predictability of tested conditions as well as relevant experimental data of past studies. A weaker interplay between cladding oxidation and mechanical strength degradation of the cladding with presence of EBC coating implies diminished importance of oxidation in material failure mechanisms in comparison with Zircaloy cladding. Consequently, failure modes of SiC cladding are likely to be different from those of Zircaloy cladding, which is hugely affected by oxidation.

Chapter 4

Brittle Fracture of SiC Cladding I: Statistical Fracture Model

4.1 Introduction

The discussions on SiC cladding oxidation in Chapter 2 and Chapter 3 illuminated the major failure modes for the SiC cladding, which would fundamentally depart from the failure modes of zirconium-based cladding, whose primary failure mechanisms are heavily affected by oxidation. The purpose of this chapter is to lay a foundation for understanding another critical failure mode of SiC cladding for LWR – brittle strength failure, and discuss its implications for fuel design, and reactor operation. Specifically, in this chapter we discusses the development of a statistical SiC cladding fracture model that can be used to provide the failure of SiC cladding in steady-state operations.

Failures of load bearing structures are either of the yielding-dominant or fracture-dominant (fast fracture) types. Yielding-dominant strength failures involve dislocation-mediated plasticity in the material. Yielding dominant failures occur in ductile materials, and examples include zirconium based alloys at room temperature. Unlike dislocation-mediated plasticity, fracture dominant failures occur before general yielding through separation of atomic planes which result in the creation of new surfaces whereas yielding-dominant failure leads to shape changes (Demkowicz, 2012). Generally, no appreciable plasticity, or only highly localized plasticity, is involved in fracture dominant failures. Fracture-dominant failures usually occur for brittle materials that lack the ability to accommodate defects generated during plastic deformation. Fracture-dominant failure is of interest in this study because it is the failure mode of silicon carbide, a brittle material.

4.2 Qualitative Understanding of SiC Cladding Fracture Modes

The structure of SiC cladding can be viewed in terms of its response/tolerance to possible fractures under excessive loading. Today, a three-layer laminated structure that consists of monolithic SiC, SiC-SiC fiber composite, and monolithic environmental barrier coating (EBC) is regarded as a potential candidate for SiC cladding design. Monolithic SiC is well known to undergo fast fracture without a sign of plasticity if

stresses are excessive. SiC/SiC fiber composites exhibit rather complex modes of failures that show some degree of pseudo-ductility (Katoh, 2007), (Nozawa, 2011), which is sometimes called brittle-like (or quasi-ductile) failure (Nozawa, 2012). In SiC-SiC fiber-composite materials, since the CVI (Chemical Vapor Infiltration) matrix is stiffer, the fiber strength is not accessed until significant matrix microcracking occurs. While CVI matrix microcracking basically follows the behavior of monolithic CVD SiC, propagating cracks from the matrix eventually meet the fibers in the composite, experiencing a barrier to the continuous propagation. At that moment, the strength of the fiber is accessed and fibers undergo elastic strain. The composite is regarded as essentially "leaky" above the matrix cracking stress although catastrophic fracture does not occur (Snead, 2013). This crack arresting mechanism by an interaction with fibers renders the SiC composite fracture toughness (~30 MPa-$m^{1/2}$) roughly 10 times the monolith (~2.5-3.0 MPa-$m^{1/2}$ for CVD SiC). Having said this, the seemingly ductile behavior of the SiC composite due to the fiber strength, in principle, is engineered pseudo-ductility caused by proper juxtaposition of brittle materials. In that regard, it can be inferred that the SiC composites, while possessing decent fracture toughness and engineered graceful failure modes, have essentially no strain tolerance to cracking.

Fracture of the SiC cladding layers (SiC monolith/SiC composite/ EBC) can occur either individually, or in company with neighboring layers. Each layer has a specific significance to performance of the cladding as well as the fuel rod. Fractures in each layer imply degradation of certain performance metrics of the cladding. Figure 4-1 illustrates qualitative evaluations for SiC cladding performance with different fracture modes in terms of fission gas retention, prevention of H_2O attack of the carbon coating of the SiC fibers in the composite during steady-states & accidents, and strength margin for accidents. The integrity of SiC monolith has prime importance in fission gas retention and load sharing in SiC cladding. Improving cladding with the addition of pseudo-ductility with additional crack-arresting capability, SiC composite has prime importance for load sharing and avoiding catastrophic shattering of the cladding as a whole. As discussed previously, the SiC composite needs to be protected from H_2O access to the carbon-coated fibers to avoid significant strength degradations of the composite, caused by consumption of the carbon coating by the H_2O – C reaction (Filipuzzi, 1994), (Yin, 2001), (Ogbuji, 1998). Therefore, without the presence of the monolithic SiC overcoat by either EBC or extended CVI overcoat, the SiC composite may undergo strength degradation even at temperatures under normal operating conditions. It is important to note that SiC composite has CVI overcoat extended for a certain thickness on the surface, which can function as an EBC with similar oxidation behavior of CVD SiC (Terrani, 2013). Therefore, even with a crack formed on the EBC layer, the composite may still be protected from H_2O access to the fibers by the presence of the CVI overcoat. Microcracks formed in the CVI matrix with cracked EBC

would leave fibers essentially unprotected from H_2O access, resulting in substantial strength degradation with loss of carbon-mediated interfacial friction between the matrix and the fibers. While meeting steady-state performance requirements in terms of fission gas retention, and load sharing, the amount or even presence of allowable cracking in the inner monolith and fiber composite should be evaluated in the context of strength margin for accidents. It is important to note that for the inner most monolithic SiC, it may not be appropriate to think of fractures in terms of amount; being monolithic, it should better be viewed in terms of allowing any propagating crack(s) or none. For the composite, the unused strength should be viewed as margin left for CVI matrix cracking to access the SiC fibers' elastic limit. Being considerably thinner in comparison to the inner most monolith and the composite, the influence of EBC on strength safety margin was considered negligible in the qualitative evaluations shown in Figure 4-1. Note that the current SiC monolith/SiC-SiC composite/SiC EBC cladding design is a result of rather a qualitative SiC cladding behavior as illustrated in Figure 4-1 ; their relative thicknesses, or perhaps even the need for each layer will be quantitatively questioned by rigorous design studies in this chapter and in discussions in following chapters.

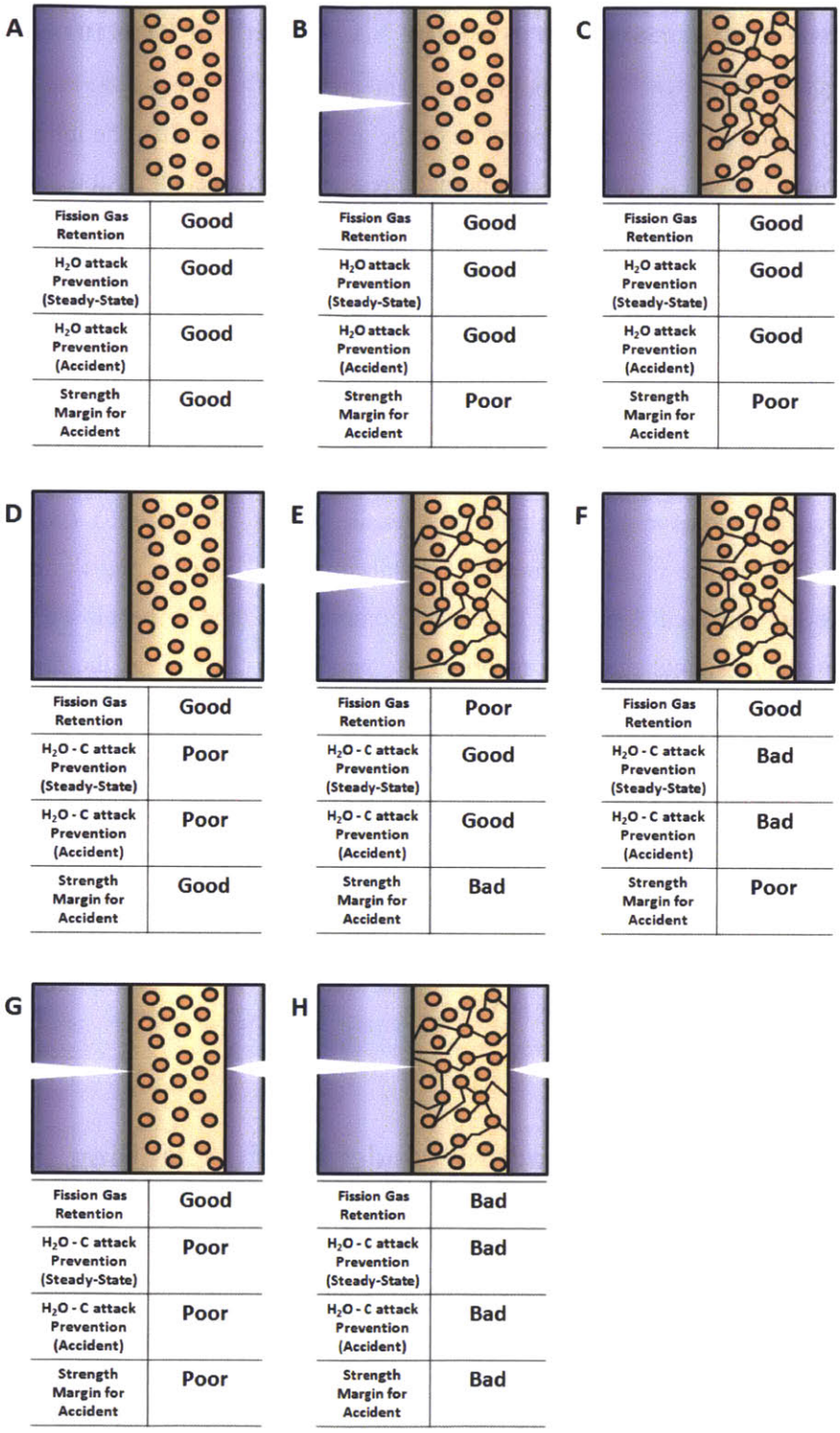

Figure 4-1 Qualitative Evaluation of SiC Cladding (SiC monolith/SiC-fiber, CVI-SiC composite/ EBC) Performance with Different Fracture Modes in terms of Fission Gas Retention, H_2O attack of Carbon Coating for SiC Fibers in the Composite in Steady-States & Accidents, and Strength Margin for Accidents (NOTE: The words good, poor, and bad should be regarded in qualitative comparative context)

4.3 Tensile versus compressive Stresses for SiC Cladding Fracture

The cylindrical fuel rod cladding experiences both tensile and compressive stresses during its life time. It is initially under compression as the operating pressure of the reactor is higher than the internal helium fill gas pressure. As burnup increases, fuel rod is internal pressurization due to fission gas release and possible Pellet-Cladding Mechanical Interaction (PCMI)[19] put the fuel rod under tensile stress. After discharge, due to absence of primary coolant pressure, the fuel rods would also be under tensile stresses at atmospheric pressure. Under accident conditions, the fuel cladding may experience additional sources for significant tensile stresses, due to both thermal shock and rapid depressurization of the core operating pressure. For metals, the strength measured in compression is approximately the same as that measured in tension. For brittle materials such as SiC, this is not true; for ceramics the strength of material under compressive stress is several times larger than under the tensile stress (Ashby, 2005), (Basu, 2011). The difference is due to the difference in microstructural resistance to crack growth and the nature of crack propagation under the two different loadings. Cracks in compression tend to be closed and propagate stably, twisting out of their original direction to propagate parallel to the axis of the loading direction (Ashby, 2005), (Basu, 2011). Compressive fracture is not caused by rapid unstable propagation of one crack, but by the slow extension of many cracks to form a crushed zone. It is not the size of the largest crack that counts but that of the average crack size (Ashby, 2005). In contrast, cracks in tension tend to open up and propagate unstably perpendicular to the applied stress. In such a case, it is the largest crack that causes failure. Considering the comparatively high susceptibility to tensile fracture, this study primarily discusses fuel rods under tensile stresses in an attempt to identify and understand the most limiting failure mechanism of SiC cladding for LWRs.

4.4 Development of Statistical Fracture Model for SiC Cladding

4.4.1 Statistical Treatment of Brittle Fracture for SiC Cladding

A metal's dislocation mediated-plasticity enables minimizing the adverse effect of any particular defect. Flow of plasticity leads to a general yielding of the material in a global sense, rendering strength to exhibit a narrow Gaussian distribution of yield and or fracture strengths with ~5% or less of standard deviation. Hence, in designing with metals, a deterministic approach is often used with a safety margin (Bengisu, 2001), (Dao, 2013). In ceramic materials, without appreciable plasticity, strength values exhibit marked dependence on specimen size and geometry and wide scatter with a typical standard deviation of

[19] PCMI places the Zr-cladding in tension even at a relatively low burnup

~25% due to randomly distributed flaw populations (Bengisu, 2001), (Dao, 2013) . That is, fracture occurs in a local sense – locally concentrated stress around pre-existing flaws/defects has no means to be accommodated but to release their strain energy by breaking bonds, leading to a creation of surfaces. A widely-used methodology to resolve such local-dependent material fracture is done through statistical approach.

Figure 4-2 illustrates a schematic comparison between the deterministic failure behavior of a ductile material and statistical failure behavior of a brittle material.

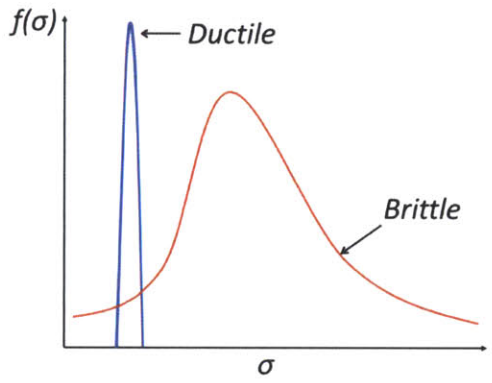

Figure 4-2 Schematic Illustration of Failure Probability Distributions for Ductile and Brittle Materials

A way of parameterizing this statistical nature of ceramics failure is through the Weibull distribution, which is, unlike the Gaussian distribution, asymmetric with one tail extending more than the other. The Weibull distribution for survival probability of a material of volume V_0 , $P_s(V_0)$ under an applied tensile stress σ_0 is shown in Eq.(4-1) (Ashby, 2005)

$$P_s(V_0) = \begin{cases} exp\left[-\left(\frac{\sigma - \sigma_u}{\sigma_0}\right)^m\right] & \sigma > \sigma_u \\ \\ 1 & \sigma < \sigma_u \end{cases} \quad (4\text{-}1)$$

Where m is the Weibull modulus that determines the shape of the Weibull curve. σ_0 is the characteristic stress that gives 63.2% (1-1/e) of failure probability. The parameter σ_0, and m are are obtained by fitting experimental data. The parameter σ_u is the threshold stress below which zero probability of failure is assumed.

As a specimen size (volume) gets bigger, there is a larger chance for the specimen to have a critical flaw size – given the volume dependency on the failure probability. This is an important observation especially in consideration of SiC cladding for LWR applications. This is because it is practically difficult to perform a statistically meaningful number of SiC cladding failure tests with the real cladding dimensions. Hence, a volume extrapolation from available data of small specimen is essential. The weakest link theory (Wachtman, 2009) enables the volume extrapolation of ceramic failure statistics by essentially assuming that each unit of volume V_0 can be failed independently. Then for a sample with different volume V=nV_0, the probability of the survival is simply $P_s(V_0)$ multiplied n times by itself

$$P_s(V) = [P(V_0)]^n = [P(V_0)]^{\frac{V}{V_0}} = \exp\left[-\frac{V}{V_0}\left(\frac{\sigma - \sigma_u}{\sigma_0}\right)^m\right] \tag{4-2}$$

Once survival probability $P_s(V)$ is obtained, failure probability $P_f(V)$ can be calculated by subtracting the survival probability from unity.

$$P_f(V) = 1 - P_s(V) \tag{4-3}$$

Note that Eq.(4-1) and Eq.(4-2) assume that the specimen is subjected to a uniform tensile stress σ. In the case of LWR cladding the stress is not constant across the cladding thickness that consists of three layers. Then, Eq.(4-2) can be written to take into account spatial variation in applied stress $\sigma(\vec{r})$.

$$P_s(V) = exp\left[-\frac{1}{V_0}\int_V \left(\frac{\sigma(\vec{r}) - \sigma_u}{\sigma_0}\right)^m dV\right] \tag{4-4}$$

In Eq.(4-4), V can be applied to each layer in a SiC cladding with σ_0 and V_0 experimental obtained for each layer in the cladding. This enables the evaluation of survival probability of each layer under a constant loading condition.

Consequently, a statististical treatment of SiC cladding is reduced to the development of the following items for Eq.(4-4).

(A) Calculation of the stress fields $\sigma(\vec{r})$ for a SiC cladding that consists of SiC monolith/SiC composite/EBC layers.

(B) Volume extrapolation for each layer in the SiC cladding from relevant experimentally obtained Weibull statistic parameters, σ_0, and m for each layer material

(C) Treatment of the threshold stress, σ_u

The following discussion will be dedicated to development of each item - (A), (B), and (C), respectively.

4.4.2 Stress Distribution in the SiC Cladding

The total stress in the SiC cladding is the sum of individual stresses that arise from (1) pressure loading, and (2) temperature gradients across the cladding thickness that induces thermal stress. Solution schemes utilize linear superposition of elastic load effects.

(A) Stress distribution under a constant loading due to internal and external pressure differences

The hoop $\sigma(r)_\theta$ and radial stresses $\sigma(r)_r$ at any position in the cladding at distance r from the center of the fuel rod are given by the *Lamé* equations for each layer of the SiC cladding shown in Figure 4-3

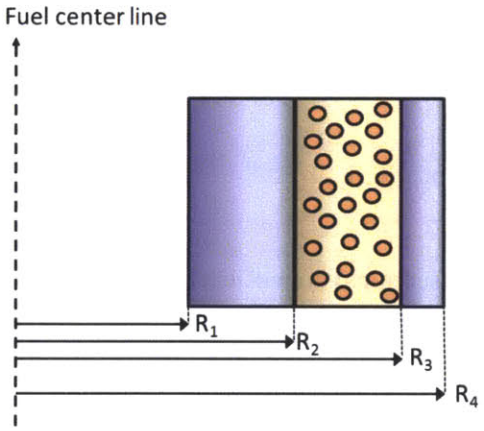

Figure 4-3 Illustration of SiC Cladding for Stress Field Calculations

$$\sigma(r)_{\theta,1} = A_1 + \frac{B_1}{r^2}, \qquad R_1 \leq r_{inner\ monolith} \leq R_2 \tag{4-5}$$

$$\sigma(r)_{r,1} = A_1 - \frac{B_1}{r^2}, \qquad R_1 \leq r_{inner\ monolith} \leq R_2 \tag{4-6}$$

$$\sigma(r)_{\theta,2} = A_2 + \frac{B_2}{r^2}, \qquad R_2 \leq r_{composite} \leq R_3 \tag{4-7}$$

$$\sigma(r)_{r,2} = A_2 - \frac{B_2}{r^2}, \qquad R_2 \leq r_{composite} \leq R_3 \tag{4-8}$$

$$\sigma(r)_{\theta,3} = A_3 + \frac{B_3}{r^2}, \qquad R_3 \leq r_{EBC} \leq R_4 \tag{4-9}$$

$$\sigma(r)_{r,3} = A_3 - \frac{B_3}{r^2}, \qquad R_3 \leq r_{EBC} \leq R_4 \tag{4-10}$$

where $A_{1,2,3}$ and $B_{1,2,3}$ are constants to be determined and $R_{1,2,3,4}$ are radial positions for the SiC cladding layers shown in Figure 4-3. Note that subscripts 1, 2, and 3 in Eq.(4-5) - (4-10) denote the inner monolith, SiC composite, and EBC, respectively.

The axial stresses for each layer $\sigma_{z,1}$, $\sigma_{z,2}$, and $\sigma_{z,3}$ are given by the following axial force balance in a cylinder with closed ends

$$P_i \pi {R_1}^2 - P_o \pi {R_4}^2 = A_{c,1}\sigma_{z,1} + A_{c,2}\sigma_{z,2} + A_{c,3}\sigma_{z,3} \tag{4-11}$$

where $A_{c,1}$, $A_{c,2}$, and $A_{c,3}$ are cross sectional area of each layer. P_i is internal pressure of fuel rod, and P_o is external pressure.

The overall system of equations has 9 unknowns, A_1, A_2, A_3, B_1, B_2, B_3, $\sigma_{z,1}$, $\sigma_{z,2}$, and $\sigma_{z,3}$ presented by Eq.(4-5) - (4-11). These unknowns can be solved by imposing nine independent boundary conditions

$$
B.C\begin{cases}
\sigma(R_1)_{r,1} = -P_i & \cdots\cdots (1)\\
\sigma(R_2)_{r,1} = \sigma(R_2)_{r,2} & \cdots\cdots (2)\\
\frac{1}{E_{\theta\theta,1}}\left[\sigma(R_2)_{\theta,1} - \nu_{r\theta,1}\sigma(R_2)_{r,1} - \nu_{z\theta,1}\sigma_{z,1}\right] = \frac{1}{E_{\theta\theta,2}}\left[\sigma(R_2)_{\theta,2} - \nu_{r\theta,2}\sigma(R_2)_{r,2} - \nu_{z\theta,2}\sigma_{z,2}\right] & \cdots\cdots (3)\\
\sigma(R_3)_{r,2} = \sigma(R_3)_{r,3} & \cdots\cdots (4)\\
\frac{1}{E_{\theta\theta,2}}\left[\sigma(R_3)_{\theta,2} - \nu_{r\theta,2}\sigma(R_3)_{r,2} - \nu_{z\theta,2}\sigma_{z,2}\right] = \frac{1}{E_{\theta\theta,3}}\left[\sigma(R_3)_{\theta,3} - \nu_{r\theta,3}\sigma(R_3)_{r,3} - \nu_{z\theta,3}\sigma_{z,3}\right] & \cdots\cdots (5)\\
\sigma(R_4)_{r,3} = -P_o & \cdots\cdots (6)\\
P_i\pi {R_1}^2 - P_o\pi {R_4}^2 = A_{c,1}\sigma_{z,1} + A_{c,2}\sigma_{z,2} + A_{c,3}\sigma_{z,3} & \cdots\cdots (7)\\
\frac{1}{E_{zz,1}}\left[\sigma_{z,1} - \nu_{\theta z,1}\left(\sigma(r)_{\theta,1} + \sigma(r)_{r,1}\right)\right] = \frac{1}{E_{zz,2}}\left[\sigma_{z,2} - \nu_{\theta z,2}\left(\sigma(r)_{\theta,2} + \sigma(r)_{r,2}\right)\right] & \cdots\cdots (8)\\
\frac{1}{E_{zz,2}}\left[\sigma_{z,2} - \nu_{\theta z,2}\left(\sigma(r)_{\theta,2} + \sigma(r)_{r,2}\right)\right] = \frac{1}{E_{zz,3}}\left[\sigma_{z,3} - \nu_{\theta z,3}\left(\sigma(r)_{\theta,3} + \sigma(r)_{r,3}\right)\right] & \cdots\cdots (9)
\end{cases}
\tag{4-12}
$$

$E_{\theta\theta}$, and E_{zz} are elastic modulus in the principal axis directions θ, and z. ν_{ij} is $-\varepsilon_j/\varepsilon_i$. Boundary condition (1) and (6) prescribe compressive radial stresses equal to the internal fuel rod pressure (P_i) and the external pressure ($-P_o$) at the innermost (R_1) and the outermost (R_4) surface of the cladding. Boundary conditions (2) and (4) impose continuity of radial stresses at the interface between the innermost monolith layer and the composite and between the composite and the EBC. Boundary conditions (3) and (5) state equal diametral strain at the interfaces so that the layers stay laminated. Boundary condition (7) is the same as Eq.(4-11), stating the axial force balance at the end-cap. Boundary conditions (8) and (9) impose a constant axial strain in the three layers. Note that $\nu_{\theta z}$ is assumed to be the same as ν_{rz} ($\nu_{\theta z} \approx \nu_{rz}$). This results in a radially uniform axial strain in each layer as $-\nu_{\theta z}(\sigma(r)_\theta + \sigma(r)_r) = -\nu_{\theta z}(A + \frac{B}{r^2} + (A - \frac{B}{r^2})) = -2\nu_{\theta z}A$. Applying the prescribed boundary conditions to eq.(4-5)-(4-11), the following nine equations hold,

$$A_1 - \frac{B_1}{{R_1}^2} = -P_i \tag{4-13}$$

$$A_1 - \frac{B_1}{{R_1}^2} - A_1 + \frac{B_1}{{R_1}^2} = 0 \tag{4-14}$$

$$\left(\frac{1-\nu_{r\theta,1}}{E_{\theta\theta,1}}\right)A_1+\left(\frac{1+\nu_{r\theta,1}}{E_{\theta\theta,1}R_2{}^2}\right)B_1+\left(\frac{\nu_{r\theta,2}-1}{E_{\theta\theta,2}}\right)A_2+\left(\frac{-1-\nu_{r\theta,2}}{E_{\theta\theta,2}R_2{}^2}\right)B_2-\left(\frac{\nu_{z\theta,1}}{E_{\theta\theta,1}}\right)\sigma_{z,1}+\left(\frac{\nu_{z\theta,2}}{E_{\theta\theta,2}}\right)\sigma_{z,2}=0 \tag{4-15}$$

$$A_2-\frac{B_2}{R_3{}^2}-A_1+\frac{B_3}{R_3{}^2}=0 \tag{4-16}$$

$$\left(\frac{1-\nu_{r\theta,2}}{E_{\theta\theta,2}}\right)A_2+\left(\frac{1+\nu_{r\theta,2}}{E_{\theta\theta,2}R_3{}^2}\right)B_2+\left(\frac{\nu_{r\theta,3}-1}{E_{\theta\theta,3}}\right)A_3+\left(\frac{-1-\nu_{r\theta,3}}{E_{\theta\theta,3}R_3{}^2}\right)B_3-\left(\frac{\nu_{z\theta,2}}{E_{\theta\theta,2}}\right)\sigma_{z,2}+\left(\frac{\nu_{z\theta,3}}{E_{\theta\theta,3}}\right)\sigma_{z,3}=0 \tag{4-17}$$

$$A_3-\frac{B_3}{R_4{}^2}=-P_o \tag{4-18}$$

$$A_{c,1}\sigma_{z,1}+A_{c,2}\sigma_{z,2}+A_{c,3}\sigma_{z,3}=P_i\pi R_1{}^2-P_o\pi R_4{}^2 \tag{4-19}$$

$$\frac{1}{E_{zz,1}}\sigma_{z,1}-\frac{1}{E_{zz,2}}\sigma_{z,2}=\frac{2\nu_{\theta z,1}A_1}{E_{zz,1}}-\frac{2\nu_{\theta z,2}A_2}{E_{zz,2}} \tag{4-20}$$

$$\frac{1}{E_{zz,2}}\sigma_{z,2}-\frac{1}{E_{zz,3}}\sigma_{z,3}=\frac{2\nu_{\theta z,2}A_2}{E_{zz,2}}-\frac{2\nu_{\theta z,3}A_3}{E_{zz,3}} \tag{4-21}$$

Eq. (4-13) - (4-21) can be solved for A_1, A_2, A_3, B_1, B_2, B_3, $\sigma_{z,1}$, $\sigma_{z,2}$, and $\sigma_{z,3}$ by transforming the equations into $A\vec{X}=\vec{b}$, and solving for $\vec{X}$ by taking the inverse of A, $\vec{X}=A^{-1}\vec{b}$. The matrix A is shown in Eq.(4-22). The unknown vector $\vec{X}$ and prescribed condition vector $\vec{b}$ are shown in Eq.(4-23)

$$\begin{bmatrix}
1 & \frac{-1}{R_1^2} & 0 & 0 & 0 & 0 & 0 & 0 & 0 \\
1 & \frac{-1}{R_2^2} & -1 & -1 & \frac{-1}{R_2^2} & 0 & 0 & 0 & 0 \\
\frac{1-\nu_{r\theta,1}}{E_{\theta\theta,1}} & \frac{1+\nu_{r\theta,1}}{E_{\theta\theta,1}R_2^2} & \frac{\nu_{r\theta,2}-1}{E_{\theta\theta,2}} & \frac{-1-\nu_{r\theta,2}}{E_{\theta\theta,2}R_2^2} & 0 & 0 & -\frac{\nu_{z\theta,2}}{E_{\theta\theta,2}} & \frac{\nu_{z\theta,3}}{E_{\theta\theta,3}} & 0 \\
0 & 0 & 1 & \frac{-1}{R_3^2} & -1 & \frac{1}{R_3^2} & 0 & 0 & 0 \\
0 & 0 & \frac{1-\nu_{r\theta,2}}{E_{\theta\theta,2}} & \frac{1+\nu_{r\theta,2}}{E_{\theta\theta,2}R_3^2} & \frac{\nu_{r\theta,3}-1}{E_{\theta\theta,3}} & \frac{-1-\nu_{r\theta,2}}{E_{\theta\theta,2}R_2^2} & 0 & -\frac{\nu_{z\theta,2}}{E_{\theta\theta,2}} & \frac{\nu_{z\theta,3}}{E_{\theta\theta,3}} \\
0 & 0 & 0 & 0 & 1 & \frac{-1}{R_4^2} & 0 & 0 & 0 \\
0 & 0 & 0 & 0 & 0 & 0 & A_{c,1} & A_{c,2} & A_{c,3} \\
-\frac{2\nu_{\theta z,1}}{E_{zz,1}} & 0 & \frac{2\nu_{\theta z,2}}{E_{zz,2}} & 0 & 0 & 0 & \frac{1}{E_{zz,1}} & -\frac{1}{E_{zz,2}} & 0 \\
0 & 0 & -\frac{2\nu_{\theta z,2}}{E_{zz,2}} & 0 & \frac{2\nu_{\theta z,3}A_{c,3}}{E_{zz,3}} & 0 & 0 & \frac{1}{E_{zz,2}} & -\frac{1}{E_{zz,3}}
\end{bmatrix} \tag{4-22}$$

$$X = \begin{bmatrix} A_1 \\ B_1 \\ A_2 \\ B_2 \\ A_3 \\ B_3 \\ \sigma_{z,1} \\ \sigma_{z,2} \\ \sigma_{z,3} \end{bmatrix}, \quad b = \begin{bmatrix} -P_i \\ 0 \\ 0 \\ 0 \\ 0 \\ -P_o \\ P_i\pi R_1^2 - P_o\pi R_4^2 \\ 0 \\ 0 \end{bmatrix} \tag{4-23}$$

(B) Thermal stresses due to a radial temperature gradient

A method to calculate the thermal stress distributions for a laminated SiC cladding for a given radial temperature distribution T(r) is presented here. An axially symmetric cylinder with a constant axial strain ($\varepsilon_{zz} = \varepsilon_0$), yields the following equations for thermal stresses (Barron, 2012):

$$\sigma(r)_{r,Th} = -\frac{\alpha E}{(1-\nu)r^2}\int \Delta T r dr + \frac{E}{1+\nu}\left(\frac{C_1}{1-2\nu} - \frac{C_2}{r^2} - \frac{\nu\varepsilon_0}{1-2\nu}\right) \tag{4-24}$$

where α is the thermal expansion coefficient, $\Delta T = T(r) - T_{ref}$ is the radial temperature distribution

with respect to its departure from strain-free reference temperature T_{ref}. C_1 and C_2 are constants to be determined with the imposed boundary conditions. Note that the elastic modulus E, and Poisson ratio ν are regarded isotropic. The hoop stress in Eq.(4-26) can be obtained from the radial stress by the relationship in Eq.(4-25). The axial stress is shown in Eq.(4-27) (Ugural, 2003).

$$\sigma(r)_{\theta,Th} = \sigma(r)_r + r\frac{d\sigma(r)_r}{dr} \tag{4-25}$$

$$\sigma(r)_{\theta,Th} = \frac{\alpha E}{(1-\nu)r^2}\int \Delta T r dr - \frac{\alpha E \Delta T}{1-\nu} + \frac{E}{1+\nu}\left(\frac{C_1}{1-2\nu} + \frac{C_2}{r^2} - \frac{\nu\varepsilon_0}{1-2\nu}\right) \tag{4-26}$$

$$\sigma_{z,Th} = E\varepsilon_0 + \frac{-E\alpha\Delta T}{1-\nu} + \frac{2\nu E C_1}{(1-2\nu)(1+\nu)} \tag{4-27}$$

Now, each stress component in the principal axis directions are presented in Eq.(4-28)-(4-36) for the three different layers in SiC cladding by using Eq.(4-24), (4-26), and (4-27).

$$\sigma(r)_{r,1,Th} = -\frac{\alpha_1 E_1}{(1-\nu_1)r^2}\int \Delta T r dr + \frac{E_1}{1+\nu_1}\left(\frac{C_1^{\mathrm{I}}}{1-2\nu_1} - \frac{C_2^{\mathrm{I}}}{r^2} - \frac{\nu_1\varepsilon_0}{1-2\nu_1}\right), \quad R_1 \le r_{inner\ monolith} \le R_2 \tag{4-28}$$

$$\sigma(r)_{\theta,1,Th} = \frac{\alpha_1 E_1}{(1-\nu_1)r^2}\int \Delta T r dr - \frac{\alpha_1 E_1 \Delta T}{1-\nu_1} + \frac{E_1}{1+\nu_1}\left(\frac{C_1^{\mathrm{I}}}{1-2\nu_1} + \frac{C_2^{\mathrm{I}}}{r^2} - \frac{\nu_1\varepsilon_0}{1-2\nu_1}\right), \quad R_1 \le r_{inner\_monolith} \le R_2 \tag{4-29}$$

$$\sigma_{z,1,Th} = E_1\varepsilon_0 + \frac{-E_1\alpha_1\Delta T}{1-\nu_1} + \frac{2\nu_1 E_1 C_1^{\mathrm{I}}}{(1-2\nu_1)(1+\nu_1)}, \quad R_1 \le r_{inner\ monolith} \le R_2 \tag{4-30}$$

$$\sigma(r)_{r,2,Th} = -\frac{\alpha_2 E_2}{(1-\nu_2)r^2}\int \Delta T r dr + \frac{E_2}{1+\nu_2}\left(\frac{C_1^{\mathrm{II}}}{1-2\nu_2} - \frac{C_2^{\mathrm{II}}}{r^2} - \frac{\nu_2\varepsilon_0}{1-2\nu_2}\right), \quad R_2 \le r_{composite} \le R_3 \tag{4-31}$$

$$\sigma(r)_{\theta,2,Th} = \frac{\alpha_2 E_2}{(1-\nu_2)r^2}\int \Delta T r dr - \frac{\alpha_2 E_2 \Delta T}{1-\nu_2} + \frac{E_2}{1+\nu_2}\left(\frac{C_1^{\mathrm{II}}}{1-2\nu_2} + \frac{C_2^{\mathrm{II}}}{r^2} - \frac{\nu_2\varepsilon_0}{1-2\nu_2}\right), \quad R_2 \le r_{composite} \le R_3 \tag{4-32}$$

$$\sigma_{z,2,Th} = E_2\varepsilon_0 + \frac{-E_2\alpha_2\Delta T}{1-\nu_2} + \frac{2\nu_2 E_2 C_1^{II}}{(1-2\nu_2)(1+\nu_2)}\ , \qquad R_2 \le r_{composite} \le R_3 \qquad (4\text{-}33)$$

$$\sigma(r)_{r,3,Th} = -\frac{\alpha_3 E_3}{(1-\nu_3)r^2}\int \Delta T r dr + \frac{E_3}{1+\nu_3}\left(\frac{C_1^{III}}{1-2\nu_3} - \frac{C_2^{III}}{r^2} - \frac{\nu_3\varepsilon_0}{1-2\nu_3}\right)\ , \qquad R_3 \le r_{EBC} \le R_4 \qquad (4\text{-}34)$$

$$\sigma(r)_{\theta,3,Th} = \frac{\alpha_3 E_3}{(1-\nu_3)r^2}\int \Delta T r dr - \frac{\alpha_3 E_3 \Delta T}{1-\nu_3} + \frac{E_3}{1+\nu_3}\left(\frac{C_1^{III}}{1-2\nu_3} + \frac{C_2^{III}}{r^2} - \frac{\nu_3\varepsilon_0}{1-2\nu_3}\right), \qquad R_3 \le r_{EBC} \le R_4 \qquad (4\text{-}35)$$

$$\sigma_{z,3,Th} = E_3\varepsilon_0 + \frac{-E_3\alpha_3\Delta T}{1-\nu_3} + \frac{2\nu_3 E_3 C_1^{III}}{(1-2\nu_3)(1+\nu_3)}\ , \qquad R_3 \le r_{EBC} \le R_4 \qquad (4\text{-}36)$$

We have seven unknowns, C_1^{I}, C_2^{I}, C_1^{II}, C_2^{II}, C_1^{III}, C_2^{III}, and ε_0. The following seven boundary equations are applied to solve for the unknowns.

$$B.C\begin{cases} \sigma(R_1)_{r,1,Th} = 0 \quad \cdots\cdots (1) \\ \sigma(R_2)_{r,1,Th} = \sigma(R_2)_{r,2,Th} \quad \cdots\cdots (2) \\ \frac{1}{E_1}\left[\sigma(R_2)_{\theta,1,Th} - \nu_1\sigma(R_2)_{r,1,Th} - \nu_1\sigma_{z,1,Th}\right] + \alpha_1\Delta T(R_2) = \frac{1}{E_2}\left[\sigma(R_2)_{\theta,2,Th} - \nu_2\sigma(R_2)_{r,2,Th} - \nu_2\sigma_{z,2,Th}\right] + \alpha_2\Delta T(R_2) \cdots (3) \\ \sigma(R_3)_{r,2,Th} = \sigma(R_3)_{r,3,Th} \quad \cdots\cdots (4) \\ \frac{1}{E_2}\left[\sigma(R_3)_{\theta,2,Th} - \nu_2\sigma(R_3)_{r,2,Th} - \nu_2\sigma_{z,2,Th}\right] + \alpha_2\Delta T(R_3) = \frac{1}{E_3}\left[\sigma(R_3)_{\theta,3,Th} - \nu_3\sigma(R_3)_{r,3,Th} - \nu_3\sigma_{z,3,Th}\right] + \alpha_3\Delta T(R_3) \cdots (5) \\ \sigma(R_4)_{r,4,Th} = 0 \quad \cdots\cdots (6) \\ \int_{R_1}^{R_2} 2\pi r\sigma_{z,1,Th}dr + \int_{R_2}^{R_3} 2\pi r\sigma_{z,2,Th}dr + \int_{R_3}^{R_4} 2\pi r\sigma_{z,3,Th}dr = 0 \quad \cdots\cdots (7) \end{cases} \qquad (4\text{-}37)$$

Note that these boundary conditions are similar to the ones in Eq.(4-12) for stress calculations under pressure loading; the radial components of thermal stresses are also continuous at the interface of any two layers with equal diametral strains, and they vanish at the inner most and the outer most surfaces. Thermal expansion self-equilibrates in the axial direction by having the axial strain ε_0 in all three layers, which leads to zero net force as stated in B.C(7). Applying the boundary conditions results in the following set of seven equations

$$\left[\frac{E_1}{(1-2\nu_1)(1+\nu_1)}\right]C_1^{\mathrm{I}} - \left[\frac{E_1}{(1+\nu_1){R_1}^2}\right]C_2^{\mathrm{I}} - \left[\frac{E_1\nu_1}{(1+\nu_1)(1-2\nu_1)}\right]\varepsilon_0 = 0 \tag{4-38}$$

$$\left[\frac{E_1}{(1-2\nu_1)(1+\nu_1)}\right]C_1^{\mathrm{I}} - \left[\frac{E_1}{(1+\nu_1){R_2}^2}\right]C_2^{\mathrm{I}} - \left[\frac{E_2}{(1-2\nu_2)(1+\nu_2)}\right]C_1^{\mathrm{II}} + \left[\frac{E_2}{(1+\nu_2){R_2}^2}\right]C_2^{\mathrm{II}} + \left[\frac{E_2\nu_2}{(1+\nu_2)(1-2\nu_2)} - \frac{E_1\nu_1}{(1+\nu_1)(1-2\nu_1)}\right]\varepsilon_0 = \frac{E_1\alpha_1}{(1-\nu_1){R_2}^2}\int_{R_1}^{R_2}\Delta T r dr \tag{4-39}$$

$$\left[\frac{1-\nu_1-2{\nu_1}^2}{(1-2\nu_1)(1+\nu_1)}\right]C_1^{\mathrm{I}} + \left[\frac{1+\nu_1}{(1+\nu_1){R_2}^2}\right]C_2^{\mathrm{I}} + \left[\frac{-1+\nu_2+2{\nu_2}^2}{(1-2\nu_2)(1+\nu_2)}\right]C_1^{\mathrm{II}} + \left[\frac{-1-\nu_2}{(1+\nu_2){R_2}^2}\right]C_2^{\mathrm{II}} + \left[\left(\frac{{\nu_1}^2-\nu_1}{(1-2\nu_1)(1+\nu_1)}-\nu_1\right)-\left(\frac{{\nu_2}^2-\nu_2}{(1-2\nu_2)(1+\nu_2)}-\nu_2\right)\right]\varepsilon_0 = \frac{\alpha_1(-1-\nu_1)}{(1-\nu_1){R_2}^2}\int_{R_1}^{R_2}\Delta T r dr \tag{4-40}$$

$$\left[\frac{E_2}{(1-2\nu_2)(1+\nu_2)}\right]C_1^{\mathrm{II}} - \left[\frac{E_2}{(1+\nu_2){R_3}^2}\right]C_2^{\mathrm{II}} - \left[\frac{E_3}{(1-2\nu_3)(1+\nu_3)}\right]C_1^{\mathrm{III}} + \left[\frac{E_3}{(1+\nu_3){R_3}^2}\right]C_2^{\mathrm{III}} + \left[\frac{E_3\nu_3}{(1+\nu_3)(1-2\nu_3)} - \frac{E_2\nu_2}{(1+\nu_2)(1-2\nu_2)}\right]\varepsilon_0 = \frac{E_2\alpha_2}{(1-\nu_2){R_3}^2}\int_{R_2}^{R_3}\Delta T r dr \tag{4-41}$$

$$\left[\frac{1-\nu_2-2{\nu_2}^2}{(1-2\nu_2)(1+\nu_2)}\right]C_1^{\mathrm{II}} + \left[\frac{1+\nu_2}{(1+\nu_2){R_3}^2}\right]C_2^{\mathrm{II}} + \left[\frac{-1+\nu_3+2{\nu_3}^2}{(1-2\nu_3)(1+\nu_3)}\right]C_1^{\mathrm{III}} + \left[\frac{-1-\nu_3}{(1+\nu_3){R_3}^2}\right]C_2^{\mathrm{III}} + \left[\left(\frac{{\nu_2}^2-\nu_2}{(1-2\nu_2)(1+\nu_2)}-\nu_2\right)-\left(\frac{{\nu_3}^2-\nu_3}{(1-2\nu_3)(1+\nu_3)}-\nu_3\right)\right]\varepsilon_0 = \frac{\alpha_2(-1-\nu_2)}{(1-\nu_2){R_3}^2}\int_{R_2}^{R_3}\Delta T r dr \tag{4-42}$$

$$\left[\frac{E_3}{(1-2\nu_3)(1+\nu_3)}\right]C_1^{\mathrm{III}} - \left[\frac{E_3}{(1+\nu_3){R_4}^2}\right]C_2^{\mathrm{III}} - \left[\frac{E_3\nu_3}{(1+\nu_3)(1-2\nu_3)}\right]\varepsilon_0 = \frac{E_3\alpha_3}{(1-\nu_3){R_4}^2}\int_{R_3}^{R_4}\Delta T r dr \tag{4-43}$$

$$\left[\frac{2\nu_1 E_1\pi\left({R_2}^2-{R_1}^2\right)}{(1+\nu_1)(1-2\nu_1)}\right]C_1^{\mathrm{I}}+\left[\frac{2\nu_2 E_2\pi\left({R_3}^2-{R_2}^2\right)}{(1+\nu_2)(1-2\nu_2)}\right]C_1^{\mathrm{II}}+\left[\frac{2\nu_3 E_3\pi\left({R_4}^2-{R_3}^2\right)}{(1+\nu_3)(1-2\nu_3)}\right]C_1^{\mathrm{III}}$$

$$+\left[E_1\pi\left({R_2}^2-{R_1}^2\right)+E_2\pi\left({R_3}^2-{R_2}^2\right)+E_3\pi\left({R_4}^2-{R_3}^2\right)\right]\varepsilon_0=\int_{R_1}^{R_2}\frac{\alpha_1 E_1\Delta T}{1-\nu_1}2\pi r dr \qquad (4\text{-}44)$$

$$+\int_{R_2}^{R_3}\frac{\alpha_2 E_2\Delta T}{1-\nu_2}2\pi r dr+\int_{R_3}^{R_4}\frac{\alpha_3 E_3\Delta T}{1-\nu_3}2\pi r dr$$

Eq.(4-38) - can be simultaneously solved for the unknowns in the form $A\vec{X}=\vec{b}$. The matrix A is shown in Eq.(4-45), and the unknown vector $\vec{X}$, and the prescribed condition vector $\vec{b}$ are presented in Eq.(4-46).

$$\begin{bmatrix}
\frac{E_1}{(1-2\nu_1)(1+\nu_1)} & -\frac{E_1}{(1+\nu_1){R_1}^2} & 0 & 0 & 0 & 0 & -\frac{E_1\nu_1}{(1+\nu_1)(1-2\nu_1)} \\
\frac{E_1}{(1-2\nu_1)(1+\nu_1)} & -\frac{E_1}{(1+\nu_1){R_2}^2} & -\frac{E_2}{(1-2\nu_2)(1+\nu_2)} & \frac{E_2}{(1+\nu_2){R_2}^2} & 0 & 0 & \frac{E_2\nu_2}{(1+\nu_2)(1-2\nu_2)} - \frac{E_1\nu_1}{(1+\nu_1)(1-2\nu_1)} \\
\frac{1-\nu_1-2{\nu_1}^2}{(1-2\nu_1)(1+\nu_1)} & \frac{1+\nu_1}{(1+\nu_1){R_2}^2} & \frac{-1+\nu_2+2{\nu_2}^2}{(1-2\nu_2)(1+\nu_2)} & \frac{-1-\nu_2}{(1+\nu_2){R_2}^2} & 0 & 0 & \left(\frac{{\nu_1}^2-\nu_1}{(1-2\nu_1)(1+\nu_1)}-\nu_1\right) - \left(\frac{{\nu_2}^2-\nu_2}{(1-2\nu_2)(1+\nu_2)}-\nu_2\right) \\
0 & 0 & \frac{E_2}{(1-2\nu_2)(1+\nu_2)} & -\frac{E_2}{(1+\nu_2){R_3}^2} & -\frac{E_3}{(1-2\nu_3)(1+\nu_3)} & \frac{E_3}{(1+\nu_3){R_3}^2} & \frac{E_3\nu_3}{(1+\nu_3)(1-2\nu_3)} - \frac{E_2\nu_2}{(1+\nu_2)(1-2\nu_2)} \\
0 & 0 & \frac{1-\nu_2-2{\nu_2}^2}{(1-2\nu_2)(1+\nu_2)} & \frac{1+\nu_2}{(1+\nu_2){R_3}^2} & \frac{-1+\nu_3+2{\nu_3}^2}{(1-2\nu_3)(1+\nu_3)} & \frac{-1-\nu_3}{(1+\nu_3){R_3}^2} & \left(\frac{{\nu_2}^2-\nu_2}{(1-2\nu_2)(1+\nu_2)}-\nu_2\right) - \left(\frac{{\nu_3}^2-\nu_3}{(1-2\nu_3)(1+\nu_3)}-\nu_3\right) \\
0 & 0 & 0 & 0 & \frac{E_3}{(1-2\nu_3)(1+\nu_3)} & -\frac{E_3}{(1+\nu_3){R_4}^2} & -\frac{E_3\nu_3}{(1+\nu_3)(1-2\nu_3)} \\
\frac{2\nu_1 E_1\pi\left({R_2}^2-{R_1}^2\right)}{(1+\nu_1)(1-2\nu_1)} & 0 & \frac{2\nu_2 E_2\pi\left({R_3}^2-{R_2}^2\right)}{(1+\nu_2)(1-2\nu_2)} & 0 & \frac{2\nu_3 E_3\pi\left({R_4}^2-{R_3}^2\right)}{(1+\nu_3)(1-2\nu_3)} & 0 & E_1\pi\left({R_2}^2-{R_1}^2\right) + E_2\pi\left({R_3}^2-{R_2}^2\right) + E_3\pi\left({R_4}^2-{R_3}^2\right)
\end{bmatrix} \qquad (4\text{-}45)$$

$$X = \begin{bmatrix} C_1^{\mathrm{I}} \\ C_2^{\mathrm{I}} \\ C_1^{\mathrm{II}} \\ C_2^{\mathrm{II}} \\ C_1^{\mathrm{III}} \\ C_2^{\mathrm{III}} \\ \varepsilon_0 \end{bmatrix}, \qquad b_{thermal} = \begin{bmatrix} 0 \\ \frac{E_1\alpha_1}{(1-\nu_1){R_2}^2}\int_{R_1}^{R_2}\Delta T r dr \\ \frac{\alpha_1(-1-\nu_1)}{(1-\nu_1){R_2}^2}\int_{R_1}^{R_2}\Delta T r dr \\ \frac{E_2\alpha_2}{(1-\nu_2){R_3}^2}\int_{R_2}^{R_3}\Delta T r dr \\ \frac{\alpha_2(-1-\nu_2)}{(1-\nu_2){R_3}^2}\int_{R_2}^{R_3}\Delta T r dr \\ \frac{E_3\alpha_3}{(1-\nu_3){R_4}^2}\int_{R_3}^{R_4}\Delta T r dr \\ \int_{R_1}^{R_2}\frac{\alpha_1 E_1 \Delta T}{1-\nu_1}2\pi r dr + \int_{R_2}^{R_3}\frac{\alpha_2 E_2 \Delta T}{1-\nu_2}2\pi r dr + \int_{R_3}^{R_4}\frac{\alpha_3 E_3 \Delta T}{1-\nu_3}2\pi r dr \end{bmatrix} \tag{4-46}$$

For steady-state conditions with no heat generation, following heat equation holds for a cylindrical geometry

$$\frac{1}{r}\frac{d}{dr}\left(kr\frac{dT}{dr}\right) = 0 \tag{4-47}$$

Integrating Eq.(4-47) twice, the general temperature solution can be obtained as shown in Eq.(4-48).

$$T(r) = C_1 \ln r + C_2 \tag{4-48}$$

where C_1 and C_2 are constants to be determined for given boundary conditions. The linear heat rate q' is then obtained by taking the temperature gradient with respect to radial direction.

$$q' = -k(2\pi r)\frac{dT}{dr} = -2\pi C_1 k \tag{4-49}$$

Applying the boundary conditions for continuous temperature at the interfaces, and the equal linear heat rates in each layer, with a constant cladding outermost surface temperature $T(R_4)=T_o$, the temperature distribution in the three layers are found

$$T(r)_1 = \frac{q'}{2\pi}\left[\frac{1}{k_1} ln\left(\frac{R_2}{r}\right) + \frac{1}{k_2} ln\left(\frac{R_3}{R_2}\right) + \frac{1}{k_3} ln\left(\frac{R_4}{R_3}\right)\right] + T_o, \qquad R_1 \leq r_{inner\ monolith} \leq R_2 \qquad (4\text{-}50)$$

$$T(r)_2 = \frac{q'}{2\pi}\left[\frac{1}{k_2} ln\left(\frac{R_3}{r}\right) + \frac{1}{k_3} ln\left(\frac{R_4}{R_3}\right)\right] + T_o, \qquad R_2 \leq r_{composite} \leq R_3 \qquad (4\text{-}51)$$

$$T(r)_3 = \frac{q'}{2\pi k_3} ln\left(\frac{R_4}{r}\right) + T_o, \qquad R_3 \leq r_{EBC} \leq R_4 \qquad (4\text{-}52)$$

Now, we can calculate the stress distributions in the cladding with relevant SiC cladding properties summarized in Table 4-1.

Table 4-1 Representative SiC Cladding Properties for Stress Calculations

<table>
<tr><th></th><th>Materials</th><th>Elastic modulus in $\theta\theta$ direction $E_{\theta\theta}$ (GPa)</th><th>Elastic modulus in zz direction E_{zz} (GPa)</th><th>Poisson ratio, $r\theta$ $\nu_{r\theta}$</th><th>Poisson ratio, θZ $\nu_{\theta z}(=\nu_{z\theta})$</th><th>Thermal conductivity k (W/m-K)</th><th>Thermal expansion coefficient α (1/K)</th></tr>
<tr><td rowspan="2">Monolithic SiC/EBC</td><td>CVD-SiC</td><td>460</td><td>460</td><td>0.21</td><td>0.21</td><td>9.5</td><td>4.6×10^{-6} at 721K Eq.(4-53)</td></tr>
<tr><td colspan="4">(Snead, 2007)</td><td>(Katoh, 2011)</td><td>(Snead, 2007)</td></tr>
<tr><td rowspan="2">Fiber-Reinforced Composite</td><td>HNLS CVI SiC/SiC</td><td>230</td><td>230</td><td>0.13</td><td>0.13</td><td>1.5</td><td>4.0×10^{-6}</td></tr>
<tr><td colspan="3">(Katoh, 2010)</td><td colspan="2">(Nozawa, 2012)</td><td>(Katoh, 2011)</td><td>(Giancarli, 2002)</td></tr>
</table>

The innermost monolith and EBC are monolithic CVD-SiC. Monolithic CVD-SiC properties are regarded as isotropic (Snead, 2007). Thermal conductivity of the cladding quality CVD-SiC is found to saturate at ~9.5 W/m-K roughly after 0.1 displacements per atom (DPA) at 400°C (Katoh, 2011). Thermal expansion coefficients of reactor cladding quality CVD-SiC were obtained by the equation developed by Snead.et.al (Snead, 2007) given in Eq.(4-53).

$$\alpha_{CVD.SiC}\begin{cases} -1.8276 + 0.0178\,T - 1.5544 \times 10^{-5}T^2 + 4.5246 \times 10^{-9}T^3 \quad \left(\frac{10^{-6}}{K}\right), for\ 125K \le T \le 1273K \\ 5.0 \times 10^{-6}\left(\frac{1}{K}\right), \qquad for\ 1273K < T \end{cases} \tag{4-53}$$

For the composite material studied by Katoh.et.al (Katoh, 2010), Hi-Nicalon™ Type-S CVI-SiC composite (HNLS CVI) - with reactor cladding quality, and near-stoichiometric - was tentatively regarded as the material choice for the fiber-reinforced composite. The HNLS CVI is a two-dimensional (2D) satin-weave fabric of Hi-Nicalon™ Type-S in the 0°/90° stacking configuration. Isotropic mechanical behavior was assumed in such a stacking configuration with woven SiC fabrics. The study by Katoh.et.al (Katoh, 2010) also investigated neutron irradiation effects on the composite tensile properties, observing reasonably narrow scatter in measured tensile modulus, whose range was 197~244 GPa, depending on neutron fluence and irradiation temperature. A series of studies observed a decreasing Young's modulus with neutron damage in both CVD-SiC and SiC composite (Snead, 2007), (Katoh, 2010), (Katoh, 2011). However, appreciable reduction in the elastic modulus occurs after a significant neutron dose, which may be not very relevant to LWR operating conditions (e.g., 460 GPa → 407 GPa, and 230 GPa → 210 GPa for the CVD-SiC, and HNLS CVI SiC/SiC composite, respectively after a few tens of DPA) (Katoh, 2010), (Katoh, 2011). Hence, in this study, as far as LWR application is concerned, representative elastic moduli for both CVD-SiC and HNLS CVI SiC/SiC composite SiC were adopted from non-irradiated values). Composite thermal conductivity was found to saturate at ~1.5 W/m-K in the through-thickness direction after 2.0 DPA in 450°C (Katoh, 2010). Hence, for a SiC cladding that consists of 50% monolith and 50% fiber-reinforced composite in terms of thickness, a thermal conductivity of ~5.5 W/m-K is expected. This estimation is in reasonably good agreement with measured thermal conductivities (~4.8W/m-K) of Triplex SiC claddings with approximately equal CVD-monolith and fiber-reinforced composite thicknesses after an exposure in simulated LWR core conditions in terms of radiation fields, temperature, and water chemistry at MITR-II (Stempien, 2011).

Stress distributions in the cladding were calculated for the following cladding layer designs whose total thicknesses remains the same as the current cladding thickness of LWRs, 0.57mm.

Table 4-2 Four Cladding Thickness Designs Used for Stress Distributions Studies

	Inner monolith thickness	Fiber-reinforced composite thickness	Environmental barrier coating (EBC) thickness	Total Cladding Thickness
Cladding –A (1:8:1)	0.057 mm	0.456 mm	0.057 mm	0.57 mm
Cladding –B (3:6:1)	0.171 mm	0.342 mm	0.057 mm	
Cladding –C (4.5:4.5:1)	0.2565 mm	0.2565 mm	0.057 mm	
Cladding –D (6:3:1)	0.342 mm	0.171 mm	0.057 mm	
Cladding –E (8:1:1)	0.456 mm	0.057 mm	0.057 mm	
Cladding –F (9:0:1) (Monolith only)	0.513 mm	0	0.057 mm	
Cladding –G (0:9:1)	0 mm	0.513 mm	0.057 mm	

A typical PWR core average linear pin power, 17.86kW/m, was used with a cladding outer surface temperature of 350°C. The current PWR cladding geometry, 9.5mm O.D and 0.57mm of thickness, was used, as the study primarily aims for minimum departure from the current LWR geometrical designs. Distributions of the radial stresses, axial stresses, and hoop stresses are shown in Figure 4-4 - Figure 4-24.

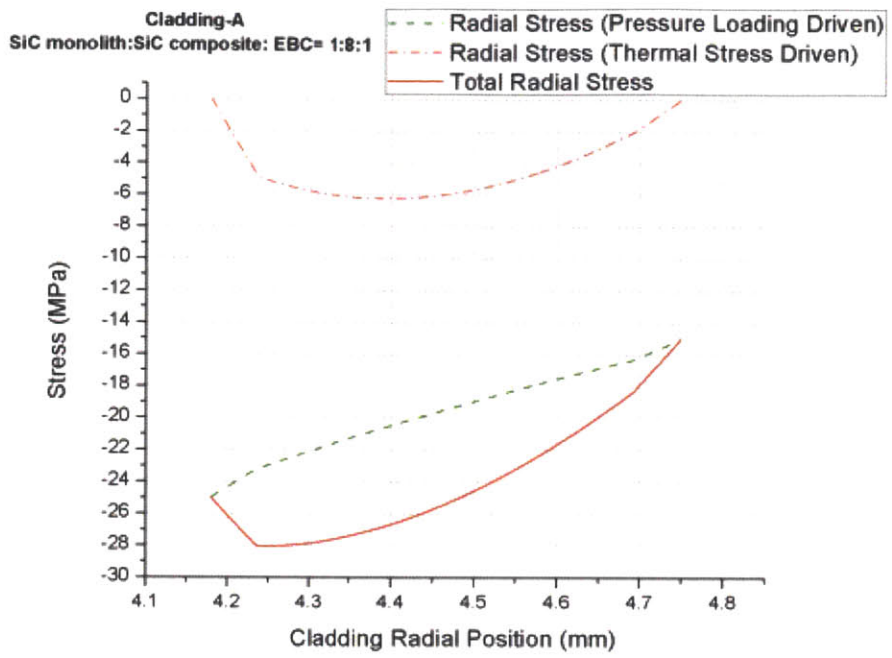

Figure 4-4 Radial Stress Distributions for SiC Cladding Layer Designs (A) Shown in Table 4-2: $\dot{q}$=17.86 kW/m, T_o=350°C, P_i=25MPa, P_o=15MPa

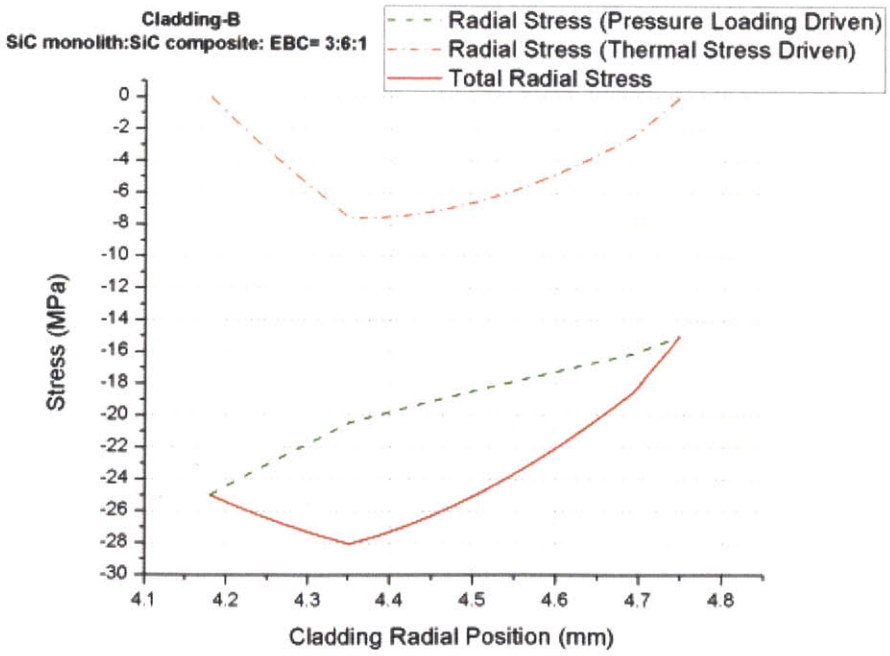

Figure 4-5 Radial Stress Distributions for SiC Cladding Layer Designs (B) Shown in Table 4-2: $\dot{q}$=17.86 kW/m, T_o=350°C, P_i=25MPa, P_o=15MPa

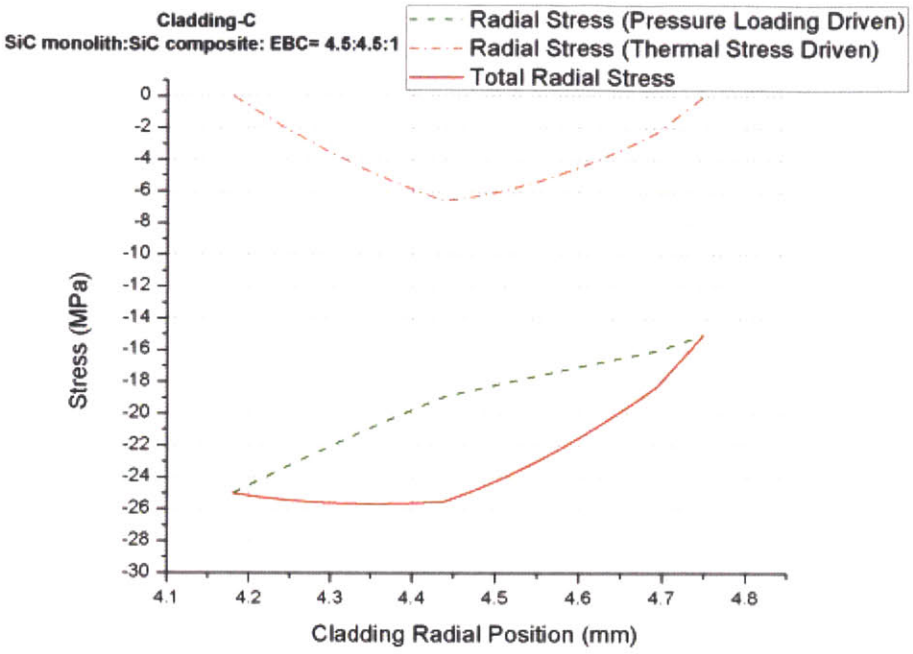

Figure 4-6 Radial Stress Distributions for SiC Cladding Layer Designs (C) Shown in Table 4-2: $\dot{q}$=17.86 kW/m, T_o=350°C, P_i=25MPa, P_o=15MPa

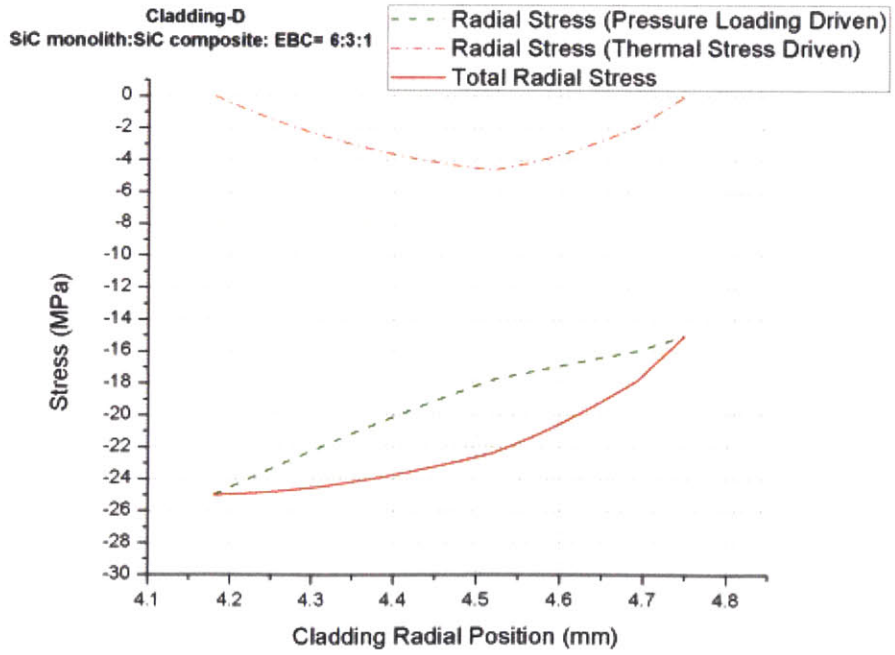

Figure 4-7 Radial Stress Distributions for SiC Cladding Layer Designs (D) Shown in Table 4-2: $\dot{q}$=17.86 kW/m, T_o=350°C, P_i=25MPa, P_o=15MPa

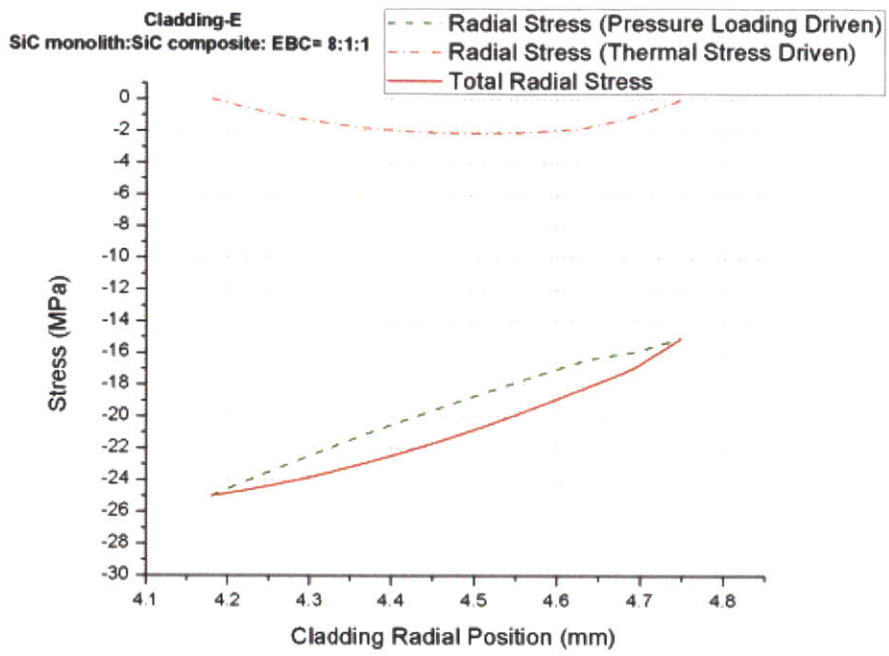

Figure 4-8 Radial Stress Distributions for SiC Cladding Layer Designs (E) Shown in Table 4-2: $\dot{q}$=17.86 kW/m, T_o=350°C, P_i=25MPa, P_o=15MPa

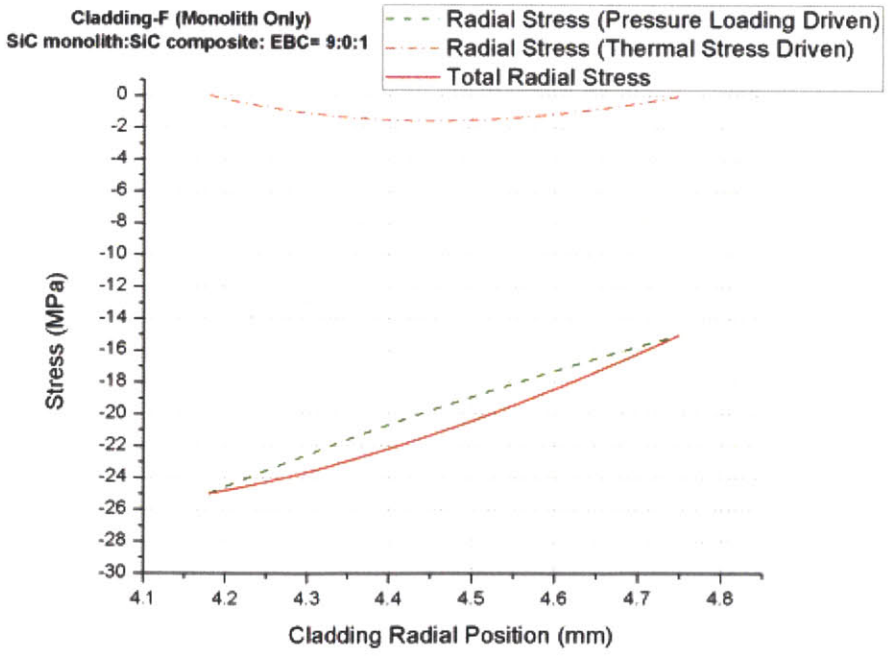

Figure 4-9 Radial Stress Distributions for SiC Cladding Layer Designs (F-monolith only) Shown in Table 4-2: $\dot{q}$=17.86 kW/m, T_o=350°C, P_i=25MPa, P_o=15MPa

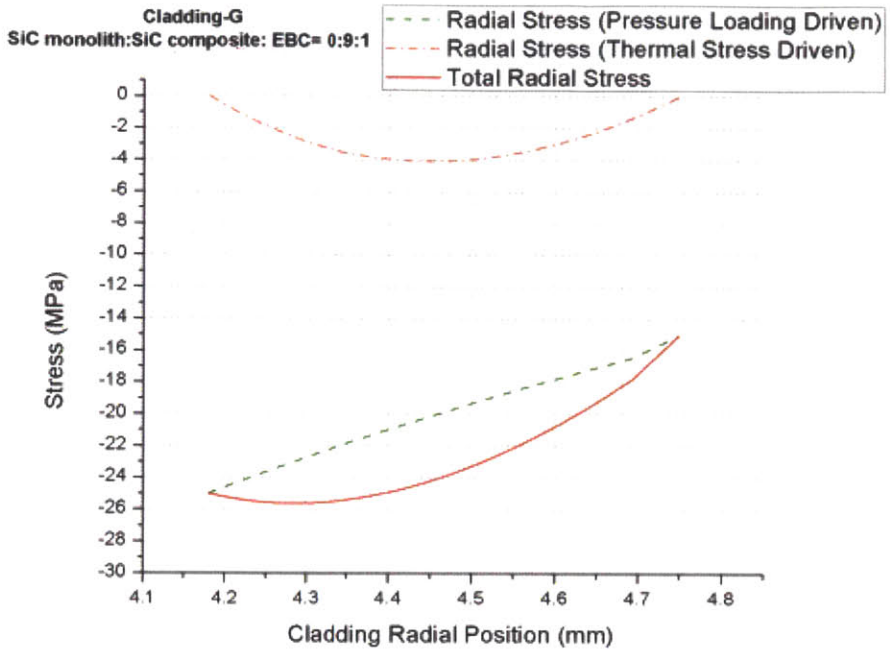

Figure 4-10 Radial Stress Distributions for SiC Cladding Layer Designs (G-no inner monolith) Shown in Table 4-2: q'=17.86 kW/m, T_o=350°C, P_i=25MPa, P_o=15MPa

In Figure 4-4 - Figure 4-28, the pressure driven radial stresses are stresses induced by pressure loading if there was no temperature gradient. The thermal stress driven radial stresses are stresses induced by differential thermal expansion if there was no pressure loading. The cladding sees a total radial stress indicated by the solid red lines, having continuous compressive stresses whose quantities are equal to internal pressure, and external pressure at the inner most, and the outer most surfaces, respectively.

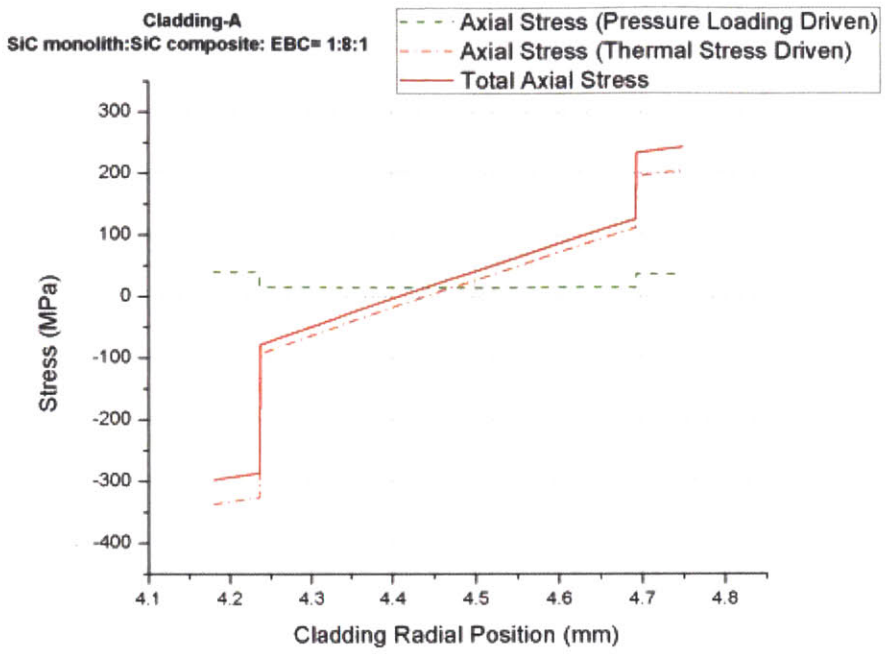

Figure 4-11 Axial Stress Distributions for SiC Cladding Layer Designs (A) Shown in Table 4-2: q'=17.86 kW/m, T_o=350°C, P_i=25MPa, P_o=15MPa

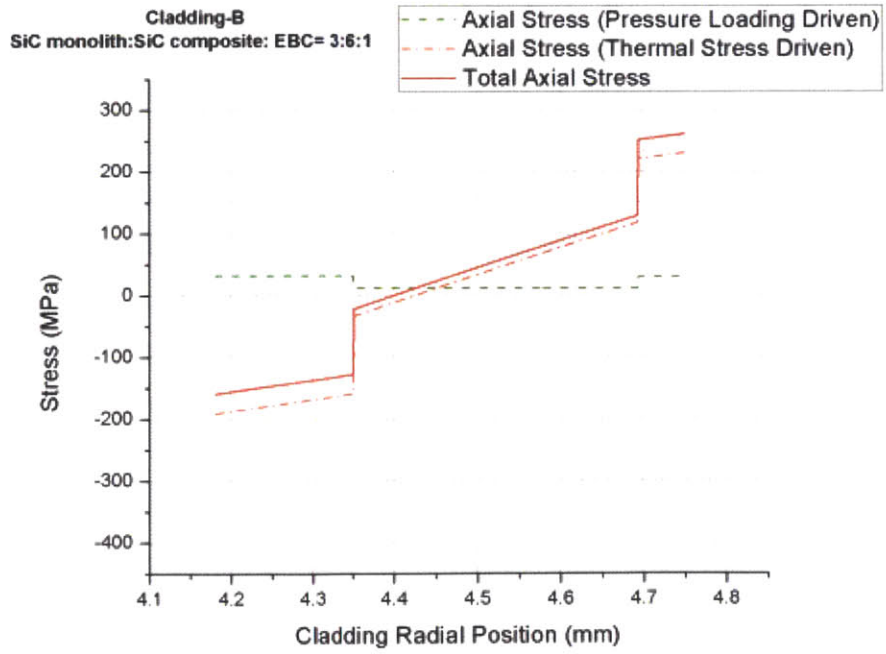

Figure 4-12 Axial Stress Distributions for SiC Cladding Layer Designs (B) Shown in Table 4-2: q'=17.86 kW/m, T_o=350°C, P_i=25MPa, P_o=15MPa

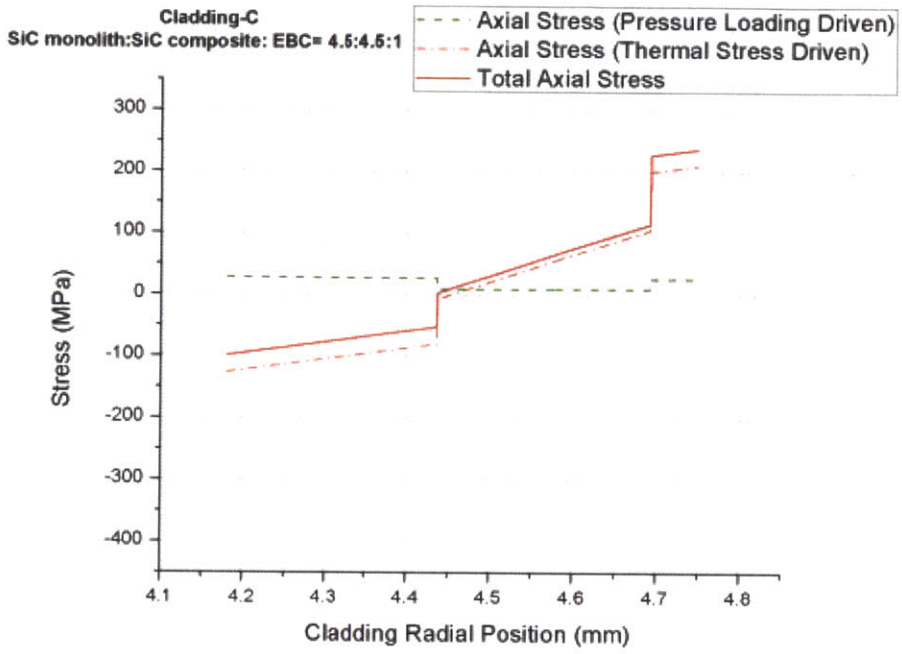

Figure 4-13 Axial Stress Distributions for SiC Cladding Layer Designs (C) Shown in Table 4-2: $\dot{q}$=17.86 kW/m, T_o=350°C, P_i=25MPa, P_o=15MPa

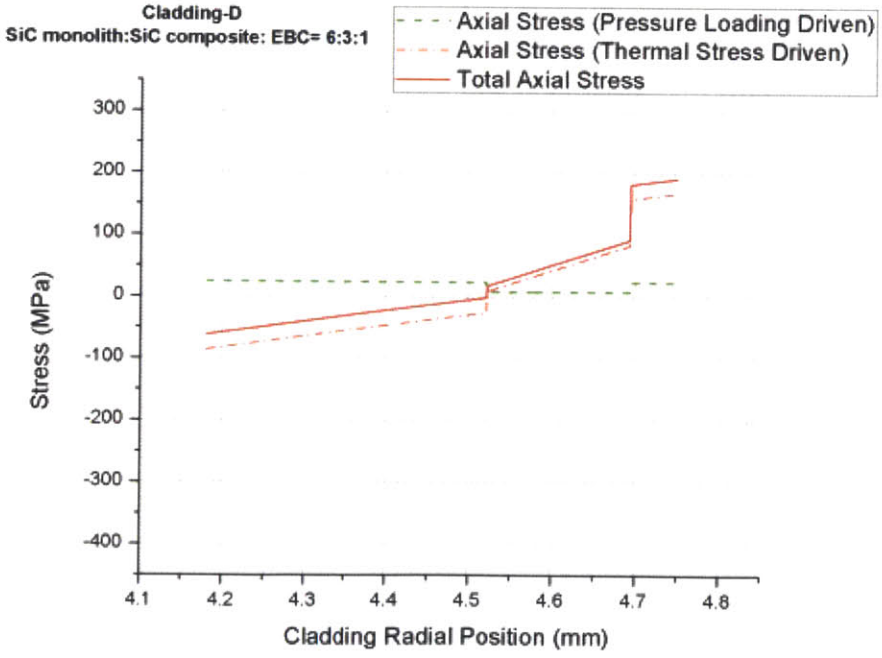

Figure 4-14 Axial Stress Distributions for SiC Cladding Layer Designs (D) Shown in Table 4-2: $\dot{q}$=17.86 kW/m, T_o=350°C, P_i=25MPa, P_o=15MPa

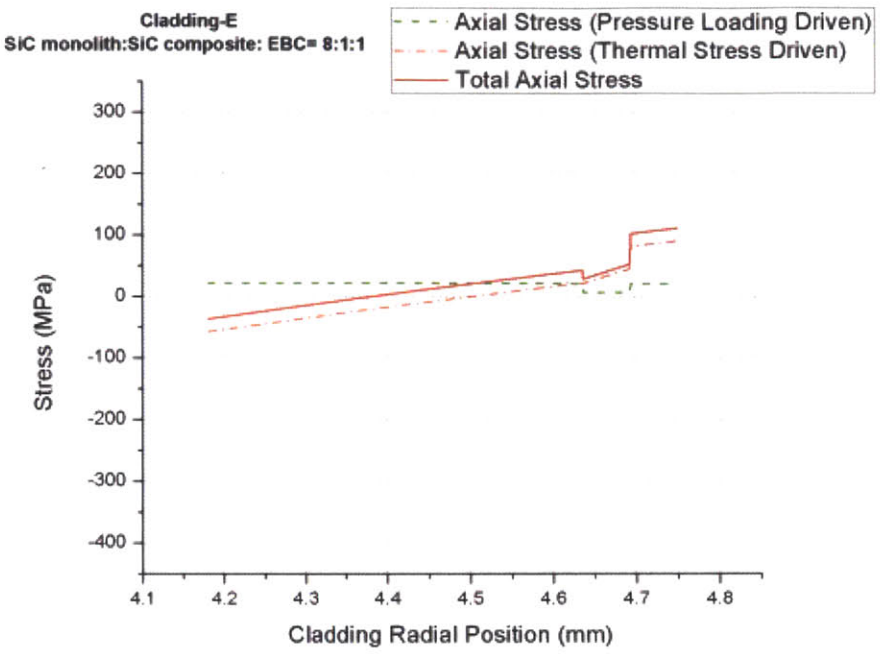

Figure 4-15 Axial Stress Distributions for SiC Cladding Layer Designs (E) Shown in Table 4-2: $q^{'}$=17.86 kW/m, T_o=350°C, P_i=25MPa, P_o=15MPa

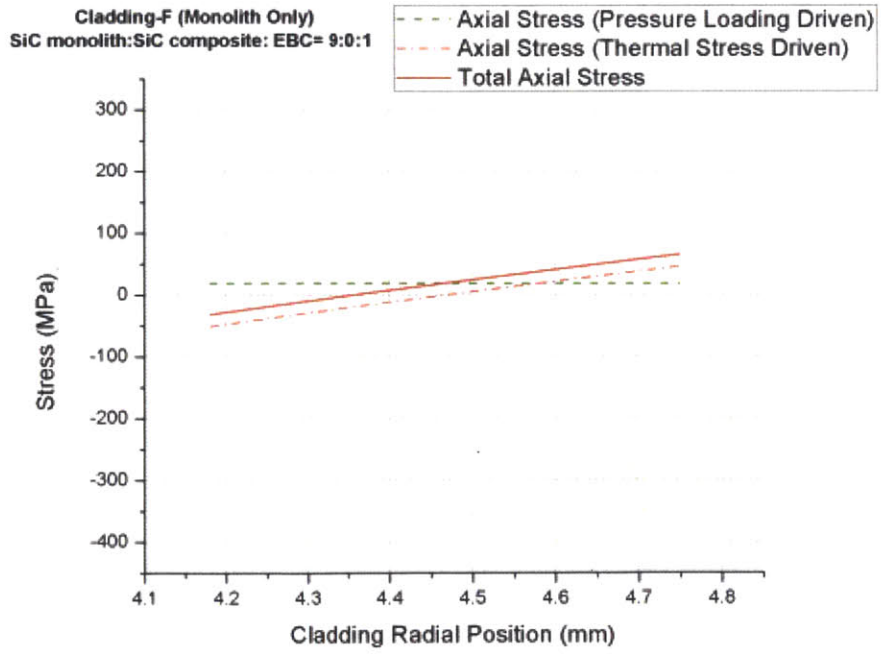

Figure 4-16 Axial Stress Distributions for SiC Cladding Layer Designs (F-monolith only) Shown in Table 4-2: $q^{'}$=17.86 kW/m, T_o=350°C, P_i=25MPa, P_o=15MPa

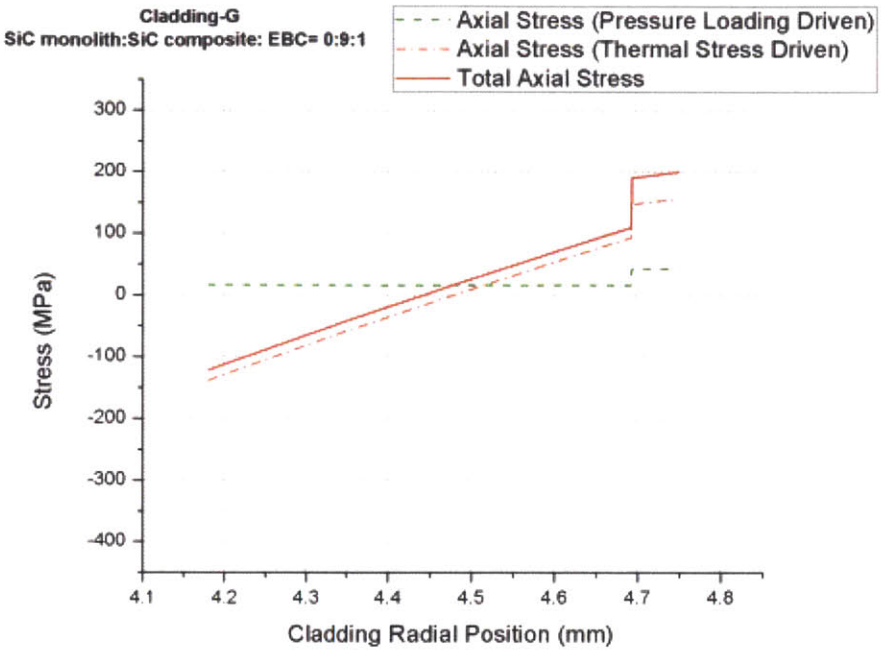

Figure 4-17 Axial Stress Distributions for SiC Cladding Layer Designs (F-no inner monolith) Shown in Table 4-2: $q' = 17.86$ kW/m, $T_o = 350^{\circ}C$, $P_i = 25$MPa, $P_o = 15$MPa

When $P_i > P_o$, pressure loading creates tensile axial stresses in all three layers with a slightly reduced stress level in the composite layer, primarily due to lower stiffness. Thermal stresses put the region of higher temperature in compression and the region of lower temperature in tension. As a result, the inner monolith sees compressive thermal stresses and the EBC sees tensile stresses. Depending on relative thicknesses of the layers, one layer may experience both compressive and tensile thermal stresses. Note that the contribution of thermal stresses to the total axial stress is significant and the influence of thermal stresses on the total axial stress fields increase with increasing portion of composite. This is because the composite exhibits a substantially lower thermal conductivity (1.5 W/m-K) than the monolith (9.5 W/m-K), resulting in a steeper temperature gradient. This effect of the differential thermal conductivity between the monolith and the composite is significantly larger than other mechanical property differences so that a change in relative thicknesses of the cladding layer significantly affects thermal stress distributions. Note that given a free axial thermal expansion boundary condition at the end cap, the axial thermal force integration gives zero net force.

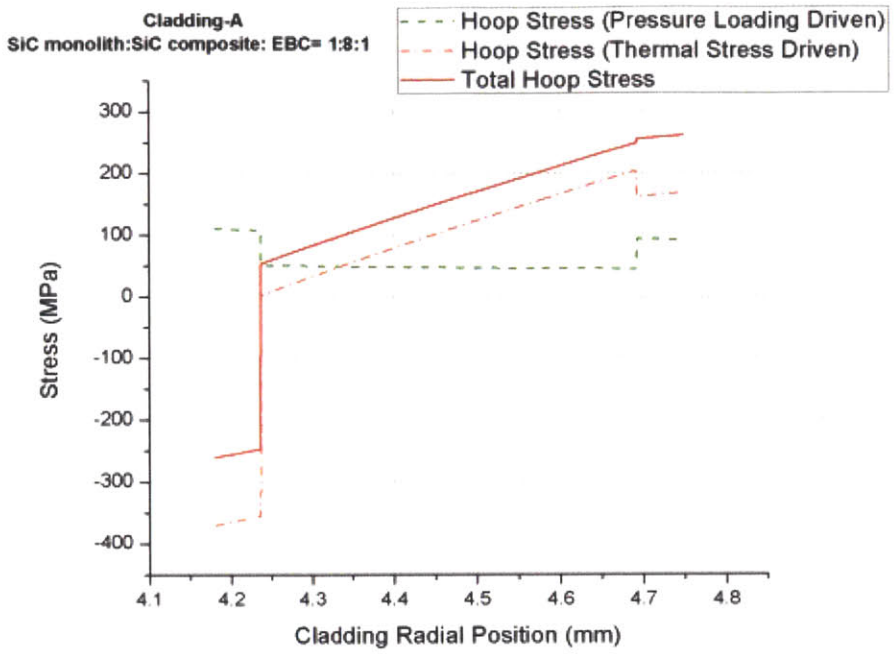

Figure 4-18 Hoop Stress Distributions for SiC Cladding Layer Designs (A) Shown in Table 4-2: $q^{'}$=17.86 kW/m, T_o=350°C, P_i=25MPa, P_o=15MPa

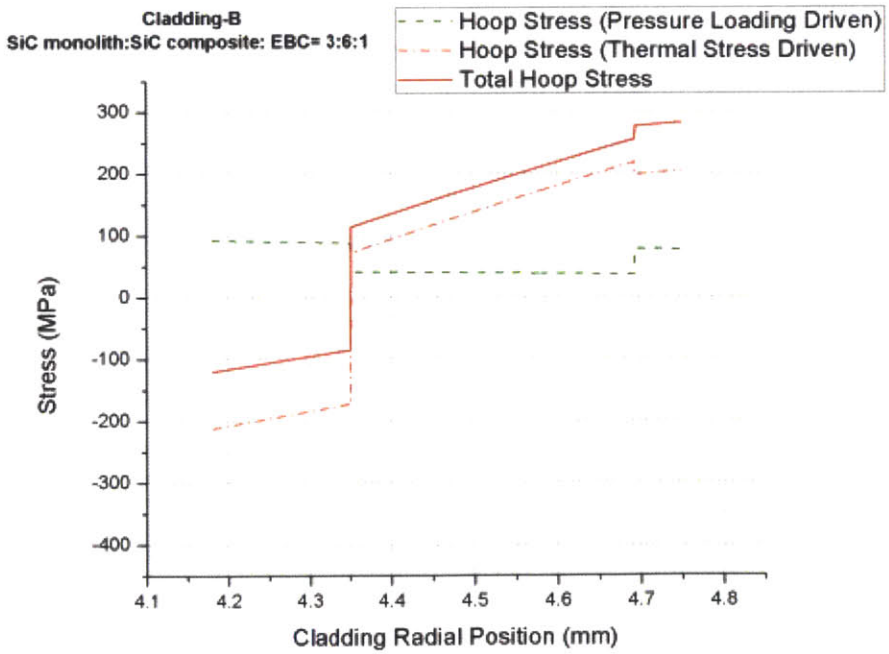

Figure 4-19 Hoop Stress Distributions for SiC Cladding Layer Designs (B) Shown in Table 4-2: $q^{'}$=17.86 kW/m, T_o=350°C, P_i=25MPa, P_o=15MPa

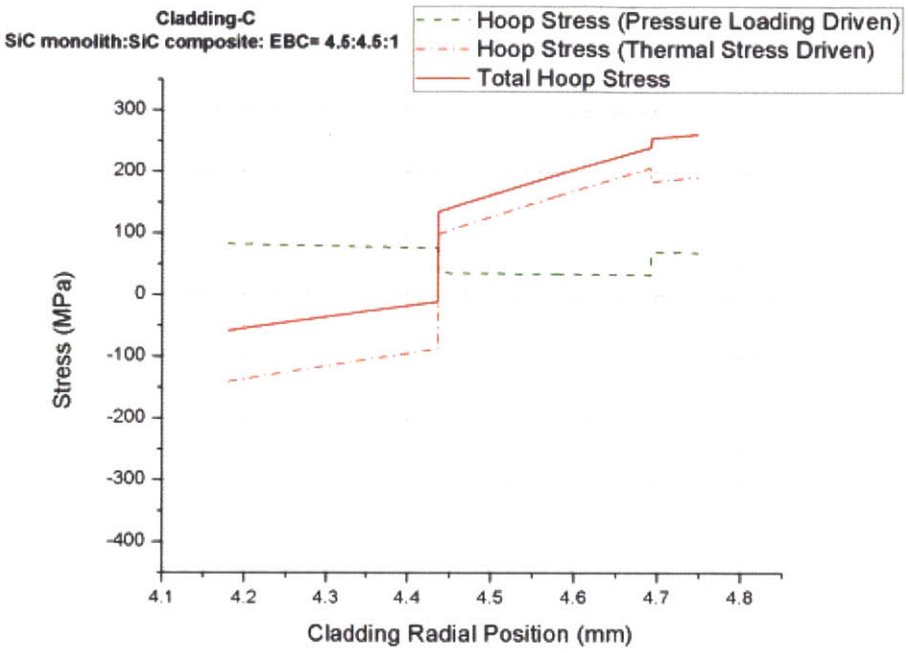

Figure 4-20 Hoop Stress Distributions for SiC Cladding Layer Designs (C) Shown in Table 4-2: q'=17.86 kW/m, T_o=350°C, P_i=25MPa, P_o=15MPa

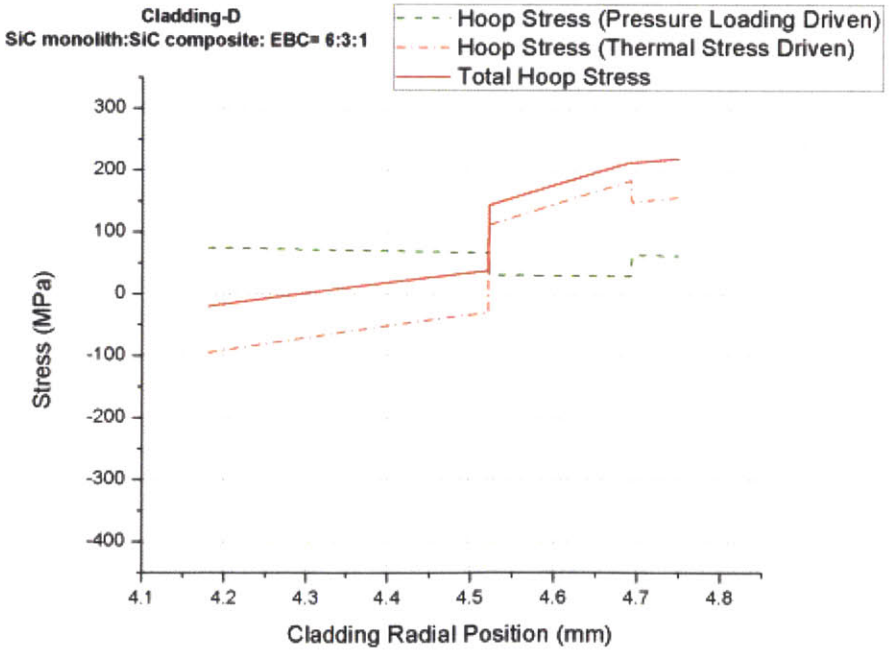

Figure 4-21 Hoop Stress Distributions for SiC Cladding Layer Designs (D) Shown in Table 4-2: q'=17.86 kW/m, T_o=350°C, P_i=25MPa, P_o=15MPa

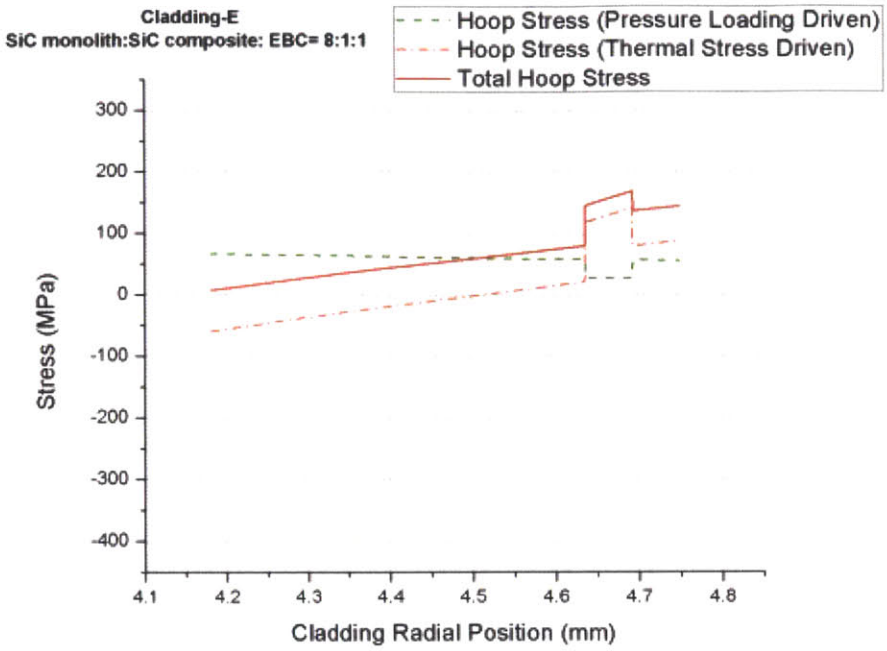

Figure 4-22 Hoop Stress Distributions for SiC Cladding Layer Designs (E) Shown in Table 4-2: $q^{'}$=17.86 kW/m, T_o=350°C, P_i=25MPa, P_o=15MPa

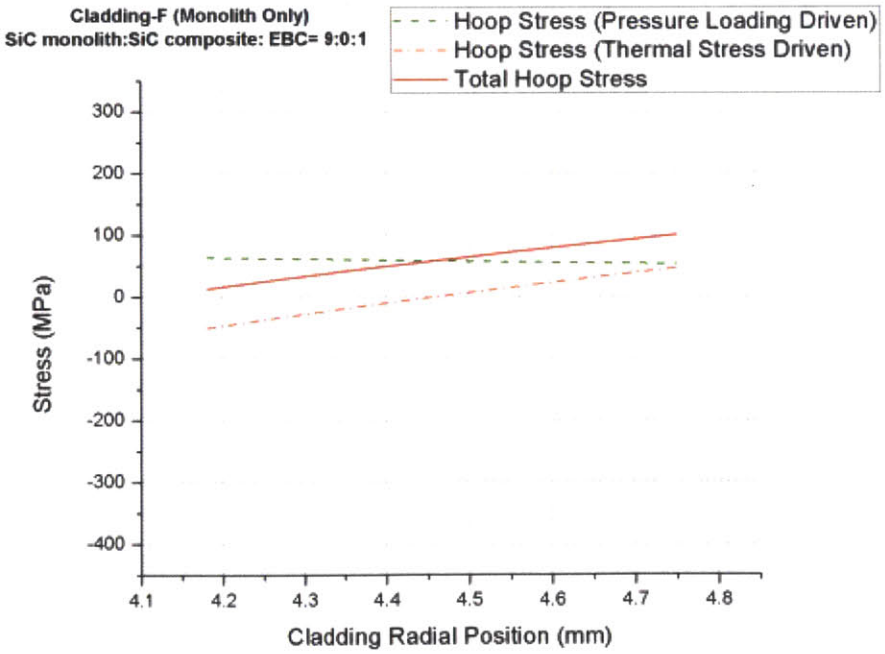

Figure 4-23 Hoop Stress Distributions for SiC Cladding Layer Designs (F-monolith only) Shown in Table 4-2: $q^{'}$=17.86 kW/m, T_o=350°C, P_i=25MPa, P_o=15MPa

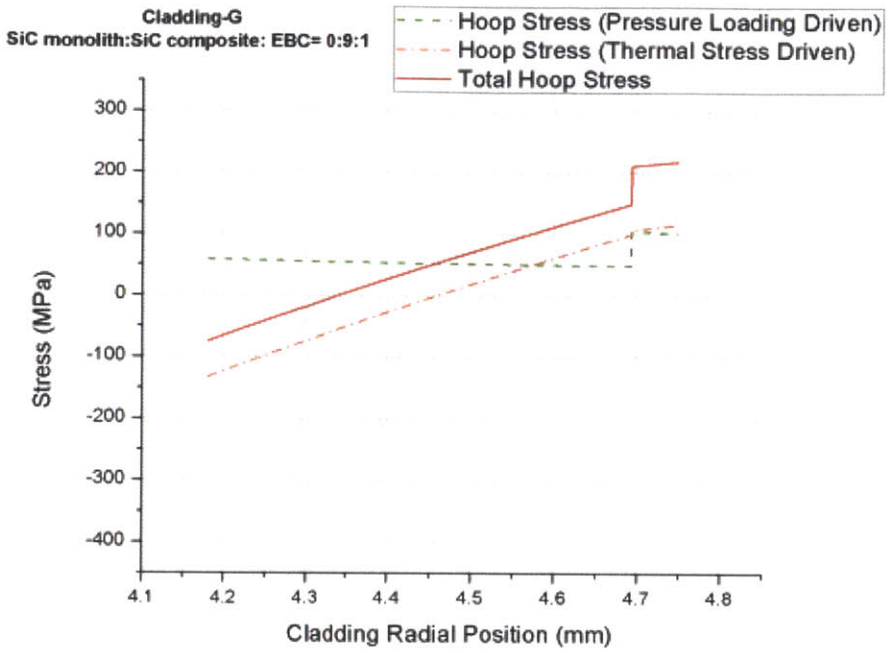

Figure 4-24 Hoop Stress Distributions for SiC Cladding Layer Designs (G- no inner monolith) Shown in Table 4-2: q'=17.86 kW/m, T_o=350°C, P_i=25MPa, P_o=15MPa

For hoop stress distributions, the pressure loading induced stress has a significant influence on the total stress. Increasing the thickness of the monolith portion reduces the pressure induced stress levels in the cladding, as can be seen in the progressively reduced pressure loading stresses from cladding-A to cladding-F. Also, higher conductivity of the monolithic SiC helps reduce thermal stress levels. Thermal stresses in the SiC cladding have both positive and negative effects; they counteract tensile stresses due to pressure loading in the inner monolith, while they add tensile stresses to the composite and EBC. Hence, a preferred strategy for managing thermal stresses in the SiC cladding would be to design the cladding layer to use its inner most compressive stresses for helping fission gas retention while maintaining stress levels below fracture stresses in the composite and EBC. The compressive thermal stresses in the inner most monolith generally lead to higher tensile stress levels in the composite and EBC layers. This case may not be preferred from the view point of prevention of H_2O access to fibers. Depending on the amount of the internal fuel rod pressurization, significance of the thermal stress on the total stress level changes. In that, thermal stresses would be an even more significant portion of the total stress in a lower burnup fuel rod. Note that the assumed 25 MPa of internal pressurization for the stress distribution results, shown

in this section, implies a considerably high burnup fuel rod of SiC cladding before PCMI[20]. Hence, the validity of the discussed significance of thermal stresses on the total cladding stresses holds true for the entire span of fuel rod in-core residence time.

From a fuel design point of view, the total hoop stresses that arise from combinations of pressure loading, thermal stresses, and different mechanical response of each cladding layer is of particular interest as it primarily serves as a basis for the safety of a fuel rod. A progressively increasing monolith layer portion from 10% to 45% of the total cladding thickness does not particularly help to reduce tensile stress levels in the cladding in general, as can be seen in Cladding-A, Cladding-B, and Cladding-C in Figure 4-25. For cladding-A, it sees a significantly high compressive stress level in the innermost monolith which can be of potential concern as the cladding may exceed its compressive strength, which is usually a few times higher than tensile strength. Cladding-D in which 60% of the cladding thicknesses comes from monolith noticeably reduces tensile stress levels in the composite and EBC at the expense of allowing a finite fraction of the monolith in tension. Further increase in the monolith fraction leads to a progressive reduction of tensile stresses in the composite and EBC. This design, at the same time, leaves the entire monolith portion under tensile stresses because the reduction in the compressive thermal stresses in the monolith portion is more significant than that of the pressure loading induced tensile stresses. Cladding-F represents the case where the SiC cladding is solely made of monolithic SiC. With no constraints for laminated layers, and higher thermal conductivity of the monolith SiC, cladding-F that consists solely of the monolith exhibits relatively lower average total tensile hoop stresses. Note that for this single layer cladding, the net thermal hoop stress over the entire cladding thickness sums up to zero (see the thermal stress line of Cladding-F in Figure 4-23). Cladding-G is essentially the SiC cladding solely made of the composite without a presence of the innermost monolith. 10% monolithic EBC may also be regarded as the CVI overcoat thickness for the prevention of H_2O ingression into fibers. For this cladding design, primarily dominated by thermal stresses due to low composite thermal conductivity, radial stress are relatively sharper, making for a relatively quicker transition from compression to tension along the cladding radial position. In this cladding design, a considerable portion of the composite is under tensile stresses, with a sharp increase of the tensile stress in EBC.

[20] PCMI for a LWR fuel rod of SiC cladding occurs at a substantially high burnup (>60MWd/kgU) because of a very little or almost negligible creep of SiC cladding on to the fuel pellet. This was first investigated by a study conducted by Carpenter.et.al (Carpenter, 2010). Also, in this study, a delayed PCMI with an updated fuel modeling with SiC cladding has also revealed that the internal pressurization causes the limiting tensile stresses for steady-state fuel operation and design. Detailed discussions can be found in Chapter 7.

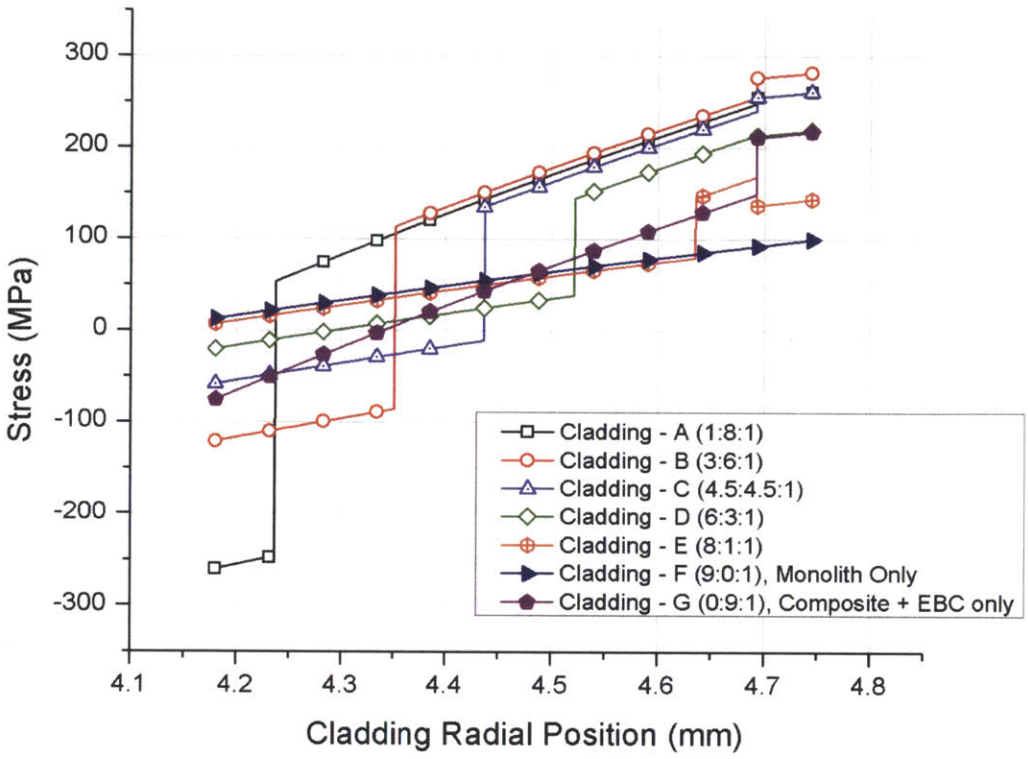

Figure 4-25 Total Hoop Stress with Different Relative Cladding Layer Thicknesses (Cladding A –G) Shown in Table 4-2: $\dot{q}$=17.86 kW/m, T_o=350°C, P_i=25MPa, P_o=15MPa, Parenthesis in the legend indicates the relative thickness fraction of innermost monolith: composite: EBC

Systematic assessment of fuel rod safety would be conducted when the calculated stress distributions are translated in terms of statistical fracture behavior. In that regard, calculated stress distributions are used with a statistical cladding fracture model in the following discussions to quantitatively define the safety characteristics of SiC cladding design & operations.

4.4.3 Treatment of the threshold stress, σ_u

The parameter σ_u in the statistical failure model, Eq.(4-4) is a stress level below which there is zero probability of failure. For many ceramic fracture studies, including SiC, σ_u is usually set to be zero ($\sigma_u = 0$), for the remote possibility of having a very large flaw in a specimen. This assumption gives the most conservative estimate of survival probability. It is important to note that although the Weibull distribution has its advantages, this is a probabilistic approach not based on the physical nature of the

fracture process and connected parameters, such as flaw size, and it may not hold for all situations (Bengisu, 2001), (Wachtman, 2009), (Lamon, 1988). Specifically, the accuracy of the Weibull distribution at low stress values has been found to be less reliable in several past studies; the failure probability found at low stress values is not well fitted with the distributions determined by abundant data at high stresses (Snead, 2007), (Byun, 2007). Nevertheless, failure data at high stresses are extrapolated to low stress values because the behavior at very low failure probability can only be explored by testing a very large number of specimens, which is usually not possible. This extrapolation results in a finite probability of failure even at very low stresses and it may underestimate the reliability of the system. Hence, the extrapolation of the probabilistic distribution to low stress values is speculative; the failure nature of SiC at low stresses may be better captured in a deterministic approach rather than the overly conservative probabilistic approach that assumes a remote possibility of a very large flaw.

For the PWR cladding applications, where about 50,500 fuel rods are subject to a transition from compression to tension with increasing burnup, even a very low probability of failure at low tension stress can imply failures of a finite number of fuel rods, which would significantly affect the maximum allowable burn-up and safety margins. Hence, speculative underestimation of reliability may imprudently rule out the feasibility of SiC cladding for LWRs. Thus, the proper application of the Weibull distribution to SiC clad fuel rods in LWRs may require an improved treatment and modeling of strength failure at low tensile stresses.

This study introduces a physical amendment into an otherwise purely statistical Weibull distribution for low tensile stress values; it does not assume a remote possibility of having a very large size pre-existing flaw which causes strength failure at low stress values, but estimates a maximum pre-existing flaw size and limiting shape for a given geometry of a thin cylindrical tube SiC. The characteristics of pre-existing flaws are primarily dictated by manufacturing techniques such as size of pores, grain boundary sizes, and existence of impurities and loading history for subcritical crack propagation (Bengisu, 2001), (Snead, 2007). This study applies the following rationale: the largest flaw size in a cylindrical SiC does not exceed 80% of tube thickness. This rationale is based on the combination of two thoughts – (1) the most vulnerable flaw to tensile hoop stresses in a tube geometry is a flaw that is perpendicular to the direction of the stress[21] and the largest size such a flaw can take is smaller than the tube thickness, and (2) CVD technologies and nondestructive testing of the ceramic during manufacturing screens out significant outliers in flaw sizes, for instance some flaws whose characteristic length is significantly larger than the

[21] The assumption was validated by internal pressurization tests for tubular SiC specimens that saw uniaxial tensile hoop stresses. Mode I fracture (K_I) was considered as the dominant fracture mode of the tested specimens.

tube thickness and positioned along the fuel rod length is screened out. This rationale implies that the larger the thickness of the tube, the lower the threshold fracture strength, σ_u.

This idea of a pre-existing crack size is important because it is essential information that captures the observed behavior of SiC failure using the stress intensity factor. The theoretical fracture strength calculated from inter-atomic potential is in the tens or hundreds of GPa – this is much higher than the MPa-level applied stresses actually required to fracture most engineering ceramics. This discrepancy results from the presence of cracks that concentrate stresses at the crack tip, allowing local decohesion processes to occur (Demkowicz, 2012). Stress intensity factors are uniquely defined by loading states, crack shape and specimen geometry; this raises an inherent uncertainty in accurately calculating the tensile strength of SiC cladding without knowing the shape and orientation of the critical flaw in a specimen. Hence, reasonable choices for stress intensity factors should be made to ensure realism in terms of the flaw characteristics in a specimen. Previous studies have found some evidence that the inner surface cracks primarily contribute to fracture in CVD SiC tube burst experiments (Byun, 2007). Therefore, in this study, stress intensity factors derived for a semi-elliptical surface crack of a finite length (80% of the cladding thickness) under stress mode I fracture (K_I), were used. Figure 4-26 illustrates a cylindrical pressure vessel with the discussed internal surface crack with length "a" and width "2c" whose internal pressure causes uniaxial hoop stresses acting to open the crack.

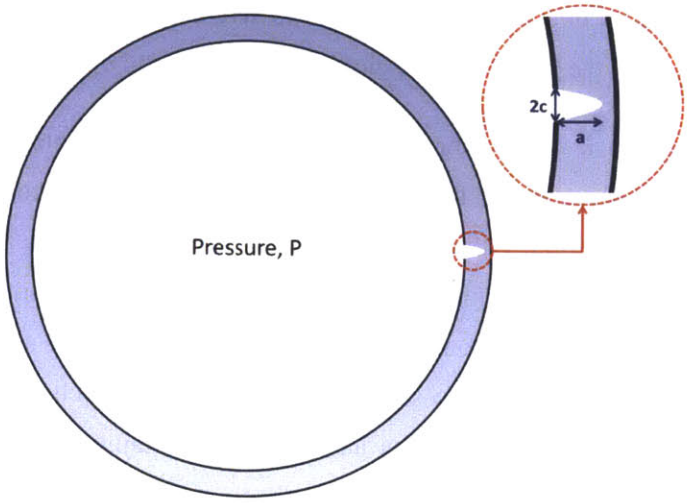

Figure 4-26 An Illustration of a Semi-elliptical Surface Crack in Cladding Thickness

The stress intensity factor for a semi-elliptical surface crack was derived by Irwin as follows (Janssen, 2002)

$$K_{\mathrm{I}}^{Hoop} = \frac{C\sigma\sqrt{\pi a}}{\phi} \tag{4-54}$$

Where K_{I}^{Hoop} is the stress intensity factor of mode I by hoop stress, σ is the average or bulk applied stress, 'a' is the length (half of the major axis of an ellipse) of the crack, C and ϕ are correction factors that capture the shape and the location effects. Raju and Newman (Janssen, 2002) produced stress intensity factor solutions of Eq.(4-54) from empirical data and found values for C as a function of the shape of the ellipse and location on the crack surface. In this study, two different shapes of semi-elliptical surface cracks named "sharp crack" and "blunt crack" were tested. The sharp crack assumes a semielliptical crack shape with the ratio a/c = 0.2 whereas the blunt crack assumes basically a semicircle shape, with the ratio a/c = 0.5. For the location information, a surface location at the end of the minor axis the crack was used, and the maximum stress intensity factor occurs at the end of the minor axis of the semi-elliptical surface crack. The resulting corrections factors were found to be C=1.851 and ϕ =1.051 for the sharp crack and C=1.355 and ϕ =1.211 for the blunt crack (Janssen, 2002).

Since the crack is in a pressurized vessel, the internal pressure (P) will also act on the crack surfaces, with a contribution to the maximum stress intensity factor of

$$K_I^P = \frac{CP\sqrt{\pi a}}{\phi} \tag{4-55}$$

Use of the superposition principle of linear elastic materials allows the total stress intensity to be obtained by simply adding all stress intensities caused by individual loads. Considering that the maximum hoop stress occurs at the inner most cladding surface,

$$\sigma_{\theta,max} = P\frac{(R_1{}^2 + R_2{}^2)}{(R_2{}^2 - R_1{}^2)} \tag{4-56}$$

Where P is the internal pressure, R_1 is cladding inner radius, and R_2 is cladding outer radius.

The maximum stress intensity factor can be obtained as follows

$$K_{I,max} = K_I^{Hoop} + K_I^P = \frac{C\sigma_{\theta,max}\sqrt{\pi a}}{\phi}\left[\frac{(R_2{}^2 - R_1{}^2)}{(R_1{}^2 + R_2{}^2)} + 1\right] \tag{4-57}$$

Applying the maximum flaw size rationale, $\sigma_{\theta,max}$ can be replaced with the threshold stress σ_u, the flaw size 'a' can be replaced with 0.8 of the cladding thickness δ, and the maximum stress intensity factor $K_{I,max}$ can be replaced by the critical stress intensity K_c.

$$K_c = \frac{C\sigma_u\sqrt{0.8\,\pi\delta}}{\phi}\left[\frac{(R_2{}^2 - R_1{}^2)}{(R_1{}^2 + R_2{}^2)} + 1\right] \tag{4-58}$$

Eq.(4-58) is then rearranged to give the following expression for the threshold stress.

$$\sigma_u = \frac{\phi K_c}{C\sqrt{0.8\,\pi\delta}\left[\frac{(R_2{}^2 - R_1{}^2)}{(R_1{}^2 + R_2{}^2)} + 1\right]} \tag{4-59}$$

Where σ_u is the threshold stress, K_c is critical stress intensity, and δ is the cladding thickness. CVD-β SiC fracture toughness was reported to vary with grain size, temperature, and irradiation – with subtle evidence of an increase with temperature and a certain degree of neutron irradiation (Snead, 2007), (Rice, 2000). Nevertheless, large scatter in these experimental results were found, which makes the trend seem inconsistent. Hence, in this study, a representative fracture toughness of non-irradiated monolithic CVD-β SiC at room temperature, 3MPa-$m^{1/2}$, was used for conservative calculations (Snead, 2007), (Snead, 2004). Threshold stress values calculated by Eq. (4-59) are compared with experimental results in Table 4-3.

Table 4-3 Minimum Fracture Stresses for Monolithic CVD SiC Tubes Under Uniaxial Hoop Stresses by Internal Pressurization*

	Tests							
	A. [Byun. et.al., 2007]	B. [Snead.et.al ., 2007]	C. [Snead, 2007]	D. [Snead.et.al ., 2007]	E. [Snead.et.al ., 2007]	F. [Carpenter.et.a l, 2010]	G. [Carpenter.et.a l, 2010]	H. [Carpenter.et.a l, 2010]
Samples	CVD, SiC	CVD, SiC	CVD, SiC Irradiated 1.9 DPA at 1019.85° C	CVD, SiC Irradiated 4.2 DPA at 1019.85° C	CVD, SiC Irradiated 4.2 DPA at 1279.85° C	CVD, SiC	CVD, SiC	CVD, SiC, Irradiated 0.66 DPA at 1279.85°C
O.D (mm)	1.08	1.22	1.22	1.22	1.22	9.75	10.29	10.54
I.D (mm)	0.89	1.02	1.02	1.02	1.02	8.79	8.79	8.79
Length (mm)	5.27	5.8	5.8	5.8	5.8	47.96	48.46	48.23
Observed Minimum Failure Stress (MPa)**	181	211	191	233	179	170	529	296
Observed Failure Probability (%)	5.5	1.6	3.0	2.3	2.1	N/A	N/A	N/A
Calculated Threshold Stress, Sharp Crack (MPa)	93	91	91	91	91	44	34	31
Calculated Threshold Stress, Blunt Crack (MPa)	146	144	144	144	144	70	53	48

* Reported stresses are the maximum hoop stresses found at the inner most tube surface
** Observed threshold stresses for A, B, C, D, and E were minimum stresses of their Weibull plots. Tests F, G, and H were single tests; the reported failure stresses are not necessarily the threshold stresses as a Weibull-distribution can't be formulated.

Note that the calculated threshold stresses in Table 4-3 are roughly 50% different for the two different crack shapes – explaining the large scatter in the observed fracture strengths. Comparisons between the observed minimum stresses and calculated stresses were made using a stress ratio parameter defined as follows

$$stress\ ratio = \frac{Observed\ Fracture\ Stress}{Calculated\ Minimum\ Fracture\ Stress} \tag{4-60}$$

According to Eq.(4-60), if the stress ratio > 1, the observed failure stress is larger than the calculated threshold stress, supporting the use of the prediction as a conservative minimum stress value. If the stress ratio <1, the calculation underestimates the minimum failure stress.

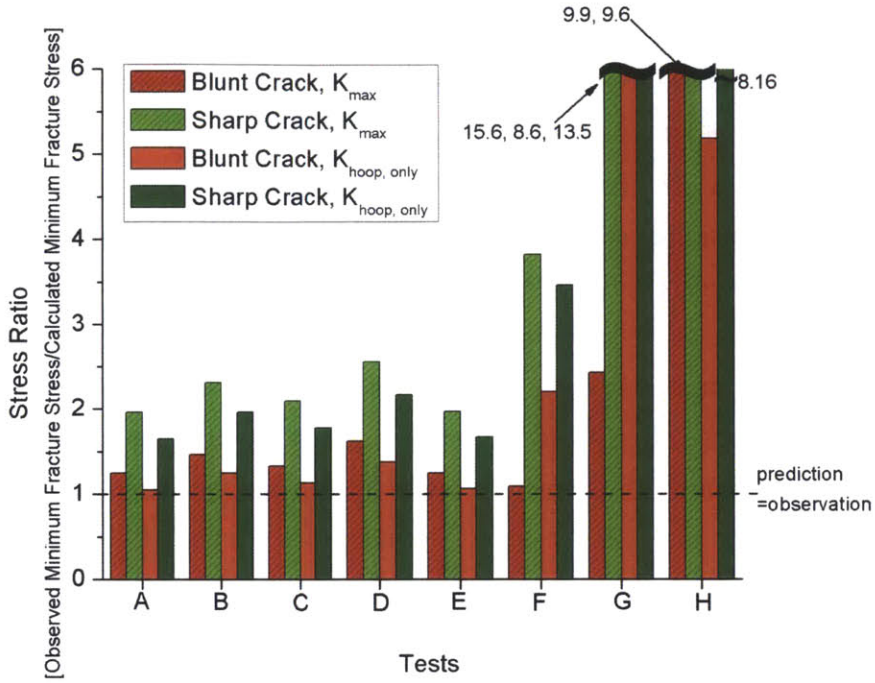

Figure 4-27 Comparisons between Observed Fracture Stress and Calculated Fracture Stresses for Eight CVD Tubular SiC Conditions

Figure 4-27 illustrates the stress ratios for the eight experiments. Care should be taken to distinguish between tests A ~ E and F ~ H. Reported failure stresses of tests A ~ E are the minimum observed fracture stresses in their Weibull plots. These minimum stresses caused failure of SiC tubes with fairly low probability ranging from 2 to 5.5 %. Experimentally observed failure stresses for tests F~H are not necessarily anywhere close to the theoretical value as they are results of single burst experiments; these stresses can be well above the minimum fracture stresses, causing failures with probabilities far greater than zero. Hence, stress ratios of tests A~E should be viewed in terms of the accuracy of the threshold stress prediction whereas stress ratios of tests F~H should be viewed in terms of checking that the failures occur at stresses above the calculated minimum values. The stress ratios shown in Figure 4-27 are exaggerated as the reported minimum failure probabilities (2~5.5%) deviate from zero. That is, the observed minimum stress values (A-E) used are those that caused failure with a finite probability - not exactly zero but 2~5.5%. This implies that the observed minimum stresses, in strict sense, are not true minimum stresses but values that are a little greater than the true minimum stresses.

The sharp crack calculations give a more conservative prediction than the blunt crack calculations, as the stress ratios of the former are greater. This is because locally concentrated stresses at the sharp crack tip are greater than those of a blunt crack tip. An ideal prediction would give a stress ratio equal or fairly close, to unity, where predicted threshold stresses equal the observed stresses. Neither of the crack geometries, sharp tip nor circular, may be the actual shape of the crack that caused the observed fractures; they act as extremes that bracket the actual random shape. Additionally, the chosen crack length 0.8 of the wall thickness acts to conservatively estimate the stress ratios. It is worth noting that none of the experiments reported in Table 4-3 were internally pressurized by a fluid. They were internally pressurized by either a polyurethane insert (A~E) or a rubberized plug (F~H). This means that for these tests, contributions of the internal pressure to the maximum stress intensity factor are practically zero, as the plug did not flow into the crack during testing. Hence, the threshold stresses calculated by only the hoop stress were found using Eq.(4-54) and shown in Figure 4-27. They give a less conservative prediction than the case that uses the maximum stress intensity factor with the superposition principle, predicting the observed threshold stresses (A~E) with higher accuracy. Like the experiments discussed, cladding service conditions with no contribution of internal pressure acting on the crack surface but only stresses caused by physical contact, such as Pellet Cladding Mechanical Interaction (PCMI), should be dealt with differently in the stress intensity factor calculations. They may not include a pressure contribution. For tensile stresses caused by internal pressurization due to fission gas, the stress intensity factor should be obtained with the superposition principle. Developing a method to more accurately predict the failure strength is not attempted in this study. This study uses the conservative failure threshold stresses found by the sharp crack calculations. The concept of the threshold stress discussed here may serve as tentative, yet somewhat speculative, additional knowledge for further development of the concept. Yet, fracture models of this study essentially treat $\sigma_u = 0$ to investigate conservative cases as a reference.

4.4.4 Weibull Parameters for Relevant SiC Fracture Modes

Although the Weibull approach is a very popular approach to capture the statistical nature of brittle fracture, it has been subject to a number of criticisms that are rooted in the lack of physical basis. Lamon stated in his work that *"The Weibull approach is pure statistics. The strength is regarded simply as a variate and handled in the same way as heuristic observations"* (Lamon, 1988). Especially, the original Weibull statistics' lack of addressing fractures by multi axial stresses has been the subject of criticisms; the original Weibull distribution model for brittle fracture shown in Eq.(4-4) is essentially a model for uniaxial stress, σ. A number of studies have been conducted to upgrade the original Weibull approach to

handle the multi axial stress effects (Petrovic, 1987), (Lamon, 1988), (Lamon, 1990), (Barnett, 1967), (Almeida, 1999), (Thiemeier, 1991), (Andreasen, 1993), (Chao, 1990).

Barnett.et.al (Barnett, 1967), Almeida.et al (Almeida, 1999), and Lamon.et.al (Lamon, 1990), presented a simple approximation to represent multiaxial effects in statistical fracture. In those approaches, the principal stresses are assumed to act independently in the tensile stress directions. As a result, the survival probability is the product of the individual survival probability for each principal direction as follows,

$$P_s(V) = exp\left[-\frac{1}{V_0}\int_V \left[\left(\frac{\sigma_i(\vec{r}) - \sigma_{u,i}}{\sigma_{0,i}}\right)^{m,i} + \left(\frac{\sigma_j(\vec{r}) - \sigma_{u,j}}{\sigma_{0,j}}\right)^{m,j} + \left(\frac{\sigma_k(\vec{r}) - \sigma_{u,k}}{\sigma_{0,k}}\right)^{m,k}\right] dV\right] \quad (4\text{-}61)$$

where the subscripts i, j, and k represent different principal stress directions. In this study, Weibull parameters (σ_0, m, and σ_u) found for uniaxial loading tests were assumed to hold for the other stress directions. With compressive radial stresses, Eq.(4-61) can now be rewritten for the SiC cladding applications as follows[22]

$$P_s(V) = exp\left[-\frac{1}{V_0}\int_V \left[\left(\frac{\sigma_\theta(\vec{r}) - \sigma_u}{\sigma_0}\right)^{m} + \left(\frac{\sigma_z(\vec{r}) - \sigma_u}{\sigma_0}\right)^{m}\right] dV\right] \quad (4\text{-}62)$$

The Weibull modulus of CVD-SiC decreases with irradiation from typical unurradiated values of 9 – 10 to 7 – 8 on average, while the material showed evidence of some degree of strengthening (Katoh, 2011). Hence, this study uses m = 7.5 as a representative Weibull modulus of irradiated CVD-SiC. However, such a reduction in Weibull modulus under irradiation exhibits a wide range of scatter depending on sample sizes and test methods (Snead, 2007). Newsome's study (Newsome, 2007) found m = 9.6 for non-irradiated CVD-SiC and 5.5 ~ 8.7 for irradiated CVD-SiC for temperature ranges from 300°C ~ 800°C. Similar results were also reported by Snead's study (Snead, 2007). The controlling mechanisms for the Weibull modulus decrease under irradiation with respect to neutron dose and the increase in strength are not yet understood. Katoh (Katoh, 2011) found that CVD-SiC Weibull modulus obtained

[22] It has been well understood that the flaw population for fracture is dependent upon the volume of the specimen as expressed in the volume term in the Weibull distribution function. Some relatively recent studies found that such well-prepared material in terms of its microstructure as CVD-SiC exhibits surface area-dependent material fracture, which is best predicted by the area-based scaling method (Byun, 2007). In the laminated cladding structures, we apply volume-based scaling for CVD-SiC for both the innermost monolith and EBC.

with miniature 3-point flexural tests are in substantially lower ranges as m=2.7~6.6 with 6.6 being the unirradiated specimen. Byun's work with miniaturized unirradiated tubular SiC specimens exhibits Weibull moduli of 5.0 and 9.7 for the same CVD-SiC material with a slight change in specimen dimensions. Such uncertainties in Weibull modulus of CVD-SiC are transferred into cladding integrity assessment in LBLOCA. Change of CVD-SiC Weibull modulus from 7.5 to 6.0 leads to a significantly different consequence of LBLOCA assessment as shown in Figure 7-35. Hence, extensive studies would be needed in the future to evaluate the Weibull modulus of the actual SiC cladding with respect to neutron dose, and temperature. Characteristic strength of 369 MPa, which was obtained by uniaxial internal pressurization test with tubular CVD-SiC specimens whose size is 1.02mm in ID, 1.22mm in OD, and 5.8mm in height after 1.9 dpa at 1020°C (Snead, 2007). CVD-SiC SiC exhibts evidence of strengthening with irradiation (Snead, 2007). Katoh.et.al (Katoh, 2011) demonstrated the insensitivity of mechanical properties of the high purity SiC and its composites to neutron irradiation to doses 30-40 dpa at temperatures 300 - 800 °C. CVD-SiC Weibull parameters used for SiC cladding modeling in LWR are summarized in Table 4-4.

Table 4-4 CVD-SiC Weibull Parameters Used for SiC Cladding Modeling

Specimen Type	Weibull modulus (m)	Weibull characteristic strength (MPa)	Specimen I.D (mm)	Specimen O.D (mm)	Specimen Length (mm)
CVD-SiC	7.5	369	1.02	1.22	5.88

Fracture of fiber-reinforced composite occurs in two stages. First, excessive elastic strain of the CVI-matrix causes significant microcracking of the matrix which is seen as an end of the proportional stress-strain behavior under tensile stresses. Before substantial microcracking of the matrix, the fibers' strength is essentially not accessed. Second, after substantial matrix microcracking, the fibers become the primary load bearing structure, undergoing elastic strain, often observed as fiber-stretching until the composite as whole reaches the ultimate stresses.

A propagating crack in CVI matrix faces strong crack-arresting mechanisms by the blocking of fibers while such a mechanical crack arresting mechanism is absent for monolithic CVD SiC. This additional crack arresting mechanism of SiC fiber composites makes cracks from a CVI matrix fracture stay local, preventing a single crack from causing a global fracture of the material. CVI matrix cracking that leads to a departure from the proportional behavior of stress-strain is essentially a dispersed fracture failure. A significant fraction of localized fractures in CVI matrix should take place in order for failure event to occur. In a global sense, the dispersed fracture failure mode is generally insensitive to size of the material (Zweben, 1970). Similar analysis holds for ultimate strength of fiber-reinforced composites as well.

Ultimate failure of the fiber composite should be seen as a dispersed fracture – significant accumulations of individual fractures should occur to cause a failure. Such dispersed fracture is a critically preferable feature of the fiber-reinforced composite material; it enables ceramic material to be used in large scales through dispersed fracture-mediated size insensitivity of strength. Yet, the strength measured on small laboratory coupons is expected to be somewhat higher than that of a larger structure (McNulty, 1997). Indeed, such a reduced size-dependent strength of fiber-reinforced composite ultimate failure by the involvement of dispersed fracture is reflected in its high Weibull modulus. Weibull parameters obtained with a cladding quality Hi-Nicalon^{TM} Type-S CVI-SiC composite (HNLS CVI) by uniaxial stress tests (Katoh, 2010) were used as a reference in this study. Table 4-5 summarizes the reference Weibull parameters for relevant fracture modes of HNLS CVI composite for LWR fuel cladding. The failure probabilities for both fracture modes are plotted in Figure 4-28.

Table 4-5 Hi-Nicalon^{TM} Type-S CVI-SiC composite (HNLS CVI) Weibull Parameters Used for SiC Cladding Modeling (Katoh, 2010)

	Weibull characteristic strength (MPa)	Weibull modulus (m)	Sample Length (mm)	Sample Width (mm)	Sample Thickness (mm)
Proportional Limit Stress	105	5	15	3	2.33
Ultimate Stress	290	17.5	15	3	2.33

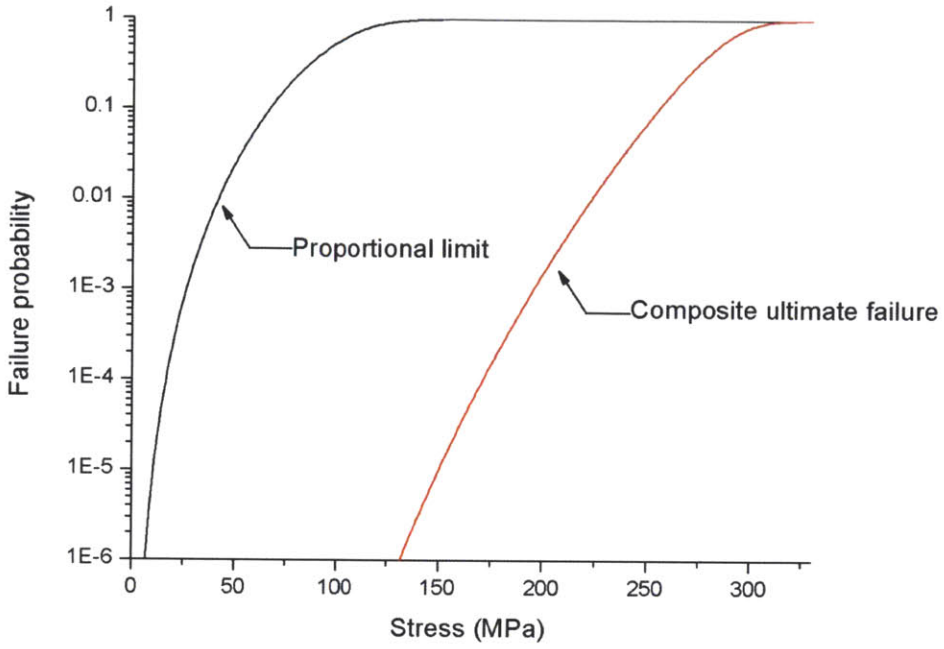

Figure 4-28 Failure Probability of HNLS CVI Composite for (1) Departure from Proportional Stress-Strain (Matrix-Micro Cracking), and (2) Failure of Load Bearing Capability (Reaching Ultimate Strength) Plotted Weibull parameters were referenced from (Katoh, 2010)

Figure 4-28 shows a few important implications for the general SiC cladding fracture behavior. First, substantial CVI micro cracking of the composite material in a considerable number of fuel rods is going to be unavoidable. Even a few tens of MPa level tensile stresses in the composite would imply a finite number of fuel rods that undergo substantial amount of CVI matrix microcracking to an extent that no more proportional behavior of stress-strain would be expected. As an example, imposing an average of ~50 MPa of tensile stresses in the composite SiC of reactor fuel rods would imply ~2% of the fuel rods in a reactor (total 50,592 fuel rods) experiencing substantial microcracking of the matrix throughout its volume. Yet, a presence of microcracking in CVI matrix would not imply fuel failure if the inner monolith is intact and fibers still function as the load bearing structure. In this regard, failure probability in terms of reaching the ultimate strength may be of primary interest in evaluating fuel rod failure rate. Note that at 100 MPa, however, most of the fuel rods in a reactor would have undergone global composite matrix cracking, which could be of particular concern for potential strength degradation of the SiC composite due to H_2O-C reaction in the presence of cracks in the EBC. High failure probability of EBC is expected predominantly a result of its monolithic behavior, whose strength degrades with increasing

material size – a characteristic not suitable for a bulk size application under tensile stresses. The inner monolith CVD-SiC, however, is significantly helped by compressive thermal stresses. The cladding design of the sole composite with 10% of EBC may seem preferable from the view point of the composite integrity as can be seen in Figure 4-17 and Figure 4-24. However, this cladding design concept that does not use the inner monolith cannot be selected because probability for the dispersed CVI matrix cracking that cannot assure desirable level of fission gas retention.

4.5 Conclusion

An important failure mode of SiC clad LWR fuel rods – fracture under tensile stresses – is investigated with a theoretical approach. A model that captures 3D stress fields in each layer in the laminated SiC cladding was developed. The stress fields resulting from pressure differences and thermal stresses were used to develop a relevant statistical fracture model for SiC cladding. In steady-state operations, positive effects of compressive thermal stresses are expected to maintain the integrity of fission-gas retaining CVD-SiC monolith. Dispersed CVI-matrix cracking is expected to prevail whose consequence causes an access of fiber strengths. EBC or CVI overcoat is also anticipated to be cracked in most of the fuel rods primarily because of excessive thermal stresses and statistically reduced strength of the large monolithic structure. An illustration of those fracture modes corresponds to case-F of Figure 4-1, which is separately shown in Figure 4-29. Given this fracture mode, investigation of H_2O ingression into a cracked EBC/CVI overcoat and through cracked CVI matrix, in terms of its effects on the composite strength, need to be conducted at some point in the future to reassess these failure probabilities of the recommended cladding designs.

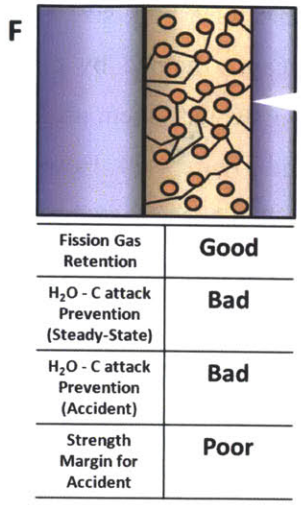

Figure 4-29 The Anticipated Prevailing SiC Cladding Fracture Mode in Steady-State Operation

Developing SiC fiber-reinforced composite with higher conductivity would benefit the integrity of the cladding significantly, as the loads arising from thermal stress are considerable fractions of the total stresses. Development of more statistically consistent Weibull parameters for both the composite and CVD-SiC, with better understanding of their size-dependent strengths in the laminated form, would significantly increase the confidence in the predictions by the statistical model of their fractures. In that regard, experimental studies on the strength failure of SiC cladding under representative operating condition are necessary at some point in the future. In addition, some modeling efforts should be made to increase precision of the current statistical approach in an extremely low failure rate regime.

This theoretical study on SiC cladding fracture, nevertheless, provides an important tool and foundation to predicting SiC cladding fracture behavior under tensile stresses in both steady-state and accident conditions. For instance, the prediction of the allowable fuel rod pressurization to meet the target tensile fuel failure rates can be readily used as a steady-state operation limit in terms of fission gas accumulation with increasing burnup. The developed models and design & operating implications discussed in this chapter will be used as an input in the following discussions of SiC cladding safety. In Chapter 7, the developed stress and statistical fracture analysis model will be coupled with fuel simulations both in steady state and in accident conditions to assess structural integrity of SiC cladding and design & operational implications. Now, some important deterministic physical mechanisms for SiC cladding brittle fracture will be addressed in the following discussions.

Chapter 5

Brittle Fracture of SiC Cladding II: Thermal Shock Experiments

5.1 Introduction

Under accident conditions, a fuel cladding may experience significant tensile stresses due to both thermal shock, and rapid depressurization of the core. In principle, SiC cladding fractures during an accident can be addressed with the statistical fracture mechanics, with temperature distributions and pressure loading ΔP across the cladding thickness imposed by the accident conditions. In that regard, the method of statistical fracture mechanics discussed in Chapter 4 can still serve as a guideline using the accident driven cladding temperature distribution $T(r,t)$, and pressure loading $\Delta P(t)$.

Yet, fracture behavior of a brittle material under a rapid thermal shock involves physical responses of the material to different conditions different from steady-state loading conditions. Understanding the response of a brittle material to rapid thermal shock would provide an additional assessment of fracture potential of the SiC cladding beyond steady-state operations.

This chapter presents and discusses an experimental investigation of the behavior of SiC, and its fracture under rapid thermal shock conditions relevant to the reflood phases of a LOCA. This exploration will expandd our understanding of SiC cladding fractures beyond steady-state operating conditions.

5.2 Quenching Experiment Procedure

5.2.1 Experiment Facility

An experimental facility was modified to bring specimens up to 1500°C and translate them into a pool of water, as illustrated in Figure 5-1. Specimens were suspended in air inside a quartz tube located at the center of the furnace. A K-type thermocouple wire connected to an air-pressure driven alumina rod was used to hold the specimen. By employing bottom-flooding with tubular samples, this experiment was designed to demonstrate similar experimental designs/conditions that were used to establish the current Zr cladding safety criteria given in 10 CFR 50.46 (Hobson, 1972), (Chung, 2005). A B-type thermocouple

read the temperature adjacent to the outer surface of the quartz tube, where the specimen is located. The temperature reading was recorded by a data acquisition system (DAS). Temperature calibrations were made with tubular α-SiC between this B-type thermocouple reading and the temperature obtained by a thermocouple attached to the sample's surface. Comparing these two temperatures, an empirical relation between the furnace temperature and the true sample surface temperature was established and used to report SiC specimen temperatures. The temperature calibration results are shown in Figure 5-2. Specimens were suspended inside the furnace until they reached a constant temperature. Then, specimens were quickly dropped into either a room temperature water pool (~22°C) or a saturated water (~100°C) pool by the air-pressure driven rod. A high speed video camera was used to record the quenching of the specimens. Recorded quenching videos were used to analyze transient boiling states for later application in modeling. Experiments with alumina were also conducted, to expand the validation of the model that will be used to predict failure.

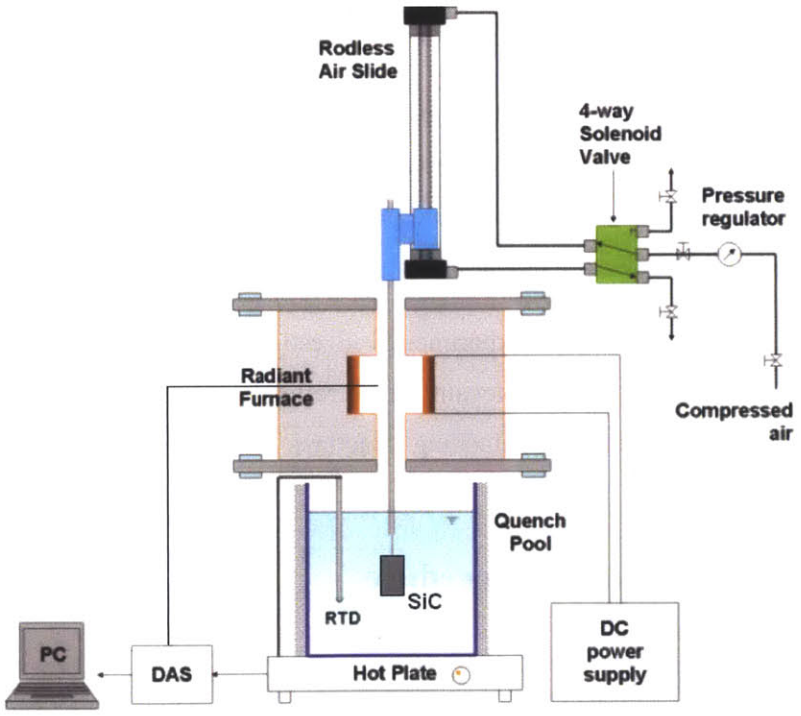

Figure 5-1 SiC Quenching Experiment Facility (DAS: Data Acquisition System, and RTD: Resistance Temperature Detector)

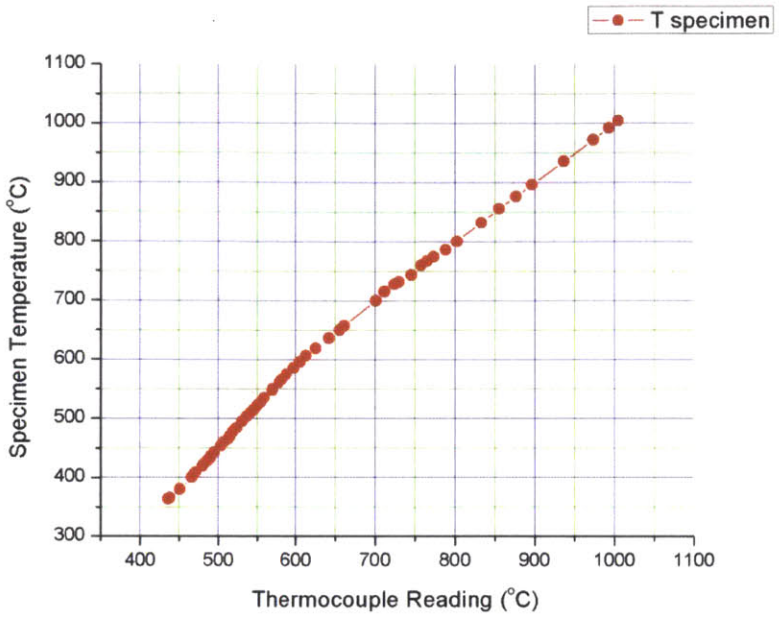

Figure 5-2 Relationship between the SiC specimen temperature and B-type thermocouple reading attached to DAS (Data Acquisition System)

Post the quenching processes, specimens went through visual examination, SEM analysis, and destructive strength measurements, selectively. For the destructive strength measurements, tubular α-SiC specimens were burst by internal pressurization tests with a polyurethane plug insert, as described in section 2.5.3. Unlike the oxidized specimens, quenched tubular α-SiC specimens did not have drilled holes on their surface. The strength of the bar shape CVD-SiC and alumina were measured with 4-point flexural tests described by ASTM C1161, 'Standard Test Method for Flexural Strength of Advanced Ceramics at Ambient Temperature' as shown in Figure 5-3.

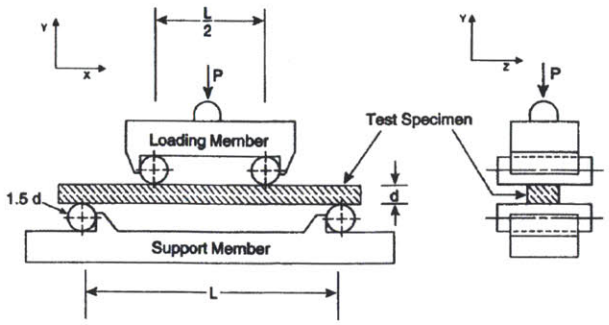

Figure 5-3 Schematic of Flexural Test with Four Point Bending Fixture (Figure from ASTM C1161)

A self-articulating 4 point bend test fixture (model number: G238XW4P) was obtained from TEST RESOURCES (Shakopee, MN) and was loaded with an Instron machine driven by a hydraulic pump, as shown in Figure 5-4.

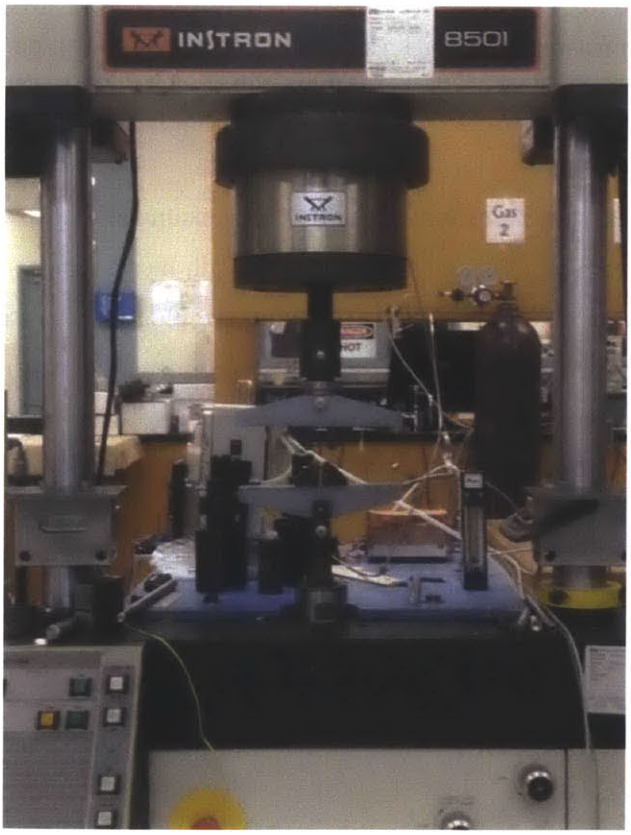

Figure 5-4 Four Point Flexural Test

5.2.2 Tested Materials

The materials used in this experimental study included (1) monolithic tubular pressure-less-sintered α-SiC, (2) CVD β-SiC, and (3) high temperature alumina. The alumina specimens were tested to generalize/and validate our understanding of thermal shock induced ceramic brittle fracture initially found with SiC specimens. The tubular α-SiC was directly obtained from Saint-Gobain; its density was 3.05g/cc, and its trade name is SE type Hexoloy. The Saint-Gobain samples had dimensions of 14.0mm OD, thickness of 1.56mm, and height of 13.0 mm. High purity CVD β-SiCs were obtained from Bomass (Somerville, MA). Its density is 3.21g/cc and is in a bar shape of the standard ASTM C 1161 size: 25mm (l) x 2mm (w) x 1.5mm (t). The alumina specimens were obtained from McMaster-Carr and the name of the product is 'Very High Temperature Nonporous High-Alumina Ceramic' whose density is 3.875g/cc. Two different dimensions were tested for the alumina specimens: 30mm (l) x 6.35 mm (w) x 6.35 mm (t), and 30mm (l) x 3.175mm (w) x 3.175 (t). Appropriate extrapolations of temperature dependent material properties were made by referring to relevant studies when necessary. The tubular α-SiC and alumina specimens were cut from a longer material to the prescribed specimen length. The cut surfaces were polished with 70μm, and 30μm diamond wheels successively to ensure no material strength degradation by additional surface flaws that might be introduced in the cutting process. Samples were ultrasonically cleaned with detergent added to water, deionized (DI) water, acetone, and methanol prior to furnace exposures.

Several tubular α-SiC were pre-cracked in their outer surface in the axial direction with a diamond cutting saw to investigate effects of macroscopic surface flaws on the brittle fracture behavior. The size of manually introduced cracks range from 200 μm to 1000 μm in their lengths and widths. Most of the specimens had a single flaw while a few had several over the entire surface area. Detailed descriptions of sizes and shapes of pre-introduced cracks are discussed in the following prediction, along with SEM analysis.

5.3 Test Matrices and Experimental Results

This section presents summarized test matrices and results of material's strength and visual examinations for each tested material type. Results of SEM analysis are presented in later sections.

5.3.1 Summary of Test Matrix and Results: Tubular α-SiC

Tubular α-SiC specimens in the temperature range from 350°C to 1265°C were quenched into either room temperature or saturated water. Three different types of pre-introduced flaws – single axial crack, multiple cracks over the entire specimen surfaces, and single axial crack through the entire specimen thickness-

were tested with specimen temperature at either 1230°C, or 1040°C quenched in room temperature water. Table 5-1 summarizes the test matrix and results for the tubular α-SiC quenching experiments.

Table 5-1 Thermal Shock Experiment Test Matrix and Key Results of Tubular α-SiC

Sample Number	Sample Temperature (°C)	Water Temperature (°C)	Specimen Fracture Hoop Stress (MPa)	Key visual charateristics	Comments
SiC α-B, 1	-	-	185.3	Cracks tend to run axially upon fracture	As-received SiC, average fracture hoop stress of 181.2 MPa
SiC α-B, 2			167.1		
SiC α-B, 3			216.0		
SiC α-B, 4			182.1		
SiC α-B, 5			172.4		
SiC α-B, 6			147.5		
SiC α-B, 7			188.5		
SiC α-B, 8			166.8		
SiC α-B, 9			165.0		
SiC α-B, 10			218.2		
SiC α-Q, 1	1170 ± 20 °C	22°C	-	Shattered	-
SiC α-Q, 2			-	Shattered	-
SiC α-Q, 3			-	Survived with visible cracks on the surface	-
SiC α-Q, 4			-	Shattered	-
SiC α-Q, 5			-	Shattered	-
SiC α-Q, 6			-	Shattered	-
SiC α-Q, 7			-	Shattered	-
SiC α-Q, 8			-	Shattered	-
SiC α-Q, 9	1033 ± 5 °C	22°C	-	Shattered	-
SiC α-Q, 10			-	Shattered	-
SiC α-Q, 11	900 ± 5 °C	22°C	-	Shattered, broken pieces in the bottom	-
SiC α-Q, 12			-	Survived with large axial cracks on the surface	-
SiC α-Q, 13			-	Shattered, large axial cracks on the surface, small fractured pieces at the bottom	-

SiC α-Q, 14			-	Shattered , large axial cracks on the surface, small fractured pieces at the bottom	-
SiC α-Q, 15			-	Survived with large axial cracks on the surface	-
SiC α-Q, 16			-	Survived with large axial cracks on the surface	-
SiC α-Q, 17			-	Survived with large axial cracks on the surface	-
SiC α-Q, 18	795 ± 5 °C	22°C	14.5	Survived with visible cracks	-
SiC α-Q, 19			15.9	Survived	-
SiC α-Q, 20			-	Shattered	-
SiC α-Q, 21			10.4	Survived	-
SiC α-Q, 22	700 ± 5 °C	22°C	8.3	Survived	-
SiC α-Q, 23			-	Survived	-
SiC α-Q, 24			14.6	Survived	-
SiC α-Q, 25			-	Survived	-
SiC α-Q, 26	600 ± 15 °C	22°C	-	Survived	-
SiC α-Q, 27			-	Survived with small visible cracks	-
SiC α-Q, 28			-	Survived with small visible cracks	-
SiC α-Q, 29			-	Survived	-
SiC α-Q, 30			-	Survived	-
SiC α-Q, 31			-	Survived	-
SiC α-Q, 32			-	Survived	-
SiC α-Q, 33			7.8	Survived	-
SiC α-Q, 34			7.8	Survived	-
SiC α-Q, 35			-	Survived	-
SiC α-Q, 36	550 ± 5 °C	22°C	-	Survived	-
SiC α-Q, 37			9.6	Survived	-
SiC α-Q, 38			9.7	Survived	-
SiC α-Q, 39	500 ± 5 °C	22°C	-	Survived	-
SiC α-Q, 40			67.5	Survived	-
SiC α-Q, 41			15.1	Survived	-

SiC α-Q, 42	450 ± 5 °C	22°C	12.9	Survived	-
SiC α-Q, 43			-	Survived	-
SiC α-Q, 44			9.0	Survived	-
SiC α-Q, 45	400 ± 5 °C	22°C	-	Survived	-
SiC α-Q, 46			16.3	Survived	-
SiC α-Q, 47			-	Survived	-
SiC α-Q, 48			13.3	Survived	-
SiC α-Q, 49	350 ± 5 °C	22°C	17.1	Survived	-
SiC α-Q, 50			178.0	Survived	-
SiC α-Q, 51			137.8	Survived	-
SiC α-Q, 52			-	Survived	-
SiC α-Q, 53	350 ± 5 °C	100 °C	235.6	Survived	-
SiC α-Q, 54			191.6	Survived	-
SiC α-Q, 55			169.9	Survived	-
SiC α-Q, 56			-	Survived	-
SiC α-Q, 57			-	Survived	-
SiC α-Q, 58	400 ± 5 °C	100 °C	189.1	Survived	-
SiC α-Q, 59			-	Survived	-
SiC α-Q, 60			200.5	Survived	-
SiC α-Q, 61			190.2	Survived	-
SiC α-Q, 62			-	Survived	-
SiC α-Q, 63	450 ± 5 °C	100 °C	144.0	Survived	-
SiC α-Q, 64			200.3	Survived	-
SiC α-Q, 65			-	Survived	-
SiC α-Q, 66	500 ± 5 °C	100 °C	-	Survived	-
SiC α-Q, 67			156.1	Survived	-
SiC α-Q, 68			156.9	Survived	-
SiC α-Q, 69	600 ± 5 °C	100 °C	173.4	Survived	-
SiC α-Q, 70			189.8	Survived	-
SiC α-Q, 71			-	Survived	-
SiC α-Q, 72	800 ± 5 °C	100 °C	167.7	Survived	-
SiC α-Q, 73			187.7	Survived	-
SiC α-Q, 74			-	Survived	-

SiC α-Q, 75	1000 ± 5 °C	100 °C	149.4	Survived	-
SiC α-Q, 76			177.2	Survived	-
SiC α-Q, 77			-	Survived	-
SiC α-Q, 78	1265 ± 5 °C	100 °C	206.13	Survived	-
SiC α-Q, 79			172.3	Survived	-
SiC α-Q, 80			151.9	Survived	-
SiC α-Q pc, 1	1040 ± 10 °C	22 °C	-	Survived	Single Pre-crack ~500μm
SiC α-Q pc, 2			-	Survived	Single Pre-crack ~500μm
SiC α-Q pc, 3			-	Survived	Single Pre-crack ~200μm
SiC α-Q pc, 4	1230± 10 °C	22 °C	-	Shattered	Single Pre-crack ~250μm
SiC α-Q pc, 5			-	Shattered	Single Pre-crack ~600μm
SiC α-Q pc, 6			-	Survived	Single Pre-crack ~500μm
SiC α-Q pc, 7			-	Shattered	Single Pre-crack ~250μm
SiC α-Q pc, 8			-	Shattered	Single Pre-crack ~500μm
SiC α-Q pc, 9			-	Survived	Single Pre-crack ~900μm
SiC α-Q pc, 10	1040 ± 10 °C	22 °C	-	Shattered	Multiple Cracks of Sizes 200~1000 μm Over the entire sample surface
SiC α-Q pc, 11			-	Shattered	Multiple Cracks of Sizes 200~1000 μm Over the entire sample surface
SiC α-Q pc, 12			-	Survived	Multiple Cracks of Sizes 200~1000 μm Over the entire sample surface, and fractured top portion of the tube
SiC α-Q pc, 13			-	Shattered	Single Axial Crack through the Entire Thickness
SiC α-Q pc, 14			-	Shattered	Single Axial Crack through the Entire Thickness

5.3.2 Summary of Test Matrix and Results: ASTM C1161 Standard CVD-SiC

CVD-SiC specimens in temperature range from 500°C to 1260°C were quenched into either room temperature or saturated water. Table 5-2 summarizes the test matrix and results for the CVD-SiC quenching experiments.

Table 5-2 Thermal Shock Experiment Test Matrix and Key Results of CVD-SiC

Sample Number	Sample Temperature (°C)	Water Temperature (°C)	Flexural Strength (MPa)	Key visual characteristics	Comments
SiC β-B, 1	-	-	676.4	-	As-received SiC
SiC β-B, 2			746.7	-	
SiC β-Q, 1	1250 ± 15 °C	22 °C	861.7	No visible crack, specimen colorized to blue	-
SiC β-Q, 2			195.1	No visible crack, specimen colorized to blue	-
SiC β-Q, 3			855.9	survived	-
SiC β-Q, 4	1110 ± 5 °C	22 °C	610.4	survived	-
SiC β-Q, 5			1124.5	survived	-
SiC β-Q, 6	800 ± 5 °C	22 °C	806.7	survived	-
SiC β-Q, 7			948.0	survived	-
SiC β-Q, 8	500 ± 5 °C	22 °C	571.7	survived	-
SiC β-Q, 9			740.1	survived	-
SiC β-Q, 10	500 ± 5 °C	100 °C	880.3	survived	-
SiC β-Q, 11			750.8	survived	-
SiC β-Q, 12	800 ± 5 °C	100 °C	994.0	survived	-
SiC β-Q, 13			1052.7	survived	-
SiC β-Q, 14	1130 ± 5 °C	100 °C	974.9	survived	-
SiC β-Q, 15	1260 ± 5 °C	100 °C	976.3	survived	-
SiC β-Q, 16			791.2	survived	-
SiC β-Q, 17			945.3	survived	-

5.3.3 Summary of Test Matrix and Results: Al_2O_3 Size-1 - 30mm (l) x 3.175mm (w) x 3.175 (t).

Al_2O_3 size-1 is the smaller of the two tested non-porous alumina types. For this material, specimens in temperature range from 500°C to 1260°C were quenched into either room temperature or saturated water. Table 5-3 summarizes the test matrix and results for the Al_2O_3 size-1 quenching experiments.

Table 5-3 Thermal Shock Experiment Test Matrix and Key Results of CVD-SiC

Sample Number	Sample Temperature (°C)	Water Temperature (°C)	Flexural Strength (MPa)	Key visual characteristics	Comments
Al_2O_3 S1-B, 1	-	-	437.8	-	As-received Al_2O_3
Al_2O_3 S1-B, 2			390.2	-	
Al_2O_3 S1-Q, 1	1110 ± 5 °C	22 °C	63.9	survived with many visible cracks on the surface	-
Al_2O_3 S1-Q, 2			79.1	survived with many visible cracks on the surface	-
Al_2O_3 S1-Q, 3	800 ± 5 °C	22 °C	93.0	-	-
Al_2O_3 S1-Q, 4			106.8	-	-
Al_2O_3 S1-Q, 5	500 ± 5 °C	22 °C	150.1	-	-
Al_2O_3 S1-Q, 6			157.3	-	-
Al_2O_3 S1-Q, 7	500 ± 5 °C	100 °C	408.4	-	-
Al_2O_3 S1-Q, 8	800 ± 5 °C	100 °C	335.5	-	-
Al_2O_3 S1-Q, 9			401.2	-	-
Al_2O_3 S1-Q, 10	1110 ± 5 °C	100 °C	391.5	-	-
Al_2O_3 S1-Q, 11			387.4	-	-
Al_2O_3 S1-Q, 12	1260 ± 5 °C	100 °C	435.3	-	-
Al_2O_3 S1-Q, 13			438.7	-	-

5.3.4 Summary of Test Matrix and Results: Al_2O_3 Size-2 - 30mm (l) x 6.35 mm (w) x 6.35 mm (t)

Al_2O_3 size-2 is the bigger of the two tested non-porous alumina types. For this material, specimens in the temperature range from 500°C to 1260°C were quenched into either room temperature or saturated water. Table 5-2 summarizes the test matrix and results for the Al_2O_3 size-2 quenching experiments.

Sample Number	Sample Temperature (°C)	Water Temperature (°C)	Flexural Strength (MPa)	Key visual characteristics	Comments
Al_2O_3 S2-B, 1	-	-	375.5	-	As-received Al_2O_3
Al_2O_3 S2-B, 2			375.0	-	
Al_2O_3 S2-Q, 1	1110 ± 5 °C	22°C	-	Shattered	-
Al_2O_3 S2-Q, 2			37.9	survived with many visible cracks on the surface	-
Al_2O_3 S2-Q, 3	800 ± 5 °C	22°C	68.0	survived with visible cracks	-
Al_2O_3 S2-Q, 4			70.8	survived with visible cracks	-
Al_2O_3 S2-Q, 5	500 ± 5 °C	22°C	111.7	-	-
Al_2O_3 S2-Q, 6			118.4	-	-
Al_2O_3 S2-Q, 7	500 ± 5 °C	100°C	96.7	-	-
Al_2O_3 S2-Q, 8			66.1	-	-
Al_2O_3 S2-Q, 9	800 ± 5 °C	100°C	149.6	-	-
Al_2O_3 S2-Q, 10			79.0	-	-
Al_2O_3 S2-Q, 11	1110 ± 5 °C	100°C	118.4	survived with visible cracks	-
Al_2O_3 S2-Q, 12			366.2	survived with no visible cracks	-
Al_2O_3 S2-Q, 13	1260 ± 5 °C	100°C	133.6	survived with visible cracks	-
Al_2O_3 S2-Q, 14			150.7	survived with visible cracks	-

5.4 Key Experimental Observations

5.4.1 Effects of Subcooling on Brittle Fracture

Figure 5-5 and Figure 5-6 show the sample strength as a function of quenching temperature and subcooling (room temperature water, 22°C or saturated water 100°C) for tubular α-SiC and bar-shape CVD-SiC. The first point in the graphs shows the original strength of the material. For those α-SiC samples that were quenched in room temperature water, substantial strength degradation was observed. The strength degradation starts at around 350°C as far as the conducted test matrix can discern and samples even shattered into pieces upon quenching at temperatures beyond 900°C. In saturated water, however, the material strength was retained up to the highest temperature tested. This difference in materials' critical temperature implies that there a difference in the fracture mechanism beyond the water bath temperature difference that the material experiences.

The same trend was observed with CVD-SiC while demonstrating an enhanced thermal shock tolerance up to 1250°C even in room temperature water, as shown in Figure 5-6. 1250°C may be regarded as the critical temperature for CVD-SiC in room temperature water specific to the sample size as tested specimens exhibit marked scatter in material strengths ranging from the intrinsic strength to the typical strength of a fractured specimen. Quenched CVD-SiC specimens tended to yield higher material strength (up to 20 ~ 30% increase) than the as-received materials. This may be a result of surface crack-blunting with SiO_2 scale formation in air (Kim, 1990), (Easler, 1981) given that surface cracks are primarily responsible for CVD-SiC fracture under tension (Snead, 2007), (Byun, 2007). Also, residual stressess in the material accumulated in the CVD process might have been relieved.

Finding the critical temperature difference between a quenched sample and water where brittle ceramics start exhibiting strength degradation upon quenching has been extensively studied. Wang and Singh' work (Wang, 1994) shows critical temperature difference of 495K, and 280K for hotpressed SiC and, pressure less sintered SiC, respectively. Also his study found that the critical temperature difference for CVD SiC is higher than 1010K. Those tests used 4 x 5 x 45 mm bar specimens.

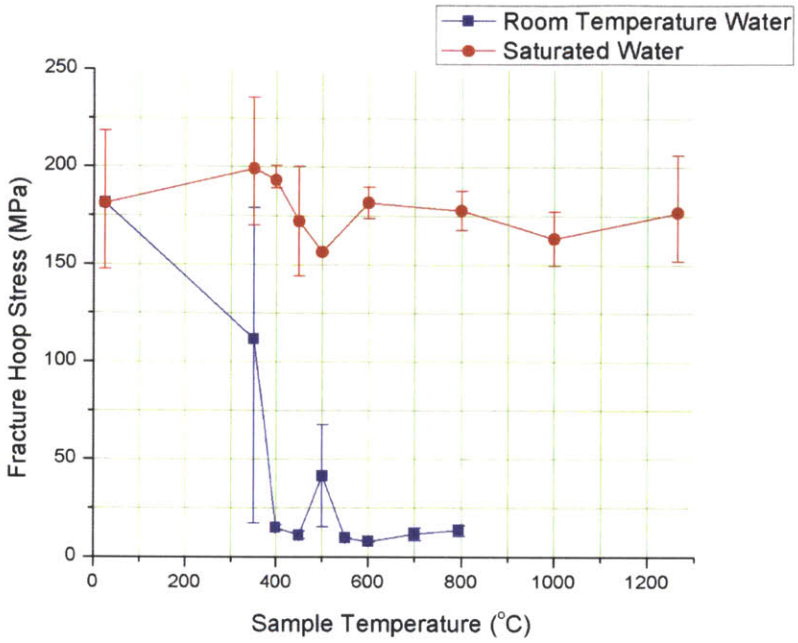

Figure 5-5 Fracture Hoop Stress of α-SiC (14.0mm OD, thickness of 1.56mm, and height of 13.0mm) as a Function of Quenching Temperature and Subcooling

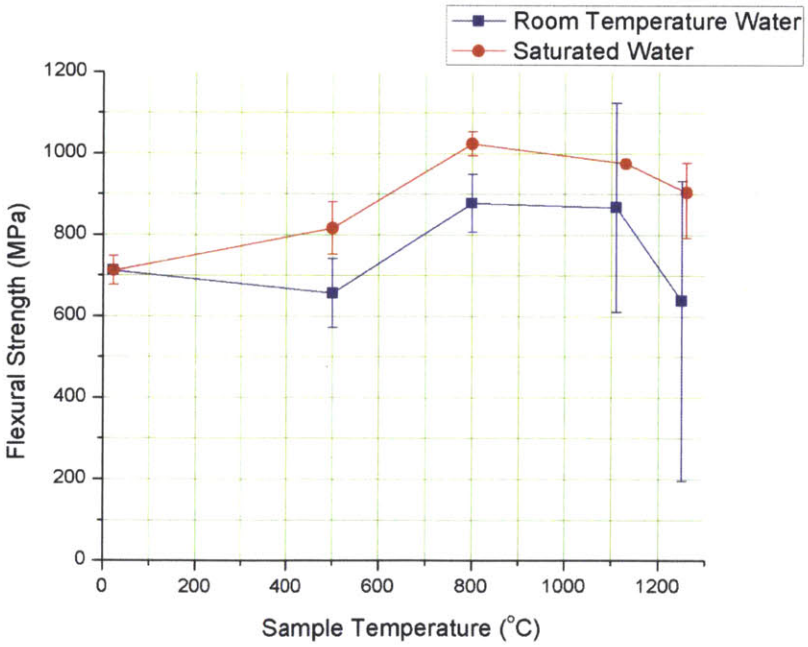

Figure 5-6 Flexural Strength of CVD-SiC (25mm (l) x 2.0mm (w) x 1.5mm (t)) as a Function of Quenching Temperature and Subcooling

Figure 5-7 shows similar strength retention of Al_2O_3 Size-1 (30mm (l) x 3.175mm (w) x 3.175mm (t)) in saturated water. Al_2O_3 Size-2 (30mm (l) x 6.35mm (w) x 6.35mm (t)), however, does not generally exhibit strength retention in saturated water, as shown in Figure 5-8. Indeed, strength retention of SiC in saturated water was observed by several past studies as an increased critical temperature difference. Becher and Warwick found sharply decreasing strength retention effect in saturated water with increasing sample thickness of Al_2O_3 (Becher, 1993). Their study found that the strength retention effect is basically eliminated in saturated water, resulting in the same critical temperature difference with room temperature water if the thickness of Al_2O_3 is greater than ~2mm. Also the study found that the critical temperature difference generally decreases linearly with sample thickness, and after a certain thickness the critical temperature differnence exhibits a modest decrease with sample size.

A handy physical parameter that has been extensively used to explain the size, and the subcooling, dependence of brittle fracture is the Biot number ($Bi = \frac{hL_c}{k}$). Appearing in transient energy equations, the Biot number essentially determines the temperature gradient inside a solid material relative to the temperature drop between the solid surface and the fluid (Incropera, 2007). The smaller the Biot number gets, the lesser the resistance to conduction within a solid body in comparison with the resistnace to convection, resulting in a flatter temperature gradient, which leads to a lower level of thermal stresses. Effects of subcooling on brittle fracture have been understood in terms of their effect on the heat transfer coefficient h in the Biot number (Becher, 1993), (Lu, 1998). Becher and Warwick state the following in consideration of the Biot number (Becher, 1993),

"Increasing the thermal conductivity of the ceramic (or decreasing the surface heat transfer of quenching media) will produce such results. Changes in thermal conductivity k can be brought about by modifications in composition and phases present when tailoring ceramics and composites. When nucleant boiling occurs at the surface if a hot specimen quenched in a room temperature bath, the surfcae heat transfer coefficient can increase by 2 to 4 orders of magnitude. If the water in contact with the specimen reaches temperatures above the boiling point, the heat transfer coefficent decreases (again by a factor of 100 to 10,000) and then rises slowly with further increase in temperature. However, when quenched into a deep water bath, the water in contact with the sample remains at a near constant condition of nucleant boiling until most of the heat is extracted from the sample and h remains very high. Use of a boiling water quench bath results in a lower h value and a decrease in its temperature dependence..."

The size of a material also has an impact on stress levels in a material; according to the Biot number definition, the heat transfer coecfficient h, characteristic solid length L_c, and conductivity k have an equal importance on stress gradients. This may explain the strength degradation of Al_2O_3 Size-2 in saturated

water; the material experienced sharper temperature gradient, hence higher stress levels, under the same saturated water quenching environment.

Yet, this general Biot number explanation may be too simple to capture the detailed mechanisms of heat transfer origin for brittle fracture. That is, the heat transfer coefficients on a solid body varies very rapidly upon quenching, imposing different levels of stresses during a short transient of time. In that sense, the heat transfer origin of a brittle fracture may be appropriately addressed with detailed understanding of transient heat transfer modes. With this enhanced understanding of transient heat tranfer modes, the brittle fracture of a solid material upon quenching can be addressed in terms of presence of a critical pre-exisitng flaw that is allowed to reach critical stress intensity with a rapidly varying heat transfer coefficient h(t). Quantitative investigations to explore the heat transfer origin of brittle fracture with recorded heat transfer modes are discussed in detail in chapter 6.

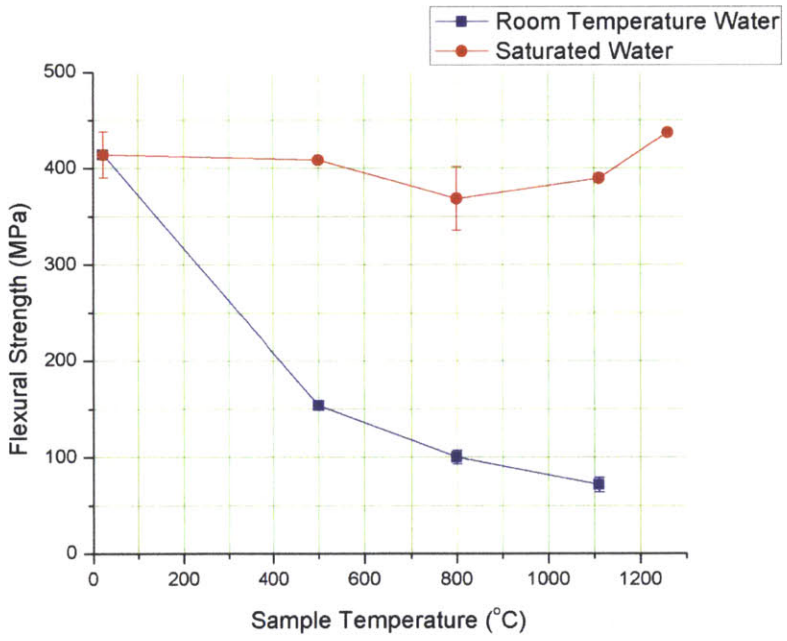

Figure 5-7 Flexural Strength of Al_2O_3 Size-1 (30mm (l) x 3.175mm (w) x 3.175mm (t)) as a Function of Quenching Temperature and Subcooling

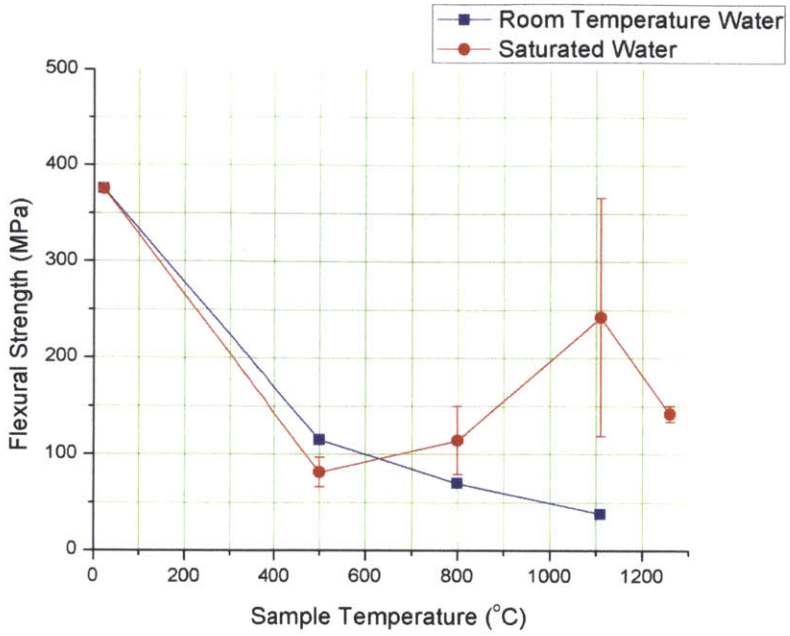

Figure 5-8 Flexural Strength of Al_2O_3 Size-2 (30mm (l) x 6.35mm (w) x 6.35mm (t)) as a Function of Quenching Temperature and Subcooling

As discussed, strength retention of brittle material in saturated quenching condition may yield important safety implications for LWR SiC cladding during accidents. The injected water in the LWR core during a LOCA is close to saturation when quenching fuel rods. This would significantly reduce cladding thermal stress level upon quenching during the reflood phase. Also, in case of severe accidents, injection of 'hot' water would be considered better than 'cold' water for cladding integrity.

5.4.2 Microstructural Analysis of Brittle Fractures

Formation of propagating cracks is responsible for the observed strength degradation. Formation of a single crack can significantly reduce the brittle material's strength. That is, a material's strength after quenching can be viewed in a binary manner in terms of a presence of a fracturing crack.

Fractured surfaces of shattered samples showed that cracks propagate through grains (transgranular fracture), Figure 5-9. Transgranular crack propagation was commonly observed for all cracked samples as illustrated in Figure 5-10. Transgranular fracture explains the fairly straight looking cracks with smooth edges, which are different from the faceted fracture surfaces resulting from intergranular fracture. To enhance fracture toughness, intergranular rather than transgranular fracture needs to be promoted.

Transgranular fracture cracks take a straight path through grains, whereas intergranular cracks do not enter grains and instead travel along the grain boundaries. This allows the branching of the crack through interlocking grains, enhancing overall toughness (Kueck, 2008).

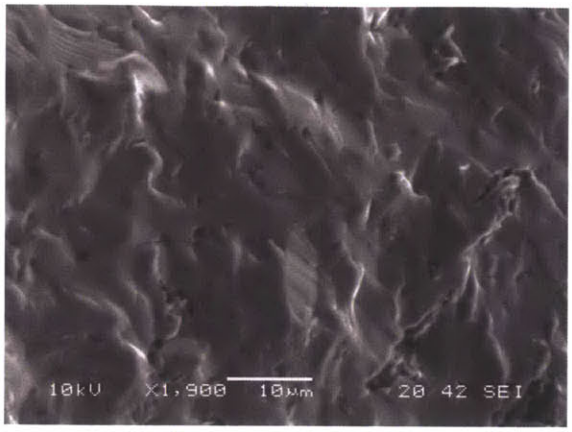

Figure 5-9 SEM Image of Transgranular Fractured Surface of a Quenched α-SiC Specimen (T=1030°C)

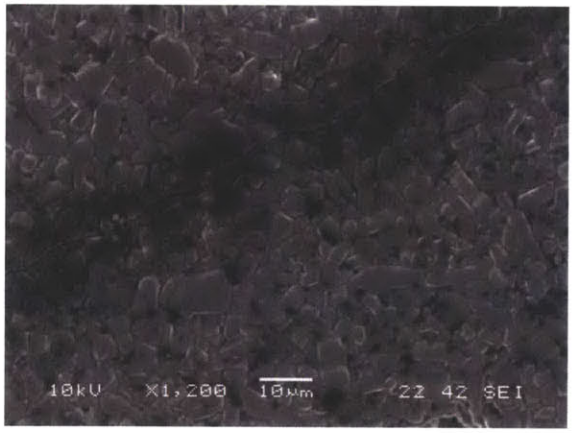

Figure 5-10 SEM Image of Transgranular Crack of a Quenched α-SiC Specimen (T=500°C)

Once formed, cracks tend to run axially and radially across the entire thickness of tubular specimens. This indicates that hoop stress is the dominant stress direction of mode I fracture that opens up the crack. Crack growth exhibited different behavior for different quenching temperatures. Higher quenching temperatures caused wider crack width as shown in Figure 5-11. Cracks that were formed from 900°C are about 25 µm wide while those from 450°C were less than 5µm. Temperature gradients inside a quenched material are steeper when quenching from higher temperatures due to the initial temperature difference. Steeper temperature gradients lead to a greater thermal expansion mismatch inside a material, causing

higher stress levels. Higher stress levels are energetically more favorable for crack propagation and a material accommodates higher strain energy release rate by creating larger cracks. Cracks exhibited a tendency to be linked up at pores as shown in Figure 5-12. This explains that pores – sites of void where no elastic potential energy can be accommodated – are energetically favorable for crack propagation. Some propagating cracks were observed to branch into multiple cracks as shown in Figure 5-13. Crack branching helps releasing elastic-strain energy by increasing fractured surface area per unit crack propagtion distance.

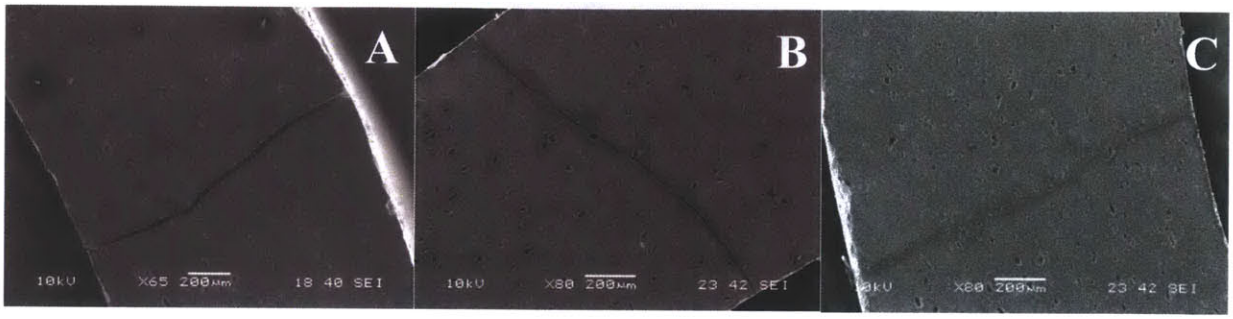

Figure 5-11 Typical Crack Formations after Quenching of α-SiC: A-900°C, B-600 °C, and C-450°C

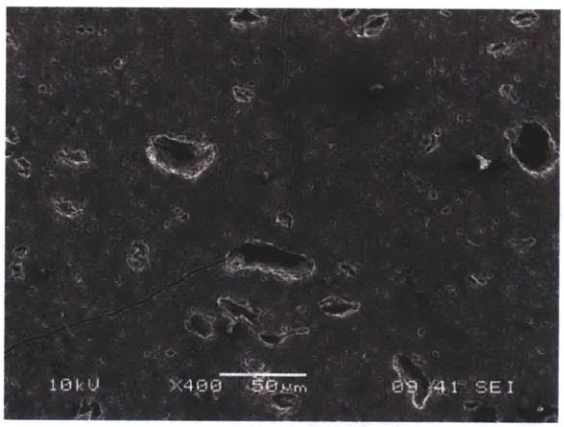

Figure 5-12 Typical Crack Branching of Quenched α-SiC (T=450°C)

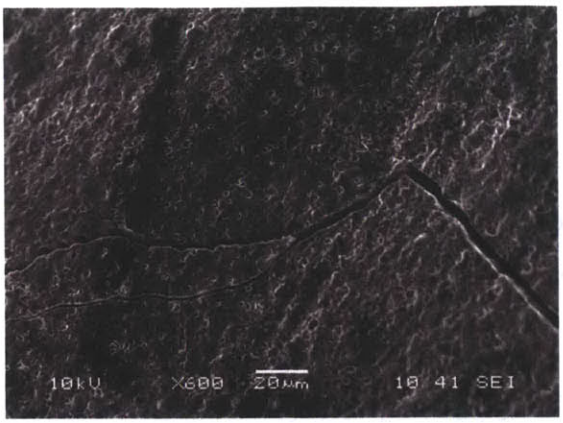

Figure 5-13 Typical Crack Branching of Quenched α-SiC (T=1170°C)

No visually discernible crack was observed with β-SiCs in the SEM analysis as all of the tested β-SiC in the test conditions did not exhibit noticeable strength degradation except for one. Some local surface morphology changes were observed in a few spots on quenched β-SiC in Figure 5-14. Further investigations are needed to explain the physical origin of the observed surface morphology changes. This may be due to possible chemical reactions with the furnace exposure in air.

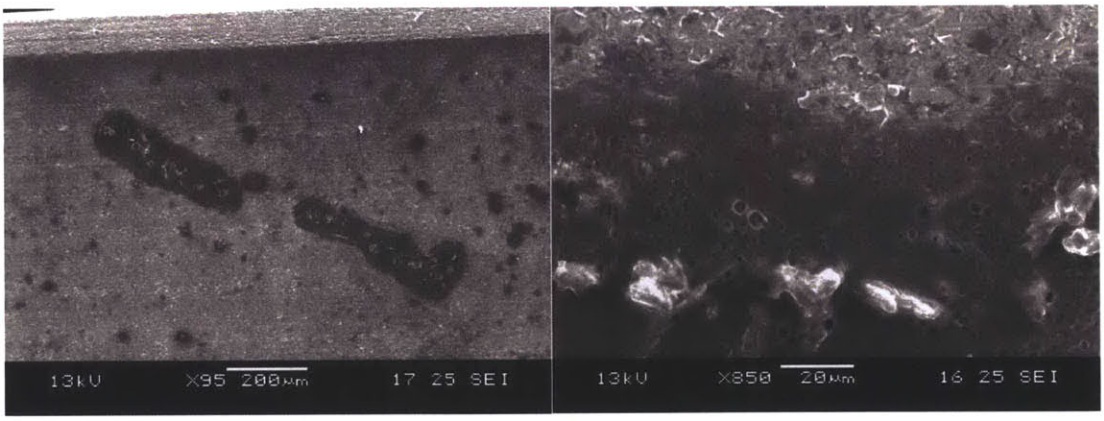

Figure 5-14 Surface Morphologies of Quenched β-SiC (T=1110°C)

Surface morphologies of as-received and quenched Al_2O_3 are shown in Figure 5-15. The crack propagation characteristic for Al_2O_3 is somewhat mixed between transgranular and intergranular. Figure 5-15 C clearly shows the deflective nature of crack propagation along the grain boundaries for Al_2O_3. There was a tendency to observe larger cracks on the thicker Al_2O_3 specimen [Al_2O_3 S2 - 30mm (l) x 6.35 mm (w) x 6.35 mm (t)] than the thinner specimen [Al_2O_3 S1 - 30mm (l) x 6.35 mm (w) x 6.35 mm (t)]

under the same quenching conditions. This is due to generally higher thermal stress levels in the bigger specimen according to the Biot number explanation for steeper temperature gradient.

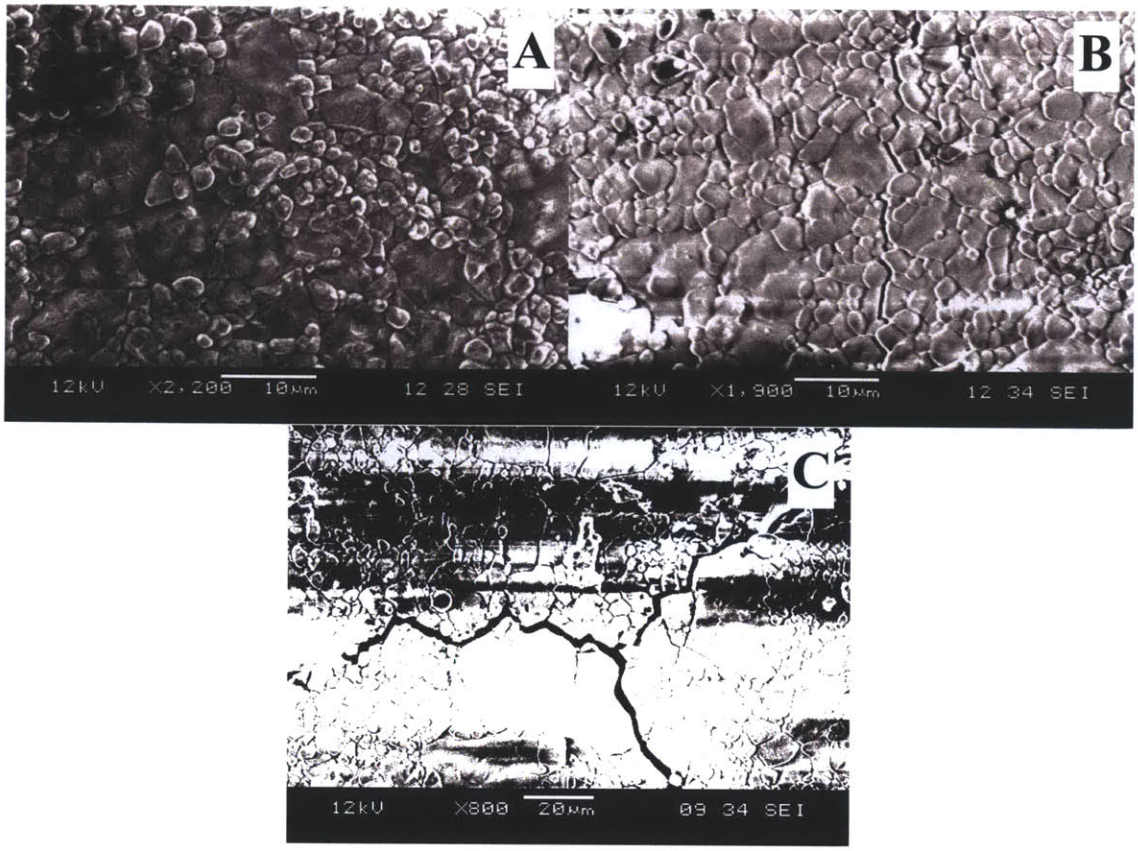

Figure 5-15 Surface Morphologies of Al_2O_3: A- As-received, B- Al_2O_3 S1, 1110°C, and C- Al_2O_3 S2, 1110°C

5.4.3 Brittle Fracture of Pre-cracked SiC

Typical geometries of pre-introduced cracks (200~1000μm) in the tubular α-SiC wall are shown in Figure 5-16. The width of the crack is fixed as the width of the cutting diamond saw (~250 μm). As a result, the end tips of the introduced cracks are quite smooth which reduce the level of a stress concentration at the end tip. In that sense, the introduced crack may be better described as a local absence of material than a stress intensifier.

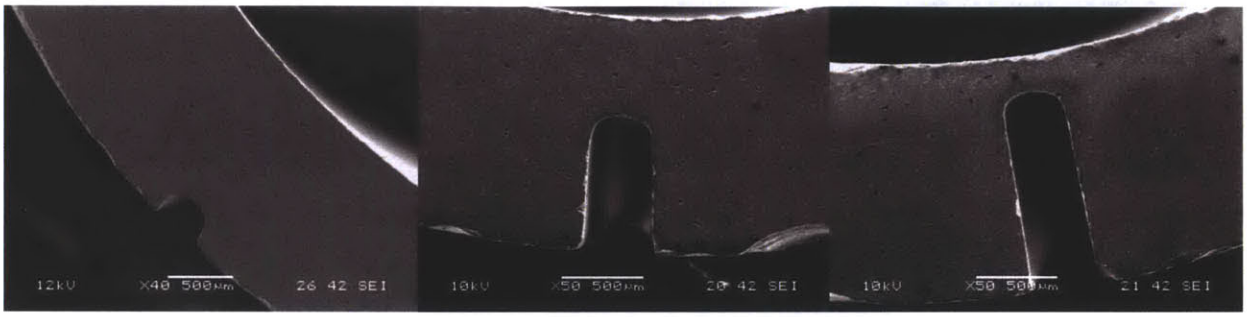

Figure 5-16 Geometries of pre-introduced cracks in the tubular α-SiC wall

The effects of pre-introduced cracks on the fracture behavior of tested specimens were not clearly observed. As shown in Figure 5-17, shattered pieces of fractured specimens did not explicitly contain the pre-cracked area in the material, implying that the introduced macroscopic crack (or region of absence of material) was not the critical flaw.

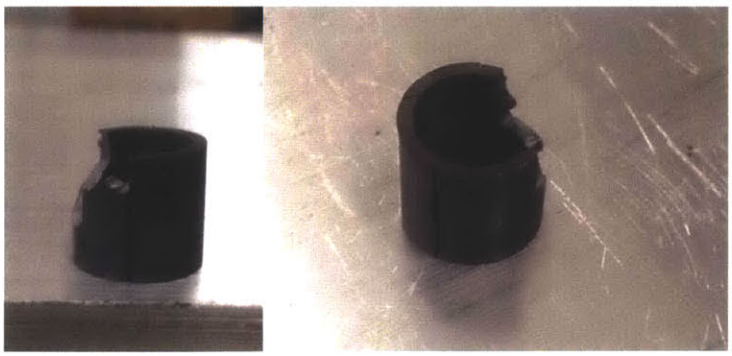

Figure 5-17 Typical Visual Fracture Characteristics of Pre-cracked tubular α-SiCs (T=1230°C)

This observation may be related to the idea of the most limiting critical flaw size in thermal shock fracture; there is a critical crack size that most intensifies the overall thermal stresses that the entire crack sees. Theoretical discussion on this subject of the critical flaw size for thermal shock follows in Chapter 6.

5.5 Conclusion

Experimental assessments demonstrated that β-SiC exhibits a superior tolerance in thermal shock in comparison with α-SiC as the former showed some evidence of strength retention up to 1260°C even in room temperature water. For α-SiC, transgranular crack propagations were found to be the dominant fracture mode.

Strength retention of both α-SiC, and β-SiC was observed in saturated water. Such strength retention of brittle material in saturated water quenching was also observed with Al_2O_3. This strength retention effect in saturated water quenching is expected to decrease with increasing material size and is demonstrated by thermal shock fracture of a thicker Al_2O_3 in saturated water. Since quenching of fuel rods in the reflood phase of LOCA in LWR occurs with injecting coolant close to saturation conditions, accurate understanding of heat transfer origin brittle fracture with respect to subcooling would be necessary for safety assurance of SiC cladding in LOCA.

In Chapter 6, theoretical aspects of the observed fracture behavior with SiC cladding are discussed. With experimentally validated models, we expect to extrapolate our understanding for brittle fracture to appropriately simulate structural integrity of SiC cladding under reflood phase in LOCA.

Chapter 6
Brittle Fracture of SiC Cladding III: Thermal Shock Fracture – Theories and Models

6.1 Introduction

Information required for an understanding of thermal-shock induced brittle fracture under water-quench conditions is two-fold - the mechanical behavior of material to sharp temperature gradients must be known, second, the thermal-hydraulic conditions that determine the heat transfer response of the material and water must be known. The relevant mechanical behavior of a material in thermal shock fracture includes thermal expansion, thermal capacity of the material, stress-concentration of pre-existing flaws under sharp temperature fields, and strength of atomistic bonding of the material. The heat transfer rate between the material and water affects stress gradients in the material. Generally speaking, much more attention has been given to the mechanical behavior of the material under thermal stresses than understanding transient heat transfer rates in most thermal shock studies. This biased focus in modeling efforts has resulted in applying high-fidelity thermal shock fracture mechanics with crude understanding of the heat transfer origin of the fracture that determines the stress field around cracks. In this chapter, an effort to explore the heat transfer origin of brittle fracture in water quench is discussed.

6.2 Heat transfer Modes of Water Quenching

Heat transfer in water quenching is closely related to boiling modes on the material's surface. Superheated material's surfaces transfer heat to the surrounding fluid. While the material heats up the neighboring fluid, a thin layer of superheated fluid near the wall is formed. A cavity on the wall initially filled with air serves as a vapor bubble growth spot. Sufficient superheating of the material's wall causes the growth of the bubble which lifts up the superheated liquid layer. Further growth of the bubble leads to a departure from the surface and the bubbles carry away the thermal layer, agitating adjacent 'cold' fluids to flow into the superheated surface. This gives rise to a high heat transfer coefficient in the nucleate

boiling process. The nucleate boiling process is affected by material's surface characteristics as surface cavities serve as initial bubble generation sites. Detailed discussions of the bubble initiation, growth, departure and nucleate boiling heat transfer can be found in the study by Han and Griffith (Han, 1962). Further surface superheat increases bubble generation rates and nucleation site density, which can be seen from increasing bubble generation frequency and reduced distance between consecutive bubbles. Beyond a critical surface superheat, the consequences of an increase in bubble generation rate is the formation of a continuous vapor film on the surface. After sufficient cooling of the surface by the film boiling, the vapor film makes a transition to the transition boiling and nucleate boiling mode, which eventually stops with further cooling of the surface.

In this study, heat transfer before commencement of the convective heat transfer mode is of interest in exploring the heat transfer origin of the thermal shock. Thus, consideration of the effects of the early thermal front propagation on growth of a surface flaw is of interest. Usually, surface cracks serve as the critical flaws because they see the highest tensile stresses in quenching transient during the early thermal front propagation in the material. Internal flaws see compressive stresses in the early quenching transient and tensile stresses, still lower than the surface tensile stresses, later in the queching transience. For this reason, material's tolerance to a cold thermal shock has often been addressed in terms of the fracture of surface cracks (Lu, 1998). Note that the transition from the film boiling to the nucleate boiling after sufficient cooling would give a high heat transfer coefficient. However, the material would not probably see as high stresses as it saw during the early transience with the conductive heat transfer, because its temperature has already become sufficiently low by the time it makes a transition to nucleate boiling.

Figure 6-1 to Figure 6-13 show boiling modes of quenched specimens during the quenching transients of the conducted experiments. It is commonly observed for both subcooled water and saturated water that the specimens were blanketed by air that they carry in when entering the water - this initial air blanket is not a result of superheat. It was observed that the size of this initial carried air increases with the cross-sectional area of the specimen. One can see in Figure 6-3 - Figure 6-5 and in Figure 6-9 - Figure 6-11 that the Al_2O_3 of the larger cross sectional area 6.35mm x 6.35mm introduces a significantly larger amount of air than the SiC bars whose cross sectional area is 3.175mm x 3.175mm. As this carried air blanket disappears, the solid surface comes to contact with the neighboring fluid.

For specimens quenched in subcooled water, a certain time period was observed before a noticeable commencement of vapor formation. This time period includes the bubble incipience, the growth (Han, 1962), and the momentum transfer of the vapor. Some clear images were obtained that show this conduction dominant quenching period as shown in Figure 6-1. Those observations of the carrier air, and

the conduction dominant heat transfer period may answer a problem raised by several studies in terms of the appropriateness of using well-known state heat transfer correlations in the early quenching transient[23]. Evidence of this conduction dominant heat transfer was also observed in the early transient of saturated quenching as shown in Figure 6-2. A thin vapor film almost instantaneously formed on the superheated solid surface and grew until it reached a stable thickness that is accompanied by wavy motion. During this process, the characteristic wavy motion of the film was suppressed and the heat transfer was primarily controlled by conduction within the vapor film. The β-SiC did not exhibit clear film boiling modes over all temperature ranges. This may be related to its relatively smaller volume whose thermal energy content was not enough to sustain an appreciable film. Similar to the conduction heat transfer in the early transient of subcooled quenching, convective heat transfer is suppressed before sufficient momentum transfer from the vapor takes place to the saturated water. A similar phenomenological conclusion was made by the experimental and the analytical investigation of Pitts et.al (Pitts, 1968) on transient vapor film formation following a large step change in wire temperature ranging from 674 °C – 950°C in saturated water. The primary conclusion of the study was that the vapor film growth in transient film boiling of saturated water was primarily determined by conduction heat transfer within the vapor film and the average time for this growth of the film to the final thickness is approximately 10 milliseconds; after this time period, the typical convective steady-state film boiling coefficient holds.

The heat transfer coefficeint before the commencement of convective boiling effects in a rapid heat transfer mode has been successfully calculated by solving the transient heat conduction equation in semi-infinite water (Sakurai, 1977). That work found that the instantaneous heat transfer coefficient asympotically reaches infinity at time t=0. This leads to instantaneous cooling of the surface temperature to the subcooled water temperature ($T_s \cong T_{bulk}$). While the surface crack size (a_c) being substantially smaller than the width of the specimen (w), the temperature field of a surface crack in the early transience can be modeled as a transient thermal front propagation in a semi-infinite solid body with an abrupt surface temperature change to T_s in Eq.(6-1) (Incropera, 2007).

$$\frac{T(x,t)-T_s}{T_i-T_s} = erf\left(\frac{x}{2\sqrt{\alpha t}}\right) \tag{6-1}$$

For the quenching in saturated water, a very thin vapor flim is formed instantaneously. In such a case, the instantaneous surface temperature T_s can be approximated from a surface energy balance of two semi-

[23] *"The well-known steady-state correlations are not appropriate for predicting early transients in quenching experiment"*, Osman and Beck (Osman, 1990) concluded after applying the transient inverse technique for the heat transfer coefficient prediction in quenching experiment.

infinite solids contacting with a negligible contact resistace due to a very thin vapor layer thickness ($\delta \approx 0$) as shown in Eq.(6-2) (Incropera, 2007).

$$T_s = \frac{(k\rho C_p)_{sat,water}^{1/2} T_{sat} + (k\rho C_p)_{solid}^{1/2} T_i}{(k\rho C_p)_{sat,water}^{1/2} + (k\rho C_p)_{solid}^{1/2}} \tag{6-2}$$

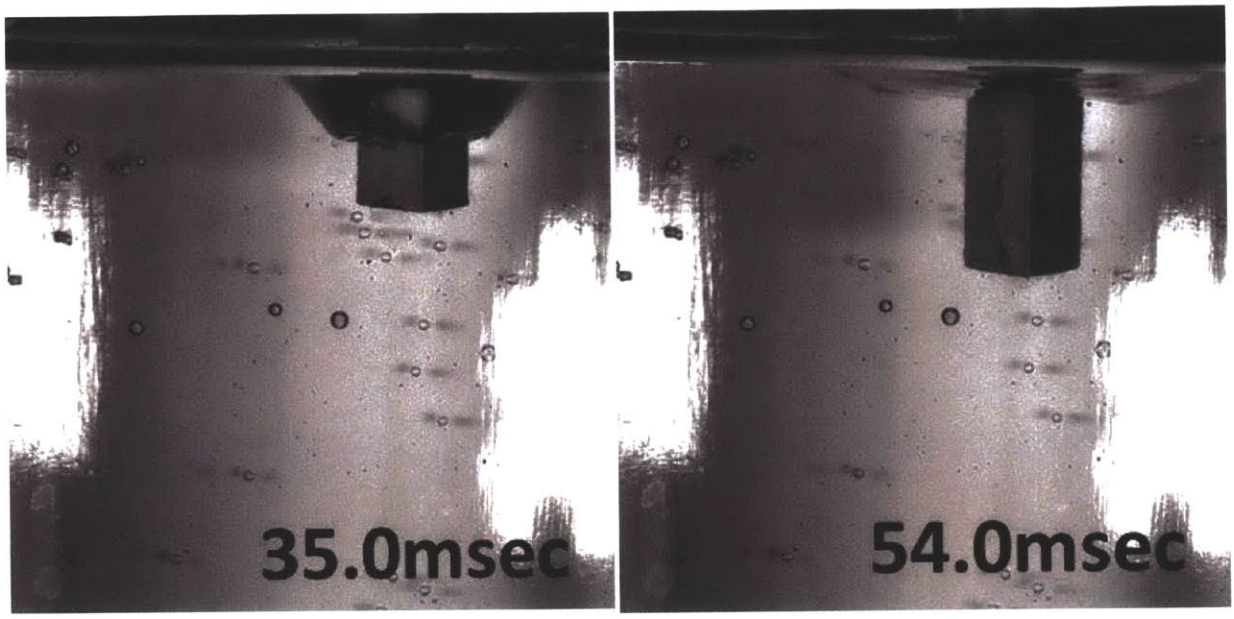

Figure 6-1 Conduction Dominant Quenching Period Before the Commencement of Boiling in Subcooled Water (22°C) with Al_2O_3 [Specimen size: 30mm(*l*) x 6.35mm (w) x 6.35mm (*t*)] at 1110°C. Note that the vapor on the left picture is the disappearing air carried upon entering

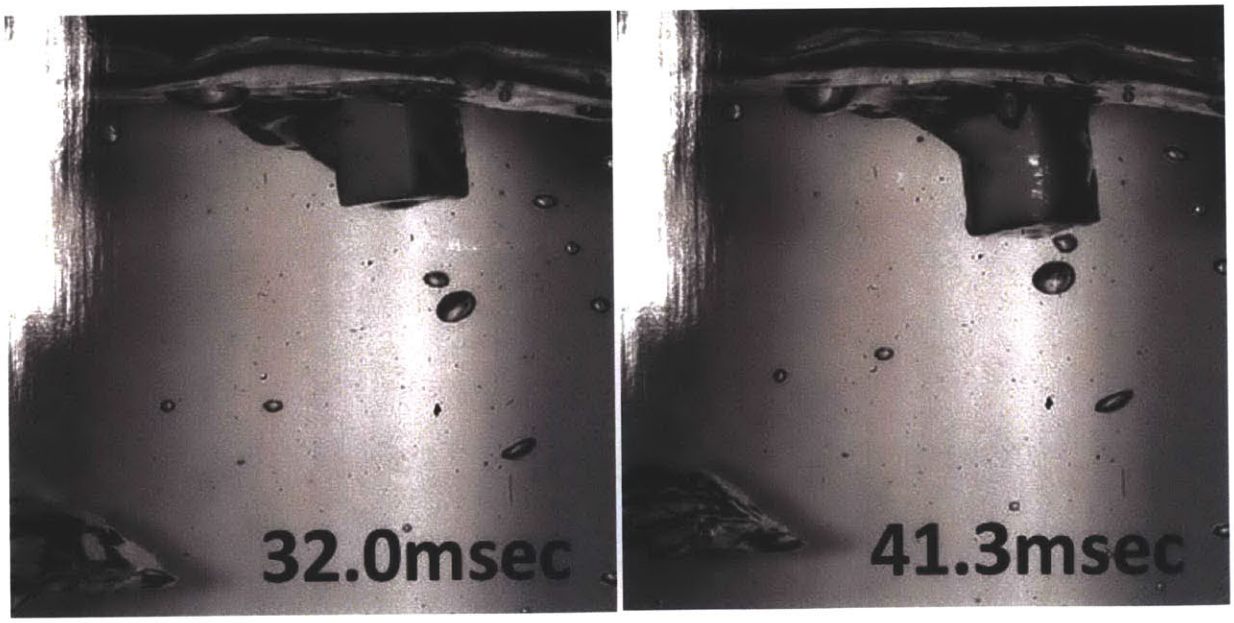

Figure 6-2 Conduction Dominant Quenching Period Before the Commencement of Boiling in Saturated Water (22°C) with Al_2O_3 [Specimen size: 30mm(*l*) x 6.35mm (w) x 6.35mm (*t*)] at 800°C.

The departure from the conduction dominant heat transfer during the very early quenching transient occurs when turbulent mixing due to vapor fluxes is significant enough to rearrange the thermal boundary layer; then, relevant boiling heat transfer coefficients should be considered [24]. Such a rearrangement of the thermal boundary layer with the vapor flux accompanies momentum transfer whose time scale is generally longer than the characteristic time for energy trasnfer in a rapid quenching situation.

After the departure from conduction dominant heat transfer with appreciable vapor generation, sufficient superheating of the solid surface would lead to the film boiling state. The saturated film boiling coefficient at a vertical surface can be obtained by Eq.(6-3) (Nishio, 1993).

$$h_{f,sat} = 0.74\frac{k_{vf}}{\lambda}\left(\frac{{Gr_v}^{\lambda} Pr_{vf}}{Sp^*}\right)^{1/4} \tag{6-3}$$

Eqs.(6-4) to (6-8) show input parameters for Eq.(6-3).

$${Gr_v}^{\lambda} = \frac{g\rho_{vf}(\rho_{lf} - \rho_{vf})\lambda^3}{\mu_{vf}^2} \tag{6-4}$$

$$\lambda = 16.2\left(\frac{Pr_{vf}^3}{{Sp^*}^3 {Gr_v}^{\lambda_0}}\right)^{1/11}\lambda_0 \tag{6-5}$$

[24] The thermal boundary layer formed as a result of this conductive heat transfer was extensively studied in the 1960s in pursuts of understanding nucleate boilibng mechanisms. Hsu (Hsu, 1962) developed and valideated a mathematical expression that relates the thermal boundary layer thickness and the incipience of boiling from surface cavities. Wiebe and Judd (Wiebe, 1971) measured the superheat thermal boundary layer at a nucleate boiling solid surface and validated the correlation between the superheat layer thickness and heat transfer coefficients reported by Marcus and Dropkin (Marcus, 1965). Those studies essentially report a strong physical relation between the thermal boundary layer thickness and heat transfer rates in nucleate boiling. For a higher heat flux at the surface, the thermal boundary layer was found to get thinner by increasing turbulence mixing effects with a higher bubbule flux, resulting in a higher heat transfer coefficeint (Wiebe, 1971). Yet, this relation may hold only when the bubble flux is substantially lower than that required for vapor blanket formation.

$$\lambda_0 = \sqrt{\frac{\sigma}{g(\rho_{ls} - \rho_{vs})}} \tag{6-6}$$

$$Sp^* = \frac{Sp}{\left(1 + \frac{Sp}{2}\right)} \tag{6-7}$$

$$Sp = \frac{C_{pvf}\Delta T_{sat}}{h_{fg}} \tag{6-8}$$

k_{vf} is the thermal conductivity of the film, Pr_{vf} is the Prandtl number of the vapor at film temperature, ρ_{vf} is the density of vapor at film temperature, ρ_{lf} is the densilty of liquid at the film temperature, μ_{vf} is the viscosity of vapor at the film temperature,

The subcooled film boiling heat transfer coeffcient can be obtained from the correlation developed by Nishio and Ohtake (Nishio & Ohtake, Vapor-film-unit model and heat transfer correlation for natural-convection film boilig with wave motion under subcooled conditions, 1993) as shown in Eq.(6-9).

$$h_{f,sub} = h_{f,sat} + 0.067\left(\frac{k_{vf}}{\lambda}\right)\left(\frac{Pr_{lf}^{0.21}}{\overline{\rho\mu}^{0.23}}\right)\left(Gr_l{}^{\lambda} Pr_{lf}\right)^{1/4}\frac{\Delta T_{sub}}{\Delta T_{sat}} \tag{6-9}$$

$$\bar{\rho} = \frac{\rho_{vs}}{\rho_{ls}} \tag{6-10}$$

$$\bar{\mu} = \frac{\mu_{vs}}{\mu_{ls}} \tag{6-11}$$

$$Gr_l{}^{\lambda} = \frac{g\rho_{lf}(\rho_{lb} - \rho_{lf})\lambda^3}{\mu_{lf}^2} \tag{6-12}$$

where Pr_{lf} is the Prandtl number of the liquid at the film temperature, ρ_{lb} is the density of liquid at the bulk fluid temperature, ρ_{vs} is the saturated vapor density, ρ_{ls} is the saturated liquid density, μ_{vs} is the saturated vapor viscosity , μ_{ls} is the saturated liquid, and μ_{lf} is the liquid visocisity of the film.

The radiation contribution to film boiling heat transfer is taken into account by the following relation (Nishio, 1999),

$$h = h_f + 0.75h_r \tag{6-13}$$

where the radiation component h_r is shown in Eq.(6-14)

$$h_r = \frac{\sigma}{(1/\varepsilon_s + 1/\varepsilon_l - 1)}\left(\frac{{T_w}^4 - {T_{sat}}^4}{T_w - T_{sat}}\right) \tag{6-14}$$

σ is the Stefan-Boltzman constant, $56.7 \times 10^{-9}\, W/m^2K^4$, and ε_s is the emissivity of the solid surface, and ε_l is the emmisivity of the liquid surface (typically ≈ 1).

In most engineering applciations, film boiling heat transfer is regarded as an 'insulating' mode of heat transfer, which often yields an unacceptably high surface temperature. The typical heat transfer coefficient for film boiling is on the order of 100 ~1000 W/m^2-K whereas the initial conductive coefficient heat transfer before the commencement of convective effects in water gives on average of ~25000 W/m^2-K in the first 5 milliseconds and asymptotiically reaches the heat transfer coefficient given by natural convection.

Because of the short period of the conductive heat transfer mode in thermal shock, its importance has been overlooked in understanding the thermal shock fracture of a brittle material. Instead, a biased emphasis has been placed on understanding the stress concentration around a pre-exisitng flaw. As a consequence, applying high fidelity thermal shock intensity factors with a crude understanding of the heat transfer origin of stresses has left the predictability of brittle fracture incomplete. Although the initial conduction-dominant heat transfer mode lasts for a short period of time in the overall quenching process, its duration may be long enough to initiate crack propagation for cracks on the surface. Hence, exploration of stress-concetration near an existing flaw during the conduction dominant heat transfer transience would be of prime importance to understanding the heat transfer origin of brittle fracture.

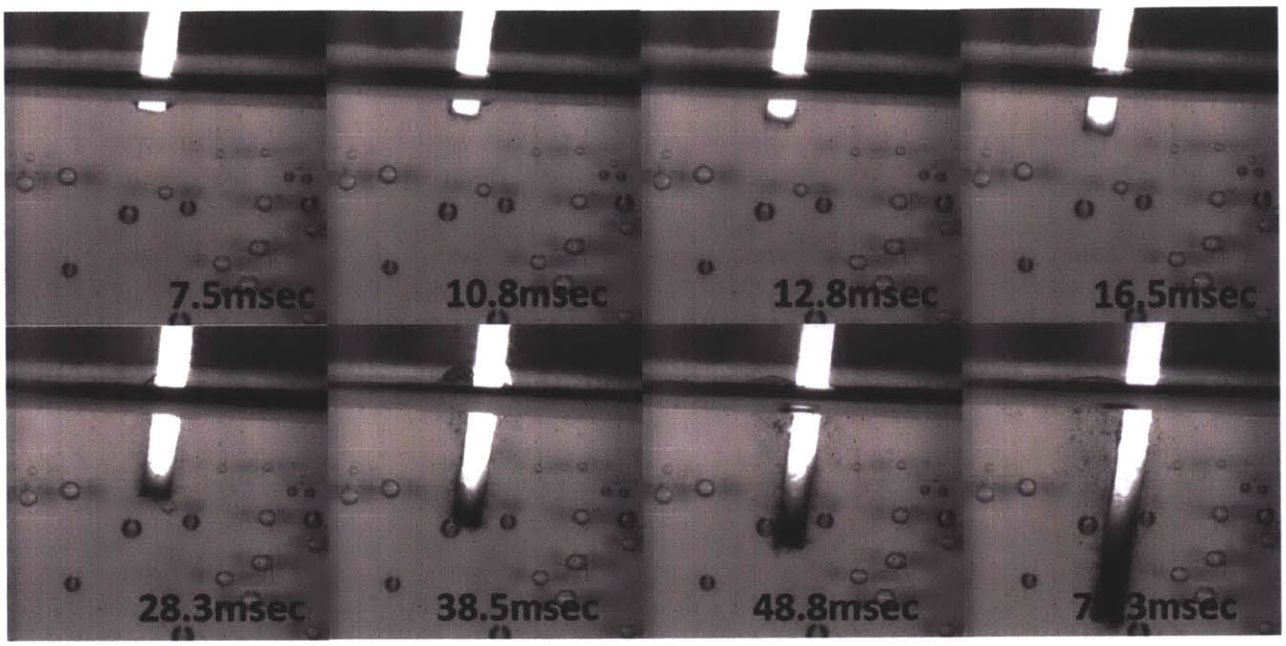

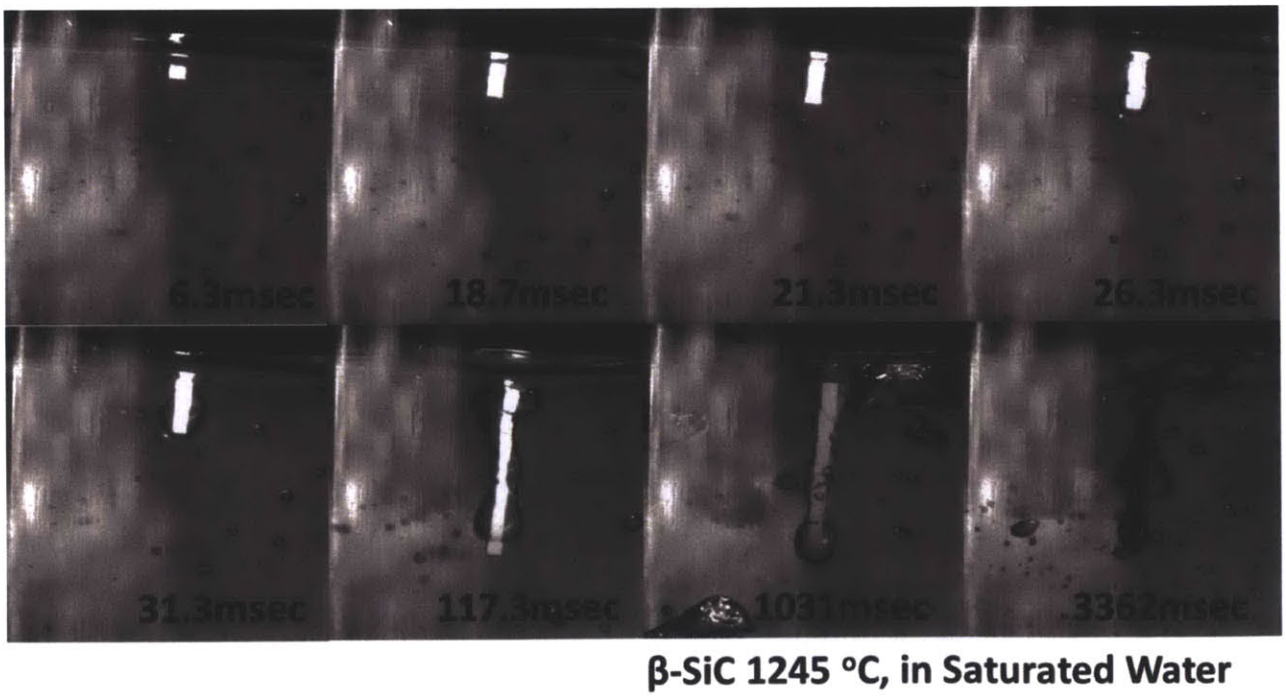

Figure 6-3 Boiling Characteristics of β-SiC at 1245°C Quenched in subcooled (22°C) and saturated (100°C) water [Specimen size: 25mm(*l*) x 2mm (w) x1.5mm (*t*)]

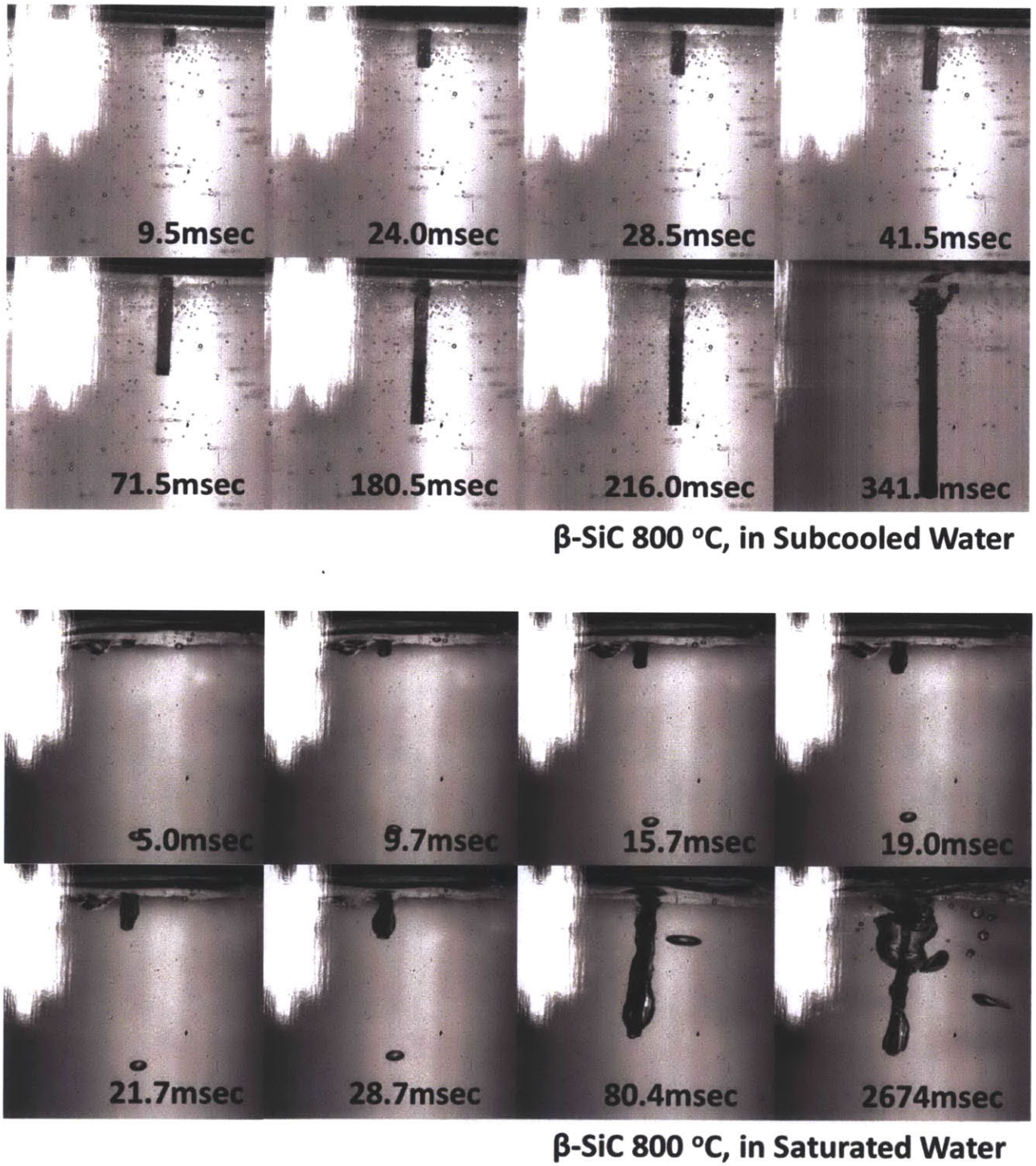

Figure 6-4 Boiling Characteristics of β-SiC at 800°C Quenched in subcooled (22°C) and saturated (100°C) water [Specimen size: 25mm(*l*) x 2mm (w) x1.5mm (*t*)]

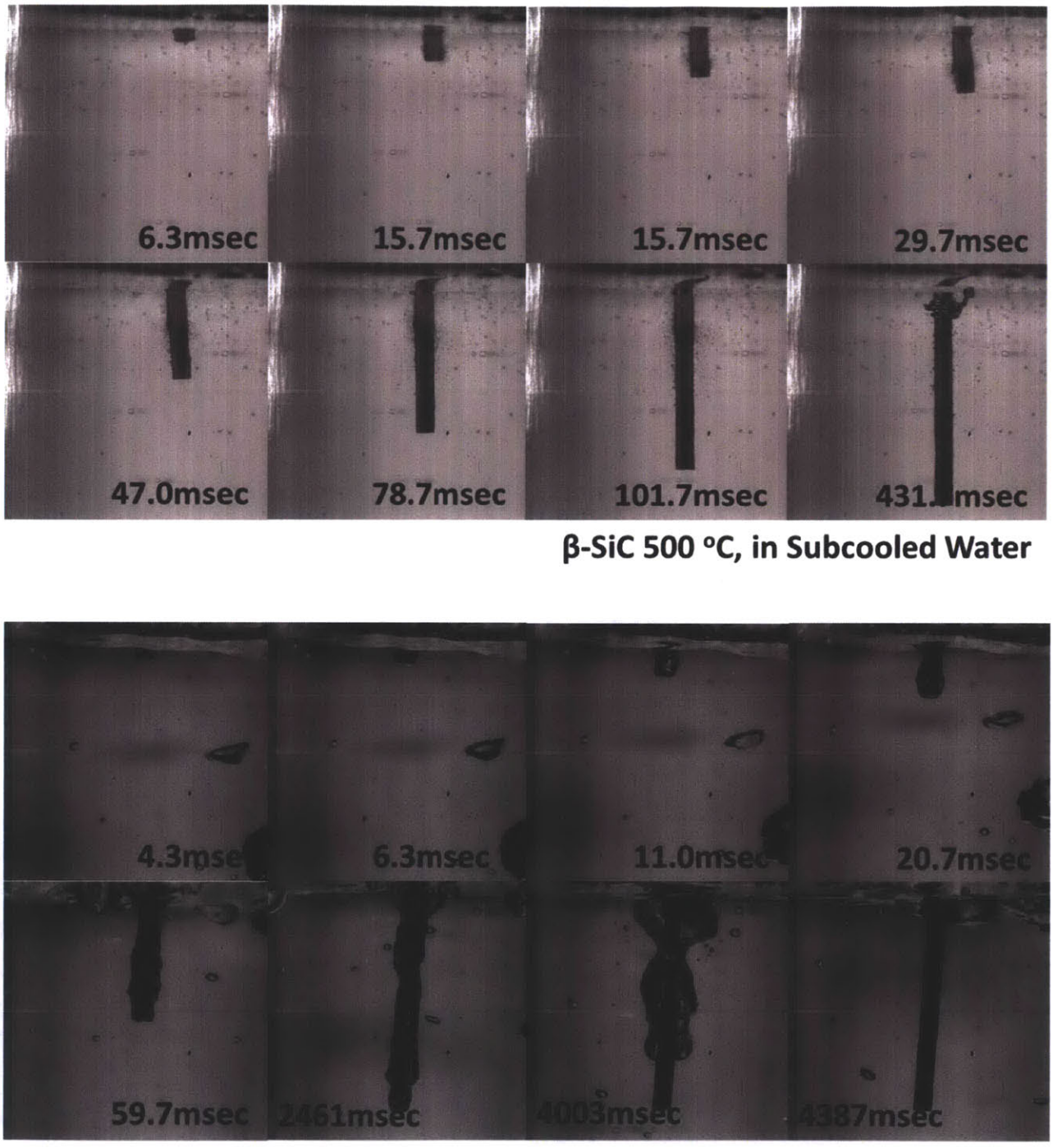

Figure 6-5 Boiling Characteristics of β-SiC at 500°C Quenched in subcooled (22°C) and saturated (100°C) water [Specimen size: 25mm(*l*) x 2mm (w) x1.5mm (*t*)]

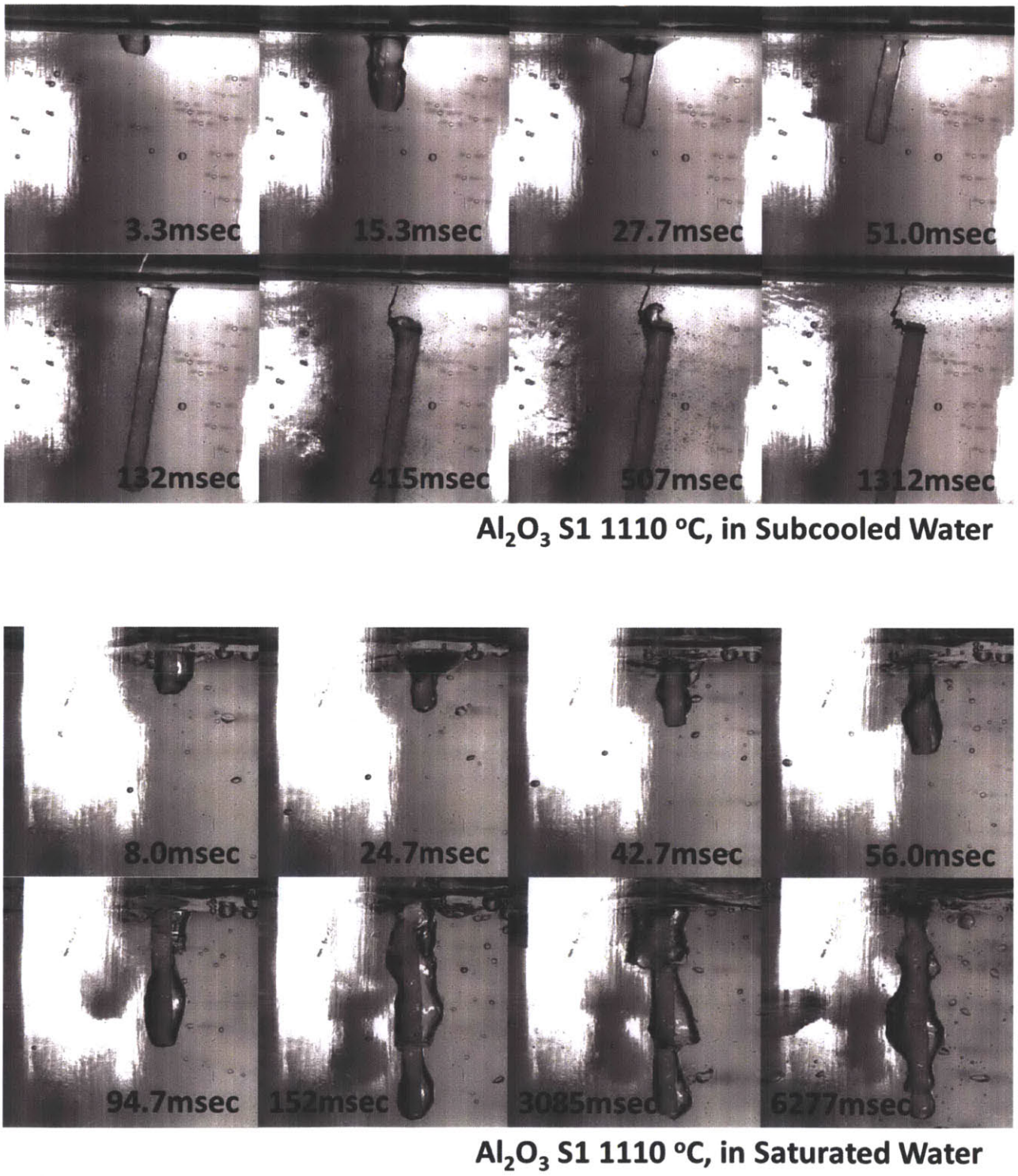

Figure 6-6 Boiling Characteristics of Al_2O_3 at 1110°C Quenched in subcooled (22°C) and saturated (100°C) water [Specimen size: 30mm(*l*) x 3.175mm (w) x 3.175mm (*t*)]

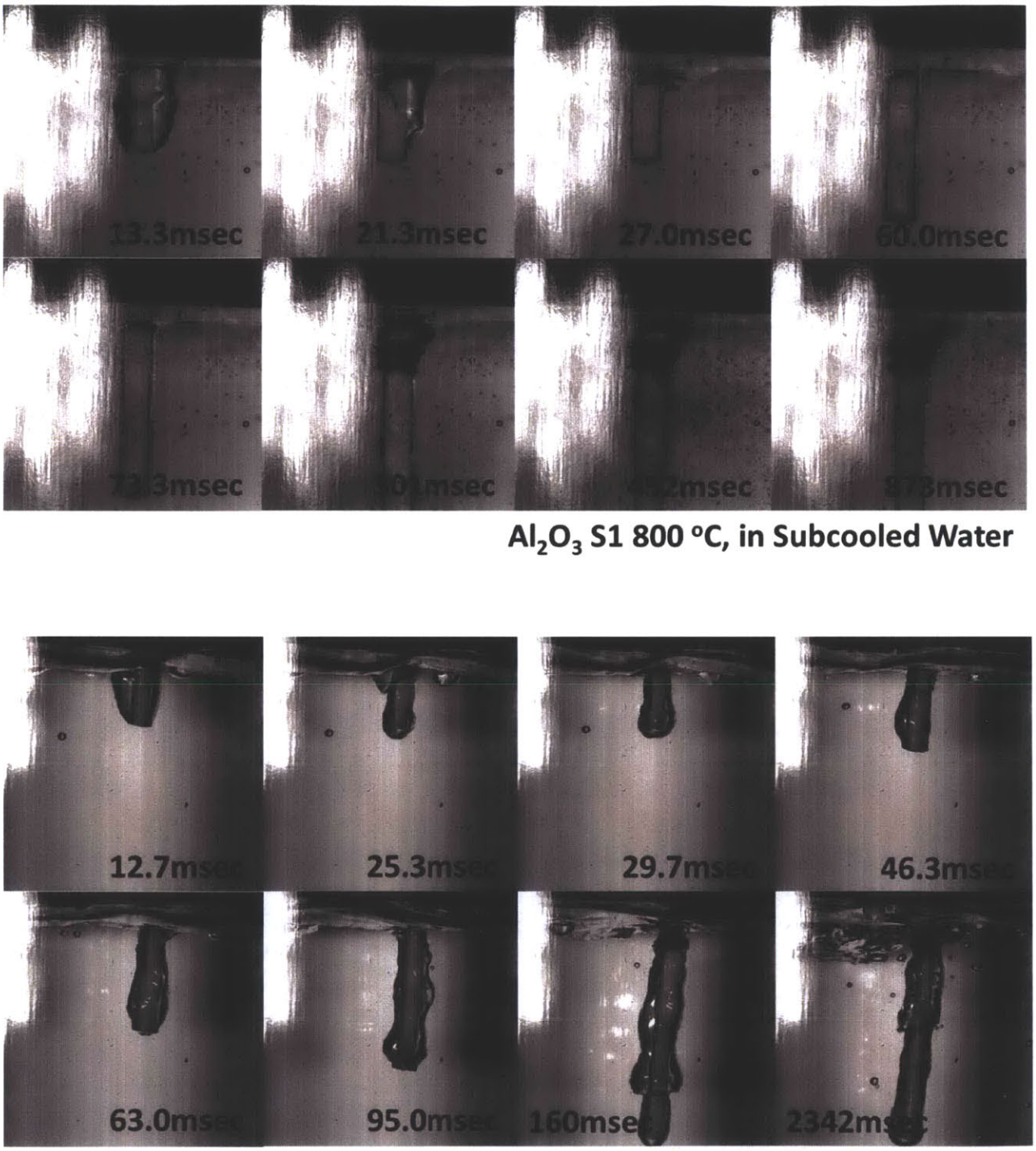

Figure 6-7 Boiling Characteristics of Al_2O_3 at 800°C Quenched in subcooled (22°C) and saturated (100°C) water [Specimen size: 30mm(l) x 3.175mm (w) x 3.175mm (t)]

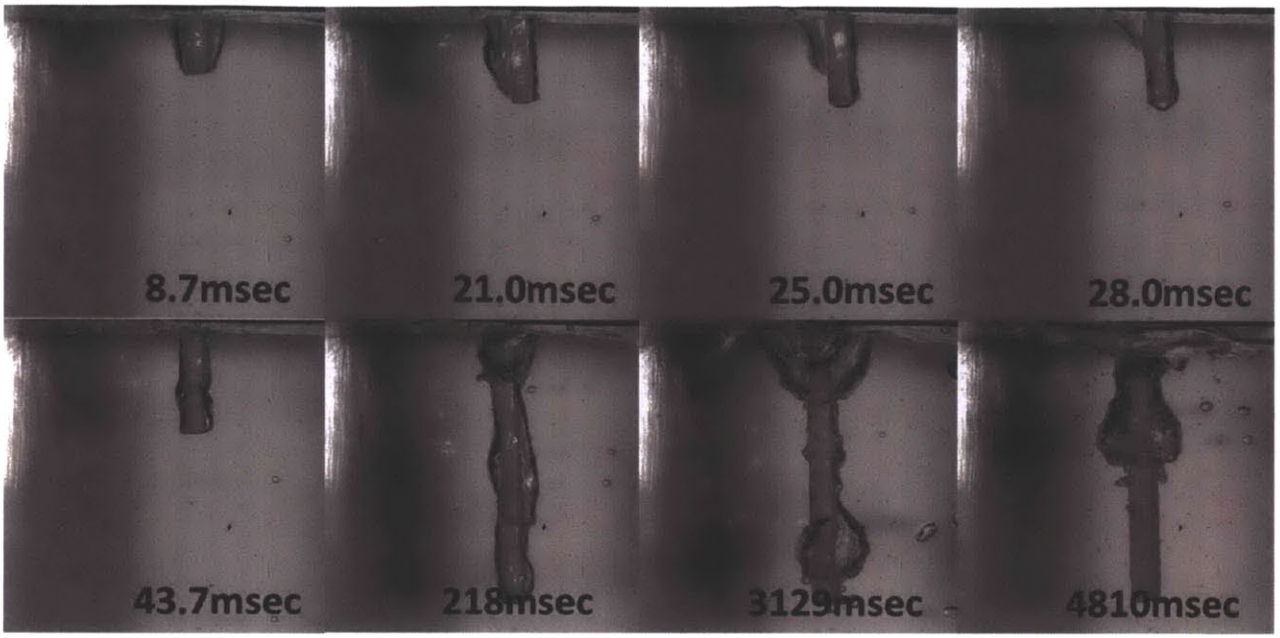

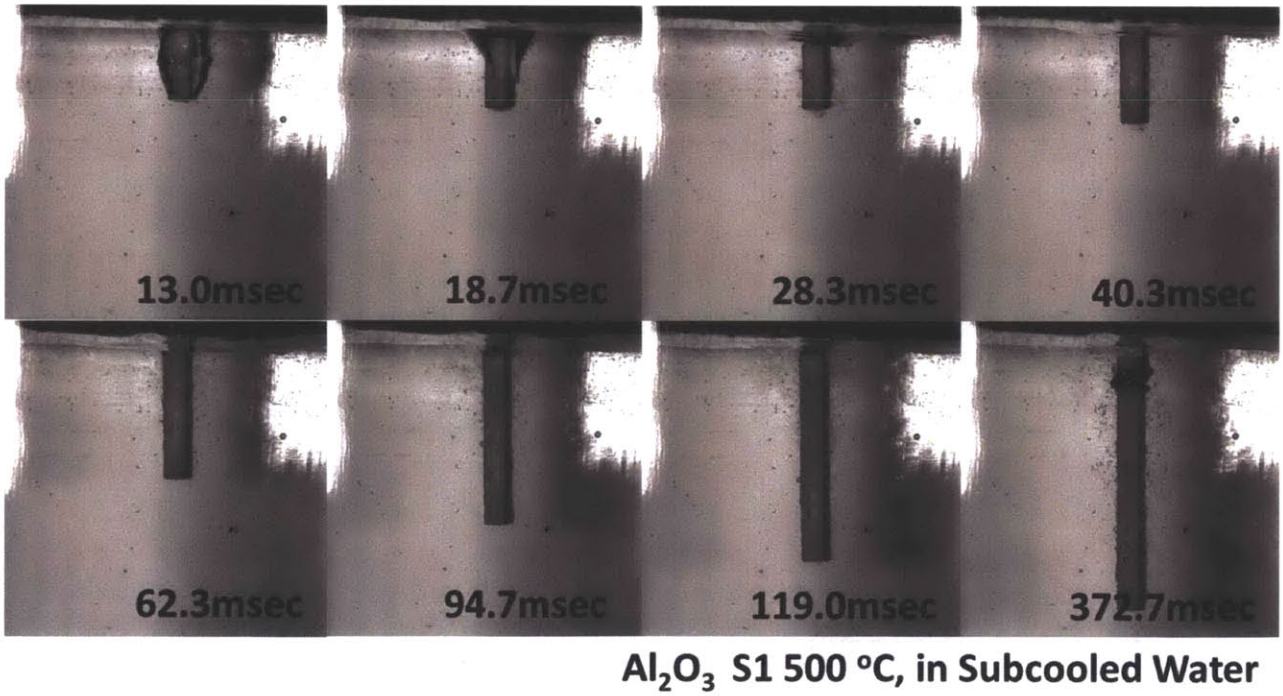

Figure 6-8 Boiling Characteristics of Al_2O_3 at 500°C Quenched in subcooled (22°C) and saturated (100°C) water [Specimen size: 30mm(*l*) x 3.175mm (w) x 3.175mm (*t*)]

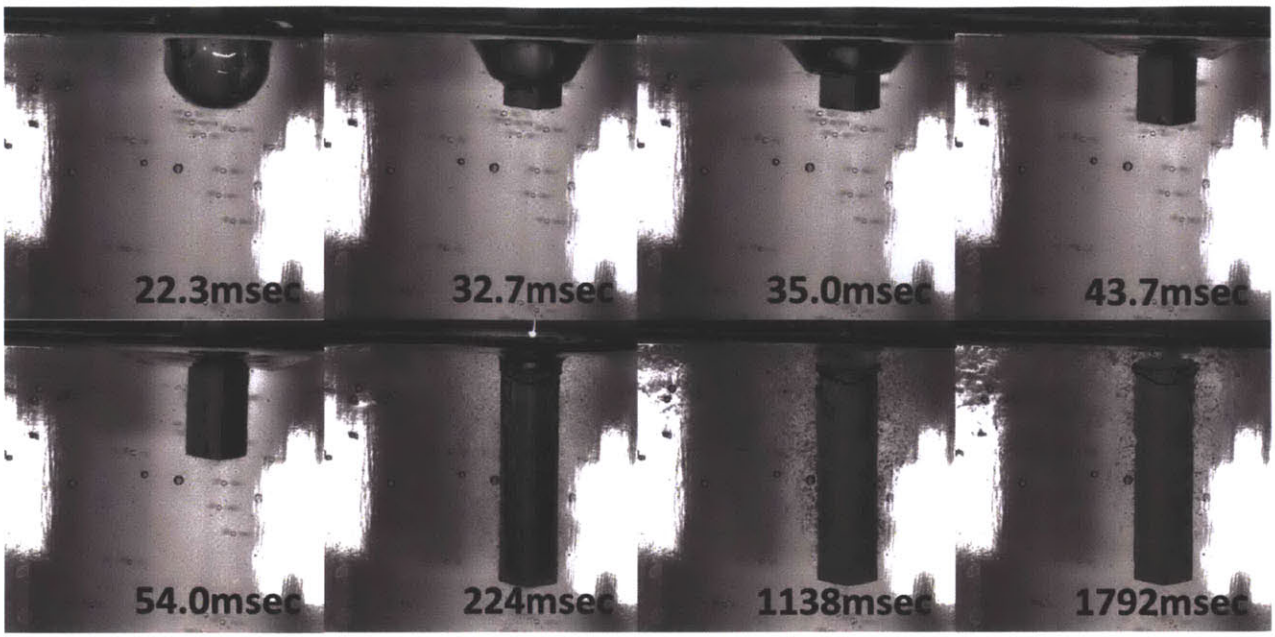

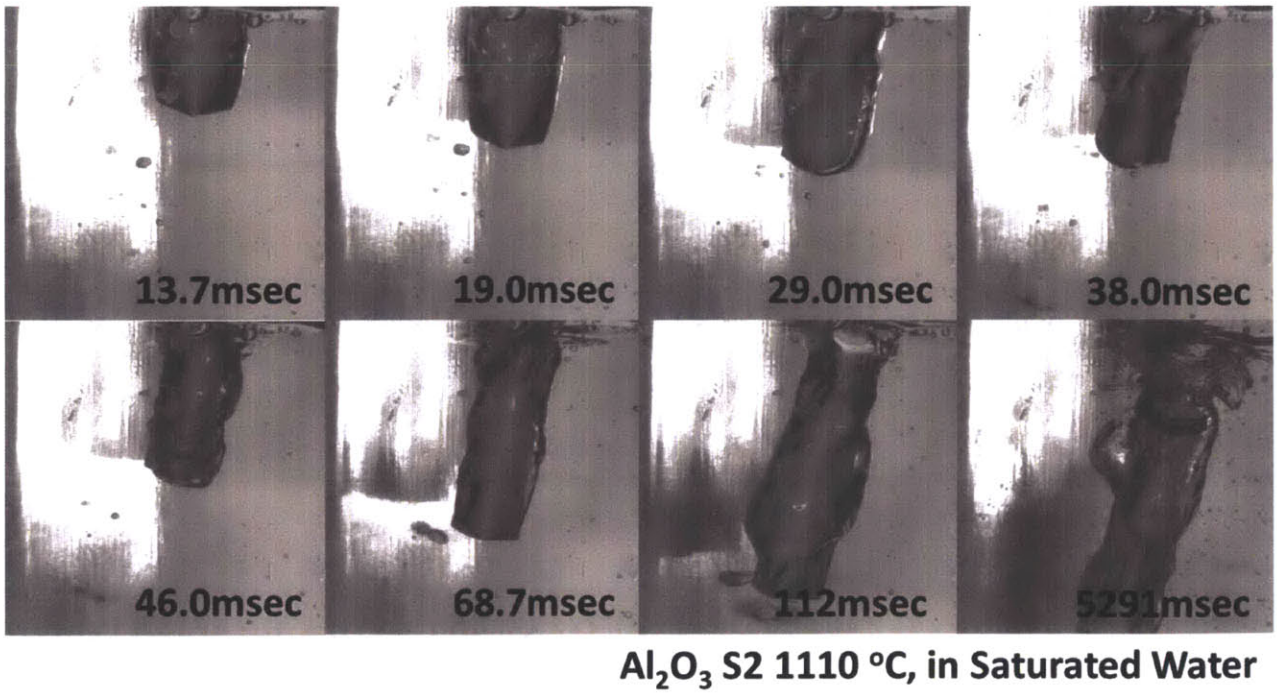

Figure 6-9 Boiling Characteristics of Al_2O_3 at 1110°C Quenched in subcooled (22°C) and saturated (100°C) water [Specimen size: 30mm(*l*) x 6.35mm (w) x 6.35mm (*t*)]

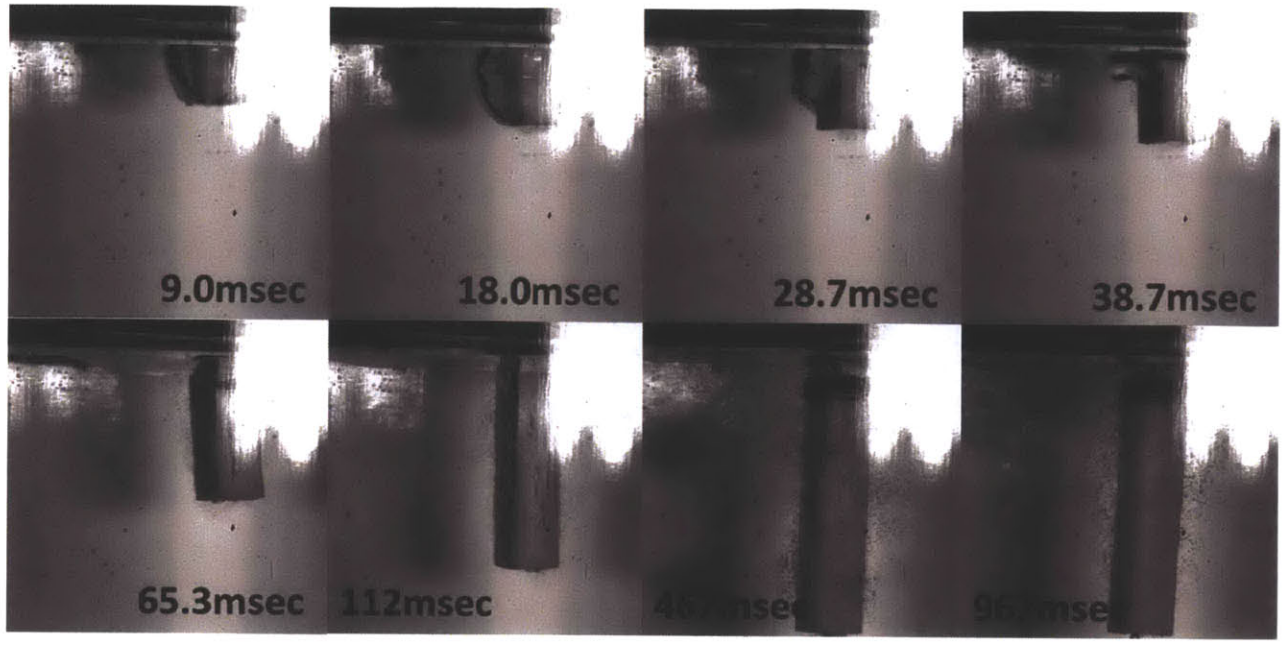

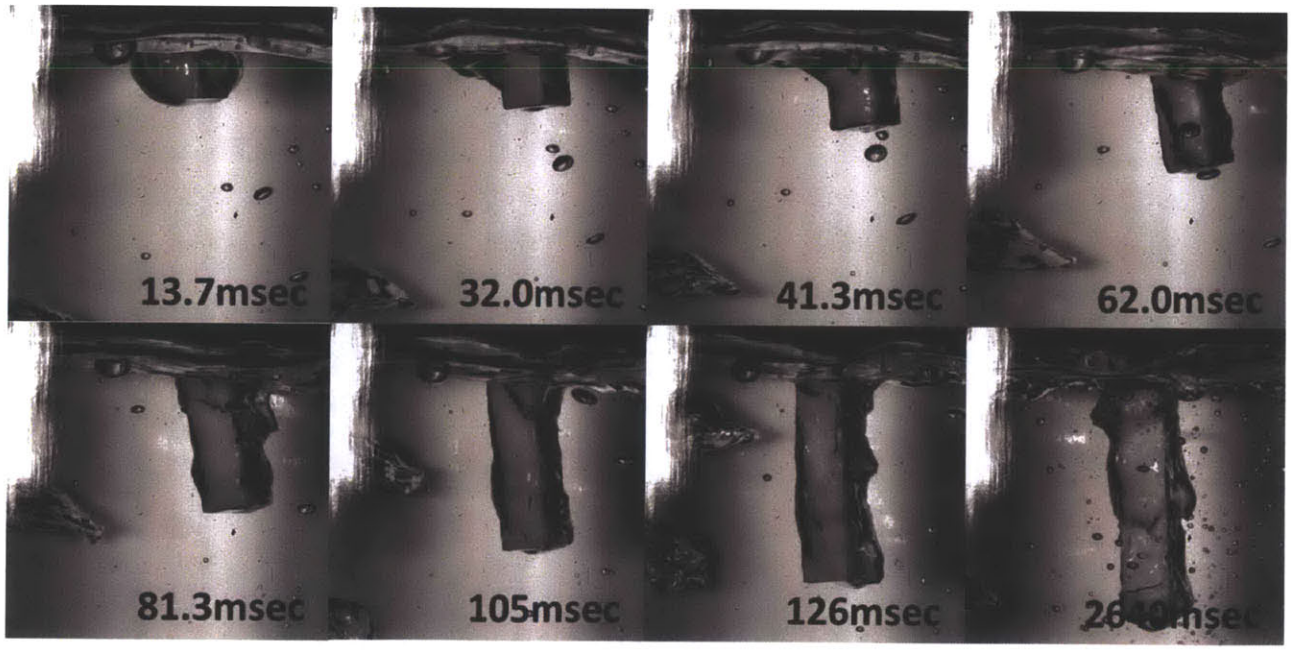

Figure 6-10 Boiling Characteristics of Al_2O_3 at 800°C Quenched in subcooled (22°C) and saturated (100°C) water [Specimen size: 30mm(l) x 6.35mm (w) x 6.35mm (t)]

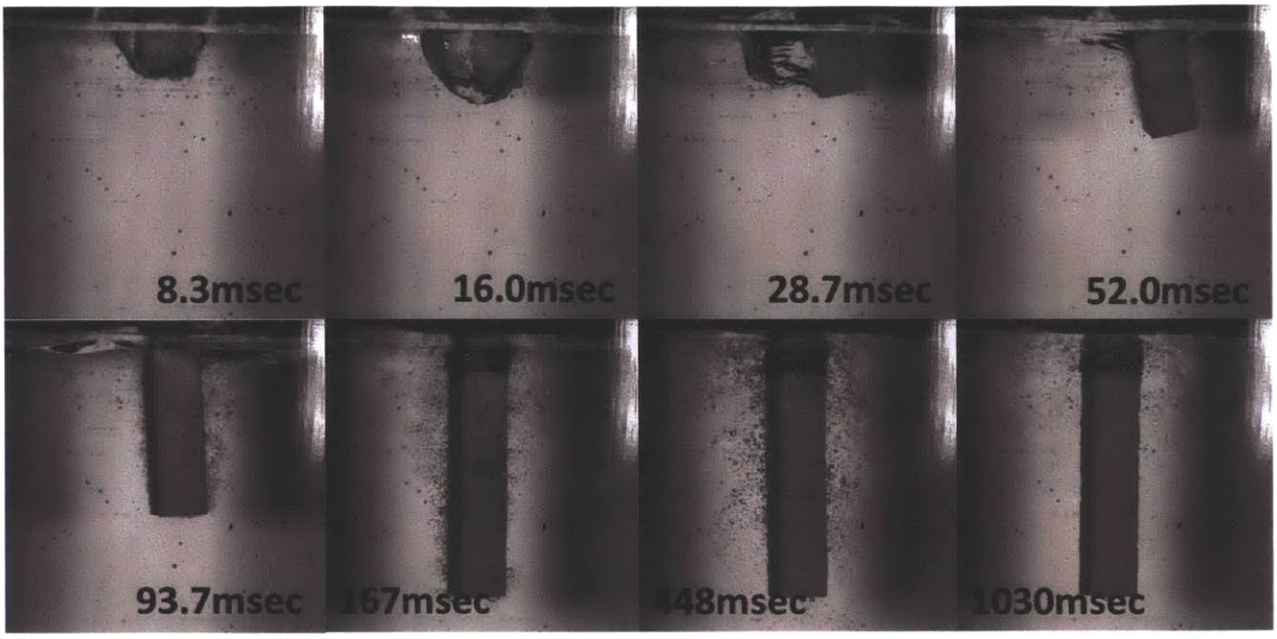

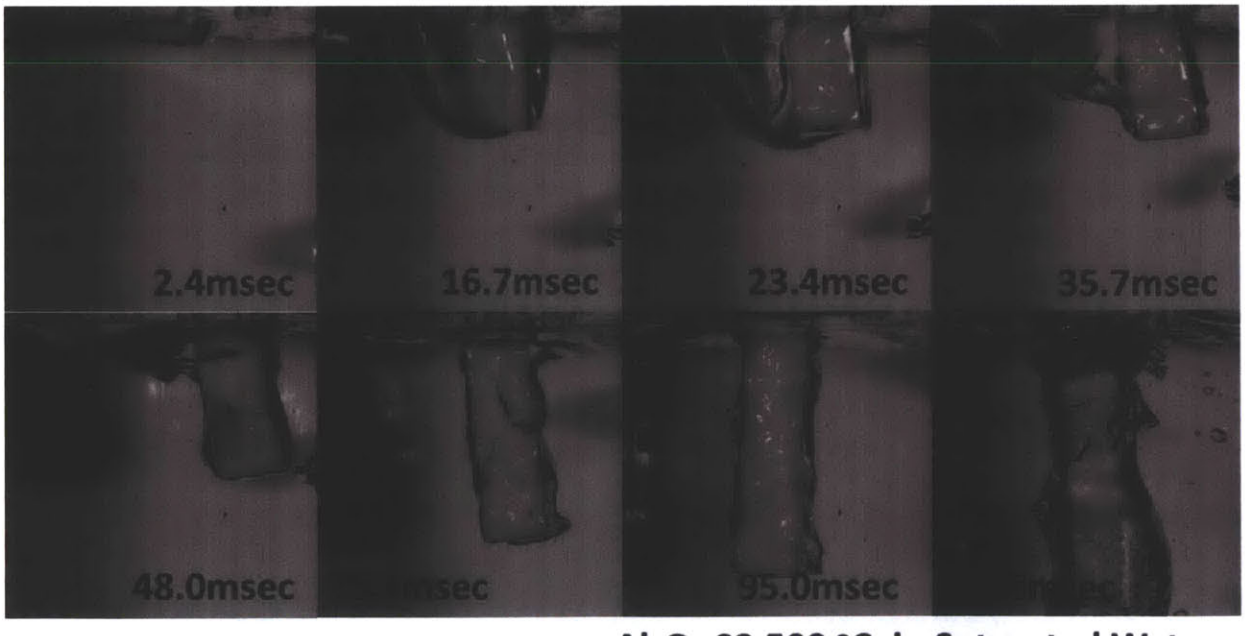

Figure 6-11 Boiling Characteristics of Al_2O_3 at 500°C Quenched in subcooled (22°C) and saturated (100°C) water [Specimen size: 30mm(*l*) x 6.35mm (w) x 6.35mm (*t*)]

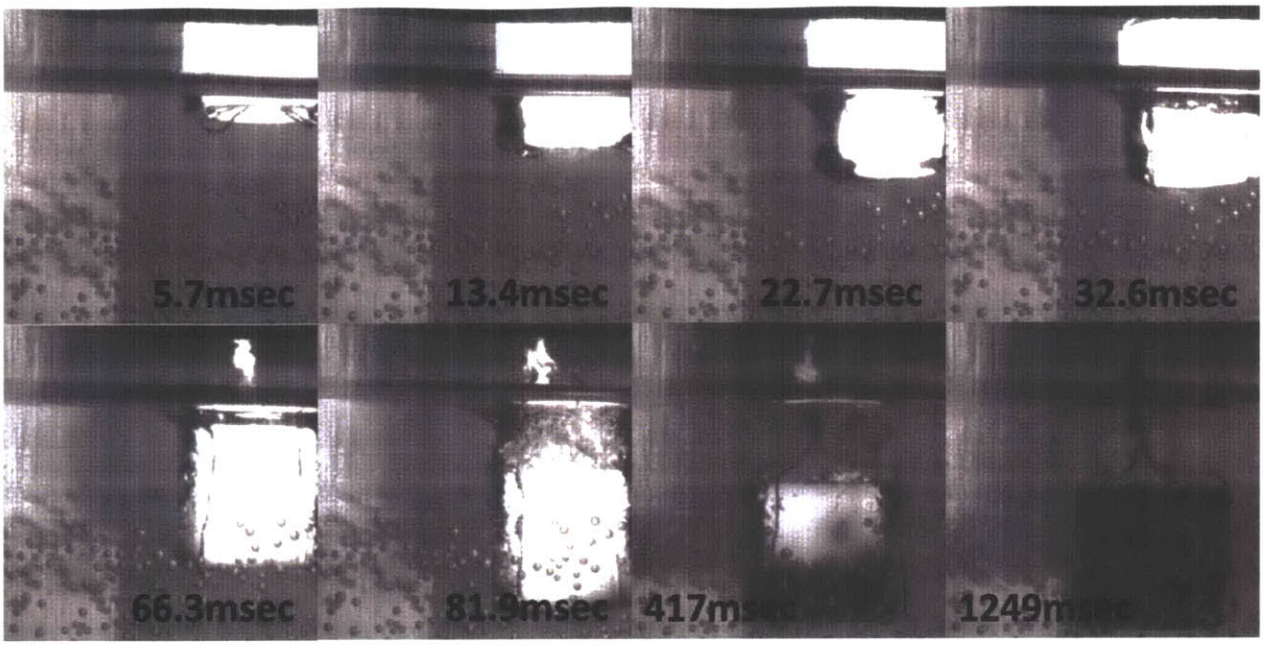

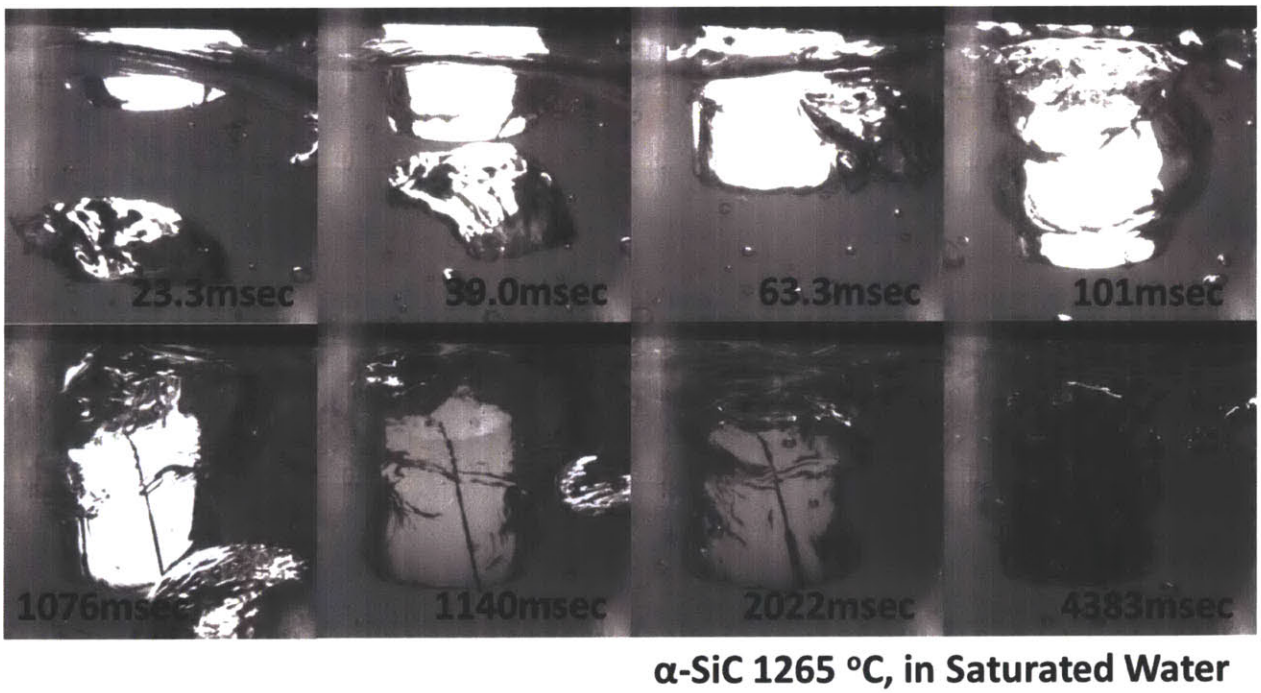

Figure 6-12 Boiling Characteristics of α-SiC at 1265°C Quenched in subcooled (22°C) and saturated (100°C) water [Specimen size: 14mm(*OD*) x 1.56mm (*t*) x 13 mm (*l*)]

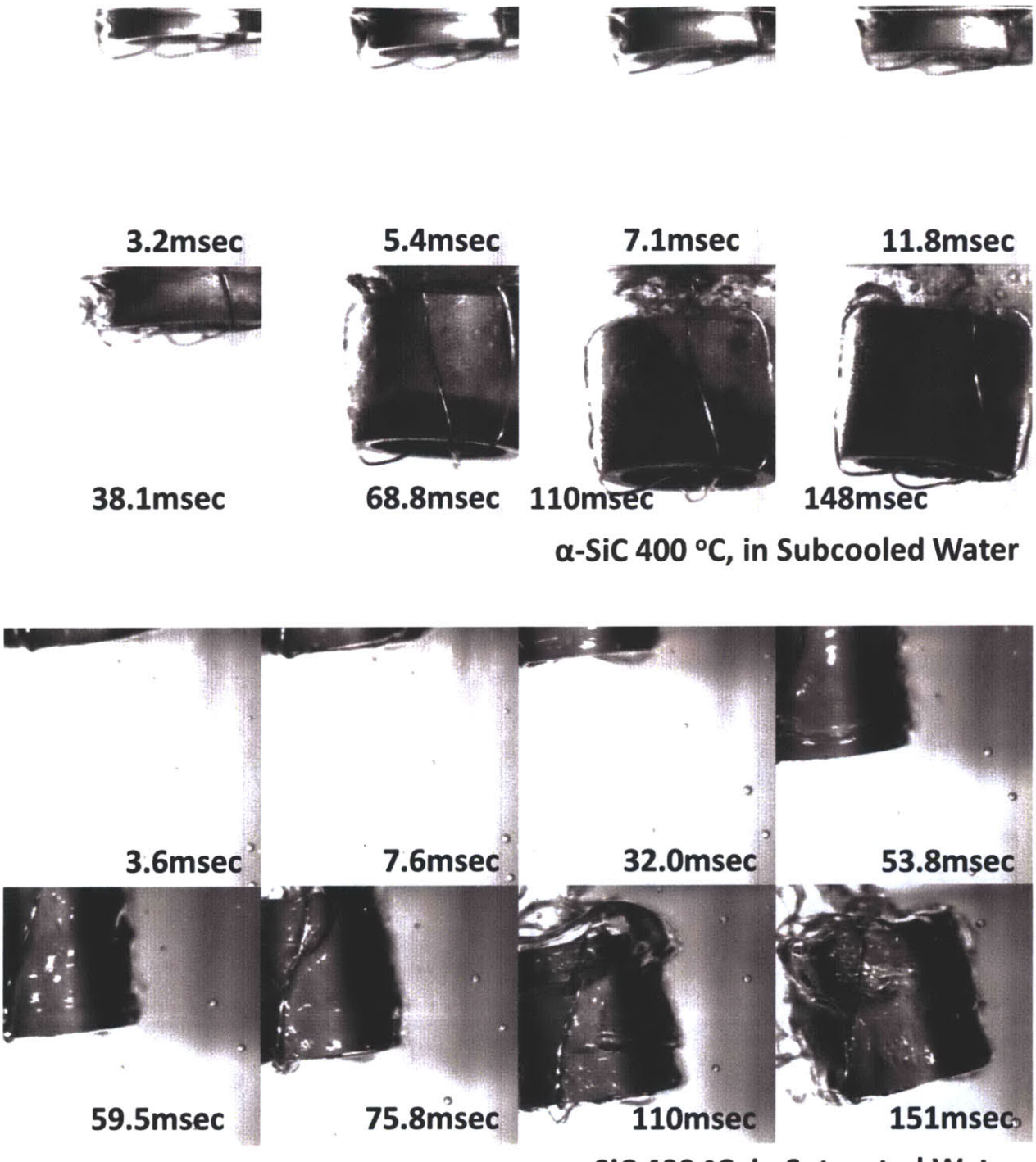

Figure 6-13 Boiling Characteristics of α-SiC at 400°C Quenched in subcooled (22°C) and saturated (100°C) water [Specimen size: 14mm(*OD*) x 1.56mm (*t*) x 13 mm (*l*)]

6.3 Thermal Shock Fracture Analysis Procedure

During a quenching transienct, thermal stresses arise from transient temperature distributions in a solid that cause differential thermal expansions. These thermal stresses are further concentrated at pre-existing flaws. If such a stress level at any location in the material reaches a critical value determined by the bonding strength of the material, then the crack starts to propagate to release its elastic-strain stored energy by creating new surfaces.

In this section, first the transient energy equations are solved to obtain the transient temperature fields. These temperature fields are then inputted into the elastic stress-strain equations to obtain the transient stress fields. Obtained transient stress fields are then used to calculate thermal stress intensity and this transient thermal intensity is used to analyze material fracture.

Eq.(6-1) is used to calculate the transient temperature distribution early in the quenching transient. The obtained temperature fields are then used as input to the elastic stress-strain equations. For a rectangular specimen, the following equation can be used to calculate the axial thermal stress for a given temperature distribution in its width (Boley, 1960)

$$\sigma_x = \alpha E\left(-T + \frac{1}{2h}\int_{-h}^{h} T dz + \frac{3z}{2h^3}\int_{-h}^{h} T z dz\right) \tag{6-15}$$

where h is half of its width, z is the location into the width.

For tubular specimens, the following equation is used to calculate the transient circumferential thermal stresses fields.

$$\sigma_\theta = \frac{\alpha E}{r^2}\left(\frac{r^2 + a^2}{b^2 - a^2}\int_a^b T r dr + \int_a^r T r dr - T r^2\right) \tag{6-16}$$

The stress intensity can then be calculated with the obtained stress fields. Evaluation of stress-intensity requires the size and geometry of pre-existing crack. Two different Griffith cracks are considered in this study: an internal crack of size $2a_{c,internal}$, and a surface crack of size $a_{c,surface}$. Their schematic illustrations are shown in Figure 6-14.

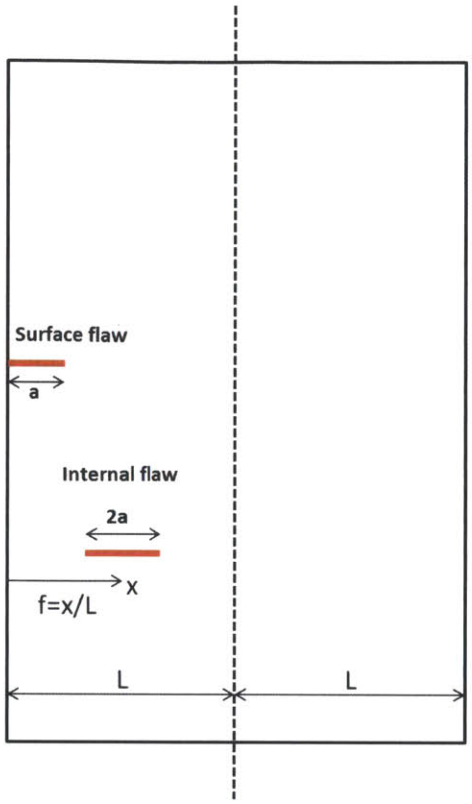

Figure 6-14 Schematic Illustration of Surface and Internal Griffith Crack (The factor f (=x/L) indicates the position of an internal crack with respect to the surface)

Their initial sizes can be obtained from the fracture loading data presented in Chapter 5 by Eq.(6-17), and (6-18), respectively (Hasezaki, 2007) (Landwehr, 2008)[25]. The flaw sizes are summarized in Table 6-1.

$$a_{c,internal} = \frac{{K_{IC}}^2}{\pi {\sigma_f}^2} \tag{6-17}$$

$$a_{c,surface} = \frac{{K_{IC}}^2}{\pi\left(1.12\sigma_f\right)^2} \tag{6-18}$$

[25] There is an adjusting factor that takes into account the geometry and the size of the solid that a pre-existing flaw sees. In this study, the sizes of pre-existing flaws are the orders of magnitude smaller than the sample size. There, samples are assumed to see an infinite slab to pre-exisiting flaws (geometry factor =1)

where K_C is the fracture toughness of the material, and σ_f is the fracture stress.

Table 6-1 The Critical Flaw Size of the Tested Specimens as Determined by the Griffith Fracture Criterion

	K_C (MPa $m^{1/2}$)	Internal Critical Flaw Size, $2a_{c,internal}$ (μm)	Surface Critical Flaw Size, $a_{c,surface}$ (μm)
Sintered α-SiC	3.1	186	74
CVD β-SiC	3.5	15	6
High Temperature Dense Al_2O_3 S1 [30mm x 3.175 mm x 3.175 mm]	4	59	24
High Temperature Dense Al_2O_3 S2 [30mm x 6.35 mm x 6.35 mm]	4	72	29

Note that the slight difference in the critical flaw size between the two different sizes of Al_2O_3 should be interpreted as the critical flaw expected for the given volume of the specimen. In that, with increasing volume of the material, the material could be expected to have a higher chance of containing the critical flaw. For CVD β-SiC, and Al_2O_3 (both are pore free), their critical flaws are of the same order or at most one order of magnitude greater than their grain sizes, 1~5μm for CVD SiC (Snead, 2007), and 1~6μm for Al_2O_3 (Munro (B), 1997). This implies that the critical flaw for those materials is essentially an assembly of grain boundaries in a connected form. Sintered α-SiC exhibits critical flaw sizes far greater than its grain boundary sizes (~5 μm) but similar to their typical pore size (10~50 μm). This demonstrates that the clusters of pores in a connected form serve as the critical flaw for the tested porous sintered α-SiC. The critical flaw sizes in Table 6-1 are used as reference crack sizes in the following discussion in the prediction of the thermal shock fracture.

In the thermal shock case, a crack sees a spatially varying stress field over its length. Usually weight functions are used to account for the spatial variation of the stress fields in the thermal stress intensity factor (TSIF). In this study, an extensively used TSIF for a surface Griffith crack of length a in the literature, Eq.(6-19)[26], was used (Abe, 1996), (Lee, 2009).

[26] Note that Eq.(6-19) gives the same expression as Eq.(6-17), $K_I = 1.12\sigma\sqrt{\pi a}$ if $\sigma(x) = \sigma$

$$K_I(t) = 2.24\sqrt{\frac{a}{\pi}}\int_0^a \frac{\sigma(x,t)}{\sqrt{a^2-x^2}}dx \tag{6-19}$$

The following equation for the TSIF was used for a central Griffith crack (Sih, 1962), (Shah, 1971).

$$K_I(t) = \frac{1}{\pi a^2}\int_{-a}^{a} \sigma(x,t)\left(\frac{a+x}{a-x}\right)^{1/2} dx \tag{6-20}$$

When stress intensity exceeds the fracture toughness ($K_I(t) > K_C$) then the material fracture occurs along with strength degradation. Appropriate temperature extrapolations of relevant material properties for α-SiC, CVD-SiC, and Al_2O_3 were done by referring to studies by Munro.et.al (Munro (A), 1997), and (Munro (B), 1997) for α-SiC, and Al_2O_3, respectively, and by Snead,et.al. (Snead, 2007) for CVD-SiC.

6.4 Heat Transfer Origin of Brittle Fracture: Transient Conduction Dominant Heat Transfer

The typical transient temperature and stress fields of a quenched specimen are shown in Figure 6-15 by showing the temperature and stress fields of Al_2O_3 specimen of size, 30mm (l) x 3.175mm (w) x 3.175mm (t). Note that while some surface regions are in tension, the inner region of the material is in compression. Hence, cracks near the solid surface are primarily relevant to thermal shock fracture during a quenching transient.

From a thermal shock fracture view point, the stress levels at surface flaws are important during the quenching transient. The infinite temperature gradient and the infinite stresses at the surface at time =0, are regulated over the finite length of the crack[27]. Average stresses that the crack sees increase with the initial thermal front propagation and start decreasing later. In Eq.(6-19), local stresses have increasing importance in TSIF, as the position gets closer to the crack tip (x→a). As a consequence of the thermal front propagation, the stress intensity at the crack tip of a pre-existing flaw exhibits time-dependent behavior which maximizes the stress concentration at the critical time, t^* ($K_I(t^*) = K_{I,max}$).

---

[27] In fracture mechanics, singularity nature of stress concentrations near the crack tip is regulated over the finite length scale.

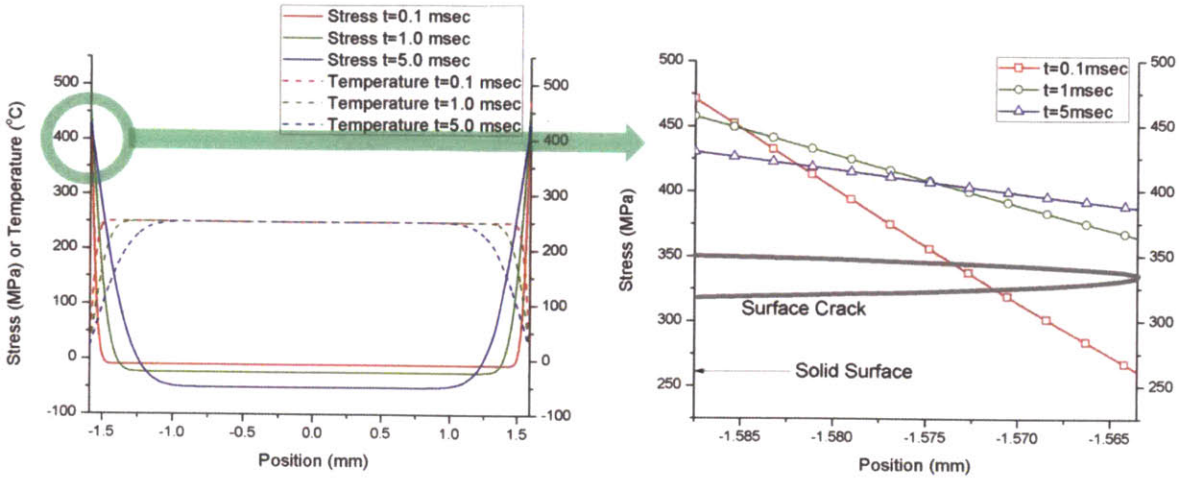

Figure 6-15 Temperature and Stress Distribution of Al_2O_3 of 3.175mm width, and the Magnified Stress Distributions along the Surface Crack Length (24μm), T=250°C, and T_{water}=22°C

The thermal stress intensity of the Griffith-surface crack of α-SiC in the early quenching transient is shown in Figure 6-16. The model predicts the critical temperature of the material that causes thermal shock fracture to be T_c ~250°C, and T_c ~1300°C for quenching in 22°C, and 100°C (saturated) water, respectively. The experimental data presented in chapter 5 finds the critical temperature to be $T_c \leq 350$ °C, and $T_c > 1265$ °C, for quenching in 22°C, and 100°C (saturated) water, respectively. The time when material starts propagating cracks can be found from when the stress intensity curve intersects the fracture toughness. Figure 6-17 shows that material fractures occur in the first 1 millisecond of the quenching transience – suggesting that conduction dominant heat transfer is the origin of the thermal stresses for the brittle fracture. The rate of stress intensity changes becomes a little slower in saturated water quenching. Yet, fracture still occurs during the conduction dominant heat transfer period as the stress intensity of the material violates the fracture toughness before the first 2 milliseconds of the quenching transient.

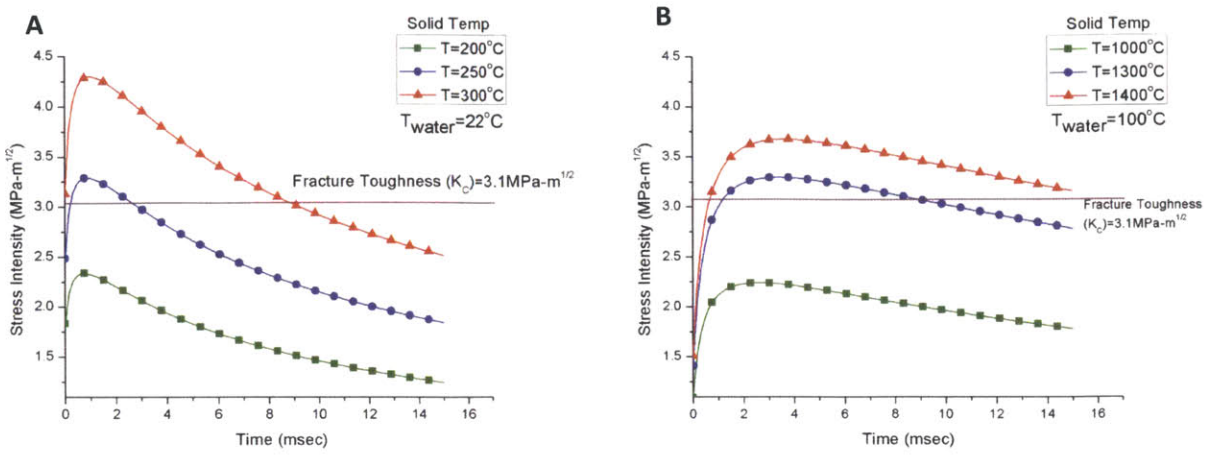

Figure 6-16 Thermal Stress Intensity Factor of Sintered α-SiC
[14mm(*OD*) x 1.56mm (*t*) x 13 mm (*l*), surface crack size 74μm]

Similar analysis holds for Al_2O_3. The model predicts the critical temperature of Al_2O_3 of the size - 3.175 mm(*w*) x 3.175mm(*t*) x 30 mm(*l*) - to be 250~300°C, and ~1000 °C for quenching in 22°C, and 100°C (saturated) water, respectively as shown in Figure 6-17. The experimental data presented in chapter 5 finds the critical temperature to be $T_c \leq 500$ °C, and $T_c > 1260$ °C, for quenching in 22°C, and 100°C (saturated) water, respectively. At the critical temperatures, fractures are expected to occur during the first 5 milliseconds and between 5~10 milliseconds of the quenching transient.

A larger material size yields a higher stress level under the identical heat transfer environment. As result, the identical Al_2O_3 with the doubled specimen width and thickness gives a lower critical temperature. The model predicts the critical temperature of Al_2O_3 of the size – 6.35 mm(*w*) x 6.35mm(*t*) x 30 mm(*l*) - to be 250°C, and ~700 °C for quenching in 22°C, and 100°C (saturated) water, respectively, as shown in Figure 6-18. The experimental data presented in chapter 5 finds the critical temperature to be $T_c \leq 500$ °C for both quenching in 22°C, and 100°C (saturated) water. Although the model did not precisely match with the experimental result of the larger Al_2O_3 for the critical temperature prediction in saturated water quenching, it reasonably well demonstrates the trend; it predicts a significant deterioration of the strength retention effect in saturated quenching by giving the decreased critical temperature 1000°C (the thinner specimen) → 700°C (the thicker specimen). The model predicts that materials' increasing vulnerability in thermal shock with increasing size is much more evident in saturated water than in room temperature water, as $\Delta T_c \approx 50$°C in 22°C water, and $\Delta T_c \approx 300$°C in 100°C water with a sample thickness change from 3.175mm to 6.35mm.

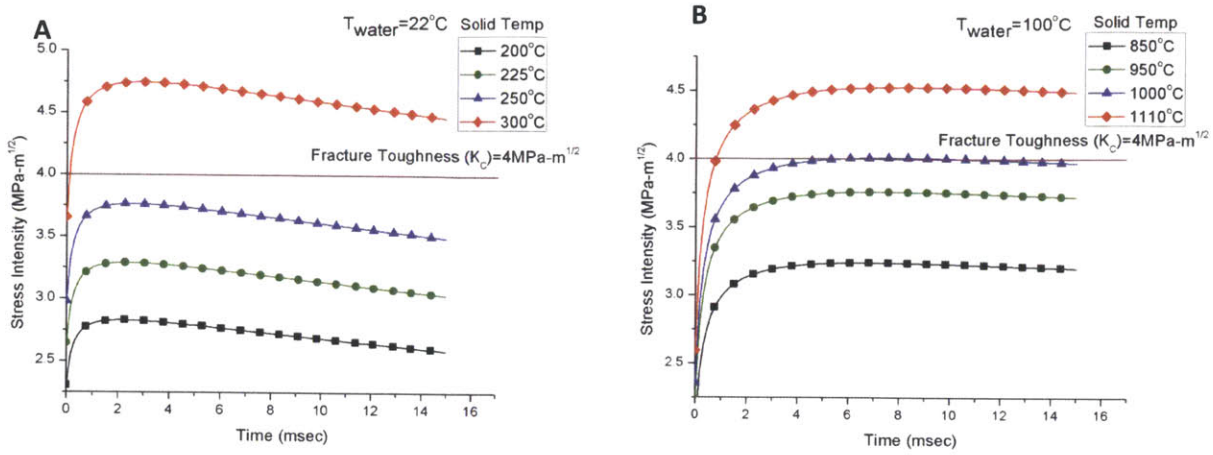

Figure 6-17 Thermal Stress Intensity Factor of Al_2O_3
[3.175 mm(w) x 3.175mm (t) x 30 mm (l), surface crack size 24μm]

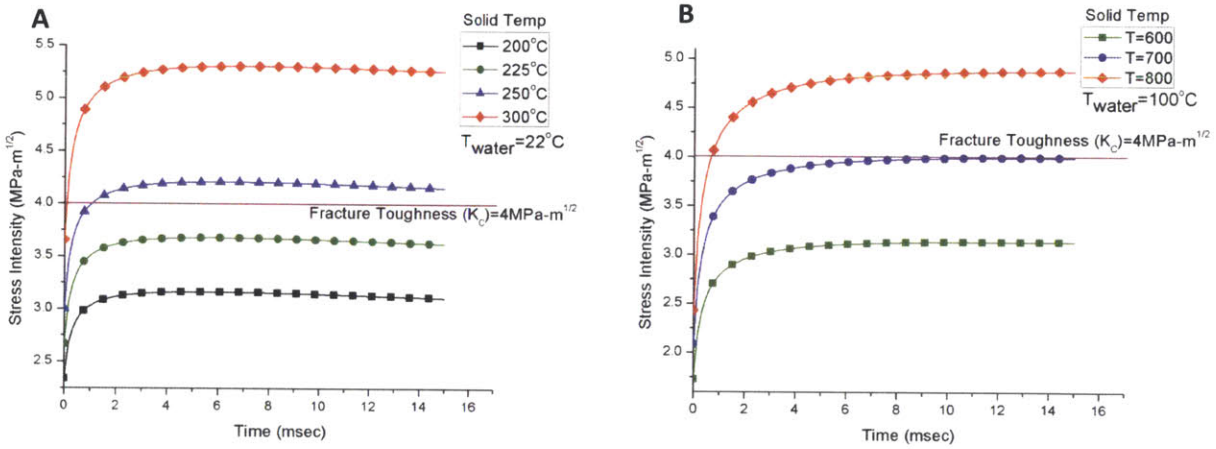

Figure 6-18 Thermal Stress Intensity Factor of Al_2O_3
[6.35mm(w) x 6.35mm (t) x 30 mm (l), surface crack size 29μm

It is worth noting that the model based on the early conductive heat transfer and a surface Griffith crack assumption gives a generally good prediction of thermal shock fracture behavior for both α-SiC and Al_2O_3. While the conductive heat transfer origin of brittle fracture may still hold for other brittle materials, the assumption of the surface crack may not be representative for some cases. For specimens with a smooth surface finish, the critical flaw has a higher chance of being an internal crack. In those cases,

TSIF of the internal Griffith crack, Eq.(6-20), would be used with the obtained characteristic internal critical flaw sizes summarized in Table 6-1.

Using TSIF of the surface Griffith crack significantly overestimates stress intensity during the quenching transient for CVD-SiC. Use of the surface crack TSIF gives critical temperature T_c =~450°C whereas the experimental investigation presented in Chapter 5 found 1260 °C ≤ T_c for CVD-SiC in 22°C water (one specimen out of three specimens exhibited strength degradation at 1260 °C). This implies that an internal crack is likely to serve as a critical flaw for CVD-SiC. Stress intensity near an internal crack changes with respect to its location in the specimen and they are bounded by stress intensities found by the surface flaw and the central flaw. Figure 6-19 shows the stress intensity of CVD-SiC for different pre-existing flaw locations with respect to the distance from the specimen surface (f=x/L, as defined in Figure 6-14, f=1is the central crack).

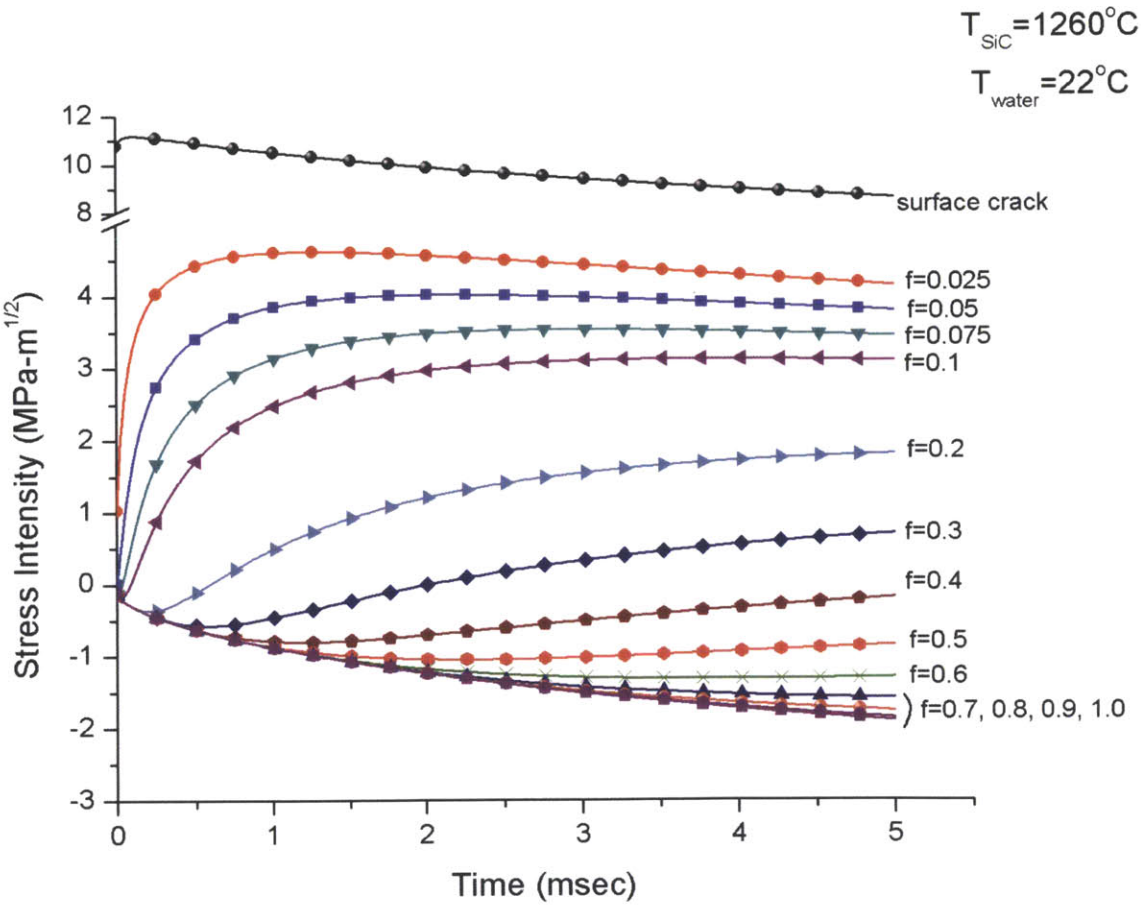

Figure 6-19 Stress Intensity of CVD-SiC [2.0mm(w) x 1.5mm (t) x 25 mm (l), surface crack size 6μm, internal crack size 15μm], T=1260°C, and T_{water}=22°C, K_c=3.5MPa-$m^{1/2}$

For the observed CVD-SiC fracture at 1260°C, it could be inferred from Figure 6-19 that a critical internal flaw located in the distance of 5%~7.5% of the half-thickness of the specimen from the surface (f=0.05-0.075) is likely to have caused the fracture. A pre-existing flaw whose location is f<0.05 would have caused fracture at temperature below 1260°C. Because of rapid thermal front propagation on the micron scale flaws, fractures occur within the first 5 milliseconds for those internal cracks located near the surface (f=0.05~0.075). Stress intensities are particularly sensitive to the location of a pre-existing flaw as it gets closer to the surface. In contrast, the stress intensity of a pre-existing flaw near the center of the specimens is not affected by its location during the early quenching transient as it barely feels the thermal front propagation (see f=0.7, 0.8, 0.9, and 1.0 in Figure 6-19).

It should be noted that a statistical approach may be more suited for the thermal shock fracture if a material's critical flaws are likely to be the internal cracks. In such a case, the random nature of the pre-existing flaw location would amplify the statistical nature of the brittle fracture beyond the flaw size distributions. Yet, for the internal flaw driven thermal shock fractures, stress intensities obtained by a surface crack could serve as a ceiling value.

The model predicts an extraordinary thermal shock tolerance of the tested CVD-SiC in saturated water. In saturated water, the ceiling stress intensity obtained by the surface crack gives a peak stress intensity around 30% of its fracture toughness for T=1800°C, as shown in Figure 6-20.

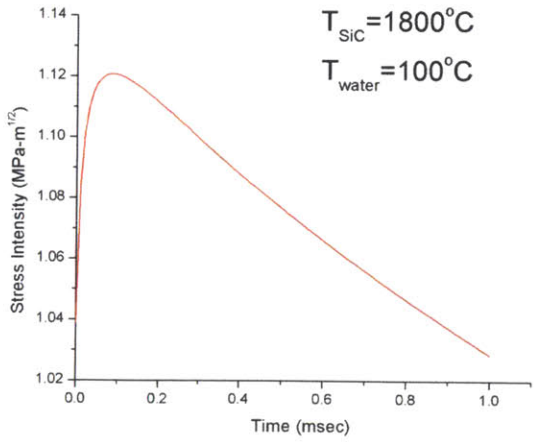

Figure 6-20 Surface Crack Stress Intensity of CVD-SiC
[2.0mm(w) x 1.5mm (t) x 25 mm (l), surface crack size 6μm], K_c=3.5MPa-m$^{1/2}$

Such an excellent thermal shock tolerance of CVD-SiC in saturated water would be better for a SiC cladding whose thickness is ~30% of the width of the tested specimens. The experimentally obtained and the calculated critical temperatures for the tested specimens are summarized in Table 6-2.

Table 6-2 Summary of Critical Temperatures for Thermal Shock Fractures

	Critical Temperature for Thermal Shock Fracture in 22°C Water (T_c, °C)		Critical Temperature for Thermal Shock Fracture in 100°C Water (T_c, °C)	
	Experiment	Calculated	Experiment	Calculated
Al_2O_3 Size 1	≤500	275	>1260	1000
Al_2O_3 Size 2	≤500	250	≤500	700
Sintered α-SiC	≤350	250	>1260	1300
CVD-SiC	1260 ≤	450	≥1260	≥1800

*Calculations were done with the surface Griffith crack assumption. CVD-SiC may be more suitably represented by the internal crack for TSIF calculation.

The fracture prediction model demonstrated that the fracture occurs during the very early phase of quenching transient, when the conductive heat transfer between the solid surface and the fluid is the primary heat transfer mechanism. This is related to the required time for the thermal front to propagate through pre-exisiting flaws near the solid surface. Characteristic thermal front propagation length δ in a solid can be expressed by assuming the temperature follows a linear distribution near the solid surface (Han, 1962)

$$\delta = \sqrt{\pi \alpha t} \tag{6-21}$$

where α is the thermal diffusivity ($k/\rho C_p$), and t is the time.

Beyond the thermal front propagation distance δ, the solid essentially does not feel the temperature perturbations at the surface. While the typical ranges of ceramic thermal diffusivities are $10^{-6} \sim 10^{-5}$ m^2/sec, the required time t for propagating through a pre-existing flaw length is shown in Figure 6-21.

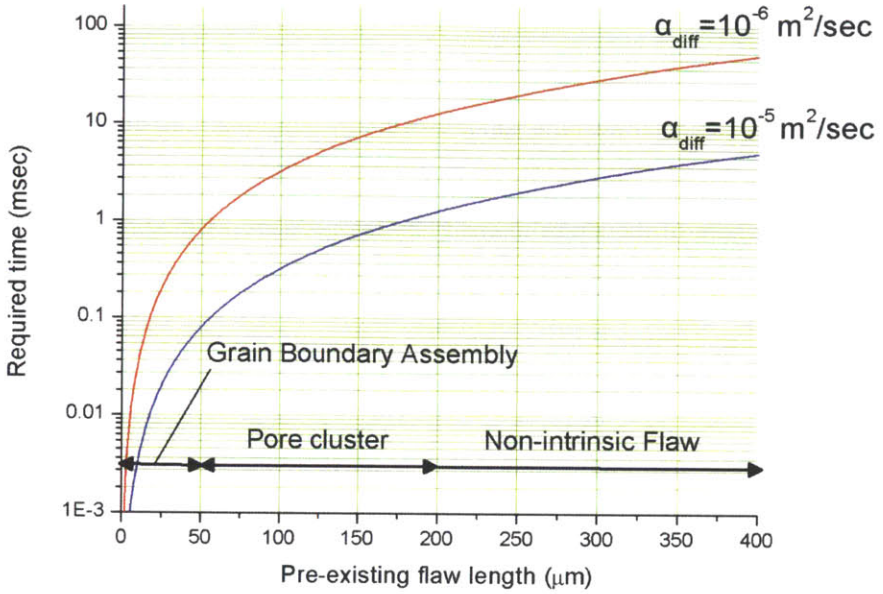

Figure 6-21 Characteristic Thermal Front Propagation Time with Ranges of Pre-Existing Flaw Length

The time t in Eq.(6-21) is closely related to the time required to reach the peak TSIF upon the arrival of thermal front on a flaw. That is, a pre-existing flaw would start to be 'activated' as it starts to feel the thermal front and the TSIF starts to decrease as the thermal front passes through the flaw. Fractures that are caused by a pre-existing flaw of a grain boundary assembly would be initiated in the order of 0.1 ~ 1 milliseconds upon the strike of the propagating thermal front on the flaw, as shown Figure 6-21. Pore clusters would require a time in the order of 1~ 10 milliseconds after the crack feels the thermal front. Hence, fractures due to material's intrinsic pre-existing flaws would take place during the conduction dominant heat transfer mode, which lasts roughly ~10 milliseconds for the near surface position. In that regard, flaws near the middle of a material would be relevant to stress fields given by the film boiling heat transfer mode later in the quenching transient. In that case, the stress levels near the flaw would be significantly lower for those internal flaws because (1) the slower heat transfer of the film boiling process, and (2) the flatter temperature gradients in the middle of the material in comparison with the surface locations at the same time.

6.5 Implications on SiC Cladding Performance with Quenching by Reflooding Water

Linear elastic fracture mechanics allows the superposition of more than one-type of loading on the crack tip stress fields by adding the individual effects. Hence, the total stress intensity of SiC cladding during accidents, $K_{total}(t)$ is the sum of the stress intensity by the pressure loading $K_{loading}(t)$ and the thermal stresses $K_{TSIF}(t)$ as shown in Eq.(6-22)[28].

$$K_{total}(t) = K_{loading}(t) + K_{TSIF}(t) \tag{6-22}$$

It was found that CVD-SiC exhibits a superior tolerance in thermal stresses in saturated water at atmospheric pressure. In saturated water, the ceiling stress intensity obtained by the surface crack gives the peak stress intensity around ~1.1 MPa-m$^{1/2}$ (~30% of the fracture toughness) for T=1800°C with the specimen 3.5 times thicker than the typical LWR cladding.

Hence, a suitable approach to assure the structural integrity of a SiC cladding during an accident condition would be to allow a safety margin, χ, on $K_{loading}(t)$ to assure that $\chi K_{loading}(t) > K_{loading}(t) + K_{TSIF}(t)$ during an accident. The detailed analysis of fuel cladding performance with respect to thermal shock during a reflood phase is discussed in chapter 7.

6.6 Conclusion

This chapter revealed that the initial heat transfer upon contact between the solid and the fluid in the early quenching transient is the controlling origin of the thermal shock induced brittle fracture. The study developed a thermal shock fracture prediction model for the early quenching transient based on the conductive heat transfer modes between the solid surface and the fluid, and the Griffith flaw assumptions. The model demonstrated reasonable predictability for the critical temperature for thermal shock fractures for room temperature and for saturated water; it captures strength retention in saturated water quenching that varies with specimen sizes. Internal flaw induced fractures are sensitively dependent on flaw locations; hence the statistical approach is suited for those cases. The developed model can be used for general brittle thermal shock induced fractures, including the quenching of SiC cladding during a reflood phase.

[28] $K_{loading}(t)$ includes the steady-state thermal stresses

Chapter 7

Simulation of Light Water Reactor Fuel with SiC Cladding

7.1 Introduction

In engineering a novel nuclear fuel rod, there is always a gap between our understanding of relevant individual physics areas and the actual fuel behavior overlapped by simultaneous multi-physics. In addition, for most cases, experimental investigations and models require extrapolations to the actual reactor environment. Fuel rod simulation is a bridge that integrates the gap between individual engineering of relevant physical phenomena into a systemic interpretation.

The studies on oxidation, and brittle fracture of SiC cladding, presented in chapters 2 – 6, explored key phenomenological aspects of SiC cladding operating performance and safety. In this chapter, these individual SiC cladding behaviors are integrated into a fuel rod simulation in a PWR. Hence, the failure mode informed fuel rod simulations are conducted to envision its performance during steady-state, and accident conditions.

7.2 Fuel Rod Simulation Approach, and Structure

The steady-state performance was investigated, as a first step in simulating the SiC clad fuel rod behavior. The steady-state oxide fuel performance code FRAPCON-3.4 was modified with relevant SiC cladding properties to an updated FRAPCON-3.4 SiC. Pin power history and axial distribution was obtained from the neutronics core design study of Bloore. et.al (Bloore, 2013). The cladding mechanical model of FRAPCON-3.4 is not suited to model SiC cladding – The original cladding mechanical model of FRAPCON is for a single layer Zircaloy cladding, whose failure occurs in a deterministic way. Hence, SiC cladding mechanical model developed in Chapter 3 that captures multilayers stress resolutions with statistical fracture mechanics was used to interpret the mechanical response of SiC claddings under simulated steady-state fuel rod conditions.

For accident analysis, the steady-state burnup initialized parameters from FRAPCON-3.4 SiC are fed into a transient-accident simulation module. This module was developed in this study to calculate the transient temperature distributions in the multilayer SiC cladding by solving transient energy equations with an input of thermal-hydraulic conditions during an accident from RELAP-3D simulations. The calculated transient cladding temperature distributions during an accident, and fuel rod pressurization are fed into the SiC cladding mechanical model developed in Chapter 4 for the stress calculations and the statistical fracture analysis. In addition, the models for oxidation rate and thermal shock fracture developed from the experimental studies in Chapter 2 ~ 6 are incorporated in the accident simulation module to evaluate SiC cladding behavior under steam-oxidation and thermal shock fracture during the accident. The described fuel rod simulation structure is illustrated in Figure 7-1.

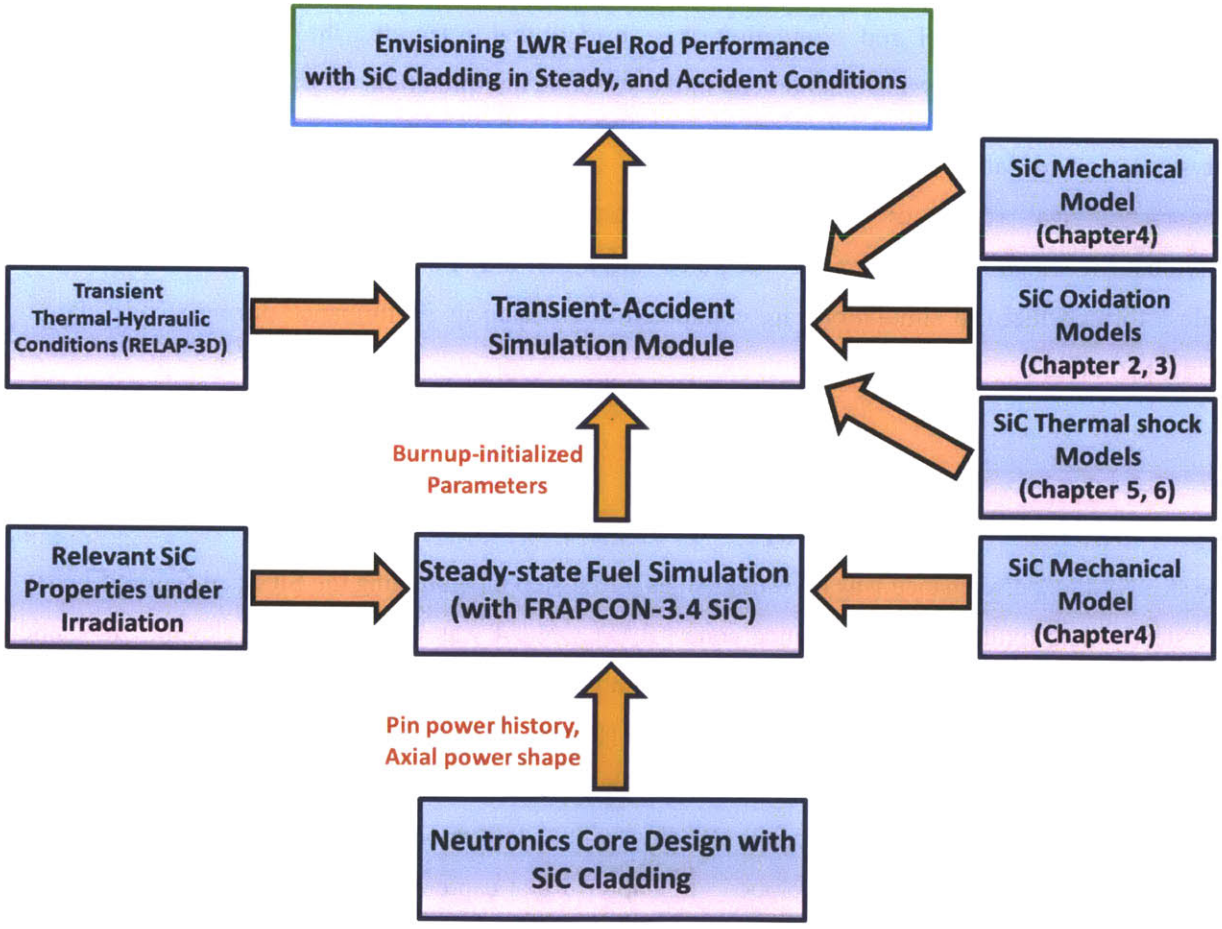

Figure 7-1 Fuel Rod Simulation Structure for Assessment of Fuel Rod Performance with SiC Cladding

With the discussed fuel rod simulation strategies, we expect to evaluate (1) allowable maximum steady-fuel rod burnup in steady-state, (2) safety margin in terms of the cladding stresses to accommodate design basis accidents, (3) key steady-state and accident behavior characteristics of LWR fuel rod with SiC cladding, and (4) design directions of the fuel rod with SiC cladding.

7.3 Steady-state Fuel Rod Simulation with FRAPCON-3.4 SiC

Steady-state performance of LWR fuel rods with SiC cladding is analyzed in this section with an updated steady-state fuel performance computer code FRAPCON 3.4 SiC coupled with the SiC cladding mechanical model presented in Chapter 4.

7.3.1 FRAPCON-3.4 Update with SiC Cladding

FRAPCON- 3.4 is the latest computer code for a steady-state fuel performance analysis developed by the Pacific Northwest Laboratory for use by the U.S NRC. The code calculates key fuel rod performance metrics at discrete steady-state operating time steps. It uses a continuum level mechanical model with empirical relations for most of the individual physical phenomena including swelling, oxidation, and fission gas release, etc. FRAPCON's input consists of pin power history and shape, fuel rod dimensions, and coolant side thermal hydraulic conditions. A full description of the code can be found in its manual (Pacific Northwest National Laboratory, 2011).

FRAPCON-3.4 was modified to SiC cladding in this study. Most of the cladding properties were adopted from previous work of Carpenter et.al for FRAPCON-3.3 update with SiC cladding (Carpenter, 2007), (Carpenter, 2010). As stated in the literature of Carpenter (Carpenter, 2010), the following cladding properties were changed

"- *Axial growth*

- *Creep*

- *Elastic limits*

- *Elastic modulus*

- *Emissivity*

- *Hardness*

- *Melting point*

- *Oxidation*

- *Shear modulus*

- *Thermal conductivity*

- *Thermal expansion"*

This study made changes to the following properties, summarized in Table **7-1** to reflect more representative SiC cladding properties

Table 7-1 Updated SiC Cladding Properties of FRAPCON-3.4 SiC

	Changes from Carpenter's SiC cladding update with FRAPCON-3.3	Reference
Thermal Conductivity	The minimum saturated thermal conductivity is 4.8W/m-K with respect to temperature and radiation dose	Thermal conductivity measurement for irradiated triplex cladding at MITR (Stempien, 2011)
Elastic Modulus	460 GPa at room temperature	Rohm and Haas CVD SiC, i.e., a polycrystalline, highpurity, and very dense, pore-free SiC
Poisson Ratio	0.21	

*The same temperature and fluence dependence was used as the previous update of FRAPCON-3.3 with SiC by Carpenter.et.al (Carpenter, 2007), (Carpenter, 2010).

The external module of the multilayer SiC cladding mechanical model presented in Chapter 4 is separately used for the mechanical analysis of the cladding with an input of plenum pressure, and cladding temperature obtained by FRAPCON 3.4-SiC. Hence, the elastic modulus and poisson ratio input for the single layer cladding calculation do not practically affect the analysis as long as the input values represents the high stiffness of the SiC cladding, which gives negligible elastic-strain for the fuel simulation. A recent investigation explored irradiation induced creep of SiC (Katoh, 2013) and setting the cladding irradiation creep = 0 seems to be a viable assumption for the purpose of the LWR fuel modeling, as the study found that the irraidation creep for SiC is signficantly smaller than that of the typical metallic material.

A typical PWR fuel rod is the reference fuel rod design of this study. The FRAPCON input parameters for the reactor operating conditions and the reference fuel rod design parameters are summarized in Table 7-2.

Table 7-2 Summary of the Reference FRAPCON-3.4 SiC Input Parameters

Design parameters	**Value**
Operating pressure	15.5 MPa
Coolant temperature	291.9 °C
Coolant mass flux	3336.6 kg/m^{2}s
Cold plenum length	0.175 m
Cladding thickness	0.57 mm
Cladding outer diameter	9.50 mm
Cladding-fuel gap thickness	0.08255mm
As-fabricated apparent fuel density	95%
Fuel pellet end-dish shoulder width (outer radius of fuel pellet minus radius of dish)	2.05mm
Outer diameter of plenum spring	8.128mm
Diameter of the plenum spring wire	1.27 mm
Enrichment	4.4%
Initial fill gas pressure (taken to be at room temperature)	2.413 MPa (Helium)
Height of each fuel pellet	0.98 cm
Height (depth) of pellet dish, assumed to be a spherical indentation	0.287 mm
Active fuel column length	3.658 m
Inner pellet void radius	1.296 mm
Number of turns in the spring	28

7.3.2 Neutronics Input for Pin Power

The pin power input for the FRAPCON-3.4 SiC was extracted from the neutronics core optimization study of Bloore.et.al (Bloore, 2013). The study utilized CASMO-4E and SIMULATE-3 to neutronically optimize burnable poison layout and core reload pattern for an 18 months long, 3 batch fuel cycle at equilirbium. In this study, the highest burn up fuel pin power history extracted from the core design of Bloore's study was used as a reference input for FRAPCON-3.4 SiC. This pin power history is shown in Figure 7-2.

The reference fuel pin power history and corresponding burnups are shown in Figure 7-2 was noramalized to its reference cycle length, and then extended to a longer cycle length. In this way, the pin power behavior with respect to the cycle length was conserved, resulting in a proportional relation between the cycle length and the brunup (e.g., 50% increase in the cycle length gives 50% increase in burnup). In the following discussions, fuel pins of the final burnup of 84MWd/kgU (25% increase from the reference pin), and 101 MWd/kgU (50% increase from the reference fuel pin) are assessed. Those burnups are based on the reference solid fuel pellets. Centrally voided fuel pellets give a higher burnup corresponding to the mass deficit.

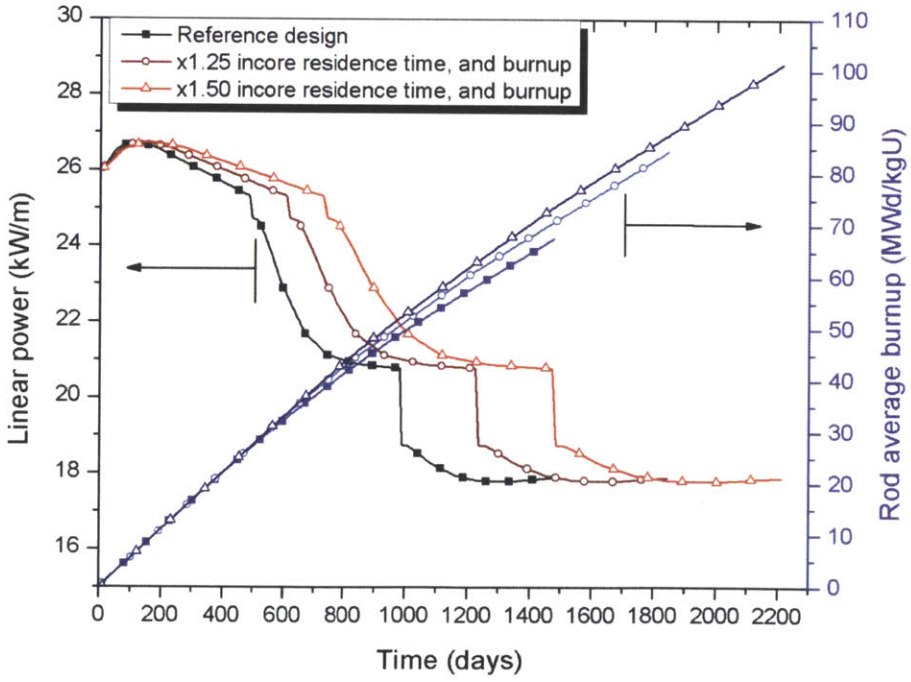

Figure 7-2 Pin Power of the Highest Burnup Fuel Pin in an Optimized Typical Westinghouse PWR Core with solid pellets with SiC Cladding [Extracted from Bloore's Work, (Bloore, 2013)]

Three axial power shapes of the highest burnup fuel pin were also obtained by the neutronics core design studies and are shown in Figure 7-3. There are three axial power shapes for each fuel reload cycle; in Figure 7-3, the first batch is shown as the beginning of life (BOL), the sencond batch as the middle of life (MOL), and the last batch as (EOL). For internally void fuel pellets, the same power history was used and the burnup increase by the fraction of fuel mass reduction (e.g 10% central void leads to 10% increase in burn up for the same power profile).

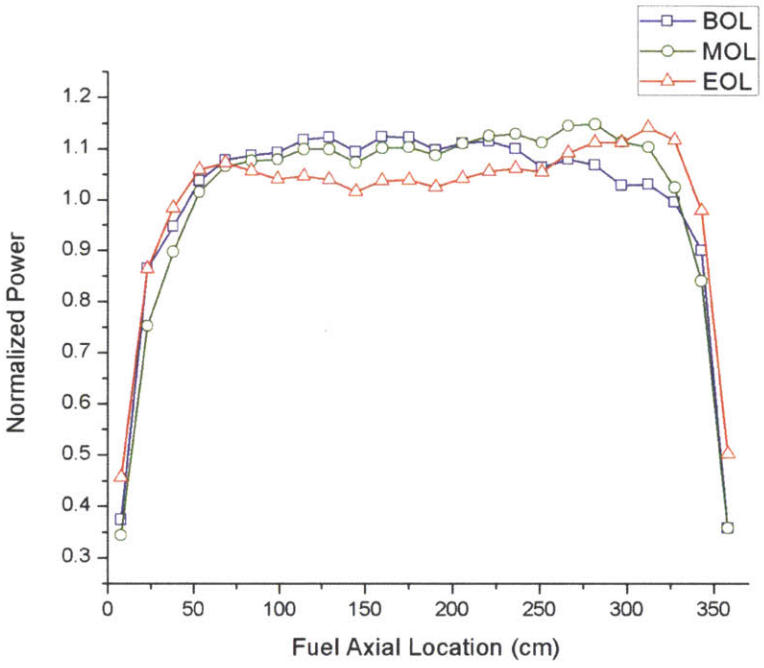

Figure 7-3 Axial Power Shape of the Highest Burnup Fuel Pin in the Optimized Typical Westinghouse PWR Core Consisting of Fuel Rods of SiC Cladding [Extracted from Bloore's Work, (Bloore, 2013)]

7.3.3 Key Fuel Behavior of LWR Fuel Rod with SiC Cladding

The radial gap between the fuel pellet and the cladding closes more slowly for the SiC cladding than the Zircaloy cladding, because the SiC cladding does not creep down on to the fuel pellet. Hence, the gap closure mechanisms for a SiC clad fuel rod are thermal expansion of fuel pellet, fuel swelling, and the elastic strain of the cladding. The results of a simulation are shown in Figure 7-4 - Figure 7-8. Note that the axial location of highest burnup node barely closes its structural radial gap at the end of the incore residence time for the standard SiC fuel rod whereas the Zircaloy cladding closes its gap during the early incore residence time at around 300 days, as shown in Figure 7-4. The fuel rod with 10% central void in

its pellets in terms of the volume fraction was also simulated. The central void in the fuel pellets further extended the gap closure time. Early gap closure in Zircaloy cladding leads to pellet-cladding mechanical interaction (PCMI), which is an issue for the structural integrity of the cladding. PCMI is the primary cause of tensile stresses for the Zircaloy cladding. In contrast, PCMI may not be the primary cause of the tensile stresses for the fuel rod with SiC cladding – the hard contact between the fuel pellet and the cladding does not occur at all in the current practice of the fuel incore-residence time (or the current practice of LWR fuel rod burnup). In Figure 7-4, the gap gets closed for the reference SiC clad fuel rod at around 1400 days. This contact, however, does not impose mechanical stresses on the cladding; the fuel first undergoes recovering its pores and cracks upon the contact before it starts to exercise tensile stresses on the cladding. This mode of contact is often termed 'soft contact'. The 'soft contact' is the relevant contact mode of the fuel and the cladding for SiC cladding unless the fuel operates far beyond the current burnup practice. Hence, plenum pressure is the primary source of the mechanical loading on the SiC cladding.

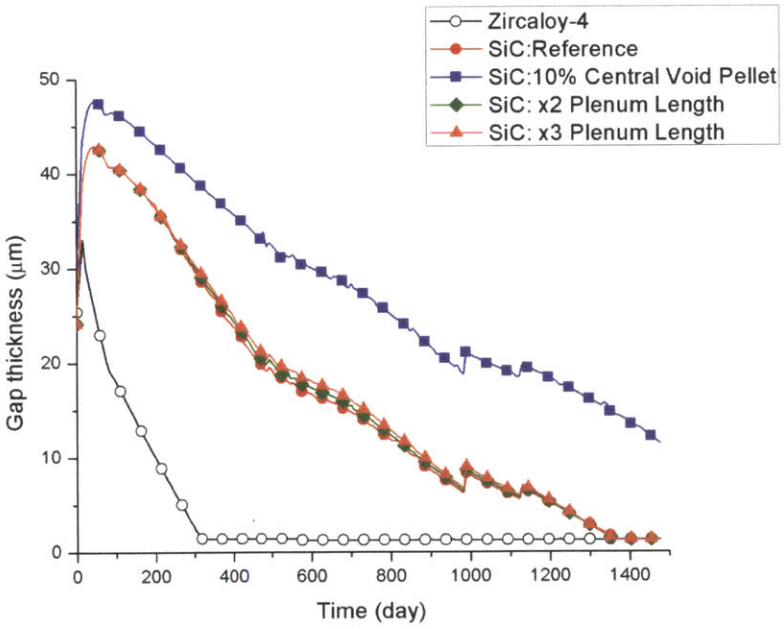

Figure 7-4 Fuel Rod Radial Gap History from FRAPCON-3.4 Simulation for the Reference Pin Power of the Peak Fuel Rod (the highest burnup node, at 2.51m from the bottom of the fuel rod is Shown)

The SiC cladding leads to a higher fuel temperature in comparison with Zircaloy cladding due to the lower thermal conductivity. The thermal conductivity of SiC cladding quickly saturates at 4.8 W/m-K after around 1 dpa of irradiation damage, while Zircaloy cladding has a thermal conductivity around ~ 15 W/m-K (Pacific Northwest National Laboratory (B), 2011). In addition the extended gap closure time

maintains the high thermal resistance of the gap, whereas the gap closure reduces the overall resistance, resulting in a fuel temperature decrease. Figure 7-5, and Figure 7-6 show the fuel centerline temperature, and the average fuel temperature, respectively. The use of SiC cladding raises fuel temperature by ~300°C. The fuel temperature difference between the zircalocy clad fuel and the SiC clad fuel decreases with the SiC gap closure and as the oxide corrosion layer grows on the Zircaloy cladding.

Increasing fuel temperature is often regarded as a source of multiple concerns; it increases fission gas release, plenum pressure, and may induce degradation of mechanical properties of the fuel materials. Also, increasing fuel temperature reduces safety margin. Clearly, the peak fuel temperature of around 1500°C is beyond the current LWR experience, which would result in serious uncertainties about the fuel performance. Therefore, a fuel pellet design with a central void is suggested primarily to reduce the fuel centerline temperature. The 10% central void can reduce the peak fuel temperature to the samel level of the current LWR fuel rod with Zircaloy cladding as shown in Figure 7-5. Pellets with central holes are routinely used in the Russian VVERs, and in the blanket section of the Westinghouse fuels. The effect on the average fuel temperature decrease by introducing a central hole is not as significant as it is for the fuel center line temperature. Figure 7-6 shows that roughly at most ~100°C of average fuel temperature reduction can be achieved by introducing the 10% central void in the fuel pellets.

FRAPCON-3.4 uses the modified Forsberg-Massih model for fission gas release of UO_2 fuel. The model caputres various parameters that affect fission gas release including temperature, burnup, pressure, and fuel microstructures (Krohn, 2006). Use of SiC cladding significantly increases fission gas release compared to Zircaloy cladding, primarily because of the fuel temperature increase as shown in Figure 7-7. In that regard, use of centrally voided pellets helps to reduce fission gas release. However, the benefit of the fission gas reduction with centrally voided fuel pellets tend to be less as burnup increases because of diminising fuel temperature reduction effects by extended gap closure time at a high burnup compared to zirconium based alloy. One can see in Figure 7-6 that the average fuel temperature of 10% centrally voided fuel pellets is even higher than reference solid fuel pellet at a high bunrup (beyond ~1000 days). As a consequence, fission gas release for the 10% central void fuel pellet exceeds that of the the reference fuel design towards the end of the incore residence time in Figure 7-7. Increasing plenum length slightly increases fission gas release while following the same behavior with respect to incore residence time of the reference fuel design. The level of the fission gas release with use of SiC cladding is signficantly beyond the current LWR experience; and it is likely to be a limiting parameter for the safety and operation of the fuel rod with SiC cladding instead of PCMI.

Fuel plenum pressure accordingly increases with fission gas release. A central void in the fuel reduces the pressure level by allowing more volume to accommodate released fission gases. Increasing plenum volume is an effective way of lowering the plenum pressure as shown in Figure 7-8. Note that for all fuel design options illustrated in Figure 7-5 - Figure 7-8 (10% central void, x2 and x3 the plenum length), the effect of plenum volume increase outweighs the increase of fission gas release, resulting in a decrease in fuel plenum pressure. The plenum pressure of the highest burnup fuel pin (68MWD/kgU) stays below the system pressure, 15.5 MPa with the suggested alterations in the fuel designs. The reference fuel design – the typcial PWR fuel rod with the sole change in cladding material from Zircaloy to SiC – would give the maximum internal pressurization, ΔP of ~4MPa.

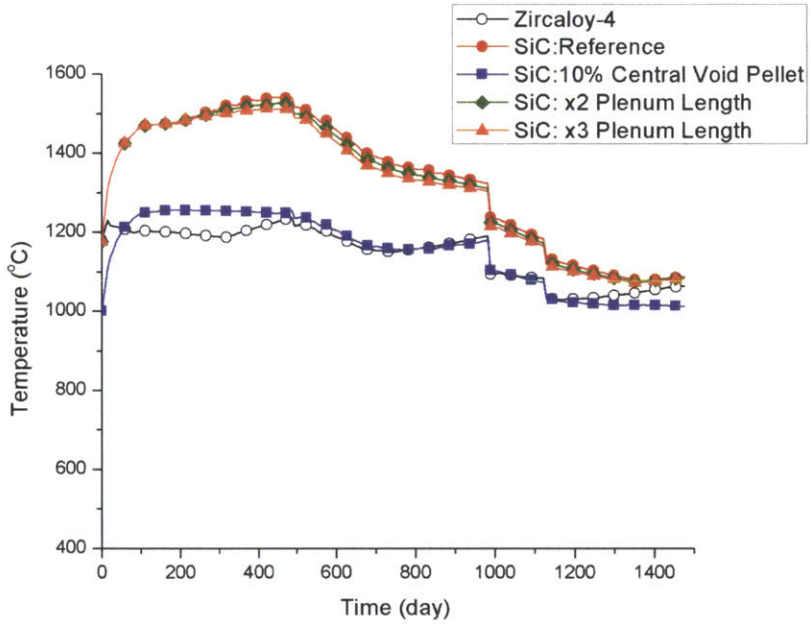

Figure 7-5 Fuel Centerline Temperature from FRAPCON-3.4 Simulation for the Reference Pin Power of the Peak Fuel Rod Burnup of 68MWD/kgU (the highest burnup node, 2.51m from the bottom of the fuel rod)

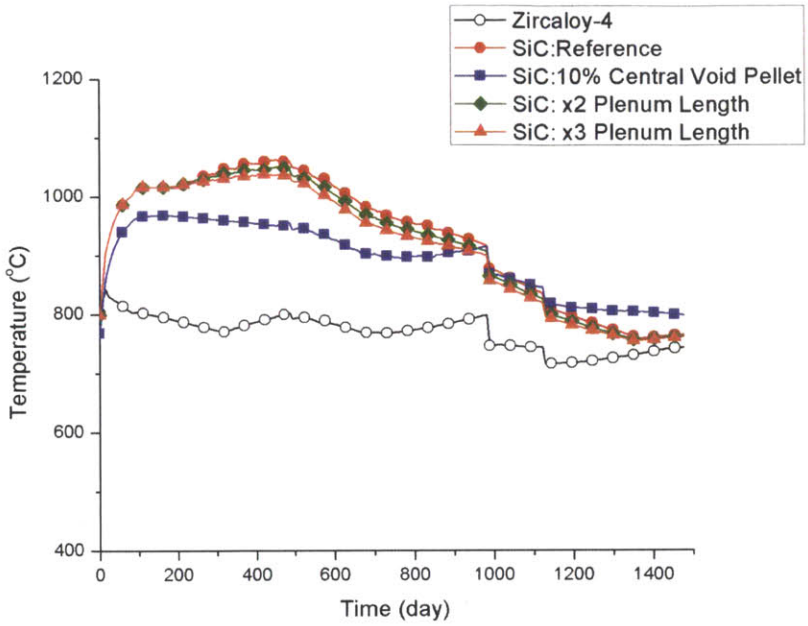

Figure 7-6 Volume Average Fuel Temperature from FRAPCON-3.4 Simulation for the Reference Pin Power of the Peak Fuel Rod Burnup of 68MWD/kgU (the highest burnup node, 2.51m from the bottom of the fuel rod)

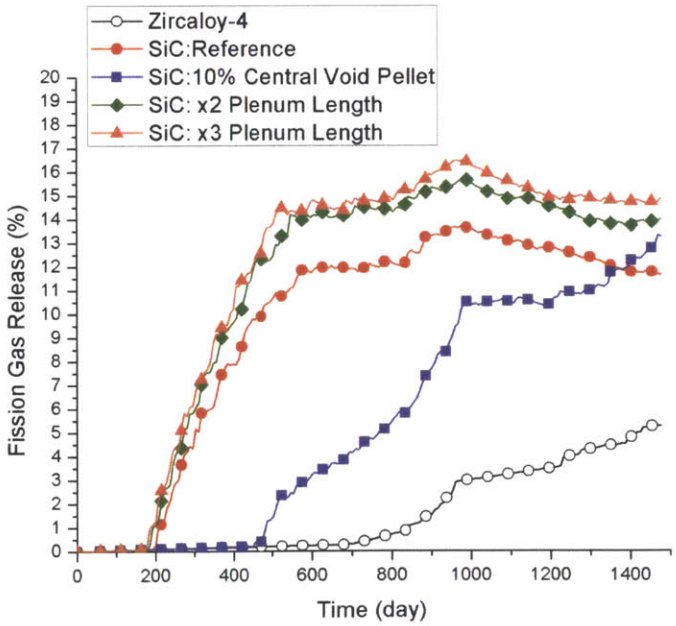

Figure 7-7 Fission Gas Release Percentage from FRAPCON-3.4 Simulation for the Reference Pin Power of the Peak Fuel Rod Burnup

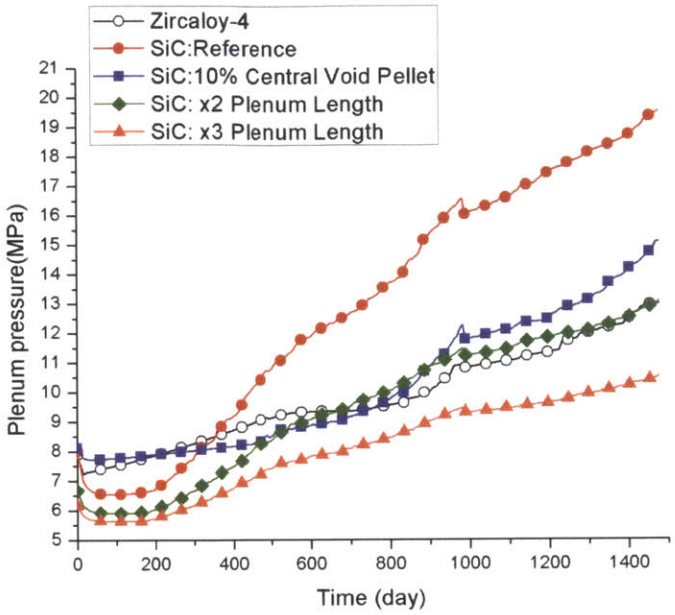

Figure 7-8 Plenum Pressure from FRAPCON-3.4 Simulation for the Reference Pin Power of the Peak Fuel Rod

7.3.4 High Burnup Assessment of LWR Fuel Rod Performance with SiC Cladding

The burnup limit of the current fuel with Zircaloy cladding has been set by the progressive embrittlement of the cladding under the reactor environment. Use of SiC cladding has a potential to increase the fuel rod burnup beyond the current limit by utilizating its material stability in the reactor environment. In this section, fuel performance analysis of SiC clad fuel beyond the current burnup limit is conducted.

(A) Peak Fuel Rod Burnup of 84MWd/kgU (solid fuel pellet), cycle length of 1845 days

The fuel and the cladding makes 'soft contact[29]' after ~1100 days of incore residence time for the solid fuel pellets while the 10% central void fuel pellet does not close the gap until the end of its incore residence time as shown in Figure 7-9. With the early saturation of the SiC reduction in thermal conductivity, fuel temperatures generally follow the same trend as the lower reference burnup case, as shown in

[29] FRAPCON-3.4 SiC reports 'gap interfacial pressure' which gives the stress caused by the solid body contact between the fuel and the cladding. This value stays 'zero' until the end of the simulation time, indicating that the apparent contact is the 'soft contact', which forces the fuel pellet to recover its pores and cracks before it starts to exert stresses on the cladding.

Figure 7-10, and Figure 7-11 . Yet, the relatively earlier gap closure of the reference solid fuel pellet with respect to the extended cycle length leads to the situation where the void fuel pellets operate at higher averge temperature than the solid fuel pellet for a considerable portion of the incore residencetime. Such a diminishing benefit of the central voided in fuel pellet is even more evident in fission gas relesease. Fission gas release of the central void fuel pellet exceeds that of the solid pellets, well in advance of the end of the cycle length in Figure 7-12. Nevertheless, the central void still lowers the final plenum pressure as shown in Figure 7-13. As a consequence of the sharp increase of the fission gas release with centrally voided fuel pellets with increasing burnup, the final plenum pressures of the fuel designs with the 10% central void in fuel pellets plus the increased plenum lengths by a factor of two or three are slightly lower than the solid fuel pellet with the increased plenum lengths. The reference fuel design gives a maximum internal pressurization, ΔP of 17.5 MPa at the end of its cycle length of 85 MWD/kgU. The fuel design with the 10% central void in pellets and twice, or three times longer plenum length gives internal pressurization, ΔP of 5 MPa, and 1 MPa, respectively, at the end of it cycle length of 85 MWD/kgU.

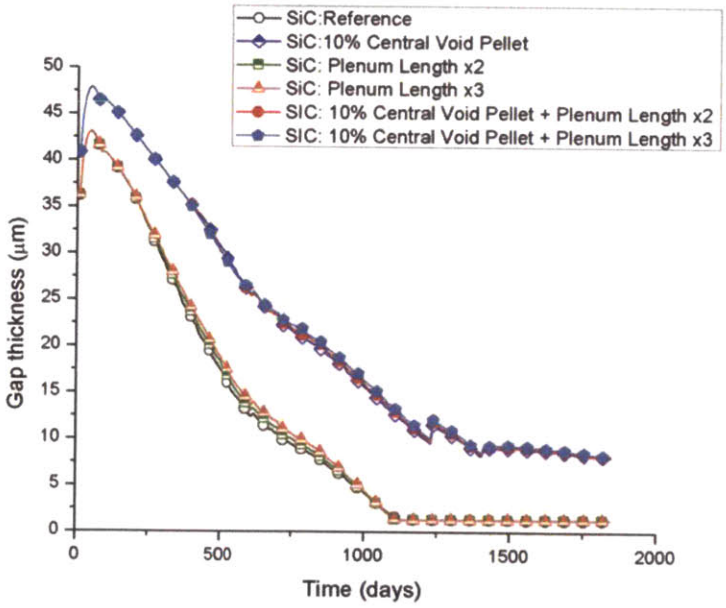

Figure 7-9 Fuel Rod Radial Gap from FRAPCON-3.4 Simulation for the Peak Fuel Rod Burnup of 85MWD/kgU after 1845 Days of Incore Residence Time (the highest burnup node, 2.51m from the bottom of the fuel rod)

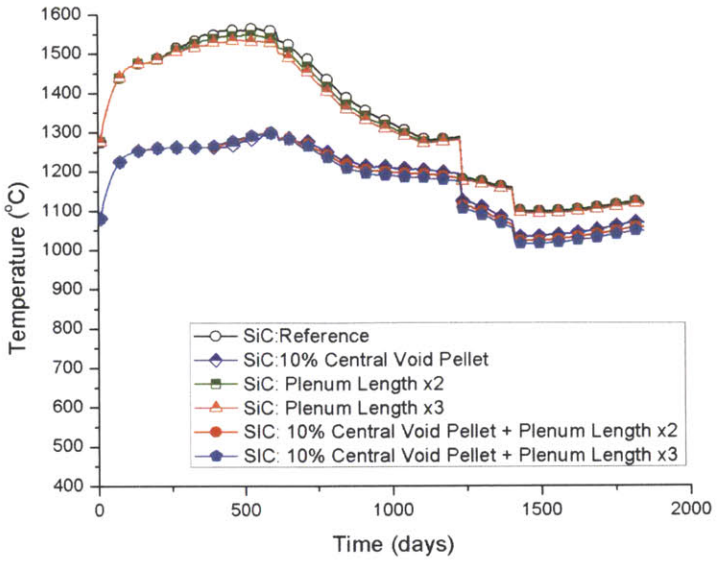

Figure 7-10 Fuel Centerline Temperature from FRAPCON-3.4 Simulation for the Peak Fuel Rod Burnup of 85MWD/kgU after 1845 Days of Incore Residence Time (the highest burnup node, 2.51m from the bottom of the fuel rod)

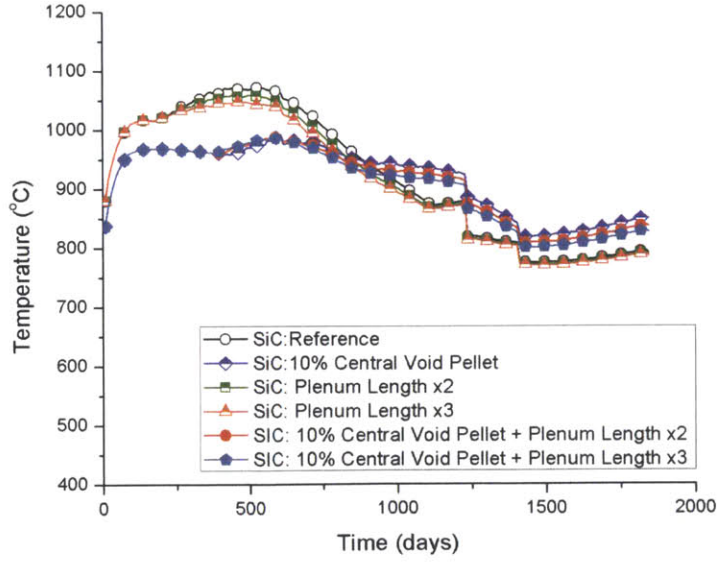

Figure 7-11 Volume Average Fuel Temperature from FRAPCON-3.4 Simulation for the Peak Fuel Rod Burnup of 85MWD/kgU after 1845 Days of Incore Residence Time (the highest burnup node, 2.51m from the bottom of the fuel rod is)

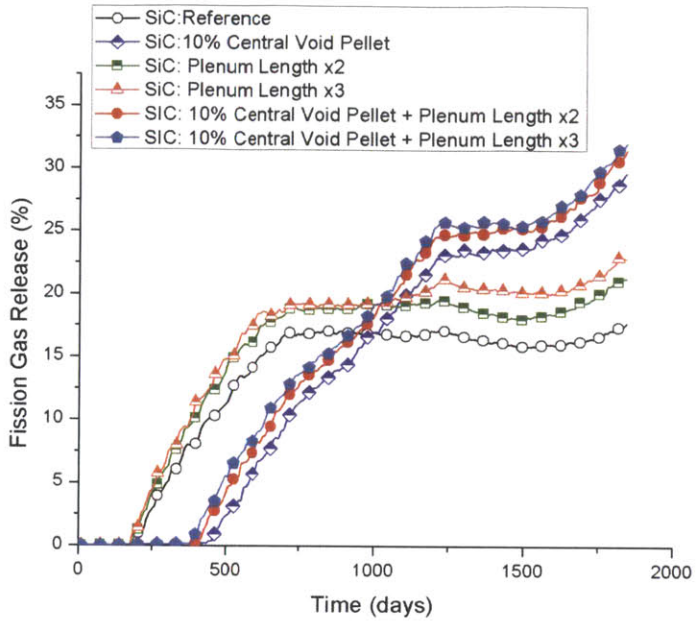

Figure 7-12 Fission Gas Release Percentage from FRAPCON-3.4 Simulation for the Peak Fuel Rod Burnup of 85MWD/kgU after 1845 Days of Incore Residence Time

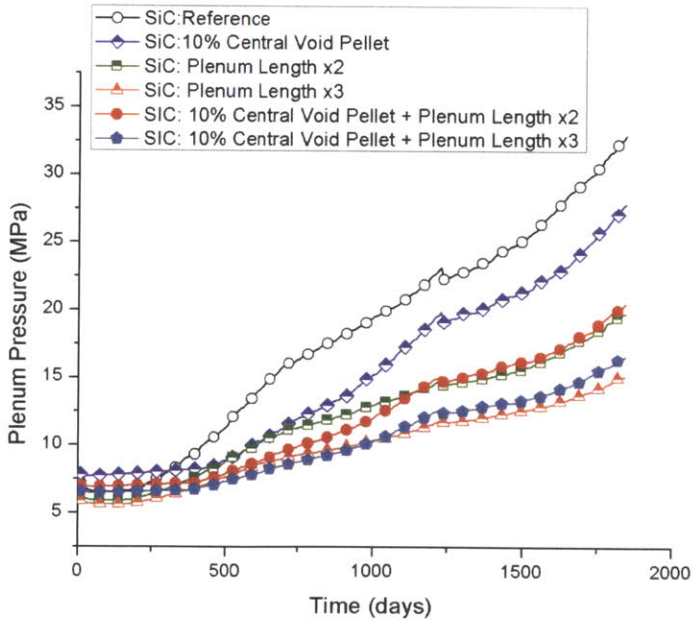

Figure 7-13 Plenum Pressure from FRAPCON-3.4 Simulation for the Peak Rod Burnup of 85MWD/kgU after 1845 Days of Incore Residence Time

(B) Peak Fuel Rod Burnup of 101 MWd/kgU (solid fuel pellet), cycle length of 2214 days

Simimlar fuel rod behavior was observed with more evident diminishing benefts of the central void in fuel pellets with a further increase in burnup. The contact of the fuel pellet and the cladding is still 'soft' at the end of the cycle length in Figure 7-14. Cladding tensile stress jumps sharply upon the transition from the 'soft contact' to 'hard contact'. Considering the brittle nature of the SiC cladding which already experiences tensile stresses by internal pressurization and thermal stresses, a rule of thumb of its operation would be to avoid hard contact. The reference fuel design gives the maximum internal pressurization, ΔP of 38MPa at the end of it cycle length for 101 MWD/kgU. The fuel design with the 10% central void in pellets and twice, three, and four times longer plenum length gives internal pressurization, ΔP of 16 MPa, 9MPa, and 5 MPa, respectively, at the end of it cycle length for 101 MWD/kgU.

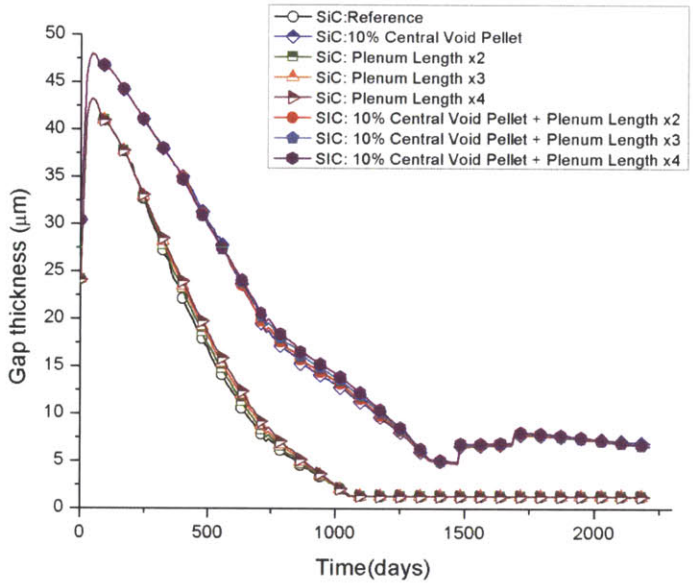

Figure 7-14 Fuel Rod Radial Gap from FRAPCON-3.4 Simulation for the Peak Fuel Rod Burnup of 101MWD/kgU after 2214 Days of Incore Residence Time (the highest burnup node, 2.51m from the bottom of the fuel rod)

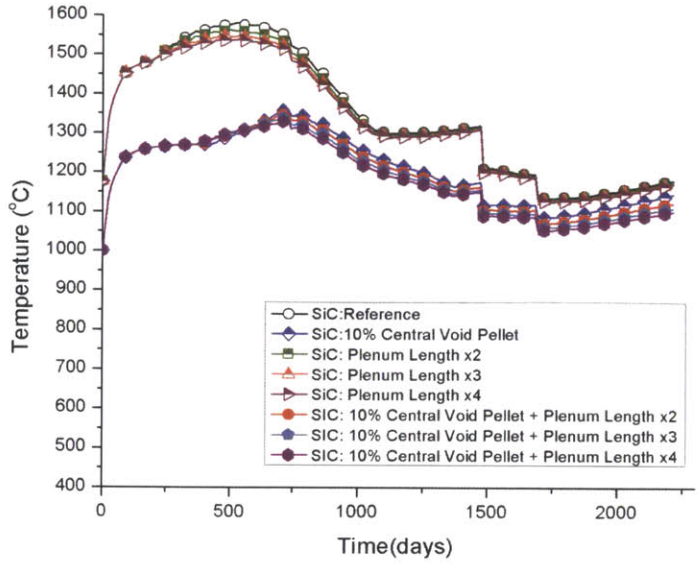

Figure 7-15 Fuel Centerline Temperature from FRAPCON-3.4 Simulation for the Peak Fuel Rod Burnup of 101MWD/kgU after 2214 Days of Incore Residence Time (the highest burnup node, 2.51m from the bottom of the fuel rod)

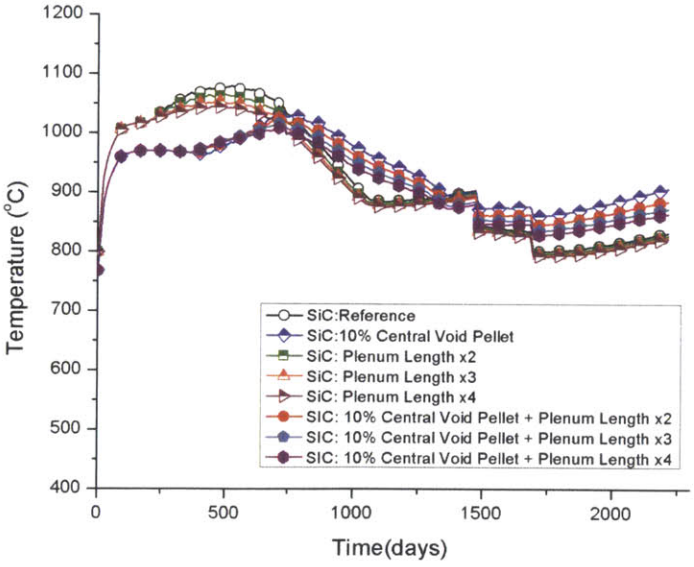

Figure 7-16 Volume Average Fuel Temperature from FRAPCON-3.4 Simulation for the Peak Fuel Rod Burnup of 101MWD/kgU after 2214 Days of Incore Residence Time (the highest burnup node, 2.51m from the bottom of the fuel rod)

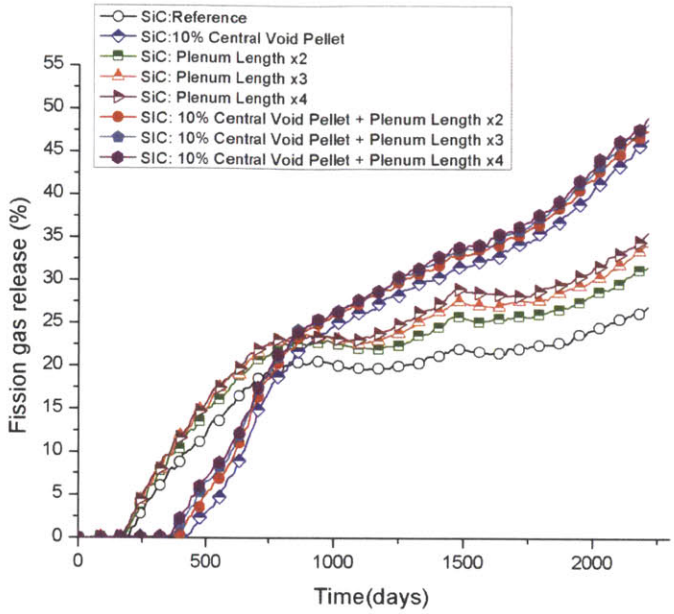

Figure 7-17 Fission Gas Release Percentage from FRAPCON-3.4 Simulation for the Peak Fuel Rod Burnup of 101MWD/kgU after 2214 Days of Incore Residence Time

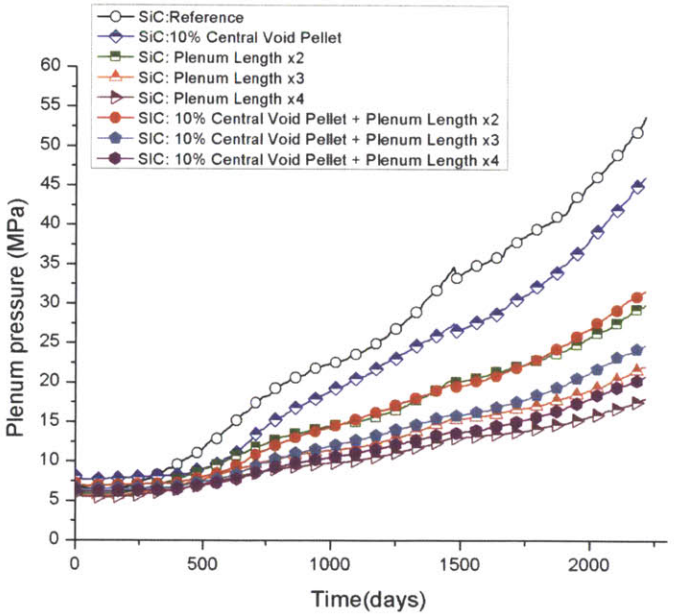

Figure 7-18 Plenum Pressure from FRAPCON-3.4 Simulation for the Peak Fuel Rod Burnup of 101MWD/kgU after 2214 Days of Incore Residence Time

7.3.5 Stress Analysis of SiC Cladding in Steady-State Operation

The prolonged open gap with SiC cladding gives an increasing flexiblity for fuel rod design in managing cladding stress levels. A design startegy or LWR fuel with SiC cladding for extended burnup is to operate the fuel rod until the fuel pellet makes a 'hard contact' with the cladding, which occurs after the fuel pellet ends recovering pores and cracks under a 'soft contact'. This requires maintaining plenum pressure within the safety assurance limit. It was found from the previous discussion that use of the SiC cladding in a typical PWR fuel rod design has a potential to achieve a rod average burnup of 101MWD/kgU with a cycle length of 2214 days (72 months) if the plenum pressure stays within a safety assurance limit. This may serve as a tentative ceiling of the burnup extension within the current fuel rod design envelop as a FRAPCON-3.4 SiC simulation predicts transition from 'soft contact' to 'hard contact' soon after that burnup.

As a primary way to lower the plenum pressure at high burnup, the fuel rod design with increased plenum length by a factor of four, shown in Figure 7-14 ~ Figure 7-18, was chosen as the fuel rod design for high burnup. Increasing plenum length would increase pressure drop of the core.Typical PWR fuel rod length in the Westinghouse designss in 3.6576 m tall (12 feet), but it could range from 2.4384m (8 feet) to 4.2672m (14 feet). Increasing the typical plenum length (17.5cm) by a factor of four will lengthen the fuel rod by 52.5cm, which is within the current design envelop of the fuel rod length (2 feet = 60.96cm). Fuel pellet with 10% central void was adopted to lower the fuel temperature to stay within the current LWR fuel experience.

Stress levels in the cladding are subject to changes with incore residence time because of fuel rod pressurization, power changes, and material property changes. Hence, the time evolution of stress levels in the cladding should be investigated. The fuel pin power history of the extended 72 months of residence in core for a final rod average burnup of 112 MWD/kgU with the 10% central central void in fuel pellet are used for burnup extension assessment. Pin power, fuel rod plenum pressure, system operating pressure, and the cladding outer surface temperature from FRAPCON-3.4-SiC simulations at the follwing three phases – beginning-of-life phase (BOL) – 22 days, middle-of-life phase (MOL) – 1107 days, and end-of-life phase (2207 days) – were used for SiC cladding stress calculations presented in Chapter 4.

Relevant irradiated material properties of SiC cladding shown in Table 4-1 and Table 4-5 were used. As discussed in Chapter 4, an inner monolith thickness greater than the half of the cladding thickness is recommended to utilize the compressive stresses in the inner monolith and reduce the volume of the composite under tensile stresses. Hence, four different SiC cladding layer designs with a monolith thickness greater than the composite thickness were evaluated as presented in Figure 7-19 - Figure 7-22.

Table 7-3 Frapcon-3.4-SiC Simulation Inputs for SiC Cladding Stress Calculation
[Standard PWR Fuel Pin Design with 10% Central Void Fuel Pellet and 4×Plenum Length, Final Rod average Burnup=112MWD/kgU with the Cycle Length of 2214 days (72 months)]

	Pin power (kW/m)	**Plenum Pressure, P_i (MPa)**	**System Pressure, P_o (MPa)**	**Cladding outer surface temperature, T_o (°C)**
Beginning of Life Phase (22 days of incore residence time)	26.1	6.2	15.5	339.9
Middle of Life Phase (1107 days of incore residence time)	21.2	11.1	15.5	334.1
End of Life (2214 days of incore residence time)	17.9	20.9	15.5	328.8

FRAPCON-3.4 SiC uses a cladding thermal conductivity of 4.8W/m-K at its lowest saturatiom value. This conductivity was experimentally measured (Stempien, 2011) for irradiated SiC cladding that consists of roughly half-monolith and half of fiber-reinforced SiC/SiC composite and a thin monolithc EBC. That is, a cladding with a thickner monolith (~9.5kW/m) than the composite (~1.5kW/m), in fact, has a higher thermal conductivity than the simulated cladding in FRAPCON-3.4-SiC. This implies that the plenum pressure could be lowered with a decreased fuel temperature by a higher cladding thermal coductivity. In this analysis, however, the plenum pressure simulated by the cladding conductivity of 4.8 W/m-k was used as a conservative approach for stress calculation of SiC cladding with a thicker inner monolith.

Figure 7-19 - Figure 7-22 show the time evolution of the stress fields of the high burnup SiC cladding for different cladding layer designs thickness. The inner monolith is subject to a noticeable increase in stress level with incore residence time while the composite undergoes relatively smaller stress changes. The inner monolith of the cladding designs C, and D, whose fractions are 0.7 and 0.8, resepctively, start seeing tensile stresses near the interface toward the end of the irradiation time.

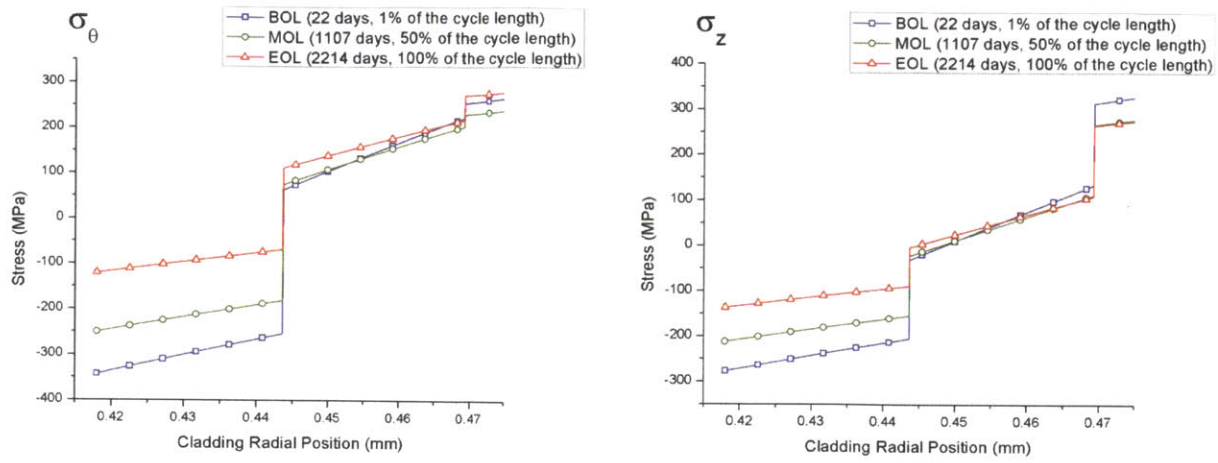

Figure 7-19 Hoop and Axial Stress of SiC Cladding with respect to In core Residence Time, [Standard PWR Fuel Pin Design with 10% Central Void Fuel Pellet and 4× the Plenum Length, Cladding Design-A: Monolith:Composite:EBC = 0.45:0.45:0.1], Final Rod average Burnup=112MWD/kgU with the Cycle Length of 2214 days (72 months)

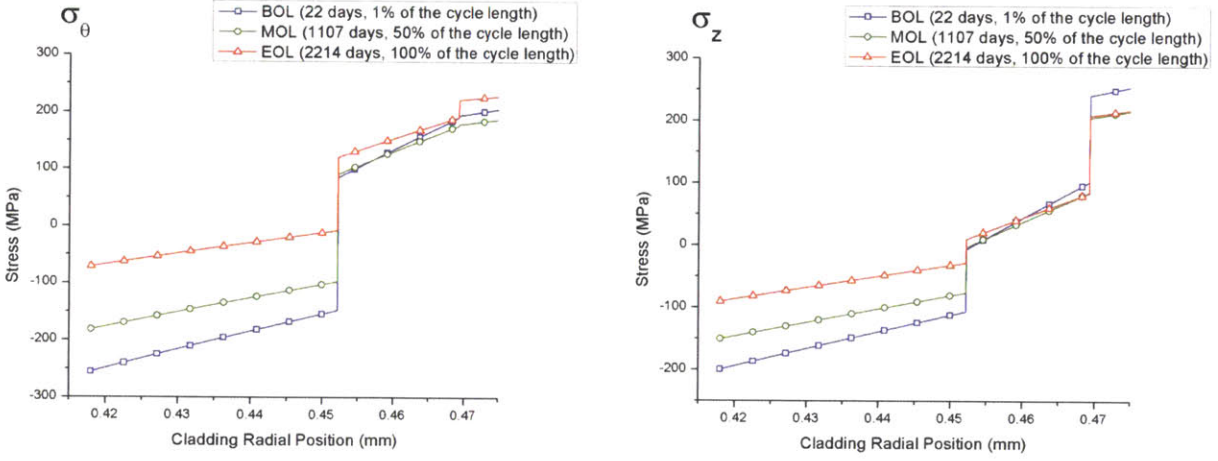

Figure 7-20 Hoop and Axial Stress of SiC Cladding with respect to In core Residence Time, [Standard PWR Fuel Pin Design with 10% Central Void Fuel Pellet and 4× the Plenum Length, Cladding Design-B: Monolith:Composite:EBC = 0.6:0.3:0.1], Final Rod average Burnup=112MWD/kgU with the Cycle Length of 2214 days (72 months)

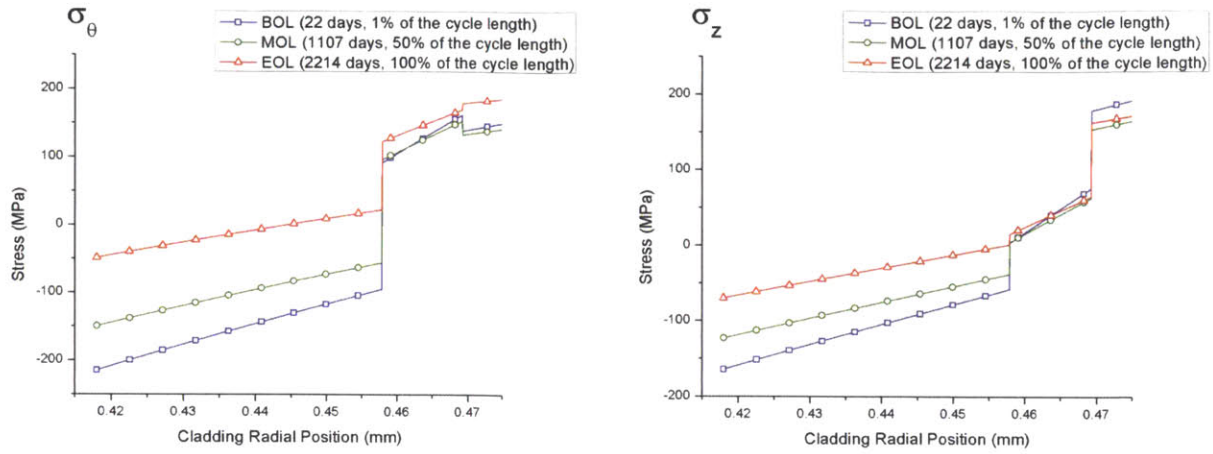

Figure 7-21 Hoop and Axial Stress of SiC Cladding with respect to In core Residence Time, [Standard PWR Fuel Pin Design with 10% Central Void Fuel Pellet and 4× the Plenum Length, Cladding Design-C: Monolith:Composite:EBC = 0.7:0.2:0.1], Final Rod average Burnup=112MWD/kgU with the Cycle Length of 2214 days (72 months)

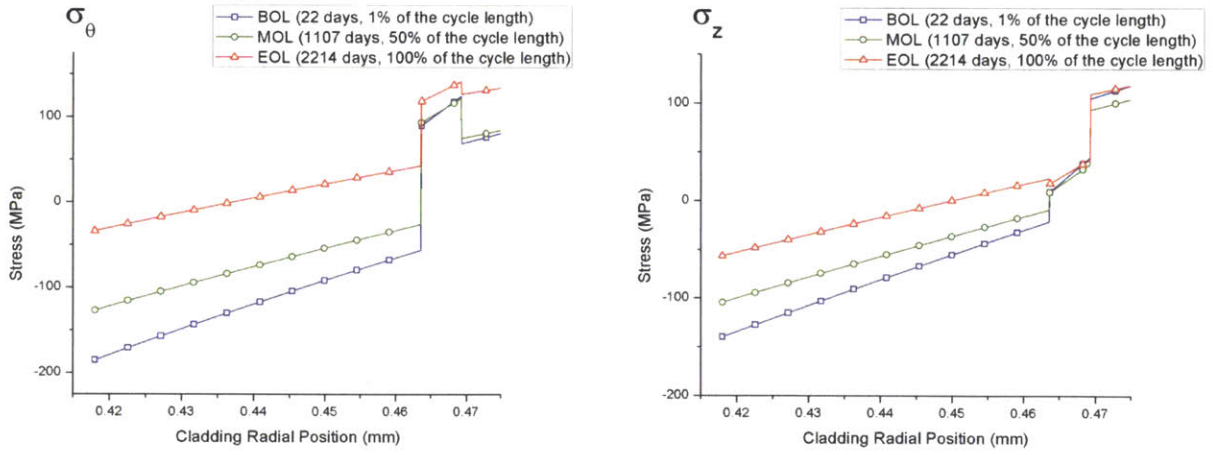

Figure 7-22 Hoop and Axial Stress of SiC Cladding with respect to In core Residence Time, [Standard PWR Fuel Pin Design with 10% Central Void Fuel Pellet and 4× the Plenum Length, Cladding Design-D: Monolith:Composite:EBC = 0.8:0.1:0.1], Final Rod average Burnup=112MWD/kgU with the Cycle Length of 2214 days (72 months)

Undergoing a locally induced fracture rather than a plasticity-mediated dispersed fracture mode, the structural integrity of the SiC cladding, under a stress field, should be analyzed by statistical means. The Weibull statistical fracture model for SiC cladding presented in Chapter 4 was used with the stress fields shown in Figure 7-19 - Figure 7-22 to obtain a relevant failure probability of the SiC cladding. Detailed explanations of the relevant SiC cladding structural failure modes and their classifications can be found in Chapter 4. Table 7-4 shows the obtained relevant failure probabilities of SiC cladding in high burnup operation.

In this study, 10% of the SiC cladding thicknesses (0.57mm or 0.8mm) is used as a reference fraction for the EBC thickness as the oxidation study discussed in Chapter 2 and Chapter 3 found that 45 ~ 110 μm of the EBC thickness is required to maintain 72 hours of separation of carbon coated fibers from any contact with H_2O in LOCA at 1500°C.

Table 7-4 Failure Probability of SiC Cladding in Steady State Operation with Standard PWR Fuel Pin Design with 10% Central Void Fuel Pellet and 4× the Plenum Length, Final Rod average Burnup=112MWD/kgU with the Cycle Length of 2214 days (72 months)

Cladding Design in terms of Relative Thickness	**Fracture Modes**	**Failure Probability**		
		BOL (22 days)	**MOL (1107 days)**	**EOL (2214 days)**
Cladding-A monolith:composite:EBC = 4.5: 4.5: 1	Monolith Failure	0	0	0
	Composite Ultimate Failure	0.1931	0.0486	0.1852
	Composite Matrix Cracking	1	1	1
	EBC Failure	1	1	1
Cladding-B monolith:composite:EBC = 6: 3: 1	Monolith Failure	0	0	0
	Composite Ultimate Failure	0.0117	0.0034	0.0182
	Composite Matrix Cracking	1	1	1
	EBC Failure	1	1	1
Cladding-C monolith:composite:EBC = 7: 2: 1	Monolith Failure	0	0	3.96×10^{-7}
	Composite Ultimate Failure	4.79×10^{-4}	2.01×10^{-4}	0.0017
	Composite Matrix Cracking	1	1	1
	EBC Failure	1	0.999	1
Cladding-D monolith:composite:EBC = 8: 1: 1	Monolith Failure	0	0	1.64×10^{-4}
	Composite Ultimate Failure	4.45×10^{-6}	3.64×10^{-6}	7.00×10^{-5}
	Composite Matrix Cracking	1	1	1
	EBC Failure	0.333	0.169	0.8175

Cladding layer design options of A, and B presented in Table 7-4 would not undergo inner monolith fracture ($P_f = 0$) as it is under compression throughout its incore residence time. However, those cladding designs over utilize compressive stresses in the monolith at the expense of stress margins in the composite. As a consequence, the composite ultimate failure probability is on the order of 10^{-1} or 10^{-2} at the end of the cycle length. A more preferred cladding layer designs would be the cladding option-C, and D. Those cladding layer designs find a better balance of keeping the inner monolith under compression, lowering tensile stress levels in the composite, and reducing composite volume. Cladding-D – a further increase of the monolith fraction from cladding-C – demonstrated an issue in managing the balance of stress levels; a significant fraction of the monolith sees appreciable tensile stresses near the interface toward the end of the cycle length as shown in Figure 7-22. As a result, the cladding design D gives an increased monolith failure probability on the order of 10^{-4} at the end of the cycle length. The cladding is regarded 'the most safe' in the middle of incore residence time because of the reduced thermal stresses without a significant internal pressurization of the rod.

The failure probability of a fuel rod, $P_{f,rod}$, can be found by calculating the probability that any of the monolith failure and ultimate failure of the composite occur in a fuel rod as follows

$$P_{f,rod} = 1 - (1 - P_{f,monolith})(1 - P_{f\ ultimate,composite}) \tag{7-1}$$

Where $1 - P_{f,monolith}$ is the survival probability of the monolith failure ($P_{f,monolith}$), and $1 - P_{f\ ultimate,composite}$ is the survival probability of the composite ultimate failure ($P_{f\ ultimate,composite}$). For cladding-C, $P_{f,rod}$ is ~0.0017, at the end of the cycle length, following that of the composite ultimate failure probability. Considering that a typical PWR reactor core has ~51,000 fuel rods, a steady state failure probability near 10^{-3} implies 'a strong feasibility' of the SiC cladding concept as less than 100 fuel rods would undergo failure in the core. Indeed, this failure probability at the end of the cycle length is only relevant to the highest burnup fuel pins whose number is far less than the number of fuel pins in a typical reactor core. The number of highly burned fuel pins may be on the order of a single assembly i.e.~ 250 pins. In that, fuel rod failure probability on the order of 10^{-3} at the end of the cycle length still implies a strong feasibility to safely achieve the cycle length. Cladding stresses and failure probabilities presented for BOL and MOL in Figure 7-19 - Figure 7-22, and in Table 7-4 are pertinent to peak fuel pins (1.5 times the average pin power 17.86 kW/m ≈ 26.79 kW/m), which are discharged before the peak allowable burnup.

A dispersed micro-cracking of the CVI matrix in the composite, and fractures of the environmental barrier coating (EBC) would be unavoidable fracture modes of the SiC cladding. However, those fractures, from

a safety perspective, are not as serious concern as the inner monolith fracture and the ultimate fracture of the composite. CVI matrix cracking is an expected mechanism of a fiber-reinforced composite for accessing the fiber strength, and would not cause a fission gas release as long as the inner monolith maintains its structural integrity. The failure probability of the EBC is based on the weakest link theory. That is, the failure probability equalling unity essentially says that it is certain that the entire volume of EBC of a fuel rod would experience at least one crack development somewhere in the material. However, in a laminated structure, a local fracture of EBC would not necessarily lead to a global failure of the layer. Hence, composite strength degradation by H_2O ingression into the fibers could still be suppressed by the presence of EBC, even if it experienced local fractures in the volume of the material.

The steady-state fuel performance analysis demonstrated that the typical fuel rod with SiC cladding (monolith:composite:EBC =7:3:1) could extend the in-core residence time to 72 months and increase burnup up to 112MWD/kgU with 10% central void fuel pellet by increasing plenum length to extra 52.5cm. This fuel design strategically utilizes the prolonged gap closure time for an extended power production time while managing plenum pressure below the safety assurance limit by increasing plenum length within the current PWR fuel desgin envelop.

Yet, the in core time of 72 months with a burnup increase up to 112MWD/kgU is a ceiling value that assumes zero safety-margin for accident scenarios. Fuel design and operation, however, should always take into account accident conditions by allowing safety margin. The following discussion is devoted to analyzing the structural integrity of the SiC cladding under a limiting accident condition.

7.4 Transient Fuel Rod Temperature In a LOCA accident

A limiting accident condition that needs to be taken into account is a design basis large break loss of coolant accident (LBLOCA). During LBLOCA, fuel rod cladding experiences extra stresses due to (1) rapid depressurization of the system which gives extra pressure difference across the cladding thickness, and (2) extra thermal stresses due to the fuel rod quenching in reflood phase.

As for the first item, the SiC cladding stress analysis and statistical fracture model developed in Chapter 4 can be readily used to account for the extra pressure loading of the fuel rod followed by the rapid depressurization of the core. Evaluating the extra thermal stresses due to the fuel rod quenching in the

reflood phase, however, needs a treatment for transient cladding temperature distribution evolution during the quencing process[30].

The implicit Finite difference method (FDM) was used to solve transient radial temperature distributions of the fuel rod . The FDM discretization scheme is shown in Figure 7-23.

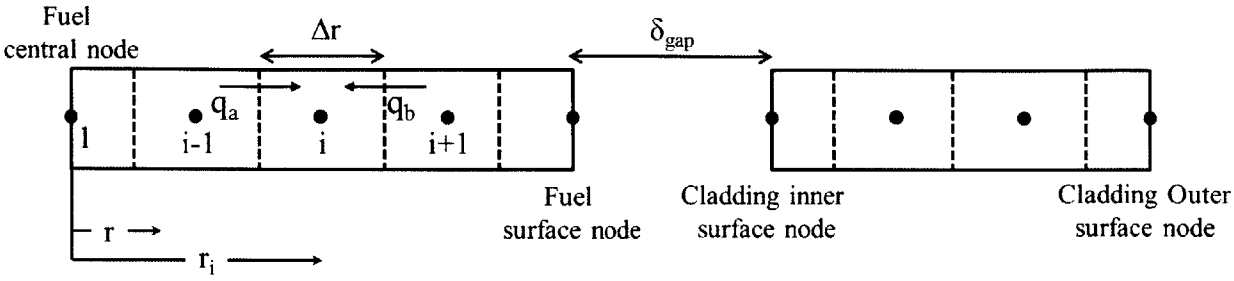

$A_{i-1}=2\pi(r_i-\Delta r/2)\Delta L$
$A_i=2\pi(r_i+\Delta r/2)\,\Delta L$
$V_i=2\pi\, r_i\, \Delta r\, \Delta L$

Figure 7-23 Finite Difference Method (FDM) Scheme for Transient Energy Equation Solver for a Cylindrical Fuel Rod

Time has also been discretized with a finite time step Δt. That is,

$$t = p\Delta t \tag{7-2}$$

where p is the number of time steps.

With that, T_i^{p+1} is the temperature at node i at time $p+1$, which is Δt after the T_i^p.

The energy conservation holds for each node as shown in Eq.(7-3).

$$\dot{E}_{in} - \dot{E}_{out} + \dot{E}_g = \dot{E}_{stored} \tag{7-3}$$

Given the undetermined direction of heat flow, the energy balance for each node conventionally assumes that all the heat flow is into the node.

(A) Fuel Central Node (i=1)

[30] . Exsiting tansient fuel code analysis code such as FRAPTRAN-1.4 (Pacific Northwest National Laboratory (C), 2011) does not account for the thermal shock of multi-layred cladding upon quenching

For the central node of the fuel (i=1), the following energy balance holds

$$k_{fuel}A_1\frac{{T_2}^{p+1}-{T_1}^{p+1}}{\Delta r}+\dot{q}V_1=(\rho C_p)_{fuel}V_1\frac{{T_1}^{p+1}-{T_1}^{p}}{\Delta t} \tag{7-4}$$

where

$$A_1=2\pi\left(\frac{\Delta r}{2}\right)\Delta L, \tag{7-5}$$

$$V_1=\pi\left(\frac{\Delta r}{2}\right)^2\Delta L \tag{7-6}$$

Δr is the differential radial distance, Δt is the time step, and ΔL is the differential axial distance. $\dot{q}$ is volumetric heat generation rate. k_{fuel}, ρ_{fuel}, and $C_{p_{fuel}}$ are the thermal conductivity, the density, and the specific heat of the UO_2 fuel.

Eq.(7-4) can be rearrange for ${T_1}^{p+1}$, and ${T_2}^{p+1}$

$$-\left(\frac{k_{fuel}}{\Delta r}A_1+\frac{\rho C_pV_1}{\Delta t}\right){T_1}^{p+1}+\left(\frac{k_{fuel}}{\Delta r}\right){T_2}^{p+1}=-\frac{(\rho C_p)_{fuel}V_1{T_1}^{p}}{\Delta t}-\dot{q}V_1 \tag{7-7}$$

(B) Fuel interior node, i

For an interior node in the fuel, i, the following energy balance equation holds

$$k_{fuel}A_{i-1}\frac{{T_{i-1}}^{p+1}-{T_i}^{p+1}}{\Delta r}+k_{fuel}A_i\frac{{T_{i+1}}^{p+1}-{T_i}^{p+1}}{\Delta r}+\dot{q}V_i=(\rho C_p)_{fuel}V_i\frac{{T_i}^{p+1}-{T_i}^{p}}{\Delta t} \tag{7-8}$$

Which can be rearranged for ${T_{i-1}}^{p+1}$, ${T_i}^{p+1}$, and ${T_{i+1}}^{p+1}$ as follows

$$\left(\frac{k_{fuel}A_{i-1}}{\Delta r}\right){T_{i-1}}^{p+1}-\left(\frac{k_{fuel}A_{i-1}}{\Delta r}+\frac{k_{fuel}A_i}{\Delta r}+\frac{(\rho C_p)_{fuel}V_i}{\Delta t}\right){T_i}^{p+1}+\left(\frac{k_{fuel}A_i}{\Delta r}\right){T_{i+1}}^{p+1}$$
$$=-\frac{(\rho C_p)_{fuel}V_i{T_i}^{p}}{\Delta t}-\dot{q}V_i \tag{7-9}$$

Where $A_{i-1}=2\pi(r_i-\Delta r/2)\Delta L$, $A_i=2\pi(r_i+\Delta r/2)\,\Delta L$, and $V_i=2\pi\, r_i\,\Delta r\,\Delta L$

(C) Fuel surface node, i

For a surface node in the fuel, i, the following energy balance equation holds,

$$k_{fuel}A_{i-1}\frac{{T_{i-1}}^{p+1}-{T_i}^{p+1}}{\Delta r}+h_{gap}A_{s,fuel}\left({T_{i+1}}^{p+1}\big|_{clad}-{T_i}^{p+1}\right)+\dot{q}V_{s,fuel}$$
$$=\left(\rho C_p\right)_{fuel}V_{s,fuel}\frac{{T_i}^{p+1}-{T_i}^{p}}{\Delta t} \tag{7-10}$$

Eq.(7-10) can be rearranged for ${T_{i-1}}^{p+1}$, ${T_i}^{p+1}$, and ${T_{i+1}}^{p+1}\big|_{clad}$ as follows

$$\left(\frac{k_{fuel}A_{i-1}}{\Delta r}\right){T_{i-1}}^{p+1}-\left(\frac{k_{fuel}A_{i-1}}{\Delta r}+h_{gap}A_{s,fuel}+\frac{\left(\rho C_p\right)_{fuel}V_{s,fuel}}{\Delta t}\right){T_i}^{p+1}$$
$$+h_{gap}A_{s,fuel}{T_{i+1}}^{p+1}\big|_{clad}=-\frac{\left(\rho C_p\right)_{fuel}V_{s,fuel}{T_i}^{p}}{\Delta t}-\dot{q}V_{s,fuel} \tag{7-11}$$

Where, $A_{s,fuel}=2\pi r_i\Delta L$, and $V_{s,fuel}=2\pi r_i\left(\frac{\Delta r}{2}\right)\Delta L$. h_{gap} is the gap conductance.

${T_{i+1}}^{p+1}\big|_{clad}$ is the inner surface node of the cladding.

(D) Cladding surface node, i

For the surface node of the cladding, i, the following energy balance equation holds,

$$h_{gap}A_{s,i,clad}\left({T_{i-1}}^{p+1}\big|_{fuel}-{T_i}^{p+1}\right)+\frac{k_{clad}}{\Delta r}A_i\left({T_{i+1}}^{p+1}-{T_i}^{p+1}\right)$$
$$=\left(\rho C_p\right)_{clad}V_{s,i,clad}\frac{{T_i}^{p+1}-{T_i}^{p}}{\Delta t} \tag{7-12}$$

Eq.(7-12) can be rearranged for ${T_{i-1}}^{p+1}\big|_{fuel}$, ${T_i}^{p+1}$, and ${T_{i+1}}^{p+1}$ as follows

$$h_{gap}A_{s,i,clad}{T_{i-1}}^{p+1}\big|_{fuel} - \left(h_{gap}A_{s,i,clad} + \frac{k_{clad}A_i}{\Delta r} + \frac{(\rho C_p)_{clad}V_{s,i,clad}}{\Delta t}\right){T_i}^{p+1} + \left(\frac{k_{clad}A_i}{\Delta r}\right){T_{i+1}}^{p+1} = -\frac{(\rho C_p)_{clad}V_{s,i,clad}{T_i}^{p}}{\Delta t} \quad (7\text{-}13)$$

where $A_{s,i,clad} = 2\pi r_i \Delta L$, $V_{s,i,clad} = 2\pi r_i \left(\frac{\Delta r}{2}\right)\Delta L$

(E) Cladding interior node, i

For the surface node of the cladding, i, the following energy balance equation holds,

$$k_{clad}A_{i-1}\frac{{T_{i-1}}^{p+1} - {T_i}^{p+1}}{\Delta r} + k_{clad}A_i\frac{{T_{i+1}}^{p+1} - {T_i}^{p+1}}{\Delta r} = (\rho C_p)_{clad}V_i\frac{{T_i}^{p+1} - {T_i}^{p}}{\Delta t} \quad (7\text{-}14)$$

Eq.(7-14) can be rearranged for ${T_{i-1}}^{p+1}$, ${T_i}^{p+1}$, and ${T_{i+1}}^{p+1}$ as follows

$$\left(\frac{k_{clad}A_{i-1}}{\Delta r}\right){T_{i-1}}^{p+1} - \left(\frac{k_{clad}A_{i-1}}{\Delta r} + \frac{k_{clad}A_i}{\Delta r} + \frac{(\rho C_p)_{clad}V_i}{\Delta t}\right){T_i}^{p+1} + \left(\frac{k_{clad}A_i}{\Delta r}\right){T_{i+1}}^{p+1} = -\frac{(\rho C_p)_{clad}V_i{T_i}^{p}}{\Delta t} \quad (7\text{-}15)$$

Where $A_{i-1}=2\pi(r_i-\Delta r/2)\Delta L$, $A_i=2\pi(r_i+\Delta r/2)\Delta L$, and $V_i=2\pi\, r_i\, \Delta r\, \Delta L$

(F) Cladding interface node, i

For the cladding interface node ,i, for the monolith and the composite, and the composite and the EBC the following energy balance equation holds,

$$k_{clad}A_{i-1}\frac{{T_{i-1}}^{p+1} - {T_i}^{p+1}}{\Delta r} + k_{clad}A_i\frac{{T_{i+1}}^{p+1} - {T_i}^{p+1}}{\Delta r} = \frac{\left[(\rho C_p)_{clad,j} + (\rho C_p)_{clad,k}\right]}{2}V_i\frac{{T_i}^{p+1} - {T_i}^{p}}{\Delta t} \quad (7\text{-}16)$$

Eq.(7-16) can be rearranged for ${T_{i-1}}^{p+1}$, ${T_i}^{p+1}$, and ${T_{i+1}}^{p+1}$ as follows

$$\left(\frac{k_{clad}A_{i-1}}{\Delta r}\right){T_{i-1}}^{p+1} - \left(\frac{k_{clad}A_{i-1}}{\Delta r} + \frac{k_{clad}A_i}{\Delta r} + \frac{\left[(\rho C_p)_{clad,j} + (\rho C_p)_{clad,k}\right]}{2}V_i\right){T_i}^{p+1}$$
$$+ \left(\frac{k_{clad}A_i}{\Delta r}\right){T_{i+1}}^{p+1} \quad (7\text{-}17)$$
$$= \frac{\left[(\rho C_p)_{clad,j} + (\rho C_p)_{clad,k}\right]}{2\Delta t}V_i{T_i}^{p}$$

Where $A_{i-1}=2\pi(r_i-\Delta r/2)\Delta L$, $A_i=2\pi(r_i+\Delta r/2)\Delta L$, and $V_i=2\pi\ r_i\ \Delta r\ \Delta L$. $(\rho C_p)_{clad,j}$ and $(\rho C_p)_{clad,k}$ are the density multiplied with the specfic heat of the two interfacing cladding layers (the monolith and the composite, or the composite and the EBC).

(F) Cladding surface node, i

For the surface node of the cladding, i, the following energy balance equation holds,

$$k_{clad}A_{i-1}\frac{{T_{i-1}}^{p+1} - {T_i}^{p+1}}{\Delta r} + h_{conv}A_{s,o,clad}(T_\infty - {T_i}^{p+1}) = (\rho C_p)_{clad}V_{s,o,clad}\frac{{T_i}^{p+1} - {T_i}^{p}}{\Delta t} \quad (7\text{-}18)$$

Eq.(7-18) can be rearranged for ${T_{i-1}}^{p+1}$, ${T_i}^{p+1}$, and ${T_i}^{p+1}$ as follows

$$\left(\frac{k_{clad}A_{i-1}}{\Delta r}\right){T_{i-1}}^{p+1} - \left(\frac{k_{clad}A_{i-1}}{\Delta r} + h_{conv}A_{s,o,clad} + \frac{(\rho C_p)_{clad}V_{s,o,clad}}{\Delta t}\right){T_i}^{p+1}$$
$$= -\frac{(\rho C_p)_{clad}V_{s,o,clad}}{\Delta t} - h_{conv}A_{s,o,clad}T_\infty \quad (7\text{-}19)$$

where $A_{i-1}=2\pi(r_i-\Delta r/2)\Delta L$, and $A_{s,o,clad} = 2\pi r_i\Delta L$. h_{conv} is the heat transfer coefficient at the cladding outer surface, and T_∞ is the bulk coolant temperature.

Note that the nodal temperature ${T_i}^{p+1}$ is coupled to the temperatures of the neighboring nodes, ${T_{i-1}}^{p+1}$, and ${T_{i+1}}^{p+1}$ (or T_∞ for the cladding outer surface node). The discretized temperatures ${T_i}^{p+1}$ at each node were numerically solved by constructing $A\vec{X} = \vec{b}$, where $\vec{X}$ is the temperature solution vector. The developed FDM code for the transient fuel rod temperature calculation with SiC cladding was validated with the steady-state analytical solution. Cladding geometry and their properties are input to the FDM code. The code, then, discretizes the geometry into the input number of nodes and output the transient temperature field. For code validation, a single case was analyzed. The input parameters used for the code validation is summarized in Table 7-5.

Table 7-5 Input Parameters for the Transient Fuel Rod Temperature Validation

UO_2 Fuel and Heat Transfer Parameters (Todreas, 2012)		SiC Cladding Parameters	
Fuel pellet O.D	8.19 mm	Cladding O.D	9.5 mm
Linear power rate ($\dot{q}$)	17.89 kW/m	Total cladding thickness	0.57mm
Fuel thermal conductivity	3.6 W/m-K	Inner monolith thickness	0.2565 mm
Fuel specific heat	300 J/kgK	Composite thickness	0.2565 mm
Fuel density	10970 kg/m^3	EBC thickness	0.057 mm
Heat transfer coefficient	10000 W/m^2 K	Monolith and EBC thermal conductivity (Katoh, 2011)	9.5 W/m-K
		Composite thermal conductivity (Katoh, 2010)	1.5 W/m-K
Bulk coolant temperature	121.9 °C	Monolith and EBC heat capacity (Snead, 2007)	300 J/kgK
		Composite heat capacity (Katoh, 2011)	300 J/kgK
Gap conductance	6280 W/m^2 K	Monolith and EBC density (Katoh, 2010)	3170 kg/m^3
		Composite density (Katoh, 2010)	2740 kg/m^3

The fuel rod intitial temperature was 800°C and the temperature distribution in the fuel rod approached the analytically obtained steady-state temperature solution with time as shown Figure 7-24. The implicit FDM is unconditionally stable in terms of convergence. This is a strong advantage of the implicit FDM relative to the explicit FDM. Numerical stability of the implicit FDM enables the use of an daptive meshing scheme for the fuel rod. In that way, computational resources can be allocated based on the physical importance of the fuel regions without affecting the convergence. But Δr is constant within each region. That is, use of finer meshes in the cladding region for a higher resolution is possible while giving relatively less computational importance for the fuel region by reducing number of meshes without a

disturbance to the numerical convergence. Hence, a high transient temperature resolution of the cladding region, hence the thermal stress, can be suitably obtained without overpaying expensive computational cost for the fuel region.

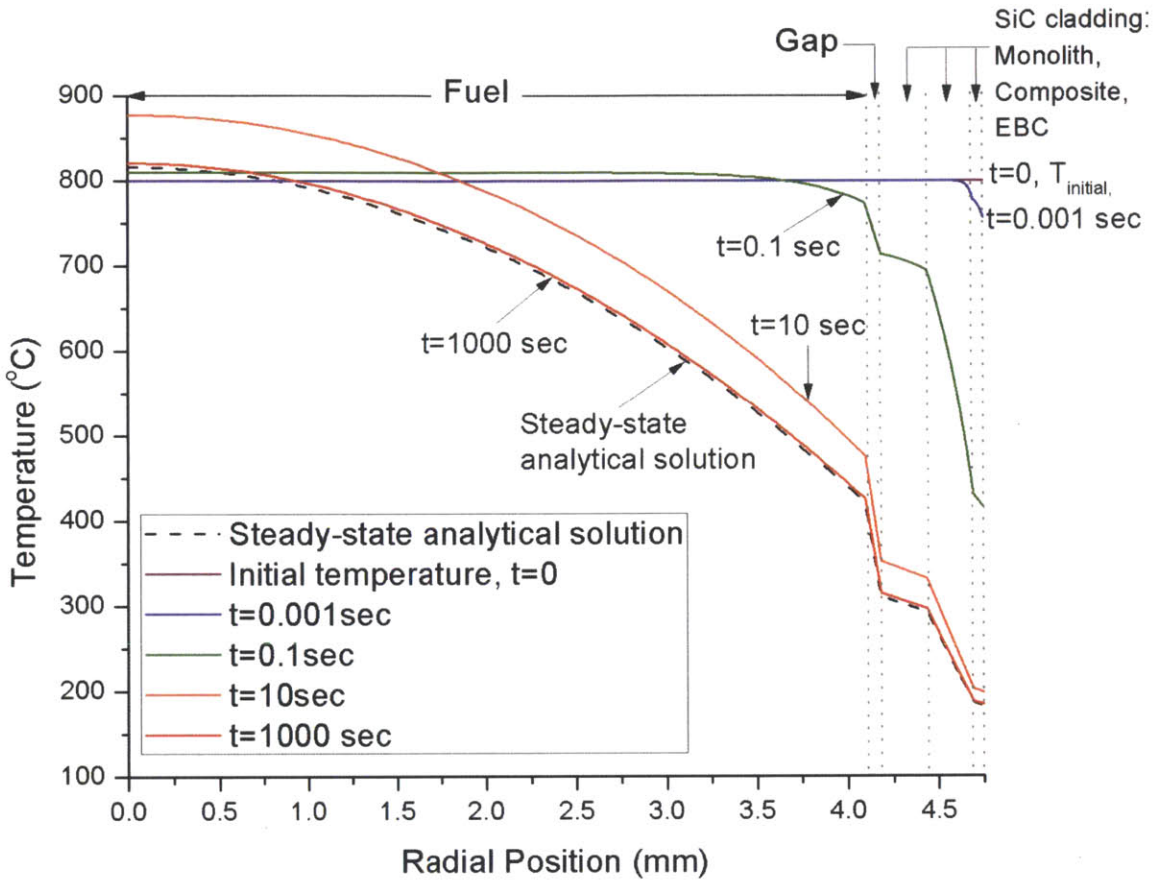

Figure 7-24 Transient Fuel Rod Temperature Evolution with SiC Cladding Obtained by the FDM Solution Scheme, and the Analytical Steady-State Solution

7.5 RELAP 5 -3D Simulation of LBLOCA Thermal Hydraulics

Simulating SiC cladding stress distributions during LBLOCA requires the reactor system thermal hydraulic conditions during the accident. Specifically, system pressure, bulk coolant temperature, and heat transfer coefficient are required inputs for the developed SiC cladding stress and fracture analysis models. RELAP-3D, developed by Idaho National Lab for the U.S NRC for transient simulation of LWR coolant systems during postulated accidents was used as the simulation code. A full description of the code can be found in the code manuals (Idaho National Laboratory, 2005). Cladding thermal

conductivities and heat capacities were modified to SiC properties used for FRACON-3.4 update with SiC cladding. The general PWR core of the 3479.22 MWth after with a large break of a cold leg was simulated. The RELAP-3D nodal scheme for a reference LBLOCA in PWR is shown in Figure 7-25.

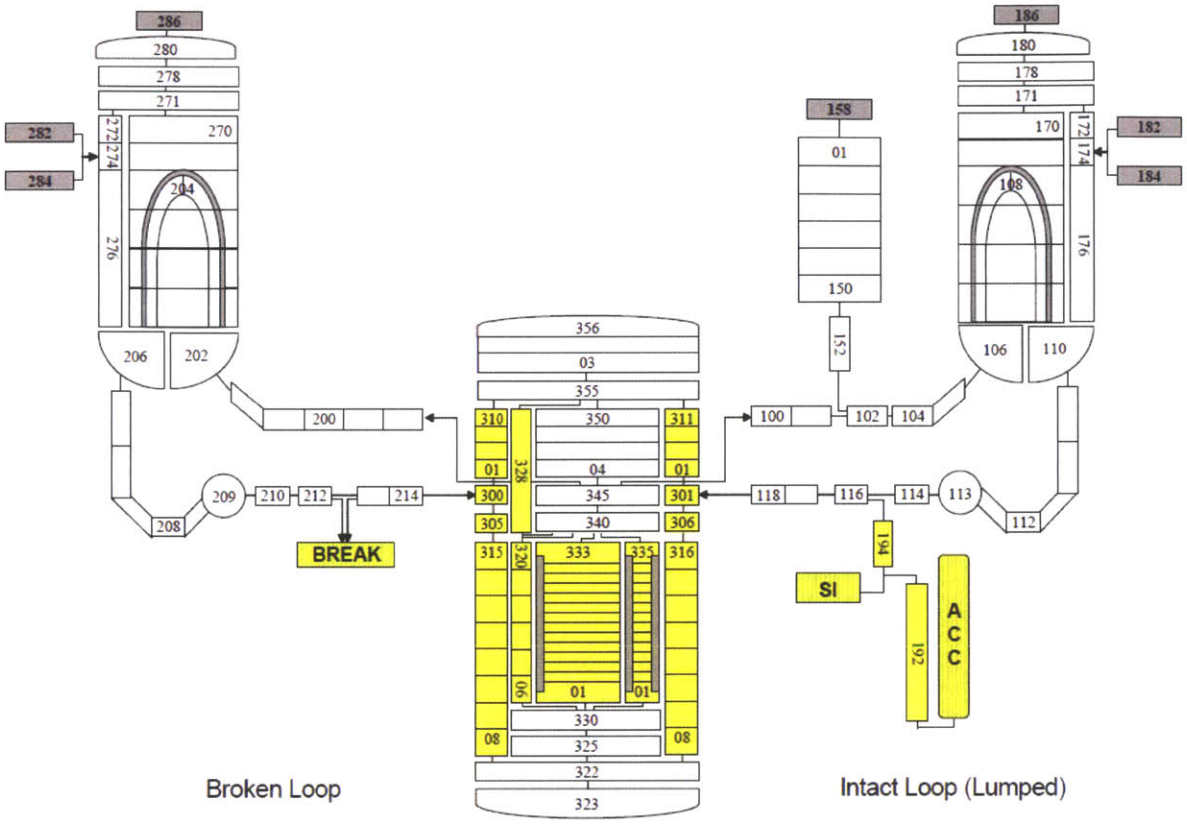

Figure 7-25 RELAP-5 Nasalization Scheme for a Reference Design Basis LBLCA of PWR
[Figure in courtesy of (Hu, 2011)]

Basically, LBLOCA behavior of a reactor core with SiC clad fuels is identical to that of Zircaloy cladding. From a safety point of view, reactor core depressurization is of prime importance. Since LBLOCA accompanies rapid depressurization of the reactor core, fuel rod claddings are subject to sudden additional pressure loading. It takes roughly 30 seconds upon the initiation of LBLOCA to complete depressurization, as shown in Figure 7-26. Fuel rod internal pressure is also subject to a change upon the initiation of LBLOCA. The transient plenum fuel rod internal temperature change was estimated by normalizing the average fuel rod gap temperature assuming ideal gas behavior. The average gap temperature was taken as the axial length from 0.45m to 3.4m. Hence, it may lead to a conservative analysis which is incorporated with some degree of safety margin by using a higher temperature than the

reality. Note that the behavior of presented fuel rod internal pressure estimation in Figure 7-26 is remarkably similar to IAEA's prediction of fuel rod plenum pressure during LBLOCA obtained by coupling FRAPTRAN-GENFLO (International Atomic Energy Agency, 2002). The SiC cladding would see the maximum differential pressure across its thickness up to 80% of its steady-state plenum pressure in LBLOCA.

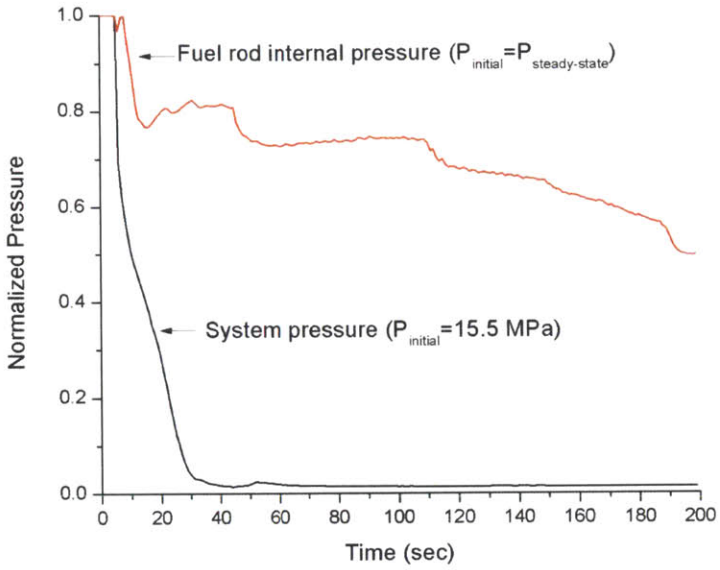

Figure 7-26 Normalized Transient Pressure of Reactor Core and Internal Fuel Rod upon LBLOCA

As a consequence of the sudden core depressurization, a large amount of water flashing takes place. The resulting steam initially passes by the fuel rod at a very fast velocity, contributing to temporary cooling of the fuel rod as can be seen by the cladding temperature drop following the initial temperature jump in Figure 7-27. This phase soon ends, after the first ~10 seconds of LBLOCA, and the unwetted portion of the fuel rod is subject to a temperature increase. Quenching of the fuel rod by the reflooding water front can be seen as a vertical temperature drop of the cladding outer surface in Figure 7-27. It can be noted that appreciable quenching of the fuel rod is relevant to the axial locations near the middle of the fuel rod; the primary cladding surface temperature decrease rates of the bottom (z=0.45m) and the upper portions (z=2.49 m) of the fuel rod are significantly slower than the rapid quenching observed for z=1.13m in Figure 7-27. The quenching of the fuel rod at z=1.13m can be described by quenching of SiC cladding at 320°C by 126°C saturated water at ~2.4 atm. The experimental study presented in Chapter 5 found that CVD-SiC whose size is 3.5 times thicker than the typical LWR cladding thickness retained its strength at 1265°C when quenched in saturated water at atmospheric pressure. The theoretical SiC thermal shock

fracture model presented in Chapter 6 predicted that the tested specimen could retain its strength well beyond 1800°C with quenching in saturated water. The heat transfer coefficient at the quenching time step for z=1.13m is found to be ~12843 W/m-K. It can be inferred from Figure 7-27 and Figure 7-28 that appreciable reflood quenching moments do not necessarily involve the peak heat transfer coefficient – yet the fastest heat transfer rate is accompanied through a large ΔT of the clad surface temperature and the fluid.

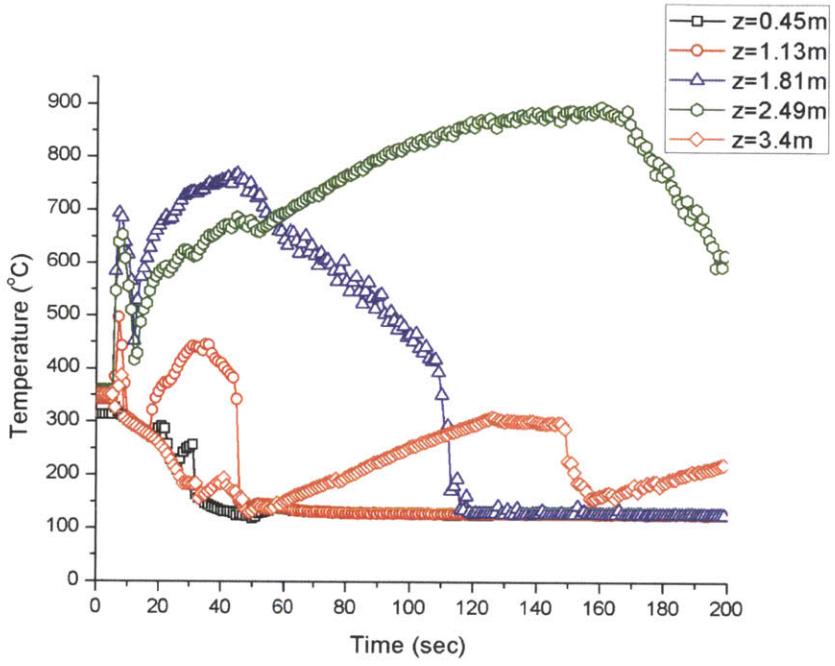

Figure 7-27 SiC Cladding Outer Surface Temperature of Peak Fuel Rod upon LBLOCA at Different Axial Locations

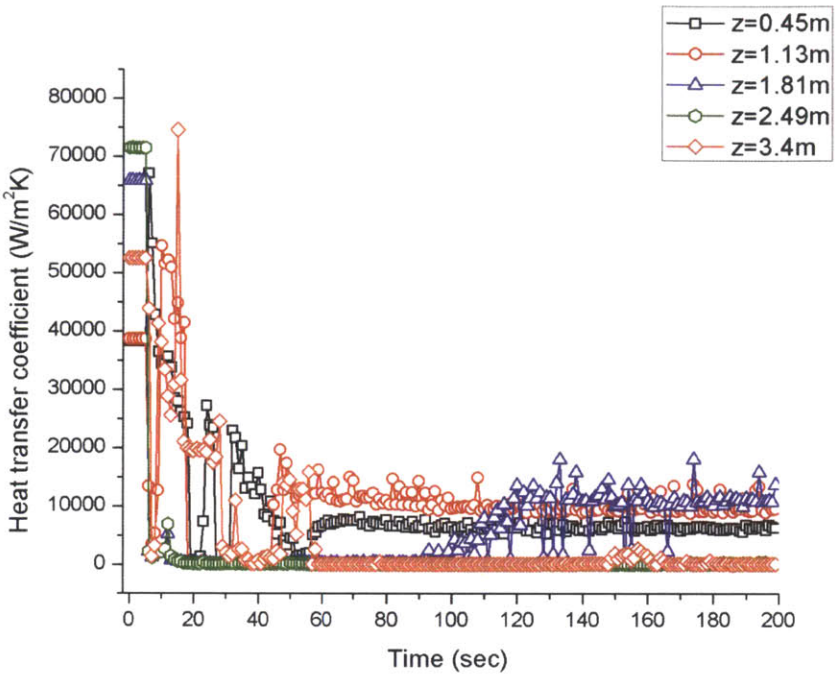

Figure 7-28 Heat Transfer Coefficient at SiC Cladding Outer Surface of Peak Fuel Rod upon LBLOCA at Different Axial Locations

During LBLOCA of PWR, reflooding water is close to saturation at the inlet after depressurization as shown in Figure 7-29. From the view point of structural integrity of the cladding, saturated water quenching is strongly preferred as it increases thermal shock tolerance of the SiC cladding by a few folds in terms of the critical temperature difference ΔT_c as discussed in Chapter 5, and Chapter 6.

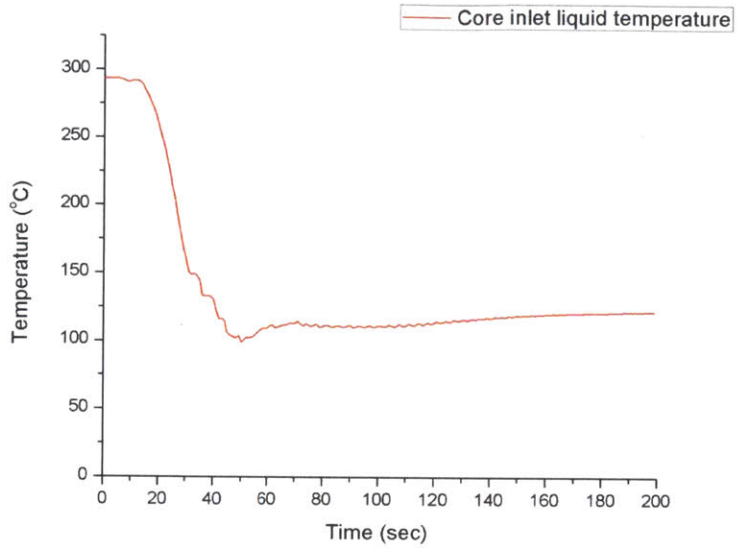

Figure 7-29 Core Inlet Liquid Temperature upon LBLOCA

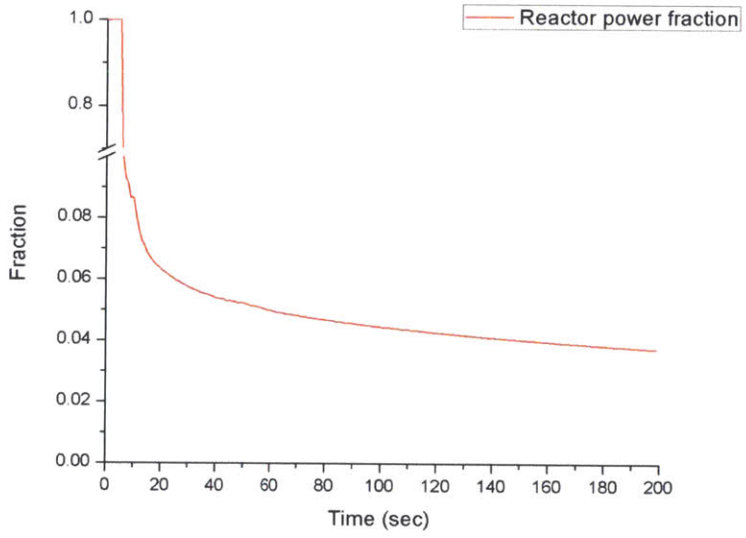

Figure 7-30 Reactor Power Fraction upon LBLOCA

7.6 Accident Considerations in SiC Cladding Design and Operation

The results of the reactor core thermal hydraulic analysis of RELAP during LBLOCA demonstrated that the safety margin of fuel rod should assure an acceptable failure rate of the cladding under (1) an increased differential pressure across the thickness, and (2) thermal shock of reflood quenching.

7.6.1 Differential Pressure Loading During LBLOCA

The SiC cladding sees the maximum differential pressure, $\Delta P \approx 0.8P_{steady\text{-}state}$ - 2.4 atm at ~40 seconds after the initiation of the reference LBLOCA. This differential pressure would be the primary determining factor of the safety margin for structural integrity of the SiC cladding. The SiC cladding stress and fracture analysis model developed in Chapter 3 are used with the burnup initialized parameter inputs from FRAPCON-3.4 SiC. The relevant LBLOCA parameters adopted from FRAPCON-3.4 SiC and RELAP for the limiting case calculation are presented in Table 7-6.

Table 7-6 SiC Cladding Stress and Fracture Analysis Inputs from FRAPCON-3.4 SiC and RELAP-5 for the Limiting Case Calculation

Cycle length	Fuel rod internal pressure (MPa)	Fuel pin power (kW/m)	System pressure	Cladding outer surface temperature (°C)
60 months, 93MWd/kgU (10% central void, 70cm plenum height)	11.5 [14.4]	0.97 [17.9]	2.4 atm [15.5 MPa]	373.8 [328.8]
72 months, 112MWd/kgU (10% central void, 70cm plenum height)	14.3 [20.9]			

* Values in brackets [] are for the limiting case at the end of in-core residence period

The representative SiC cladding mechanical properties and Weibull distribution parameters in Table 4-1, Table 4-4, and Table 4-5, presented in Chapter 4 were used; high purity CVD-SiC was used for the inner monolith and the EBC, and Hi-Nicalon^{TM} Type-S CVI-SiC composite (HNLS CVI) was used for the composite. Failure probabilities for the relevant SiC cladding fracture modes for the limiting case at steady-state and LBLOCA with the maximum burnup fuel rod for 60 months, and 93MWd/kgU (10% central void) are shown in Figure 7-31.

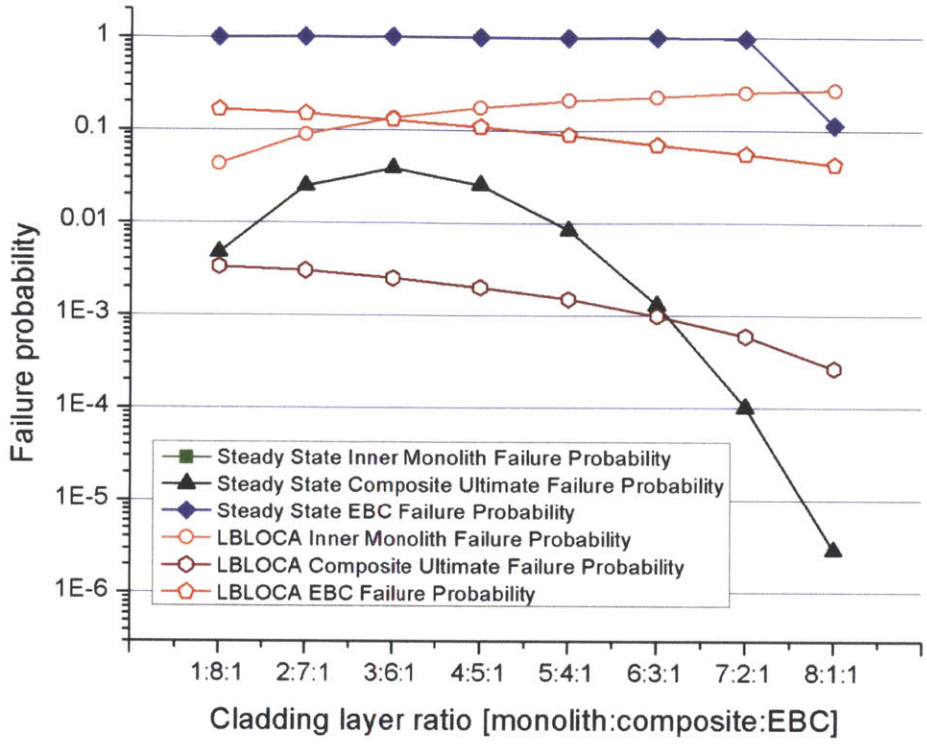

Figure 7-31Failure Probabilities of Relevant SiC Cladding Fracture Modes: Limiting Case for Steady-state and LBLOCA with the Highest Burnup Fuel Rod [60 months, 93MWd/kgU (10% central void, 70cm plenum height)]

In steady-state operation, the inner monolith stays under compression (P_f, monolith = 0) for all the presented cladding layer designs (1:8:1 ~ 8:1:1 in monolith:composite:EBC (fixed at 10%)). This is because of the compressive thermal stresses induced by the temperature gradient, and the compressive pressure loading (P_i=14.3 MPa, and P_o=15MPa) with a larger plenum volume at the end of the cycle length. While EBC and CVI matrix cracking (P_f, CVI cracking = 1) prevail, the SiC cladding's structural integrity is heavily determined by the ultimate failure of the composite under steady state operation. In Figure 7-31, the composite ultimate failure probability increases with increasing inner monolith fraction from the layer design of 1:8:1 = monolith:composite:EBC and then it starts decreasing beyond a certain fraction (3:6:1 in Figure 7-31). The increase of the steady-state composite ultimate failure rate with reduced composite fraction at high composite fraction ranges (>60% of the cladding thickness) are primarily because the peak stress level in the composite increases with decreasing composite fraction. That is, the stress increase outweighs the volume reduction in determining the failure probability at high

composite fraction ranges. The reverse trend – decreasing steady-state composite ultimate failure probability with a decreasing composite fraction – follows the peak stress levels in the composite; the composite starts experiencing a lower peak stress level with further reduction in its fraction. While the peak stress level plays a key determining factor, the volume reduction slightly accelerates the decreasing failure probability after the critical point. Such a high sensitivity of the composite failure rate to stress levels are rooted in its high Weibull modulus, m = 17.5 (typical engineering monolithic ceramic: m= 5~10, ceramic composite: m = 10~20, metal: m > 50), (Dao, 2013). As the Weibull modulus gives a measure of the statistical nature of material' failure, a higher Weibull modulus gives increasingly higher importance to stresses closer to the characteristic stress (σ_0) in determining the failure probability[31], which leads to a size-insensitive strength – the primary reason that the volume change effect is not seen in the composite failure trend.

In LBLOCA, integrity of the monolith poses an issue for safety. Without strong compressive thermal stresses, the inner monolith region is subject to tensile stresses. Generally, use of a large monolithic ceramic material under tensile stress should be avoided due to its 'volume-dependent strength', reflected in its small Weibull modulus. With increasing monolith fraction, the monolith sees higher level of tensile stresses in LBLOC situation. Also, its increasing volume further increases the chance of failure.

The SiC cladding failure probability could be evaluated by calculating the chance that any of the load bearing capability of monolith or the composite fails, as expressed in Eq.(7-1), $P_{f,rod} = 1 - (1 - P_{f,monolith})(1 - P_{f\ ultimate,composite})$. This parameter essentially gives a measure of the failure probability of the overall cladding dependency on its load-bearing components and is shown in Figure 7-32 .

[31] Theoretically, $m = \infty$ gives $P_f = 0$ unless $\sigma = \sigma_o$.

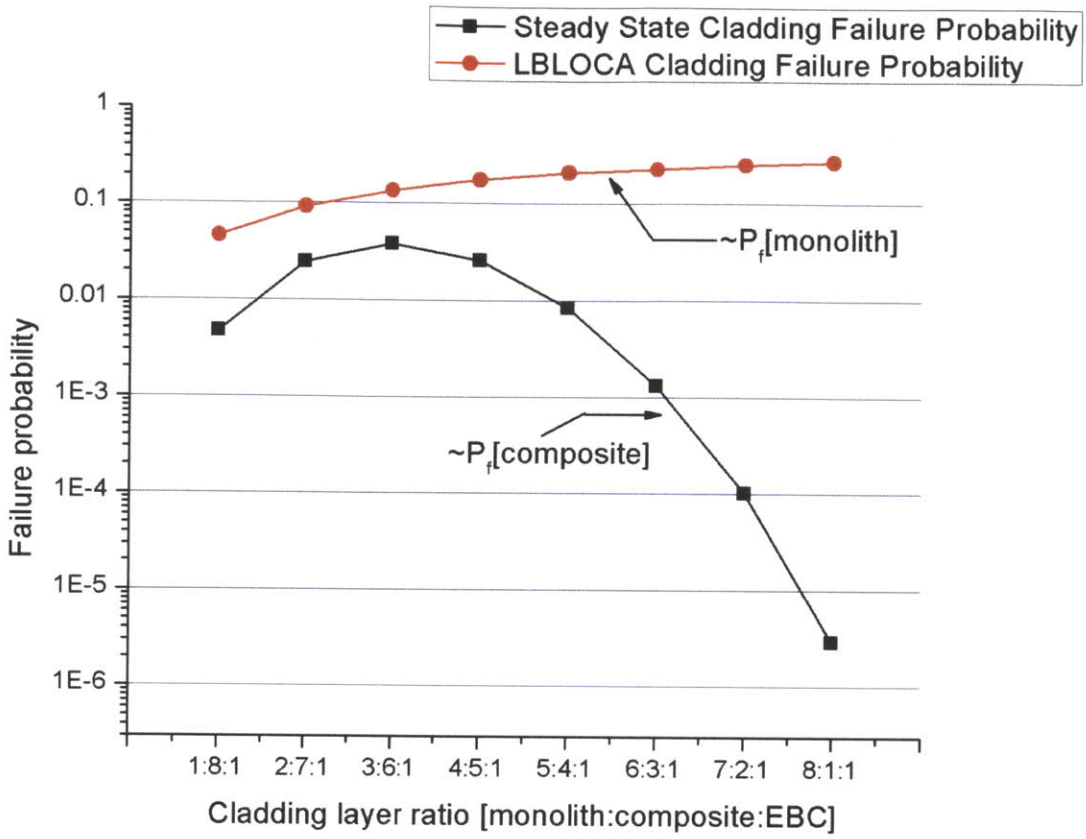

Figure 7-32 Failure Probability of the Overall Load Bearing Capability of SiC Cladding for the Limiting Cases of Steady-state and LBLOCA with the Highest Burnup Fuel Rod
[60 months, 93MWd/kgU (10% central void, 70cm plenum height)]

The evaluated cladding failure probabilities follow those of the monolith, and the composite, for LBLOCA, and steady-state operation, respectively. From the view point of LBLOCA safety, use of a smaller monolith layer fraction (1:8:1 = monolith:composite:EBC, in thickness) is preferred, so as to reduce the tensile stress level and the volume of the monolith. However, from the view point of steady-state safety, the higher monolith fraction beyond the critical cladding layer ratio (3:6:1) is preferred, given that the monolith is under compression by thermal stresses.

In determining the optimal cladding layer design, a few additional factors that are not shown in Figure 7-32 must be considered. As addressed in the previous discussion, the fuel rod plenum pressure from FRAPCON-3.4 was obtained with the thermal conductivity of SiC cladding consisting of equal thickness fraction of CVD-SiC, and fiber-reincforced SiC/SiC composite (Stempien, 2011). Given that the thermal conductivity of the SiC composite (~1.5W/m-K) is significantly lower than that of the monolith (~9.5 W/m-K), the failure probabilities presented for the cladding layer designs with the monolith layer fraction

less than 50% are underestimated values. The actual plenum pressure would be higher than the used values because of an underestimated fuel temperature. Reversely, the cladding layer designs with the monolith fraction greater than 50% give conservative failure probabilities by overestimating the plenum pressure with higher fuel temperature. Considering, the 'hidden' player of the fuel conductivity effect on plenum pressure, the cladding layer design – 6:3:1, 7:2:1, and 8:1:1 would further benefit. Yet, a significant reduction of the composite thickness could also cause a departure from the pseudo-ductile behavior of the composite. Typical SiC fiber diameter size for a reactor cladding quality fiber-reinforced SiC/SiC composite are ~11μm (Katoh, 2010). A composite layer whose thickness is 10% or 20% of the typical LWR cladding thickness (~0.57mm) would only allow ~five to~ ten layers of the woven SiC fiber fabrics. The crack arresting capability of the fiber reinforced SiC composite may be maximized beyond a certain number of woven fiber fabrics. In addition, a further reduction of the composite layer fraction could increase the vulnerabilityof the cladding. Therefore, this study tentatively uses a cladding layer design of 60% inner monolith, 30% composite, and 10% EBC in terms of their relative thickensses in 0.57mm of total cladding thickness as a tentative SiC cladding design, for 60 months of incore residence time, and the maximum burnup of 93MWd/kgU (10% central void, 70cm plenum height).

To assess the accident margin in determining maximum allowable burnup, the extended incore residence time of 72 months for a maximum burnup of 102MWd/kgU (10% central void, 70cm plenum height) is assessed in the same manner. Figure 7-33 and Figure 7-34 present failure probabilities for relevant SiC cladding fracture modes, and the overall load bearing capability of SiC cladding for the extended burnup and cycle length. The steady state operation barely meets the acceptable range of cladding failure rate ($\sim 10^{-3} - 10^{-2}$) for the peak burnup fuel pins with cladding layer designs whose monolith portion is greater than 60% of the total thickness. However, in LBLOCA, the monolith failure probability reaches ~1, demonstrating that SiC cladding has essentially 'no capability' to assure safety of fuel rod under LBLOCA with the extended the cycle length for peak burnup of 102MWd/kgU (10% central void).

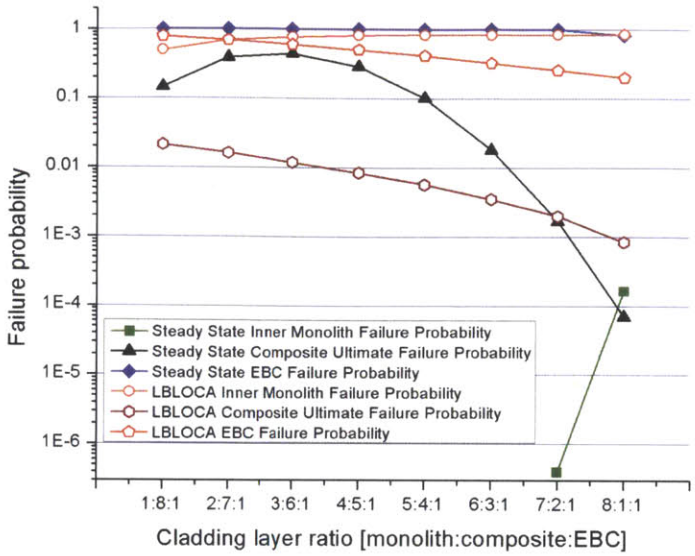

Figure 7-33Failure Probabilities of Relevant SiC Cladding Fracture Modes: Limiting Case for Steady-state and LBLOCA with the Highest Burnup Fuel Rod [72 months, 102MWd/kgU (10% central void, 70cm plenum height)]

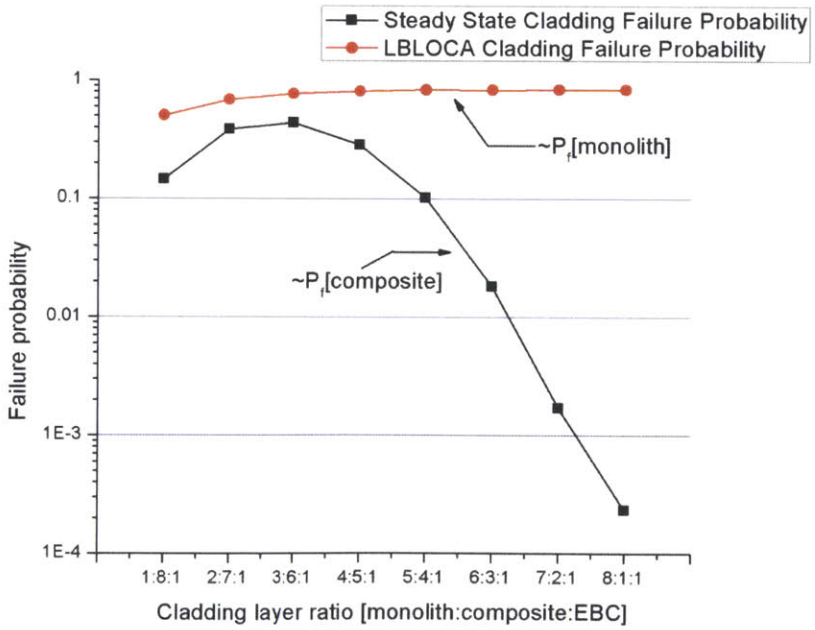

Figure 7-34 Failure Probability of the Overall Load Bearing Capability of SiC Cladding for the Limiting Cases of Steady-state and LBLOCA with the Highest Burnup Fuel Rod [72 months, 102MWd/kgU (10% central void, 70cm plenum height)]

It is worth noting that the structural integrity of the SiC cladding in LBLOCA is heavily affected by the Weibull modulus of CVD-SiC for the inner monolith and EBC as shown in Figure 7-35.

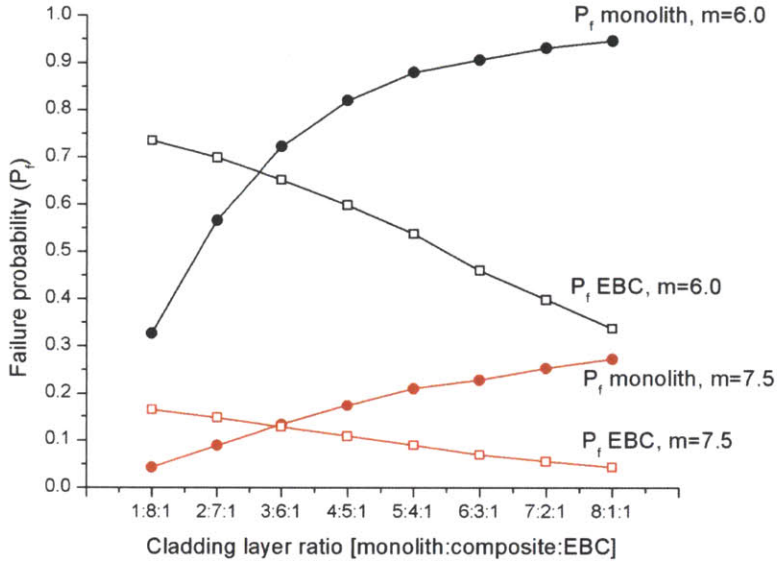

Figure 7-35 Weibull Modulus (m) Dependent Failure Probability of CVD-SiC Layers (inner monolith, n, and EBC) LBLOCA, [Highest Burnup Fuel Rod, 60 months, 93MWd/kgU (10% central void, 70cm plenum height)]

The Weibull modulus decreases with irradiation from typical unurradiated values of 9 – 10 to 7 – 8 on average, while the material showed evidence of some degree of strengthening (Katoh, 2011). Hence, this study uses m = 7.5 as a representative Weibull modulus for irradiated CVD-SiC. However, such a reduction in Weibull modulus under irradiation exhibits a wide range of scatter depending on sample sizes and test methods (Snead, 2007). Newsome's study (Newsome, 2007) found m = 9.6 for non-irradiated CVD-SiC and 5.5 ~ 8.7 for irradiated CVD-SiC for temperature ranges from 300°C ~ 800°C. Similar results were also reported by Snead's study (Snead, 2007). The controlling mechanisms for the Weibull modulus decrease under irradiation with respect to neutron dose and the increase in strength are not yet understood. Katoh (Katoh, 2011) found that CVD-SiC Weibull modulus obtained with miniature 3-point flexural tests are in substantially lower ranges as m=2.7~6.6 with 6.6 being the unirradiated specimen. Byun's work with miniaturized unirradiated tubular SiC specimens exhibits Weibull moduli of 5.0 and 9.7 for the same CVD-SiC material with a slight change in specimen dimensions. Such uncertainties in Weibull modulus of CVD-SiC are transferred into cladding integrity assessment in LBLOCA. Change of CVD-SiC Weibull modulus from 7.5 to 6.0 leads to a significantly different

consequence of LBLOCA assessment as shown in Figure 7-35. Hence, extensive studies would be needed in the future to evaluate the Weibull modulus of the actual SiC cladding with respect to neutron dose, and temperature.

7.6.2 Reflood Quenching during LBLOCA

The safety margin should account for quenching during LBLOCA on top of the maximum differential pressure across the cladding thickness. Quenching of fuel rods occurs differently for different axial locations of the fuel rod, as shown in Figure 7-27. In this assessment, the axial location (z=1.13m, Δz=0.22647m[32]) where the cladding experiences the most severe quenching in terms of the instantaneous surface temperature drop was analyzed for the limiting case assessment. The fuel decay heat at the quenching moment was calculated by multiplying the steady-state fuel pin power at the end of the cycle length with the power fraction of RELAP simulation at the quenching instant (t=~45 seconds) in Figure 7-30. The gap conductance from FRAPCON-3.4 SiC at the end of irradiation was used. The FDM code for transient fuel rod temperature calculation with SiC cladding presented in section 7.4 was used to calculate the transient temperature distribution. The initial temperature distributions were obtained by the steady-state analytical solution with a cladding surface temperature from the previous time step obtained from RELAP-5. The surface heat transfer coefficient at the quenching time step obtained from RELAP-5 (12843 W/m-K at 46 seconds) was used. The recommended cladding design of 60% inner monolith, 30% composite, and 10% EBC in terms of their relative thicknesses in the 0.57mm total cladding thickness was evaluated under LBLOCA after 60 months of maximum incore residence time, and at the maximum burnup of 93MWd/kgU (10% central void, 70cm plenum height). The quenching occurs in saturated water at 2.4 atm (T=~126°C).

The quenched CVD-SiC specimens in Chapter 4 represent fresh cladding material without oxidation and exposure to irradiation. The thermal shock behavior of an irradiated CVD-SiC may exhibit a reduced thermal shock tolerance primarily because of the reduced cladding thermal conductivity after radiation. The reduced conductivity results in a lower interface temperature upon contact with water, and that in turn results in larger thermal stresses. This safety analysis of the cladding used the lower conductivity to estimate the value of the stresses. Yet, on the other hand, the actual laminated SiC cladding structure will compensate for such a reduced thermal shock tolerance of the CVD-SiC to some extent with an additional crack arresting capability due to the presence of the composite. Further studies are needed to investigate

[32] This Δz=0.22647m is the nodal length of the RELAP simulation. Hence, fracture (failure) probabilities with the quenching were evaluated for that segment of the fuel rod.

the crack propagation behavior at the interface between the composite and the EBC. The influence of the surface modification due to oxidation after exposure to incore environment on thermal shock fracture behavior may be relatively a small change, compared to the effect of the thermal conductivity, because the surface affects only a limited distance from the surface (less than 10 μm).

The transient cladding temperature distribution is shown in Figure 7-36. The obtained temperature is used to calculate the stress. The internal fuel rod pressurization (11.5MPa) was 80% of the steady state plenum pressure (14.4 MPa) at the end of the incore residence time for maximum burnup of 93MWd/kgU (10% central void, 70cm plenum height) in Table 7-6. The system pressure of 2.4 atm was used. Figure 7-37 shows the calculated transient hoop stresses during the quenching transience.

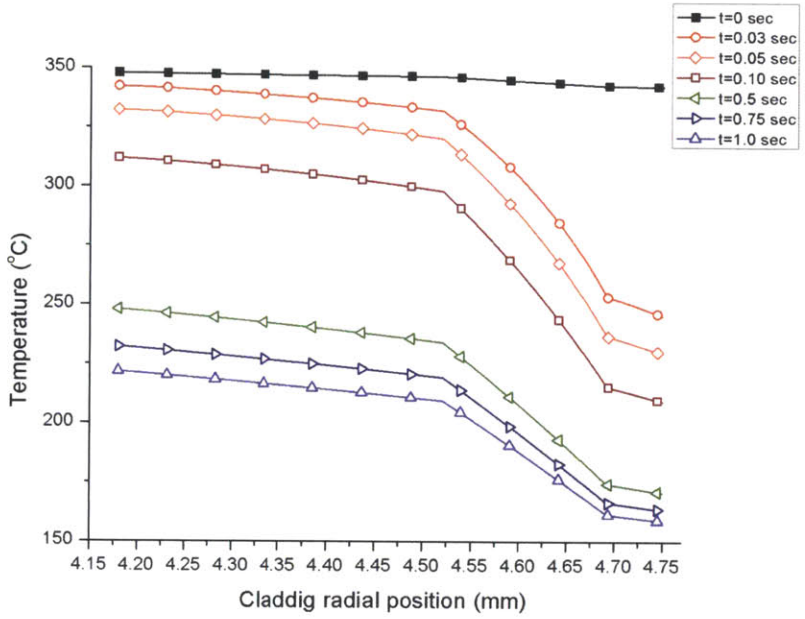

Figure 7-36 Transient SiC Cladding Temperature during the Limiting Quenching Moment of the Peak Burnup Rod in LBLOCA Refood Phase, [Highest Burnup Fuel Rod, 60 months, 93MWd/kgU (10% central void, 70cm plenum height), Cladding layer design – 6:3:1 = monolith:composite:EBC]

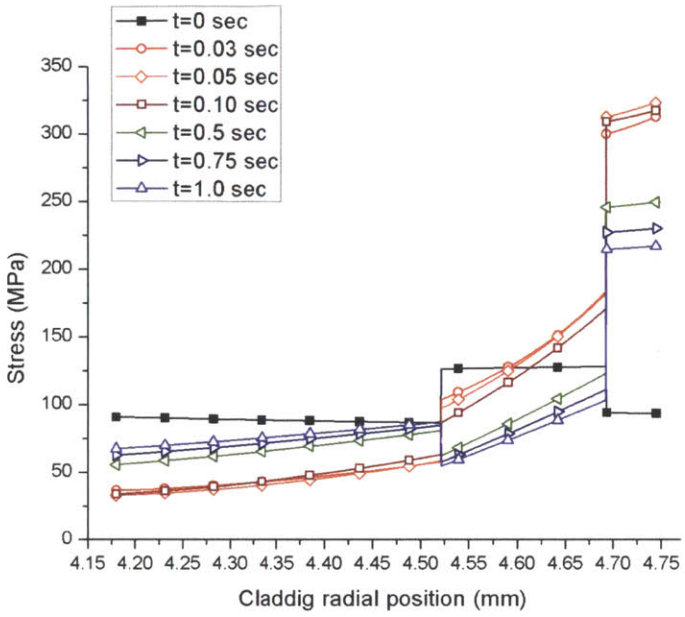

Figure 7-37 Transient SiC Cladding Hoop Stress during the Limiting Quenching Moment of the Peak Burnup Rod in LBLOCA Refood Phase, [Highest Burnup Fuel Rod, 60 months, 93MWd/kgU (10% central void, 70cm plenum height), Cladding layer design – 6:3:1 = monolith:composite:EBC, P_i=11.5MPa, P_o=2.4 atm]

Stress levels in the EBC sharply increases upon quenching. Also, the composite stress first increases but its magnitude is far smaller than the increase of the EBC. The steeper temperature gradient of the SiC cladding upon quenching leads to compressive stresses in the monolith region, hence the stress level in the monolith decreases upon quenching. As the temperature gradient becomes less steep with further cooling of the cladding, the monolith stress level increases, approaching its initial stress level. The composite stress level further decreases below the initial level with cooling of the material. These transient stress fields were used to calculate relevant transient cladding failure probability using the Weibull distribution presented in Chapter 4. Figure 7-38 shows the transient SiC cladding failure probabilities.

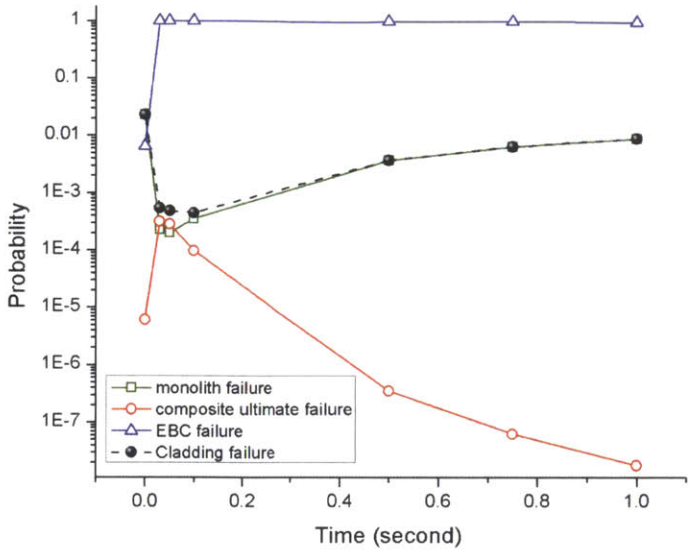

Figure 7-38 Transient SiC Cladding Failure Probability of during the Limiting Quenching Moment of the Peak Burnup Rod in LBLOCA Refood Phase (z=1.13m, Δz=0.22647m), [Highest Burnup Fuel Rod, 60 months, 93MWd/kgU (10% central void, 70cm plenum height), Cladding layer design – 6:3:1 = monolith:composite:EBC, P_i=11.5MPa, P_o=2.4 atm]

During the early quenching transient, the composite ultimate failure probability increases while the monolith failure probability concurrently decreases. This behavior is in agreement with the increasing stress level in the composite, and the decreasing stress level in the monolith during the initial quenching transient. The monolith failure probability starts increasing, approaching the initial failure probability. The composite failure probability further decreases below the initial failure probability. The overall cladding failure probability for the load bearing capability basically follows the monolith failure probability as it gives significantly higher failure probability than that of the composite in LBLOCA. This probabilistic analysis could be potentially misleading; the analysis essentially demonstrates 'no structural impact' of the reflood stage quenching on SiC cladding.

As far as the composite and the monolith are considered, this is true. However, fractures of EBC under high tensile stress levels induced by quenching may form an energetic crack, propagating into the composite, imposing extra energetic impact on the structural integrity of the cladding. Fracture of EBC upon thermal shock may require a different physical model as it may involve sharp temperature gradients across a pre-existing crack as discussed in Chapter 5 and 6. The experimental study, and the thermal shock fracture model presented in Chapter 5 and 6 found that CVD-SiC exhibits extraordinary thermal

shock capability. The quenching of CVD-SiC specimen whose thickness is ~3.5 times the actual reference cladding thickness demonstrated that it maintained its original strength when quenched at 1265°C in saturated water at 1atm.

7.7 Fuel Performance of LWR Rod with a Thicker SiC Cladding Thickness

Thus far, the SiC cladding thickness is assumed to be the same thickness as the current Zircaloy thickness, 0.57mm. The current manufacturers of the prototype SiC cladding, however, estimate that they can achieve a thickness of 0.8mm as the tentative minimum value. Hence, it is important to assess SiC cladding performance with the currently available manufacturing technology. This section basically follows the same presented assessment procedure and methods with the cladding thickness of 0.8mm. The increase in cladding thickness occurred in the outward direction, maintaining the same fuel pellet diameter. Neutronics study on PWR core with the SiC clad fuel found that the cladding thickness increase of 0.23 mm (0.57→0.8mm) does not hurt neutronic features of the core significantly with a small change of hydrogen to heavy-metal ratio (H/HM) (Bloore, 2013).

7.7.1 Steady-state Fuel Behavior of LWR Fuel Rod with a Thicker SiC Cladding, 0.8mm

Key steady-state fuel rod behavior with the thicker SiC cladding, is shown in Figure 7-39 - Figure 7-53, for reactor core designs of the peak burnups of 75MWD/kgU (1476 days), 93 MWD/kgU (1845 days), and 112MWD/kgU (2214 days).

A noticeable change in fuel rod behavior is the temperature increase of the fuel rod. Fuel rod temperatures for both the peak and the average values increased by ~50°C with the cladding thickness change form 0.57 mm to 0.8mm. This increase in temperature increases fission gas release from the fuel pellets, leading to a higher plenum pressure.

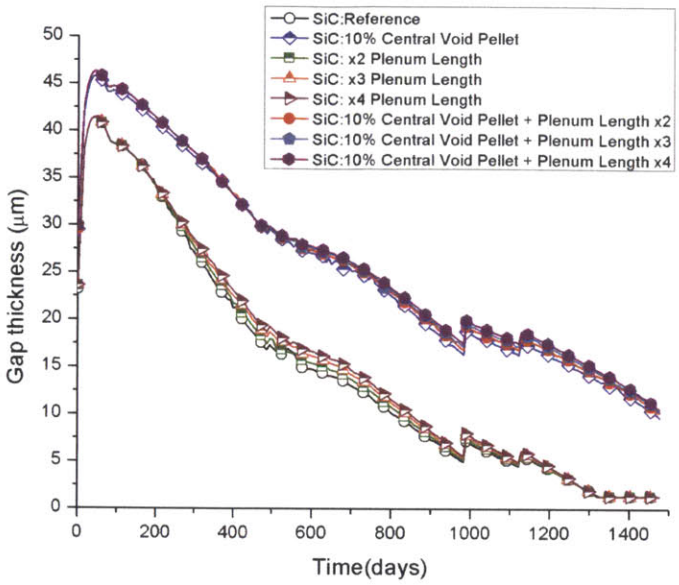

Figure 7-39 Fuel Rod Radial Gap from FRAPCON-3.4 Simulation for the Peak Fuel Rod Burnup of 75MWD/kgU after 1476 Days of Incore Residence Time, Cladding Thickness=0.8mm (the highest burnup node, 2.51m from the bottom of the fuel rod)

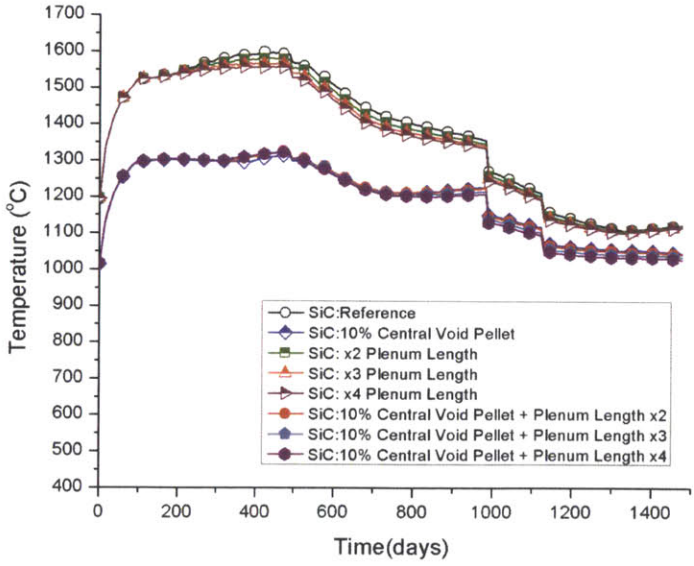

Figure 7-40 Fuel Centerline Temperature from FRAPCON-3.4 Simulation for the Peak Fuel Rod Burnup of 75MWD/kgU after 1476 Days of Incore Residence Time, Cladding Thickness=0.8mm (the highest burnup node, 2.51m from the bottom of the fuel rod)

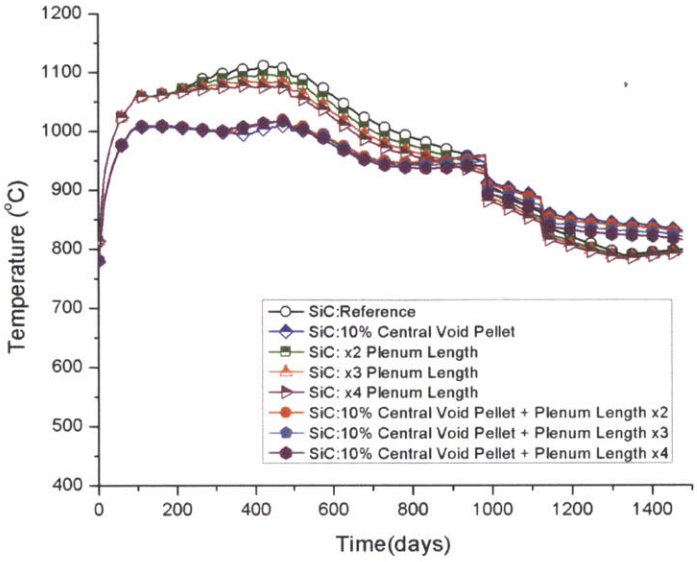

Figure 7-41 Volume Average Fuel Temperature from FRAPCON-3.4 Simulation for the Peak Fuel Rod Burnup of 75MWD/kgU after 1476 Days of Incore Residence Time, Cladding Thickness=0.8mm (the highest burnup node, 2.51m from the bottom of the fuel rod is)

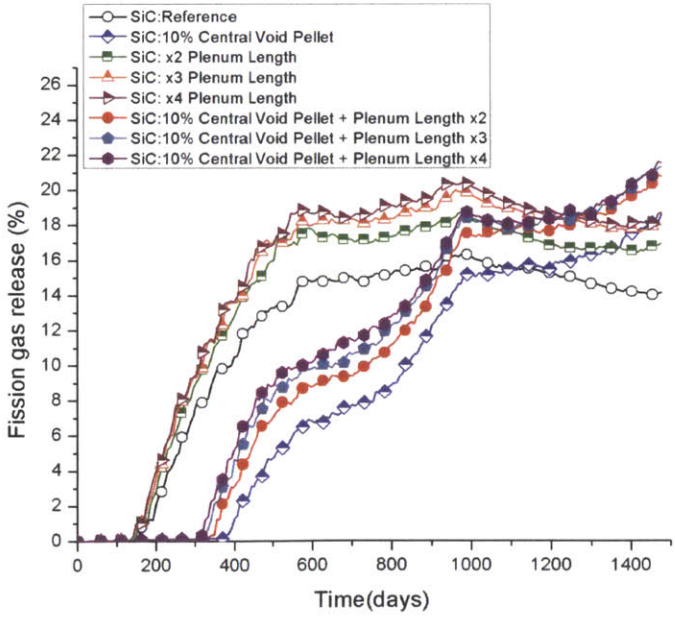

Figure 7-42 Fission Gas Release Percentage from FRAPCON-3.4 Simulation for the Peak Fuel Rod Burnup of 75MWD/kgU after 1476 Days of Incore Residence Time, Cladding Thickness=0.8mm

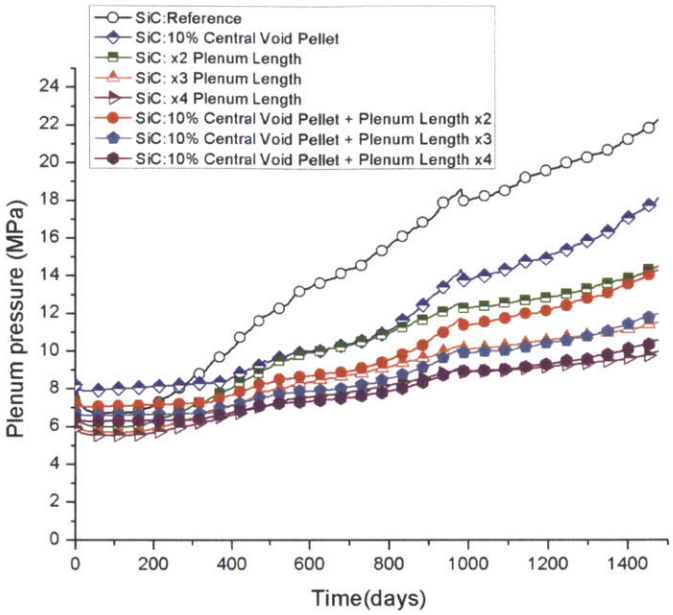

Figure 7-43 Plenum Pressure from FRAPCON-3.4 Simulation for the Peak Fuel Rod Burnup of 75MWD/kgU after 1476 Days of Incore Residence Time

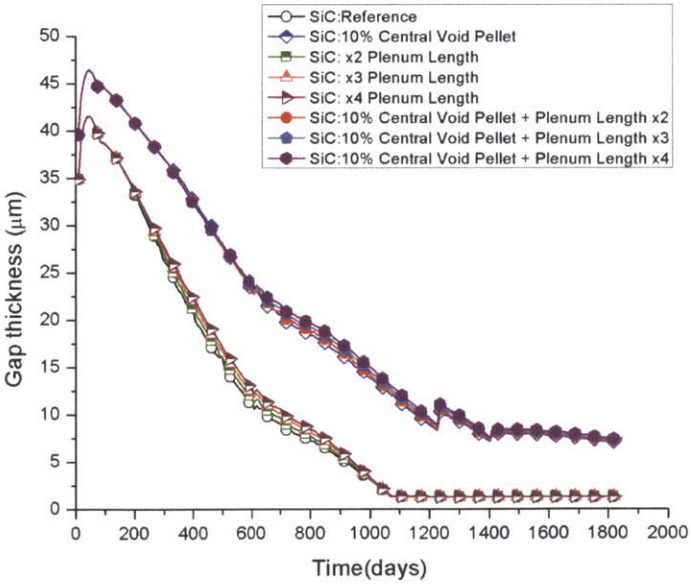

Figure 7-44 Fuel Rod Radial Gap from FRAPCON-3.4 Simulation for the Peak Fuel Rod Burnup of 93MWD/kgU after 1845 Days of Incore Residence Time, Cladding Thickness=0.8mm (the highest burnup node, 2.51m from the bottom of the fuel rod)

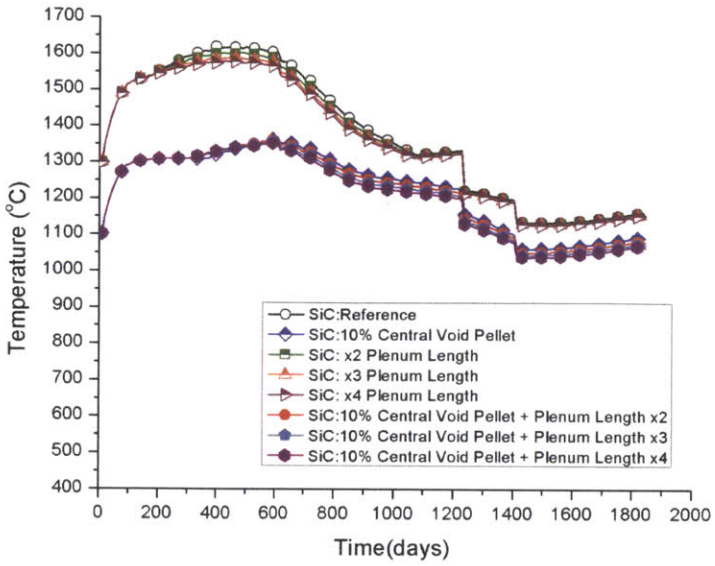

Figure 7-45 Fuel Centerline Temperature from FRAPCON-3.4 Simulation for the Peak Fuel Rod Burnup of 75MWD/kgU after 1476 Days of Incore Residence Time, Cladding Thickness=0.8mm (the highest burnup node, 2.51m from the bottom of the fuel rod)

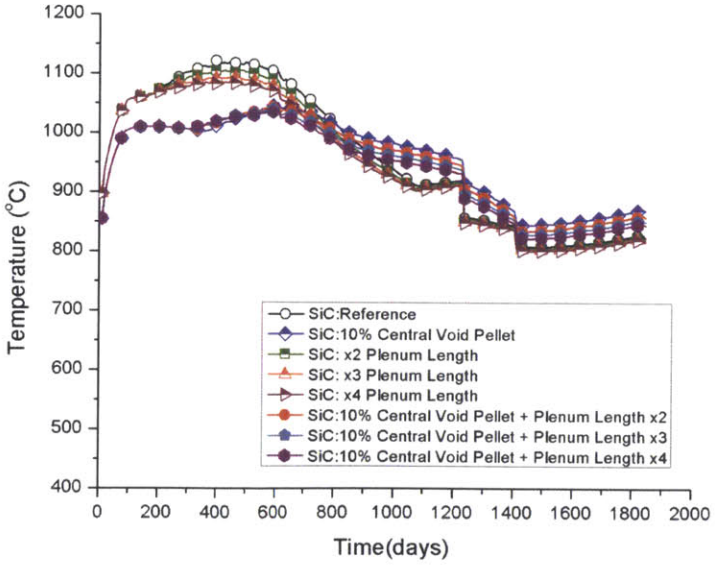

Figure 7-46 Volume Average Fuel Temperature from FRAPCON-3.4 Simulation for the Peak Fuel Rod Burnup of 93MWD/kgU after 1845 Days of Incore Residence Time, Cladding Thickness=0.8mm (the highest burnup node, 2.51m from the bottom of the fuel rod is)

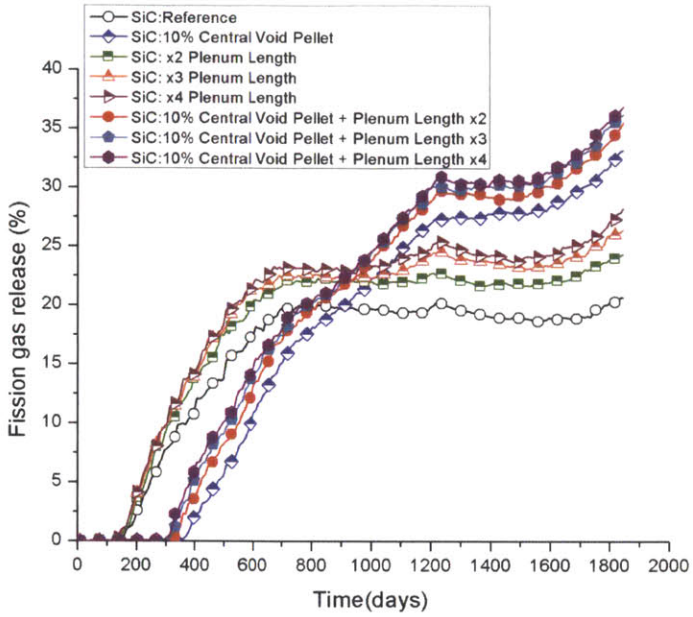

Figure 7-47 Fission Gas Release Percentage from FRAPCON-3.4 Simulation for the Peak Fuel Rod Burnup of 93MWD/kgU after 1845Days of Incore Residence Time, Cladding Thickness=0.8mm

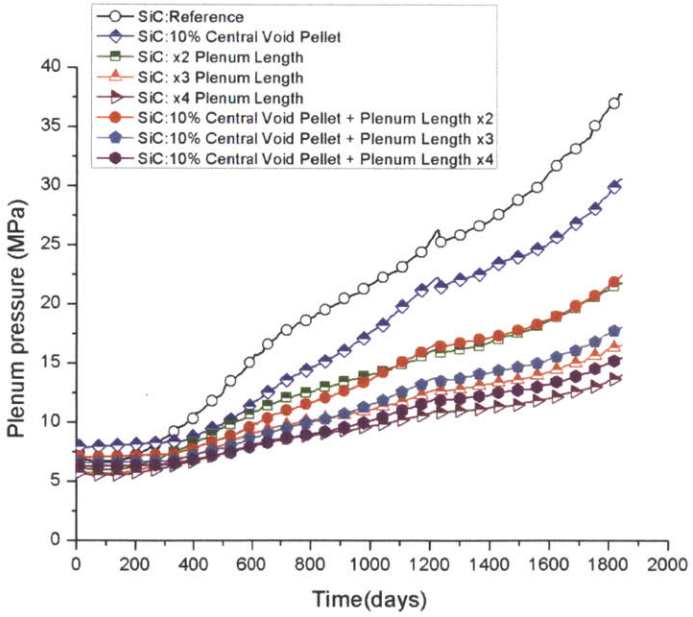

Figure 7-48 Plenum Pressure from FRAPCON-3.4 Simulation for the Peak Fuel Rod Burnup of 93MWD/kgU after 1845 Days of Incore Residence Time

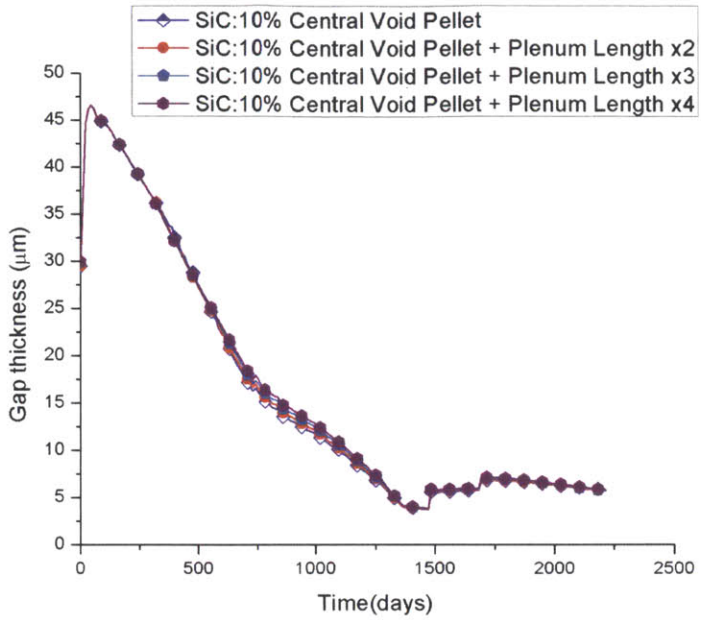

Figure 7-49 Fuel Rod Radial Gap from FRAPCON-3.4 Simulation for the Peak Fuel Rod Burnup of 112MWD/kgU after 2214 Days of Incore Residence Time, Cladding Thickness=0.8mm (the highest burnup node, 2.51m from the bottom of the fuel rod)

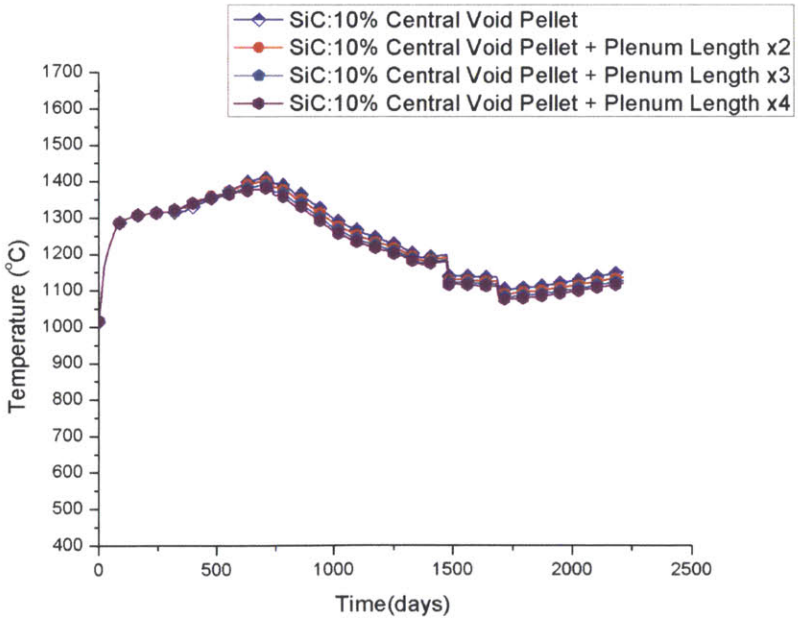

Figure 7-50 Fuel Centerline Temperature from FRAPCON-3.4 Simulation for the Peak Fuel Rod Burnup of 112MWD/kgU after 2214 Days of Incore Residence Time, Cladding Thickness=0.8mm (the highest burnup node, 2.51m from the bottom of the fuel rod)

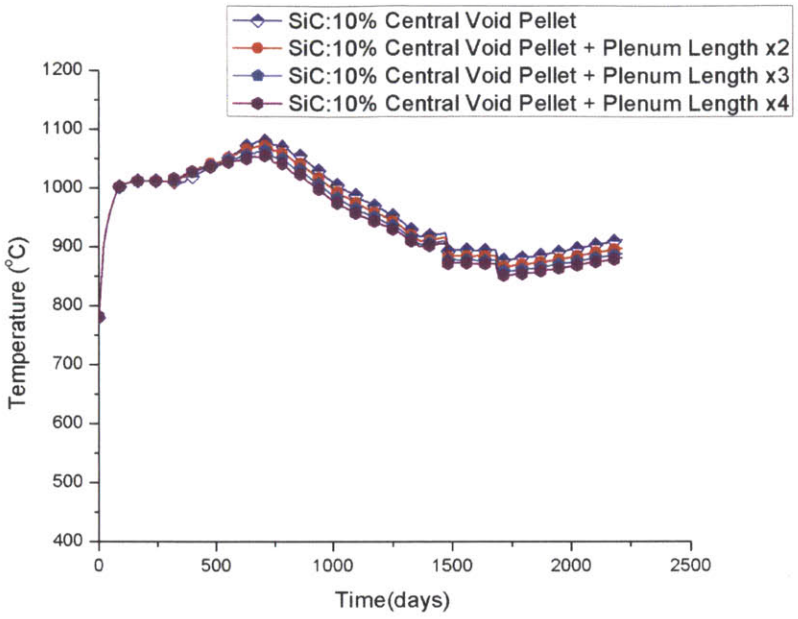

Figure 7-51 Volume Average Fuel Temperature from FRAPCON-3.4 Simulation for the Peak Fuel Rod Burnup of 112MWD/kgU after 2214 Days of Incore Residence Time, Cladding Thickness=0.8mm (the highest burnup node, 2.51m from the bottom of the fuel rod is)

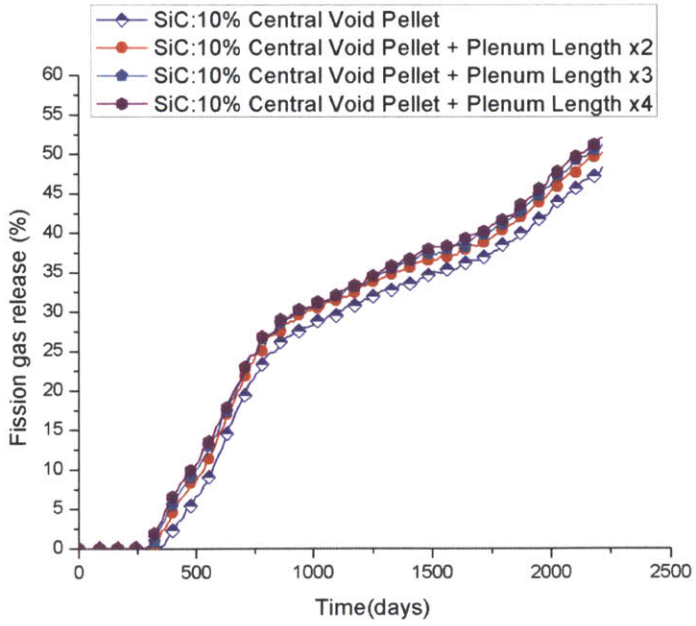

Figure 7-52 Fission Gas Release Percentage from FRAPCON-3.4 Simulation for the Peak Fuel Rod Burnup of 112MWD/kgU after 2214 Days of Incore Residence Time, Cladding Thickness=0.8mm

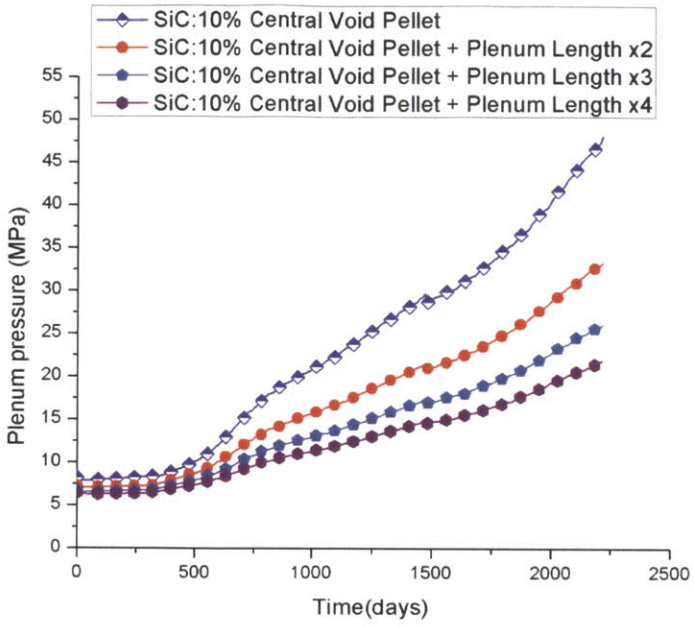

Figure 7-53 Plenum Pressure from FRAPCON-3.4 Simulation for the Peak Fuel Rod Burnup of 112MWD/kgU after 2214 Days of Incore Residence Time

7.7.2 Stress and Fracture Analysis of a Thicker SiC Cladding (0.8mm) in Steady-State Operation

Burnup initialized parameters for SiC cladding stress calculation are summarized in Table 7-7. For LBLOCA conditions, 80% percent of the fuel internal pressure was used, and 2.4 atm was used for the system pressure. 5.419% of the fuel pin power was used as it was found to be the relevant decay power for the limiting case calculation in LBLOCA from RELAP simulation. Cladding outer surface temperatures of 385.7 °C, 379.5 °C, and 373.8°C were used for LBLOCA calculations at BOL, MOL, and EOL, respectively.

Table 7-7 Sumamry of Cladding Stress Calculation Inputs from FRAPCON-3.4SiC Simulation

	Fuel Design	Input Parameters	BOL	MOL	EOL
75 MWD/kgU (with 10% central void), 3 batch, 48 months	Standard PWR Fuel Pin with 0.8mm SiC cladding 10% central void pellets	Internal pressure, P_i (MPa)	7.9	10.6	18.2
		Fuel pin power, $\dot{q}$ (kW/m)	26.1	21.2	17.9
		Cladding outer surface temperature, T_o (°C)	339.9	334.1	328.8
	Standard PWR Fuel Pin with 0.8mm SiC cladding 10% central void pellets + x4 Plenum Length (70cm)	Internal pressure, P_i (MPa)	6.3	7.6	10.6
		Fuel pin power, $\dot{q}$ (kW/m)	26.1	21.2	17.9
		Cladding outer surface temperature, T_o (°C)	339.9	334.1	328.8
93 MWD/kgU (with 10% central void), 3 batch, 60 months	Standard PWR Fuel Pin with 0.8mm SiC cladding 10% central void pellets + x4 Plenum Length (70cm)	Internal pressure, P_i (MPa)	6.3	9.6	15.5
		Fuel pin power, $\dot{q}$ (kW/m)	26.1	21.2	17.9
		Cladding outer surface temperature, T_o (°C)	339.9	334.1	328.8
112 MWD/kgU (with 10% central void), 3 batch, 72 months	Standard PWR Fuel Pin with 0.8mm SiC cladding 10% central void pellets + x4 Plenum Length (70cm)	Internal pressure, P_i (MPa)	6.3	12.0	21.9
		Fuel pin power, $\dot{q}$ (kW/m)	26.1	21.2	17.9
		Cladding outer surface temperature, T_o (°C)	339.9	334.1	328.8

Increasing cladding thickness helps reduce mechanical stress levels induced by pressure loading. However, at the same time, it increases thermal stress levels. For materials with a high thermal conductivity, where most of its stresses come from the mechanical loading, increasing the thickness brings an overall positive effect by reducing the total stress levels of the cladding. However, for materials with a low thermal conductivity, where thermal stress accounts for a significant contribution to the total stress, increasing its size may hurt the structural integrity of the material, as the increase in thermal stress outweighs the decrease in mechanical stresses.

Fuel rod cladding in the beginning of life (BOL) is predominantly affected by thermal stresses because of limited internal pressurization. During this period, a negative effect of increasing cladding thickness is the most evident in the entire incore residence time of the fuel rod. Figure 7-54 and Figure 7-55 show that the stress levels of the composite are significantly higher at BOL with the 0.8mm cladding thickness. The monolith experiences stronger compressive stresses with the 0.8 mm cladding thickness, however, this is of little value in terms of the structural integrity of the cladding. Hence, it can be inferred that the increase in the cladding thickness may introduce an overall negative effects for cladding integrity during steady-state operation where thermal stresses make a significant fraction of the total stress.

Yet, the situation could be different during LBLOCA, when fuel pin power is much lower than the steady-state (~5 % of the steady-state), and the mechanical loading is higher with the core depressurization. Figure 7-56 and Figure 7-56 show that the stress levels in both the monolith and the composite decrease with the thicker SiC cladding, 0.8mm in LBLOCA. Hence it can be inferred that the thickness SiC cladding should be determined by finding the optimal balance between safety during steady-state and safety during LBLOCA.

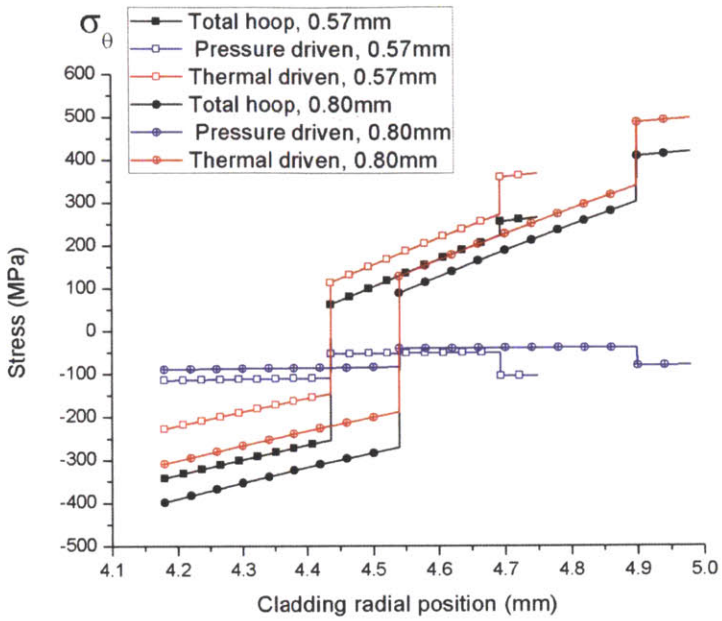

Figure 7-54Steady State Hoop Stress (σ_θ) Distribution of SiC Cladding for 0.57mm, and 0.8mm Thickness [45% inner monolith, 45% composite, 10% EBC] at BOL

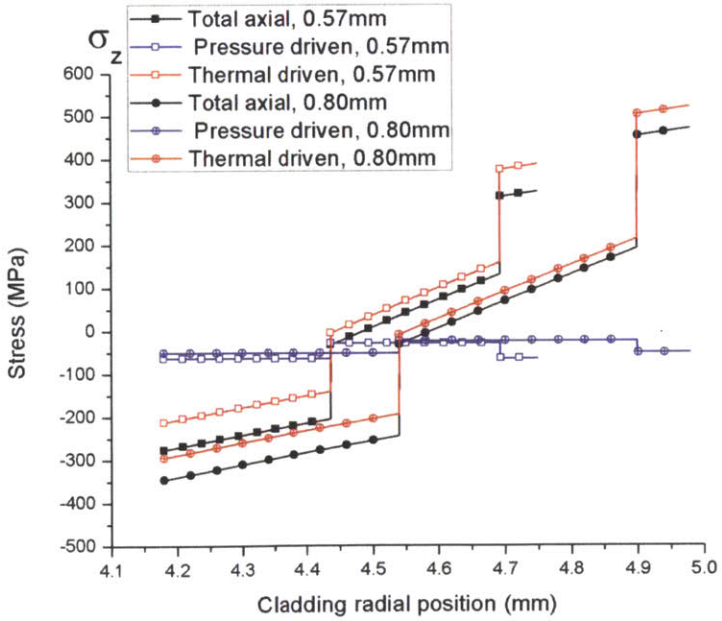

Figure 7-55Steady State Axial Stress (σ_z) Distribution of SiC Cladding for 0.57mm, and 0.8mm Thickness [45% inner monolith, 45% composite, 10% EBC] at BOL

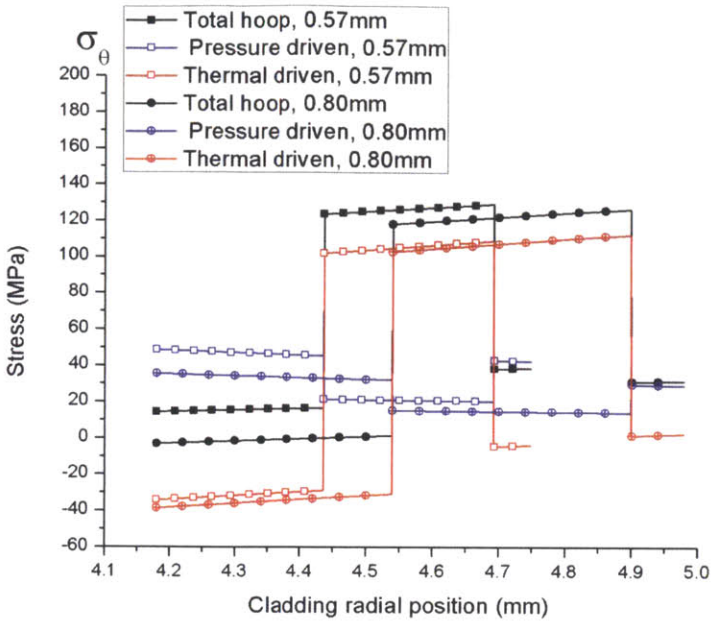

Figure 7-56LBLOCA Hoop Stress (σ_θ) Distribution of SiC Cladding for 0.57mm, and 0.8mm Thickness [45% inner monolith, 45% composite, 10% EBC] at BOL

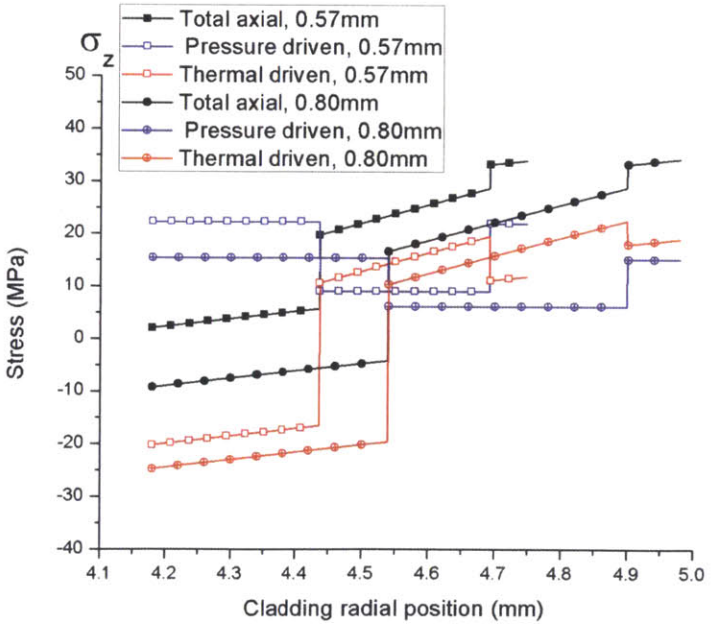

Figure 7-57LBLOCA Axial Stress (σ_z) Distribution of SiC Cladding for 0.57mm, and 0.8mm Thickness [45% inner monolith, 45% composite, 10% EBC] at BOL

Obtained stress distributions were used to calculate the cladding failure probability, defined as $P_{f,rod} = 1 - (1 - P_{f,monolith})(1 - P_{f\ ultimate,composite})$, as shown in Eq.(7-1). Failure probability of the reference fuel rod with the thicker SiC clad (0.8mm), whose other design features are identical to the current PWR fuel rod in the reference core design (peak burnup of 75MWD/kgU (with 10%central void) at 1476 days of the incore residence time), is shown in Figure 7-58.

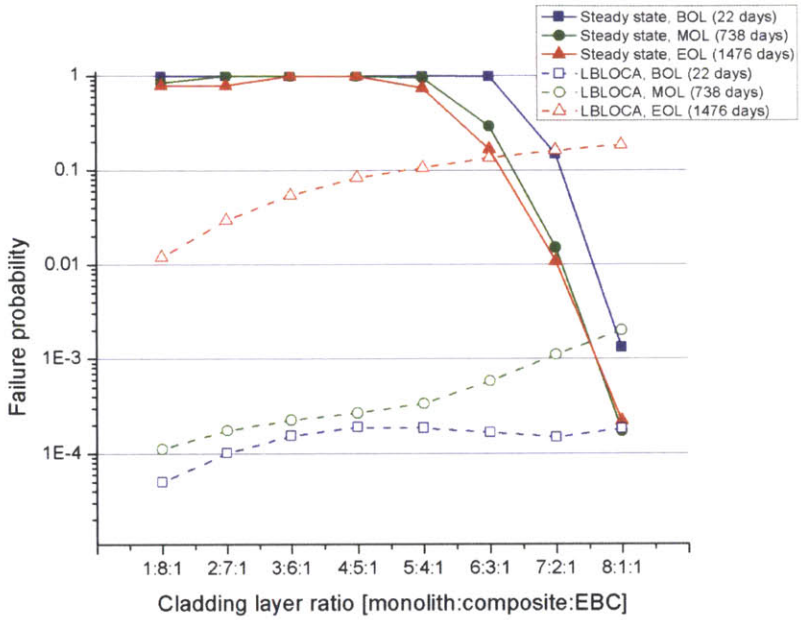

Figure 7-58 Cladding Failure Probabilities of the Fuel Pin with the Peak Burnup of 75MWD/kgU at 1476days [10% Central Void in Fuel Pellets, 0.8mm Cladding Thickness]

The cladding failure probability is at its highest value during BOL at steady-state, due to a high thermal stress. This failure probability in steady-state is basically the failure probability of the composite while a significant fraction (or all) of the monolith is under compression. As discussed previously, failure probabilities of BOL and MOL are pertinent to majority of fuel rods in a core which are discharged before they reach the allowed peak burnup. In that regard, unless the cladding design with a very high inner monolith fraction is used (beyond the 80% of the total cladding thickness), the cladding failure probabilities are not at an acceptable level. Yet, it is not assured if the composite could still function with the expected pseudo-ductile behavior if its size is smaller than a certain level. In LBLOCA, for the thicker cladding thickness (0.8mm), cladding failure probability is dictated by that of the composite for cladding designs of small monolith fractions. For cladding designs of large monolith fractions, the cladding failure probability tends to be dictated by that of the monolith. In the intermediate ranges, where the monolith

fraction is similar to that of the composite, cladding failure probability is affected by failure probabilities of both the monolith and the composite.

This study recommends a SiC clad fuel rod design with 4 times the plenum length (resulting length of 70cm) as a tentative SiC clad fuel rod design to reduce the plenum pressure. Cladding failure probabilities with this fuel rod design for reactor core designs of the peak burnups of 75MWD/kgU (1476 days), 93 MWD/kgU (1845 days), and 112MWD/kgU (2214 days) are shown in Figure 7-59, Figure 7-60, and Figure 7-61, respectively. With the thicker cladding (0.8mm), the steady-state cladding failure probability at BOL serves as a limiting value, and it is not subject to a significant change unless the fuel pin power changes. Fuel rod failure probability during LBLOCA increases with increasing burnup due to higher fuel rod internal pressurization. The failure probability during LBLOCA for the fuel rod with the peak burnup of 112MWD/kgU at 2214days of incore residence time is above the acceptable level as it is close to unity. Yet, before considering safety margin required for LBLOCA, the thicker cladding's structural integrity is primarily limited by the steady-state thermal stresses. Unless an improved composite thermal conductivity above 1.5W/m-K with the pertinent irradiation condition is found, the feasibility of the SiC cladding with 0.8mm thickness is not strong. Hence, increasing SiC cladding thickness should accompany an improvement of thermal conductivity especially in the composite to obtain the same level of cladding safety in terms of its structural integrity.

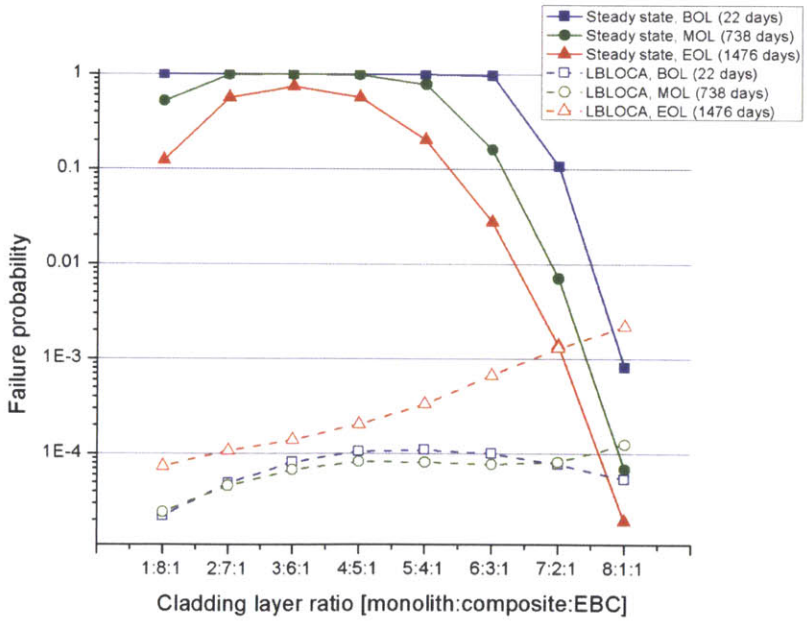

Figure 7-59 Cladding Failure Probabilities of the Fuel Pin with the Peak Burnup of 75MWD/kgU at 1476days [10% Central Void in Fuel Pellets + 4×Plenum Length, 0.8mm Cladding Thickness]

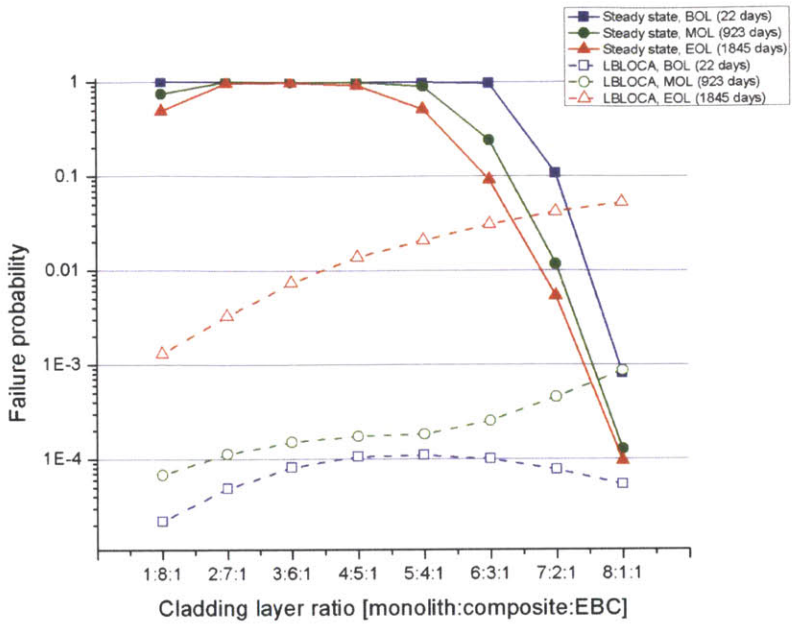

Figure 7-60 Cladding Failure Probabilities of the Fuel Pin with the Peak Burnup of 93MWD/kgU at 1845days [10% Central Void in Fuel Pellets + 4×Plenum Length, 0.8mm Cladding Thickness]

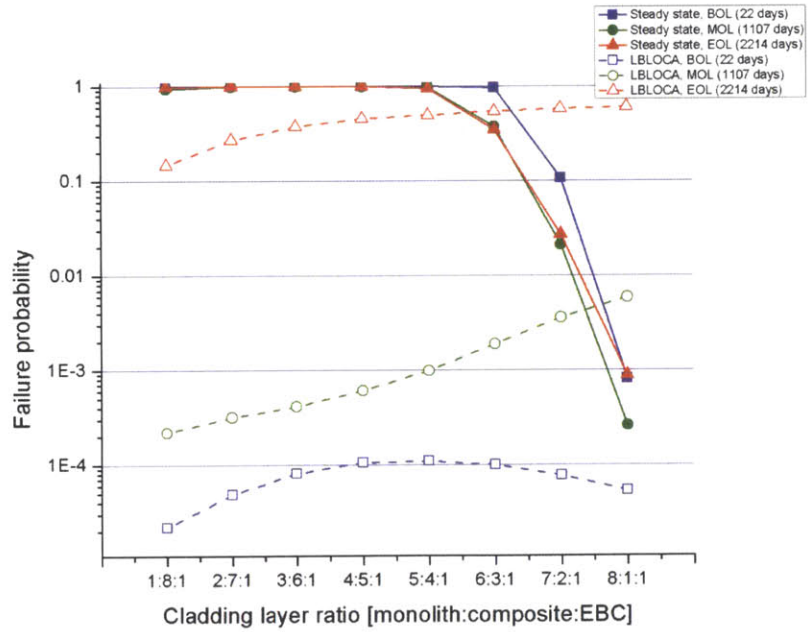

Figure 7-61 Cladding Failure Probabilities of the Fuel Pin with the Peak Burnup of 112MWD/kgU at 2214days [10% Central Void in Fuel Pellets + 4×Plenum Length, 0.8mm Cladding Thickness]

7.8 Manufacturing Guidline for SiC Cladding

This study can be used to generate guidelines for manufacturing of SiC cladding with desirable characteristics. Key manufacturing guidelines were assessed based on the currently thought to be manufacturable cladding thickness, 0.8 mm. Figure 7 62, Figure 7 63, and Figure 7 64 show steady state cladding failure probabilities as a function of composite Weibull modulus and composite thermal conductivity for three different peak fuel rod burnups. A cladding layer design with thicknesses of 60% inner monolith, 30% fiber-reinforced composite, and 10% EBC was used, as it was found in previous sections to be a suitable composition in terms of the cladding structural integrity. During steady state operation, the cladding failure probability is determined primarily by the failure of the composite layer while the inner monolith is under compression. Composite thermal conductivity of 1.5 W/m-K was used as a reference value after exposure to relevant irradiation and temperature. Potential benefit of improving the composite thermal conductivity was assessed by considering doubling the thermal conductivity, to 3.0W/m-K.

The feasibility of the SiC cladding with the reference thermal conductivity (1.5 W/m-K) is questionable at BOL, when the fuel pin power is at its maximum, since the composite will have unacceptably high thermal stresses. A higher Weibull modulus does not help in this case as shown in Figure 7-62, since the failure probability would be only marginally reduced. Increasing the thermal conductivity of the composite significantly contributes to lowering the steady-state cladding failure probability, making the SiC cladding concept feasible. For the reference peak fuel pin of 48 months of in-core residence time (to achieve burnup of 75MWD/kgU with 10% central void in the pellet), to give the same energy from the core design of the zirconium based alloy cladding, a composite thermal conductivity of 3.0 W/m-K and a Weibull modulus (m) greater than 19 leads to a peak pin failure probability below 10^{-3} at BOL as can be seen Figure 7-62. Failure probability for MOL and EOL is lower than that of BOL, unless the rod is highly internally pressurized. As a consequence, for the peak fuel burnup of 75MWD/kgU and 93MWD/kgU, failure probability of BOL serves as the limiting value. For peak fuel rod burnup of 112 MWD/kgU, the failure probability at EOL is approximately the same as that at BOL, due to significant internal pressurization. Of course, it is also possible to lower the thermal stress by reducing the linear hat rate of the peak fuel pin, but that would make the core neutronic design more constrained, to keep the peaking factors below those assumed in our study.

In this study, steady state fuel rod failure probability of 10^{-3} is tentatively regarded as the maximum allowable peak fuel rod failure rate. This would imply that one out of each thousand hot fuel rods would undergo some degree of cracking, which may lead to fission gas release. Hence from the steady state

point of view, manufacturing the SiC composite with a minimum thermal conductivity of 3.0 W/m-K and Weibull modulus of 19 under exposure to relevant irradiation and temperature is desirable. .

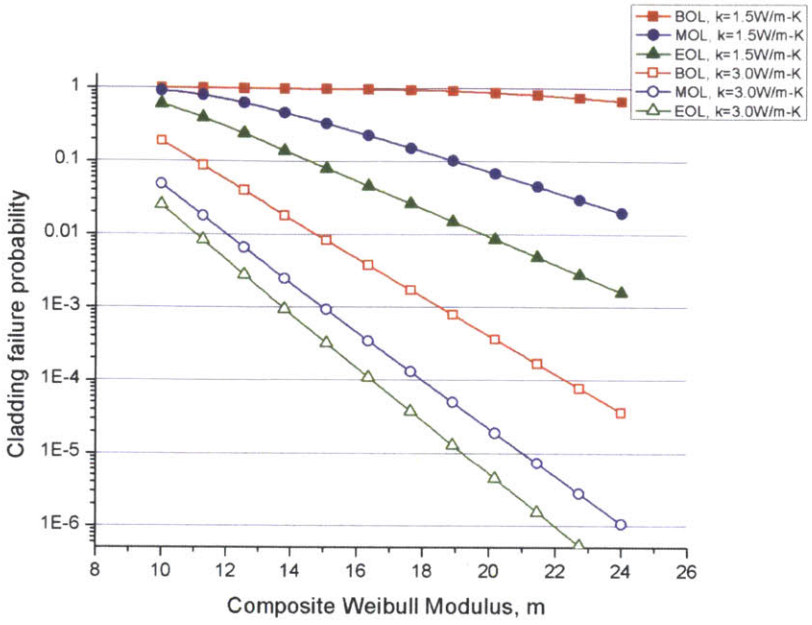

Figure 7-62 Steady State Cladding Failure Probability of the Fuel Pin with the Peak Burnup of 75MWD/kgU at 1476days as a function of Composite Weibull Modulus, and Composite Thermal Conductivity [10% Central Void in Fuel Pellets + 4×Plenum Length, 0.8mm Cladding Thickness]

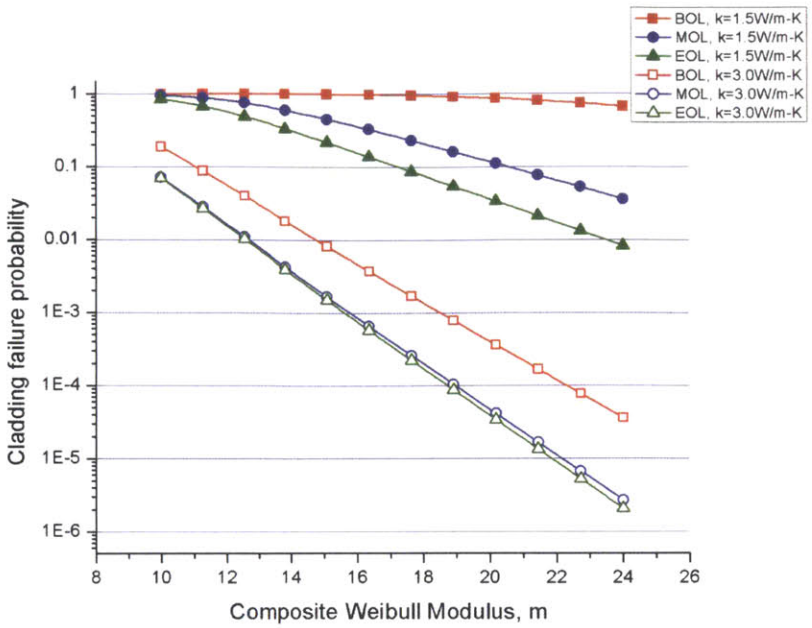

Figure 7-63 Steady State Cladding Failure Probability of the Fuel Pin with the Peak Burnup of 93MWD/kgU at 1845days as a function of Composite Weibull Modulus, and Composite Thermal Conductivity [10% Central Void in Fuel Pellets + 4×Plenum Length, 0.8mm Cladding Thickness]

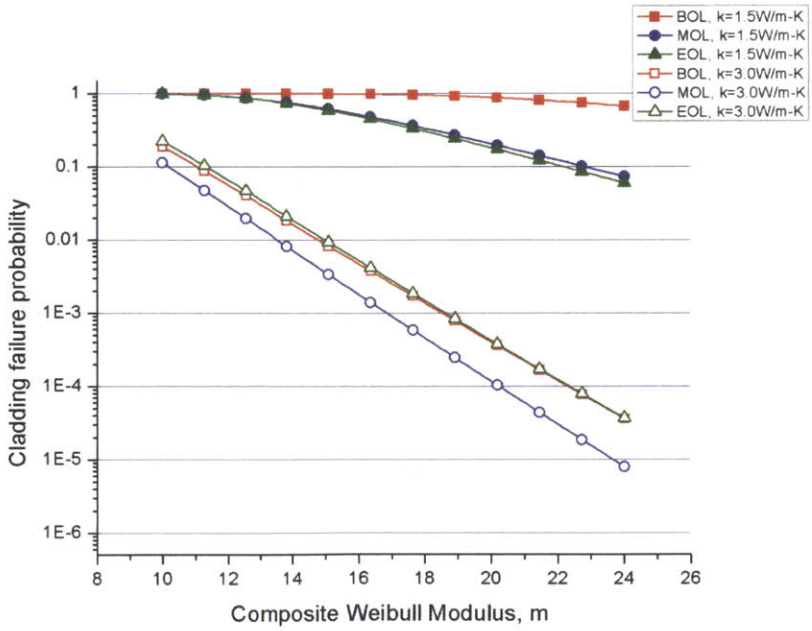

Figure 7-64 Steady State Cladding Failure Probability of the Fuel Pin with the Peak Burnup of 112MWD/kgU at 2214days as a function of Composite Weibull Modulus, and Composite Thermal Conductivity [10% Central Void in Fuel Pellets + 4×Plenum Length, 0.8mm Cladding Thickness]

Yet, the target manufacturing guidelines should also take into account limiting accident cases. Figure 7-65, Figure 7-66, and Figure 7-67 show the fuel rod failure probabilities during LBLOCA for the peak fuel rod burnup of 75MWD/kgU, 93MWD/kgU, and 112MWD/kgU, respectively. As previously discussed, failure probability of the peak burnup fuel rod at EOL gives the highest failure probability in LBLOCA and serves as the limiting value.

In this study, the EOL peak burnup fuel rod failure probability range of $10^{-2} \sim 10^{-1}$ is regarded tentatively as the maximum allowable failure rate during a LBLOCA. Given that a composite Weibull modulus greater than 19 was found to be necessary for the structural integrity of the SiC cladding during steady state, a Weibull modulus of the monolith greater than 6 is recommended to permit the peak fuel rod burnup of 75MWD/kgU from the view point of LBLOCA safety margin. Similarly, Weibull modulii of CVD-SiC monolith greater than 7, and 9.5 were recommended to permit the peak fuel rod burnup of 93MWD/kgU, and 112MWD/kgU, respectively.

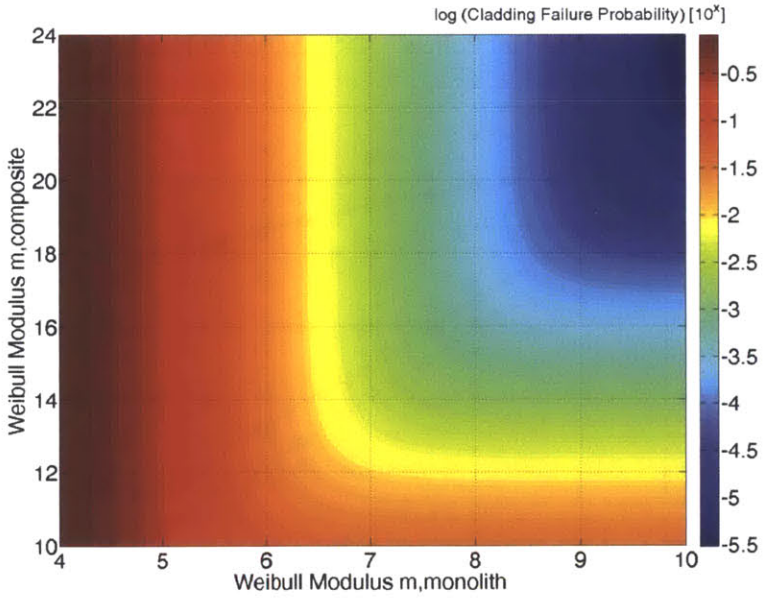

Figure 7-65 LBLOCA SiC Cladding Failure Probability of the Fuel Pin with the Peak Burnup of 75MWD/kgU at 1476days as a function of Monolith Weibull Modulus, and Composite Weibull Modulus [10% Central Void in Fuel Pellets + 4×Plenum Length, 0.8mm Cladding Thickness + 3.0W/m-K Composite Thermal Conductivity]

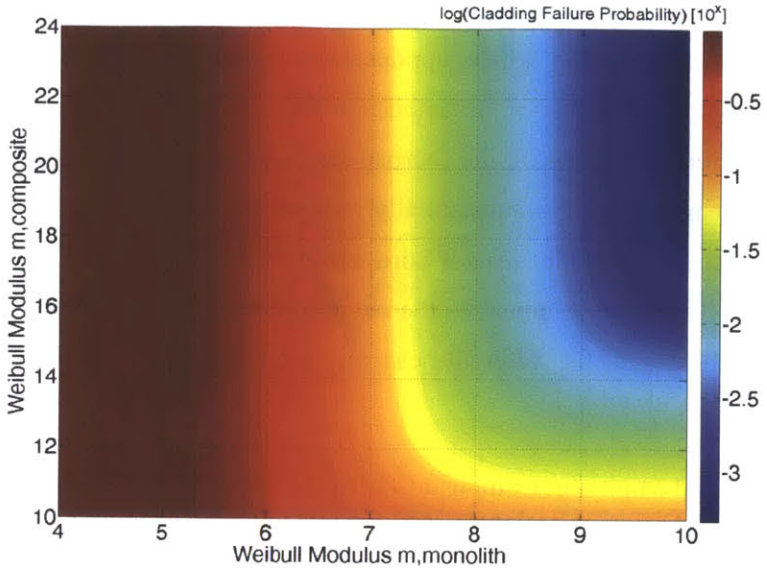

Figure 7-66 LBLOCA SiC Cladding Failure Probability of the Fuel Pin with the Peak Burnup of 93MWD/kgU at 1845 days as a function of Monolith Weibull Modulus, and Composite Weibull Modulus [10% Central Void in Fuel Pellets + 4×Plenum Length, 0.8mm Cladding Thickness + 3.0W/m-K Composite Thermal Conductivity]

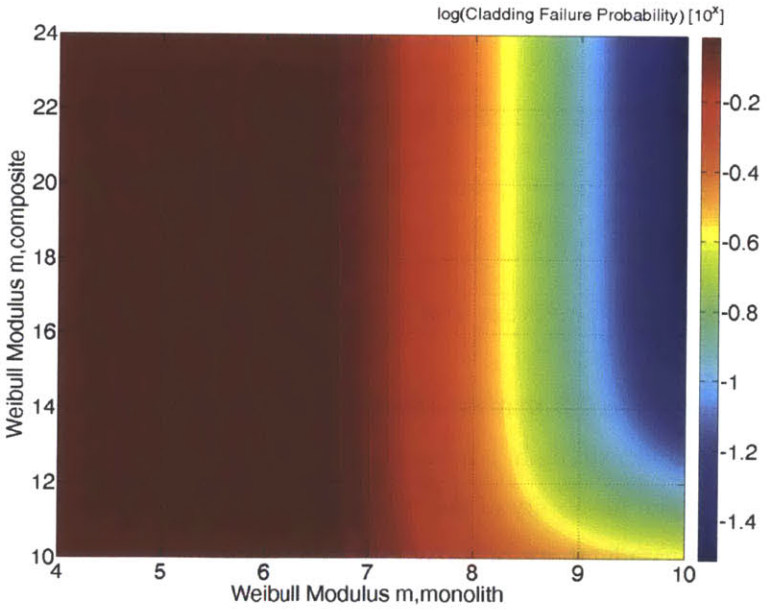

Figure 7-67 LBLOCA SiC Cladding Failure Probability of the Fuel Pin with the Peak Burnup of 112MWD/kgU at 2214 days as a function of Monolith Weibull Modulus, and Composite Weibull Modulus [10% Central Void in Fuel Pellets + 4×Plenum Length, 0.8mm Cladding Thickness + 3.0W/m-K Composite Thermal Conductivity]

It is important to note that the failure probabilities reported in this study ($\sim 10^{-4} \sim 10^{-3}$) are based on the peak fuel linear heat generation rate which applies to roughly ~20 assemblies out of a total 193 assemblies in BOL, and approximately ~15 assemblies at EOL. Because steady state failure probabilities of the SiC cladding sensitively depend on the thermal stress level in the composite, the other fuel pins with a smaller pin power may exhibit a substantially reduced failure probability. Therefore, the overall fuel pin failure probabilities in an entire reactor core will be lower by at least an order of magnitude in than the reported values. Table 7-8 summarizes the recommended thermal conductivity of the composite and SiC cladding Weibull Moduli for different peak fuel rod burnups when the SiC cladding is 0.8mm thick. .

Table 7-8 Recommended Minimum Composite Thermal Conductivity and Weibull Modulii of SiC Cladding for Different Peak Fuel Rod Burnups [0.8mm Cladding Thickness]

	Composite Thermal Conductivity (W/m-K)	Monolith Weibull Modulus	Composite Weibull Modulus
75 MWD/kgU (with 10% central void), 3 batch, 48 months	3.0	6	19
93 MWD/kgU (with 10% central void), 3 batch, 60 months	3.0	7	19
112 MWD/kgU (with 10% central void), 3 batch, 72 months	3.0	9.5	19

*Those values are after exposure to relevant irradiation (< ~20 dpa) and temperature (300°C ~ 400°C) in LWR core

It should be inferred from Table **7-8** that the allowable peak burnup is essentially determined by the statistical spread of the monolith strength, whereas the composite thermal conductivity and the statistical spread of its strength determine feasibility of the concept in terms of steady state failure probability. Note that the composite thermal conductivity of 3.0W/m-K, CVD-SiC monolith Weibull modulus of 6, and HNLS composite Weibull modulus of 19 are required to make the steady-state performance of the 0.8mm thick SiC clad comparable with the current steady state perfomrnace of fuel rod with zirconium based alloy (48month incore residence time). Ranges of experimentally obtained Weibull modulii for CVD-SiC and HNLS composite (Snead, 2007), (Katoh, 2010) include the listed values in Table **7-8**, as shown Figure 7-68. It was found that in addition to manufacturing technology and the composite architecture, the

Weibull modulus sensitively depends on the loading conditions. Hence, further investigations are needed to assess the Weibull modulus of the composite layer under relevant incore loading conditions.

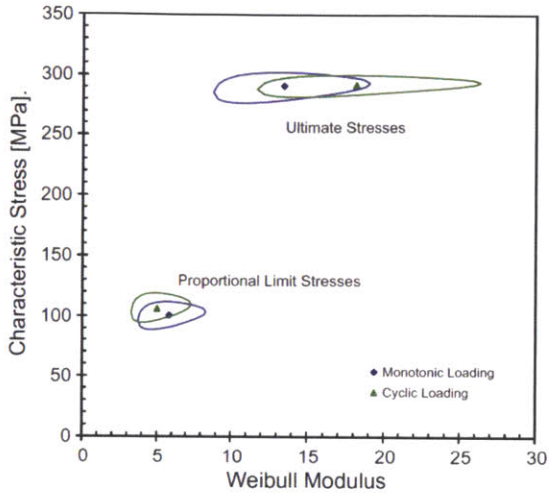

Figure 7-68 ORNL's Statistical Parameters for '*Tensile Stress Proportional Limit and Ultimate Stresses for Hi-Nicalon^{TM} Type-S Composite tested in Monotonic and Cyclic Loading Modes*' [Figure adopted from a published work of Katoh.et.al, (2010, Katoh)]

SiC/SiC Tyranno^{TM}-SA3 fiber reinforced SiC/SiC composite exhibited the lowest thermal conductivity of 3.3 W/m-K after 2.0 dpa under 450°C while HNLS fiber reinforced SiC/SiC composite exhited the lowest thermal conductivity of 1.5 W/m-K under the identical environment (Katoh, 2010). Hence, further research is needed to assess the manufacturing process cost of the SiC cladding with those desirable features. Further improvement of the monolith and composite conductivity would alleviate the requirement of the Weibull modulii.

7.9 Conclusion

This study found that SiC cladding can achieve a maximum allowable burnup beyond the current limit set by the Zircaloy cladding (62MWd/kgU with solid fuel pellet); SiC cladding can achieve incore residence time of 72 months for a peak burnup of 93MWd/kgU (10% central void in pellets). The recommended fuel rod and cladding design, within the current design envelop of LWR fuel rod; are 10% central void in fuel pellets, 3.6576 m (12 feet) active fuel rod height, 70 cm plenum length, and a cladding layer design of 60% inner monolith, 30% composite, and 10% EBC in terms of their relative thicknesses (in 0.57mm of the total cladding thickness). This fuel rod design strategically utilizes the prolonged gap closure with

the SiC cladding to extend the power production time while managing internal pressure level within the safety assurance limit. With the central voids in fuel pellets, the fuel maximum temperatures are lowered to be in the same level as the current LWR experience. This cladding is expected to give a peak burnup fuel rod failure probability on the order of 10^{-3} and a failure probability on the order of 10^{-1} (~0.2) in LBLOCA. This failure probability applies only to the fuel pins with the highest burnup. The SiC cladding performance was found to be strongly dependent on the Weibull modulus. For fuel modeling purposes, Weibull modulii of 7.5, and 17.5 were used for CVD-SiC and the fiber-reinforced composite based on literatures relevant to the SiC. Increasing cladding thickness was found to introduce the overall negative effect to structural integrity with the current estimates of the cladding thermal conductivity. This is because increasing cladding thickness increases the total cladding stress level at steady-state operation by inducing a higher thermal stresses, which outweighs a decrease in mechanical stresses. As a consequence, cladding failure probabilities reach an unacceptable range at BOL, with the cladding thickness of 0.8mm. This implies that increasing SiC cladding thickness should accompany an improvement of thermal conductivity to compensate for otherwise a higher thermal stress. Thus, it will be possible to maintain the same level of assurance about cladding structural integrity. For cladding thickness of 0.8mm, a composite thermal conductivity of 3.0W/m-K, CVD-SiC monolith Weibull modulus of 6, and HNLS composite Weibull modulus of 19 were estimated as the lower limit values to make the steady-state performance of SiC clad fuel rod comparable to the fuel rod with zirconium based alloy (48month incore residence time). Nonetheless, it should be noted that unless a significant improvement takes place in terms of structural integrity of the material, SiC clad fuel rods may not be able to meet the current level of fuel failure rates with zirconium based alloy clad fuel rod due to the statistical nature of ceramic fracture. An increased number of steady state fuel rod failures may be compensated by increased allowable burnup, achieving higher temperature margin in DBAs, and reduction in cladd melting and hydrogen generation under conditions beyond DBAs.

Chapter 8

Summary of Conclusions, and Recommendation for Future Work

8.1 A New Paradigm for Reactor Safety Improvement

LWR safety has been historically addressed in one dimensional frame; safety assurance principles have predominantly relied upon emergency safety assurance systems which are not the subject of accidents. These safety assurance systems include ECCS, hydrogen recombiners, and even actions of human intervention. Therefore, the advanced LWR nuclear fuel development tended to be primarily driven by interest in operational capability enhancements, given that no major accidents whose consequences were severely exacerbated by fuel-tolerance had taken place before the Fukushima accidents in 2011.

This study proposed making the nuclear fuel, the potential subject of accidents, a new axis on the nuclear safety assurance efforts; in a sense that its performance during accidents is regarded with highlighted attention, equal to that given to the emergency safety assurance systems. Understanding that the zirconium-based alloy cladding has become a limit on further advancement of LWRs safety as well as operational efficiency, this study investigated Silicon Carbide (SiC) as a replacement for the current zirconium-based cladding for LWRs. SiC is a widely-used, proven high temperature refractory material that demonstrates exceptional stability under irradiation. The preferred composition of the SiC cladding for LWR is a three-layer laminated structure that consists of an inner SiC monolith/SiC composite/SiC environmental barrier coating (EBC). This structure attempts to compensate for lack of ductility of the monolithic SiC with pseudo-ductile behavior of the composite, while containing the fission products inside the fuel rod with the innermost monolithic SiC. The EBC prevents oxidants from ingresssing through the carbon coated fibers of the composite, which leads to degradation of the composite's strength.

Research is being conducted by a number of major research institutions around the world to evaluate SiC's preliminary characteristics as a cladding material for LWRs. Yet, in depth safety and performance assessments of SiC cladding fuel and its key performance metrics during steady-state and accident situations remain essentially unexplored – leaving the concept open to speculation. Hence, a systematic approach to safety assessment of SiC cladding for LWRs is timely. This study quantitatively evaluated

key performance metrics LWR fuel rod with SiC cladding in terms of its safety, and operational efficiency by using a holistic methodology that connects experiment, modeling, and simulations.

8.2 Summary of Key Considerations and Findings

The oxidation behavior of SiC and zirconium-based alloy claddings are vastly different under relevant steam rich post-LOCA environment in a nuclear reactor: weight losses were observed for SiC while weight gains occur for zirconium-based alloy claddings. Silica, i.e. SiO_2, undergoes a reaction with water vapor (H_2O), which involves outward diffusion of product species through a fluid boundary layer formed on the material surface. This mechanism is absent in zircaloy oxidation, as the resultant zirconium oxide (ZrO_2) remains essentially inert in terms of chemical reactions with water vapor. Therefore, oxidation of SiC eventually leads to material loss through SiO_2 volatilization, while oxidation of Zr-4 results in weight addition through capturing of oxygen atoms.

The volatilization process introduces a key difference between SiC and Zircaloy oxidation – dependence on water vapor flow rate. The products of volatilization should be removed from the reaction sites in order for the reaction to proceed forward, and the effect of the fluid boundary layer on the material controls this process. The volatilization product species diffuse outward through the boundary layer formed on the material surface. Generally, the thicknesses of the boundary layers of fluids decrease with increasing flow rates, resulting in a shorter diffusion path. Therefore, the observed trend of increasing rare of weight loss with increasing flow rate due to the volatilization reaction, which is not observed for Zr-4 oxidation, is a new phenomenon that has to be accounted for.

Material loss rates tend to become more sensitively dependent on flow rates at higher temperatures because SiO_2 volatilization is likely to be limited by material transport rates through the fluid boundary layers (as opposed to the kinetics of the reaction, which are more limiting at low tempearure). Two correlations for SiC material loss with SiO_2 volatilization were developed, demonstrating acceptable predictability of tested conditions as well as relevant experimental data of past studies; one utilizes the chemical equilibrium of the volatilization reaction, and the other uses the kinetics approach. The correlations were used to estimate the required thickness of environmental barrier coating to prevent ingression of oxidants into carbon coated fibers in the underlying fiber reinforced composite layer under relevant LOCA accidents. EBC thickness between 45 ~ 110 μm is recommended to maintain 72 hours of protection of carbon coated fibers from any contact with steam at 1500°C in a LOCA. The developed correlations can be readily incorporated into any accident analysis fuel code.

The conducted experiments demonstrated that the oxidation of SiC is about three orders of magnitude slower than that of Zr-4. SiC oxidation can be accelerated by two potential situations; (1) Thinning of the protective silica layer with volatilization that leads shorter solid-state diffusion paths for gaseous species, and (2) Morphological degradation of the protective silica layer with formation of bubbles/pores and cracks that essentially allows 'instantaneous transport" of gaseous species through the oxide scale. Nevertheless, thanks to its chemical bonding, if used as a cladding material, SiC provides a demonstrably slower conversion in severe environments than zirconium-based alloys. This significantly slower reaction of SiC-H2O, with its minimal influence on its mechanical strength, may serve as a critical advantage of the use of SiC as a cladding material for LWRs over the current zircaloy cladding. The experimentally demonstrated weaker interplay between cladding oxidation and mechanical strength degradation of the cladding in the presence of EBC coating implies diminished importance of oxidation in material failure mechanisms in comparison with zircaloy cladding. Consequently, the SiC oxidation investigations illuminated that the major failure modes for the SiC cladding would fundamentally depart from the failure modes of zirconium-based cladding, which are heavily affected by oxidation (and the embrittlement resulting from the hydrogen generated in the rapid oxidation process).

As part of the exploration of key failure modes of SiC cladding, the study investigated brittle fracture of SiC cladding under tensile stresses. Experimental assessments demonstrated that β-SiC exhibits a superior tolerance to thermal shock in comparison with α-SiC, as the former showed some evidence of strength reduction upon quenching from temperatures up to 1260°C in saturated or even in room temperature water. For α-SiC, transgranular crack propagations were found to be the dominant fracture mode. Strength retention of both α-SiC, and β-SiC was observed in saturated water quenching. Such strength retention of brittle material in saturated water quenching was also observed with Al_2O_3. This strength retention effect in saturated water quenching was found to decrease with increasing material size as was demonstrated by thermal shock fracture of a thicker Al_2O_3 in saturated water. Since quenching of fuel rods in the reflood phase of LOCA in LWR occurs with injecting coolant close to saturation conditions, the observed strength retention of SiC cladding is expected to manifest itself after the reflood quenching. However, the transient thermal stresses during the reflood phase yield a reduced stress intensity addition to the pressure driven stress intensity.

A theoretical thermal shock study was conducted by developing a model to explain the observed brittle thermal shock fracture behavior. The investigation revealed that the initial heat transfer upon contact between the solid and the fluid in the early quenching transient is a controlling factor in the thermal shock induced brittle fracture. The study developed a thermal shock fracture prediction model for the early quenching transient based on the conductive heat transfer modes between the solid surface and the fluid,

and the Griffith flaw growth assumptions. The model demonstrated reasonable predictability og the critical temperature for thermal shock fractures at room temperature and at saturated water; it captures strength retention in saturated water quenching that varies with specimen sizes. Internal flaw induced fractures are sensitively dependent on flaw location; hence the statistical approach is suited for those cases. The developed model can be used for general brittle thermal shock induced fractures, including the quenching of SiC cladding during the reflood phase of a LOCA.

A mechanical model that calculates stress fields in each layer in the laminated SiC cladding, subject to pressure loading and temperature gradient, was developed. The stress fields were used in an appropriate statistical fracture model for SiC cladding, using Weibull distribution with relevant parameters found from past studies for each layer in SiC cladding. Stress and fracture analysis of SiC cladding with the developed mechanical model show that in steady-state operation, the positive effects of compressive thermal stresses are expected to maintain the integrity of the inner layer of the cladding, which is the fission-gas retaining CVD-SiC monolith. In the CVI-matrix of the intermediate layer, cracking is expected to occur whose consequence is an access from the coolant to the monolith. EBC or CVI overcoat is also anticipated to be cracked in most of the fuel rods primarily because of excessive thermal stresses and statistically reduced strength of the large monolithic structure. The stress and statistical fracture analysis demonstrated that developing SiC fiber-reinforced composite with higher conductivity would benefit the integrity of the cladding significantly, as the loads arising from thermal stress are considerable fractions of the total stresses. Determination of more statistically consistent Weibull parameters for both the composite and CVD-SiC, with better understanding of their size-dependent strengths in the laminated form, would significantly increase the confidence in the predictions by the statistical model of their fractures.

The developed SiC cladding stress and fracture analysis model were coupled to fuel rod simulation. The fuel rod simulations found that the SiC cladding can achieve a maximum allowable burnup beyond the current limit set by the Zircaloy cladding (62MWd/kgU with solid fuel pellet); SiC cladding can achieve incore residence time of 74months for a peak burnup of 93MWd/kgU (10% central void in pellets). The recommended fuel rod and cladding design, within the current design envelop of LWR fuel rod; are 10% central void in fuel pellets, 3.6576 m (12 feet) active fuel rod height, 70 cm plenum length, and a cladding layer design of 60% inner monolith, 30% composite, and 10% EBC, in terms of their relative thicknesses (within 0.57mm of the total cladding thickness). This fuel rod design strategically utilizes the prolonged period of an open fuel pin gap of a SiC cladding to extend the power production time, while keeping the internal pressure level within the safety assurance limit. With the central voids in fuel pellets, the fuel maximum temperatures are lowered to be at the same level as the current LWR experience. This cladding

is expected to give a peak burnup fuel rod failure probability on the order of 10-3 , and a failure probability on the order of 10-1 (~0.2) in LBLOCA. This failure probability applies only to the fuel pins with the highest burnup. The SiC cladding performance was found to be strongly dependent on the Weibull modulus. For fuel modeling purposes, Weibull modulii of 7.5, and 17.5 were used for the CVD-SiC and the fiber-reinforced composite based on literatures relevant to the SiC. For cladding thickness of 0.8mm - an easier to manufacture, 30% larger SiC cladding thickness than today's cladding, a composite layer thermal conductivity of 3.0W/m-K, CVD-SiC monolith layer Weibull modulus of 6, and HNLS composite Weibull modulus of 19 were estimated as minimum values to make the steady-state performance of SiC clad fuel rod comparable with the current steady state perfomrnace of fuel rod with zirconium based alloy (48month incore residence time). Nonetheless, it should be noted that unless a significant improvement of structural integrity of the material takes place, SiC clad fuel rods would not be able to meet the current level of fuel failure rates with zirconium based alloy clad fuel rod due to the statistical nature of ceramic fracture. Increased number of steady state fuel rod failures may be compensated by increased allowable burnup,, achieving higher temperature margin in DBAs, and reduction in cladd melting and hydrogen generation in beyond DBAs. Table 8-1 summarizes key performance characteristics of SiC cladding in comparison with zirconium based cladding.

Table 8-1 Comparison of Key Cladding Performance Characteristics of Zirconium Based Alloy and Silicon Carbide* (Based on this work except where moted)

	Zirconium based alloy cladding	SiC cladding
Structure	Monolith	Three laminated layers Monolith/Composite/EBC
Fuel rod design	Reference design	10% central void + 4 times the plenum length compared to the reference design (tentative)
Allowable peak fuel rod burnup	62MWD/kgU (solid pellet)	~85 MWD/kgU (solid pellet)
Primary factor for burnup limit	PCMI with cladding embrittlement with oxidation and irradiation	Fuel rod pressurization due to fission gas
Key strategies for burnup increase, and increased safety margin	Coolant chemistry optimization, and cladding composition optimization	Fuel rod design, cladding design optimization
Potential for burnup and safety margin increase	Low	High
Oxidation with steam**	Parabolic weight gain (~1000)	Linear weight loss (~1)
Strength failure behavior	Deterministic	Statistical
Key temperature limits	~900°C: clad softening and ballooning ~1200°C: steam oxidation ~1760 °C: melting point	Temperature limits should be considered in terms of fuel rod internal pressurization ~ No appreciable mechanical property degradation up to 1800°C [CVD-SiC] (Snead, 2007) ~ Limited oxidation <1500°C ~2760 °C: SiC sublimation point (Snead, 2007)

*Fuel rod design and the peak allowable burnup of SiC cladding are subject to changes with modifications of used properties and statistical parameters based on further research. The reported value, ~85 MWD/kgU is for an 0.57mm cladding thickness with the current knowledge of relevant properties.
** Numbers in the parenthesis () show relative material consumption rates

The advantages and drawbacks of the use of SiC cladding are summarized in Table 8-2. Although the inherently statistical nature of ceramic fracture currently leads to a high cladding failure rate in steady state operation, there is room for reaching beyond the currently allowable peak fuel burnup level (62MWD/kgU) if the SiC cladding achieved desirable Weibull modulus and thermal conductivity values. Use of SiC cladding would significantly alleviate the current limit on cladding temperature, oxidation, and hydrogen generation limit, which may lead to an increase in safety margin for LOCA. Further investigations are needed to assess characteristics of SiC cladding strength in terms of maintaining 'the coolable geoemtry' of subchannels. For 'long term cooling' criteria similar to the current Zr fuel, and using centrally voided fuel pellets, the reactor core design undergoes minimal changes, with fuel pellet temperatures staying at the same level as the current fuel rod with zirconium based alloy,. Use of SiC cladding could significantly benefit beyond design basis accidents by signficiantly reduction the potential for cladding melting and rapid hydrogen generation. Its admirable high temperature tolerant mechanical properties reduce the minimum needed SiC-clad fuel submergence level, which could lead to time gain before emergency water is needed.. It should be noted that given time for reaction with steam, SiC cladding could lead to more than double (~2.2 times) the amount of hydrogen generated with zirconium based cladding if all of the cladding were reacted[33].However, such a situation is not relevant to realistic accident cases where complete loss of heat removal capability lasts for a limited period of the time (relative to the time needed given the kinetics of the reaction). In addition, even if such a rare situation of long term absence of water cooling occurs, the survival of other structural materials of the core may emerge as a limiting issue before the consumption of the entire SiC cladding.

---

[33] Density of Zr-4 is ~6.6 g/cc (Whitmarsh, 1962) with molar mass of 91g/mol. This gives molar density of 0.0725 mol/cc . Since Zr-H_2O reaction causes two moles of H_2 generated per one mole of Zr reacted (Todreas, 2012), the equivalent hydrogen generation is found to be 0.145 mol(H_2)/cc. Similarly, the density of CVD-SiC, and HNLS composte is 3.21g/cc, and 2.75g/cc, respectively with SiC molar mass of 40g/mol. Assuming the SiC cladding consists of half CVD-SiC and the other half HNLS composite in terms of volume, the molar density of SiC cladding is found to be ~0.0745mol/cc. Since SiC oxidation causes three moles of H_2 generated per one mole of SiC reacted, as shown Eq.(2-1), the equlivalent hydrogen generation is found to be 0.224 mol(H_2)/cc. Since SiC cladding thickness could be 30% thicker than that the current zirconium based alloy cladding, the factor of ~1.44 (in terms of volume increase) shoul be multiplied to the equivalent hydrogen generation, which gives about 2.2 times the amount of hydrogen generation with Zr-4. This hydrogen generation would be even higher if the increased plenum length and SiC grid spacers were taken into account.

Table 8-2 Summary of Advantages and Drawbacks on the Use of SiC Cladding in Comparison with Zirconium Based Alloy Cladding

<table>
<tr><th></th><th>Advantage</th><th>Drawback</th></tr>
<tr><td>Steady state operation</td><td>Potential for Burnup Increase
[SiC > 62MWD/kgU (Zr)]</td><td>*Inherently Higher Fuel Rod Failure Rates
[~10^{-5} (Zr) → 10^{-4} ~ 10^{-3} (SiC), annual]</td></tr>
<tr><td rowspan="2">Design Basis Accident (LBLOCA)</td><td>10 CFR 50.46, ECCS Criteria

Peak Cladding Temperature
[1204°C (Zr) → >1500 °C (SiC)]

Maximu Cladding Oxidation
[17% ECR (Zr) → Not applicable (SiC)]

Maximum Hydrogen Generation
[less than 0.01% of the entire cladding reacted (Zr) → Not applicable (SiC)]</td><td></td></tr>
<tr><td colspan="2">10 CFR 50.46, ECCS Criteria
(Items that require further investigation)

Coolable Geometry
[Core geometry remains amenable to cooling]

Long-term Cooling
[Decay heat removal for extended period]</td></tr>
<tr><td>Beyond Design Basis Accident</td><td>Reduction of Cladding Melting
[1760°C (Zr) → 2750 °C(SiC)]

Reduction in Hydrogen Generation Rate
[Three orders of magnitude slower at 1200°C for SiC]

Reduced Needed Submergence Level
→ Time Gain for Human Intervention</td><td>Higher Amount of Hydrogen Generated if all of the Cladding Reacted with Water</td></tr>
</table>

* The indicated steady state SiC cladding failure probability is based on the higest exposure pin, which is the peak pin in the first two cycles. Hence, the average failure is lower.

8.3 Conclusion

The harsh environments of LWR reactor core bring challenging conditions for cladding materials beyond those that constitute 'the norm' for the material usage. Although a zirconium based alloy fits well the conditions of normal operation, it is essentially not a suitable material to be used in a highly corrosive environment at temperatures higher than 600°C, such as PWR core environment in accidents. Conversely, although SiC gives an excellent fit to corrosive environment, its usage under tensile stresses in large size is generally avoided due to the brittleness of the material. Engineered SiC cladding with fiber reinforced composite layer with EBC demonstrated that the structural issues of the brittleness of the material can be significantly alleviated while preserving its admirable chemical and irradiation stability, leaving the concept to be a potent option for further advancement of LWRs in both safety, and operational efficiency. This study laid a foundation for analyzing key aspects of SiC clad LWR fuel safety, which can serve as the groundwork for advanced investigations. After this work, we expect that the momentum of the SiC cladding research transforms to 'assessment-informed' material development and manufacturing.

8.4 Recommendation for Future Work

The concept of using SiC as LWR cladding material is still left with a few key unexplored areas, which need to be answered in the future. As an outcome, this study revealed key areas for future investigations. Those areas can be divided into either of the two categories – advanced assessment, or advanced material development

8.4.1 Advancement in Assessment Capabilities

(A) Advanced Statistical Treatment of SiC Cladding Fracture

The statistical analysis of SiC cladding fracture is key to evaluating the structural performance of the cladding, upon safety of the nuclear power plant is centered. The statistical treatment of SiC cladding fracture was addresses on individual layer basis in this study. Yet, a further improvement in SiC cladding fracture can be made with an advanced laminated model that captures re-arrangement of stress fields with a failure of individual layer(s). In addition, validity of the weakest link theory for individual components of the SiC cladding in a laminated form should be investigated. This issue boils down to - how to properly

extrapolate the strength, and fracture behavior of the lab scale specimen to the actual cladding, which exist in a laminated form.

(B) Advanced Understanding of Composite Mechanical Behavior

Behavior of the composite holds the key to alleviating the brittle nature of the SiC cladding. This study treated the fiber-reinforced composite as another layer of the SiC cladding. As a result, the fiber-reinforced composite was mechanically treated in the same manner as the monolith using representative composite properties. However, mechanical behavior of a fiber-reinforced composite involves more complex mechanisms, as it involves interactions between fibers, and between fibers and matrices. Orientation of fibers and the influence of the direction of woven fiber fabrics on the mechanical behavior of the composite should be further analyzed. In addition, a slightly different thermal expansion coefficient of the fibers and the matrix causes additional local stresses. Indeed, mechanical behavior of fiber reinforced composites with respect to its fiber architecture has been extensively studied in consideration of various applications including aerospace application, and combustion engines, etc. Yet, very limited literature is available for the fiber reinforced composite specific SiC cladding applications for LWRs.

Although the reported high Weibull modulus of the composite leads to reduced 'volume sensitivity for the material strength' with the weakest link fracture assumption, a more fundamental investigation of the composite statistical fracture with respect to its size as a cladding material needs be conducted.

(C) Oxidation Tolerance of the Fiber Composite with Cracked EBC

This found that the matrix of the fiber-reinforced composite is expected to undergo extensive micro-cracking in service as a LWR cladding. EBC, being monolithic, also would experience some degree of fracture, leaving some surface of the composite uncoated. Given those situation, the oxidation tolerance of the fiber composite against the localized water/steam ingression is of critical importance.

(D)Tolerance for Mechanical Impact

Mechanical impact, such as vibration against pieces of grid spacers, may be a probable failure mode of SiC cladding. Relatively less attention has been given to this subject. Yet, it could be an important player in the design, and operation of SiC cladding.

8.4.2 Advanced Material Development

(A) SiC Cladding with High Weibull Modulus under Irradiation

This study found that the Weibull moduli of both the monolith and the composite are crucially important as they significantly affect the feasibility of the concept. The Weibull modulus of SiC materials exhibited a decrease up to a factor of two after irradiation (Snead, 2007) as a function of neutron dose, and temperature. The mechanism for such a decrease is not understood. Developing the SiC monolith and the composite with high Weibull moduli could significantly open up the design window of the fuel rod, and operational efficiency with alleviated 'statistical brittleness' of the material, which also leads to a reduced size-sensitivity of the strength. An effort should be made to further investigate the conclusion of this study that the Weibull moduli of 6~7, and 15~17 are the low limits for irradiated CVD-SiC, and fiber reinforced composite, to assure competitiveness of the SiC cladding concept against the current Zircaloy cladding.

(B) Increasing Thermal Conductivity of the Cladding

The study revealed that thermal conductivity of the SiC cladding is a parameter that has crucial effects on structural integrity of the cladding. It influences the amount fission gas release from the fuel pellets by affecting the fuel temperature. The amount of fission gas release determines the internal fuel rod pressurization which is the primary source of mechanical loading of the SiC cladding. In addition, thermal conductivity determines the temperature gradient in the cladding, which affects the cladding thermal stress levels. Thermal stress is a significant portion of the total stress for the SiC cladding. Increasing SiC cladding thermal conductivity would reduce both the fuel internal pressure level, and the thermal stress level, which will lead to an increased safety margin. Generally, low thermal conductivity of the SiC cladding after irradiation arises from very low thermal conductivity of the composite (~1.5W/mK) (~9.5W/mK for CVD-SiC). There may be room lfor improved composite conductivity by careful material design.

(C) Cladding Manufacturing

Economic production of quality-assured SiC cladding needs to be addressed. Since, the use of SiC cladding for LWR assumes minimal changes of the current core design, the manufacturing goal should be set to achieve the current cladding size as closely as possible

(D) In-Reactor Testing of a Combined Fuel-Cladding

In-reactor testing of a combined fuel-cladding as a lead fuel pin, and as lead fuel assemblies must be conducted as it is a key required step of an advanced fuel development process. Such a testing will explicitly reveal the performance characteristics, and feasibility of the SiC cladding concept.

Bibliography

Abe, H. (1996). CRACK GROWTH OF CARBURIZED MATERIALS DUE TO THERMAL STRIPING IN SODIUM. *Engineering Fracture Mechanics, 55*(4), 679-687.

Almeida, J. B. (1999). Application of Weilbull statistics to the failure of coatings. *Journal of Materials Processing Technology*, 257-263.

Andreasen, J. H. (1993). Statistics of Brittle Failure in Muhiaxial Stress States. *Journal of the American Ceramic Society, 76*(11), 2933-2935.

Ansel C. Ugural, a. S. (2003). *Advanced strength and applied elasticity* (4th edition ed.). New Jersey: Prentice Hall PTR.

Arnold, R. P., McKrell, T. J., & Kazimi, M. S. (2011). *Silicon Carbide Oxidation in High Temperature Steam.* Cambridge: MIT Center for Advanced Nuclear Energy Systems.

Ashby, M. F., & Jones, D. (2005). *Engineering materials 1: an introduction to properties, applications and design* (3rd Edition ed.). Boston: Elsevier Butterworth-Heinemann.

Balani, B. B. (2011). *Advanced Structural Ceramics.* New Jersey: John Wiley & Sons, Inc.

Barnett, R. L., Hermann, P. G., Wingfield, J. R., & Connors, C. L. (1967). *FRACTURE OF BRITTLE MATERIALS UNDER TRANSIENT MECHANICAL AND THERMAL LOADING.* IIT Research Institute. Air Force Flight Dynamics Laboratory Research and Techtinology Division Air Force Systems Command.

Barron, R. F., & Barron, B. R. (2012). *Design for Thermal Stresses.* New Jersey: John Wiley & Sons.

Basu, B., & Balani, K. (2011). *Advanced Structural Ceramics.* New Jersey: John Wiley & Sons, Inc.

Becher, P. F., & Warwick, W. H. (1993). Factors Influencing The Thermal Shock Behavior of Ceramics. In G. A. Schneider, & G. Petzow, *Thermal Shock and Thermal Fatigue Behavior of Advanced Ceramics* (pp. 37-48). Dordrecht: Kluwer Academic Publishers.

Bengisu, M. (2001). *Engineering Ceramics.* New York: Springer.

Bloore, D. A., & Kazimi, M. S. (2013). *Reactor Physics Assessment of Thick Silicon Carbide Clad PWR Fuels (MIT-ANP-TR-147).* Cambridge: MIT Center for Advanced Nuclear Energy Systems.

Boley, B. A., & Weiner, J. H. (1960). *Theory of Thermal Stresses.* New York: Dover Publications, Inc.

Brossard, P. (2012, March). LWR fuels Innovation & Simulation activities at CEA. *MIT Symposium on Advanced LWR Fuels.* Cambridge: MIT.

Byun, T., Lara-Curzio, E., Lowden, R. A., Snead, L. L., & Katoh, Y. (2007). Miniaturized fracture stress tests for thin-walled tubular SiC Specimens. *Journal of Nuclear Materials, 367-370*, 653-658.

Cappelen, H., Johansen, K. H., & Motzfeldt, K. (1981). Oxydation of Silicon Carbide in Oxygen and in Water Vapour at 1500C. *Acta Chemica Scandinavica*, 247-254.

Carpenter, D. M., Ahn, K., Kao, S., Hejzlar, P., & Mujid, K. S. (2007). *Assessment of Silicon Carbide Cladding for High Performance Light Water Reactors (MIT-NFC-TR-098).* Cambridge: MIT Center for Advanced Nuclear Energy Systems.

Carpenter, D. M., Kohse, G. E., & Kazimi, M. S. (2010). *An Assessment of Silicon Carbide as a Cladding Material for Light Water Reactors.* Cambridge: MIT Center for Advanced Nuclear Energy Systems.

Chao, L.-Y., & Shetty, D. K. (1990). Equivalence of Physically Based Statistical Fracture Theories for Reliability Analysis of Ceramics in Multiaxial loading. *Journal of the American Ceramic Society, 73*(7), 1917-1921.

Chaumat, V., Gasse, A., Pascal, S., & Jeremie, B. (2006). Brazing of C/SiC Composites with the BraSiC® Process for High Temperature Applications. *High Temperature Ceramic Matrix Composites.*

Cheng, B. (2012, March). Breakthrough Technologies for Improving Fuel Safety Margins. *MIT Symposium on advanced LWR Fuels*. Cambridge: MIT.

Choi, H., & Gutierrez, O. (2013). A Study on SiC Cladding Option for Light Water Reactor Fuel. *International Congress on Advances in Nuclear Power Plants 2013 (ICAPP2013).* Jeju Island: ICAPP 2013.

Chu, M.-C., Cho, S.-J., Park, H.-M., Yoon, K.-J., & Ryu, H. (2004). Crack-healing in reaction-bonded silicon carbide. *Material Letters, 58*, 1313-1316.

Chung, H. M. (2005). Fuel Behavior Under Loss-of-Coolant Accident Situations. *Nuclear Engineering and Technology, 37*(4), 327-362.

Costello, J. A., & Tressler, R. E. (1981). Oxidation Kinetics of Hot-Pressed and Sintered α-Sic. *Journal of the American Ceramic Society, 64*(4), 327-331.

Costello, J. A., & Tressler, R. E. (1986). Oxidation Kinetics of Silicon Carbide Crystals and Ceramics: I, In Dry Oxygen. *Journal of the American Ceramic Society, 69*(9), 674-681.

Dao, M. (2013, March 7). Lecture 9: Fracture in Ceramics (Part II). *Lecture Slide of MIT Graduate Course, Fracture and Fatigue (3.35)* . Cambridge, MA: MIT Department of Materials Science and Engineering.

Deal, B. E., & Grove, A. S. (1965). General Relationship for the Thermal Oxidation of Silicon. *Journal of Applied Physics, 36*(12), 3770-3778.

Demkowicz, M. J. (2012, Fall Semester). 3.22 Mechanical Behavior of Materials: Lecture 21 Brittle Fracture. Cambridge, MA, U.S: MIT Department of Material Science and Engineering.

Derewnicki, K. P. (1985). Experimental studies of heat transfer and vapour formation in fast transient bo iling. *International Journal of Heat and Mass Transfer, 28*(11), 2085-2092.

Ding, S., Zeng, Y.-P., & Jiang , D. (2006). Thermal shock resistance of in situ reaction bonded porous silicon carbide ceramics. *Materials Science & Engineering*, 326-329.

Dobisesky, J. P., Pilat, E. E., & Kazimi, M. S. (2011). *Reactor Physics Considerations for Implementing Silicon Carbide Cladding into a PWR Environment.* Cambridge: MIT Center for Advanced Nuclear Energy Systems.

DOE, U. (1994). *Spent Nuclear Fuel Discharges from U.S Reactors 1992.* Survey Management Division. Washington, DC: U.S Department of Energy.

Easler, T. E., Bradt, R. C., & Tressler, R. E. (1981). Strength Distributions of Sic Ceramics After Oxidation and Oxidation Under Load. *Journal of the American Ceramic Society, 64*(12), 731-734.

Feinroth, H. (2012, March). Silicon Carbide Triplex Fuel Cladding BWR SiC Channel Boxes. *MIT Symposium on Advanced LWR Fuels.* Cambridge: MIT.

Feinroth, H. (2013, May 1). CTP's Silicon Carbide Triplex Cladding. *SiC/Accident Tolerant Fuel (ATF) Meeting.* Cambridge, Massachusetts, US: MIT Department of Nuclear Science and Engineering.

Filipuzzi, L., Camus, G., & Naslain, R. (1994). Oxidation Mechanism and Kinetics of 1D-SiC/C/SiC Composite Materials:1, An Experimental Approach. *Journal of the American Ceramic Society, 77*(2), 459-66.

Fox, D. S., Opila, E. J., & Hann, R. E. (2000). Paralinear Oxidation of CVD SiC in Simulated Fuel-Rich Combustion. *Journal of the American Ceramic Society, 83*(7), 1761-1767.

Geiger, G. H., & Poirier, D. R. (1973). *Transport phenomena in metallurgy.* Massachusetts: Addison-Wesley Publishing Company.

Giancarli, L., Golfier, H., Nishio, S., Raffray, R., Wong, C., & Yamada, R. (2002). Progress in blanket designs using SiCf/SiC composites. *Fusion Engineering and Design, 61-62*, 307-318.

Gilme, W., & Cawley, J. (1998). Stress Concentration Due to Fiber-Matrix Fusion in Ceramic-Matrix Composites. *Journal of the American Ceramic Society, 81*(10), 2597-2604.

Gnielinski, V. (1986). HEAT TRANSFER AND PRESSURE DROP IN HELICALLY COILED TUBES. *8th International Heat Transfer Conference, 6*, pp. 2847-2854.

Han, C.-Y., & Griffith, P. (1962). *The Mechanism of Heat Transfer in Nucleate Pool Boiling.* Department of Mechanical Engineering. Cambridge: Massachusetts Institute of Technology.

Hasezaki, K., Nakashita, A., Kaneko, G.-y., & Kakuda, H. (2007). Unburned Carbon Behavior in Sintered Coal Fly-Ash Bulk Material by Spark Plasma Sintering. *Materials Transactions, 48*(12), 3062-3065.

Hashimoto, A. (1992). The effect of H2O gas on volatilities of planet-forming major elements: I. Experimental determination of thermodynamic properties of Ca-, Al-, and Si-hydroxide gas molecules and its application to the solar nebula. *Geochimca er Cosmochrmrca Acta, 56*, 511-532.

Henrie, J. O., & Postma, A. K. (1982). *Analysis of the Three Mile Island (TMI-2) Hydrogen Burn.* Rockwell International Corporation.

Henrie, J. O., & Postma, A. K. (1987). *Lessons Learned from Hydrogen Generation and Burning During the TMI-2 Event.* Rockwell Hanford Operations.

Hesham E. Khalifa, C. P. (2012, March). Development of High Purity β-SiC Joints for LWR Cladding. *MIT Symposium on Advanced LWR Fuels*. Cambridge: MIT.

Hewitt, G. F., & Collier, J. G. (2000). *Introduction to Nuclear Power* (2nd ed.). New York: Taylor & Francis.

Hirayama, H., Kawakubo, T., & Goto, A. (1989). Corrosion Behavior of Silicon Carbide in 290oC Water. *Journal of the American Ceramic Society, 72*(11), 2049-2053.

Hobson, D. O. (1972). *Ductile-brittle behavior of Zircaloy fuel cladding.* Tennesse: Oak Ridge National Laboratory.

Hobson, D. O., & Rittenhouse, P. L. (1972). *Embrittlement of Zircaloy-Clad Fuel Rods by Steam During LOCA Transients.* Tennesse: Oakridge National Laboratory.

Hsu, Y. Y. (1962). On the Size Range of Active Nucleation Cavities on a Heating Surface. *Journal of Heat Transfer*, 207-213.

Hu, R. (2011, April 13). Class Material of 22.313 Thermal-Hydraulics in Power Technology in Spring Semester 2011 at MIT Graduate School. *Laboratory Problem #4 Crud Effect on Cladding Temperature during LBLOCA, Combined Relap5 simulation and predictions by stand-alone models*. Cambridge, MA, U.S.A: MIT Department of Nuclear Science and Engineering.

Idaho National Laboratory. (2005). *RELAP5-3D© CODE MANUAL VOLUME I: CODE STRUCTURE, SYSTEM MODELS, AND SOLUTION METHODS (INEEL-EXT-98-00834, Revision 2.4).* Idaho Falls, Idaho: DOE/NE Idaho Operations Office.

Incropera, F. P., Dewitt, D. P., Bergman, T. L., & Lavine, A. S. (2007). *Fundamentals of Heat and Mass Transfer* (6th ed.). New Jersey: John Wiley & Sons.

International Atomic Energy Agency. (2002). *Fuel behaviour under transient and LOCA conditions (IAEA-TECDOC-1320).* Vienna, Austria: IAEA.

Irene, E. A., & Ghez, R. (1997). Silicon Oxidation Studies: Roles of H2O. *Journal of the Electrochemical Society, 124*(11), 1757-1761.

Jones, M. F. (2005). *Engineering materials 1: an introduction to properties, applications and design* (3rd Edition ed.). Boston: Elsevier Butterworth-Heinemann.

KAERI. (n.d.). Online Plotter for MCNP and ENDF cross section data.

Kakac, S., Shah, R. K., & Aung, W. (1987). *Handbook of Single-Phase Convective Heat Transfer.* New York: John Wiley & Sons.

Katoh, Y., Nozawa, T., Snead, L. L., Ozawa, K., & Hiroyasu, T. (2011). Stability of SiC and its composites at high neutron fluence. *Journal of Nuclear Materials, 417*, 400-405.

Katoh, Y., Snead, L. L., Henager Jr, C. H., Hasegawa, A., Kohyama, A., Riccardi, B., & Hegeman, H. (2007). Current status and critical issues for development of SiC composites for fusion applications. *Journal of Nuclear Materials, 367-370*, 659-671.

Katoh, Y., Snead, L. L., Nozawa, T., Kondo, S., & Busby, J. T. (2010). Thermophysical and mechanical properties of near-stoichiometric fiber CVI SiC/SiC composites after neutron irradiation at elevated temperatures. *Journal of Nuclear Materials, 403*, 48-61.

Katoh, Y., Snead, L. L., Parish, C. M., & Hinoki, T. (2013). Observation and possible mechanism of irradiation induced creep in ceramics. *Journal of Nuclear Materials, 434*, 141-151.

Kazimi, M. S. (2013, May 1). Fuel Modeling with SiC Cladding. *SiC/Accident Tolerant Fuel (ATF) Meeting*. Cambridge, Massachusetts, US: MIT Department of Nuclear Science and Engineering.

Khalifa, H. E., Deck, C. P., & Back, C. A. (2012, March). Development of High Purity b-SiC Joints for LWR cladding. *MIT Symposium on Advanced LWR Fuels*. Cambridge, MA, US: MIT Center for Advances in Nuclear Energy (MIT-CANES).

Kim, H., & Moorehead, A. J. (1990). Effects of Gaseous corrosion on the strength of SiC and Si3N4. *Ceramic Transactions, 10*, 81-96.

Kingery, W. D., Bowen, H. K., & Uhlamnn, D. R. (1976). *Introduction to Ceramics* (2nd ed.). New York: John Wiley & Sons.

Knorr, J., Lippmann, W., Reinecke, A. -M., Wolf, R., Kerber, A., & Wolter, A. (2008). SiC encapsulation of (V)HTR components and waste by laser beam joining of ceramics. *Nuclear Engineering and Design*(238), 3129-3135.

Krohn, M. H. (2006). *Modeling of Fission Gas Release in UO2 [Report Number:B-MT(SRME)-56].* West Mifflin, Pennsylvania: Bechtel Bettis, INC.

Kueck, A. M., Kim, D. K., Ramasse, Q. M., De Jonghe, L. C., & Ritchle, R. O. (2008). Atomic-Resolution Imaging of the Nanoscale Origin of Toughness in Rare-Earth Doped SiC. *Nano Letters, 8*(9), 2935-2939.

Kurt Terrani, B. P. (2012, March). Cladding Steam Corrosion Studies. *MIT Symposium on Advanced LWR Fuels*. Cambridge: MIT.

Lahoda, E. (2012, March). UN fuel in SiC Cladding. *MIT Symposium on Advanced LWR Fuels*. Cambridge: MIT.

Lamon, J. (1988). Statistical Approaches to Failure for Ceramic Reliability Assessment. *Journal of the American Ceramic Society, 71*(2), 106-112.

Lamon, J. (1990). Ceramics Reliability: Statistical Analysis of Multiaxial Failure Using the Weibull Approach and the Multiaxial Elemental Strength Model. *Journal of the American Ceramic Society, 73*(8), 2204-2212.

Lance L. Snead, T. N.-S. (2007). Handbook of SiC properties for fuel performance modeling. *Journal of Nuclear Materials, 371*, 329-377.

Landwehr, S. E., Hilmas, G. E., Fahrenholtz, W. G., Talmy, I. G., & DiPietro, S. G. (2008). Microstructure and mechanical characterization of ZrC–Mo cermets produced by hot isostatic pressing. *Materials Science and Engineering A, 497*, 79-86.

Lee , W., & Snead, L. L. (2013). Fully Ceramic Micro-encapsulated (FCM) Replacement Fuel Assembly for LWRs. *International Congress on Advances in Nuclear Power Plants 2013 (ICAPP 2013).* Jeju Island: ICAPP 2013.

Lee, J., Hu, L.-w., Saha, P., & Kazimi, M. S. (2009). Numerical analysis of thermal striping induced high cycle thermal fatigue in a mixing tee. *Nuclear Engineering and Design, 239*, 833-839.

Lee, Y., McKrell, T. J., Yue, C., & Kazimi, M. S. (2013). Safety Assessment of SiC Cladding Oxidation Under Loss of Coolant Accident. *Nuclear Technology*.

Lim, S.-w., Chun , J.-h., Chung, B.-d., & Lee, W. (2013). Accident Tolerance of FCM Replacement Fuel for LWRs. *International Congress on Advances in Nuclear Power Plants 2013 (ICAPP 2013).* Jeju Island: ICAPP 2013.

Locke, D. H. (1975). Review of experience with water reactor fuels 1968–1973. *Nuclear Engineering and Design, 33*(2), 94-124.

Lu, T. J., & Fleck, N. A. (1998). THE THERMAL SHOCK RESISTANCE OF SOLIDS. *Acta Materialia, 46*(13), 4755-4768.

Luthra, K. L. (1991). Some New Perspectives on Oxidation of Silicon Carbide and Silicon Nitride. *Journal of the American Ceramic Society, 74*(5), 1095-1103.

M. Janssen, J. Z. (2002). *Fracture Mechanics* (2nd Edition ed.). Delft: Delft University Press.

Marcus, B. D., & Dropkin, D. (1965). Measured Temperature Profiles Within the Superheated Boundary Layer Above a Horizontal Surface in Saturated Nucleate Pool Boiling of Water. *Journal of Heat Transfer*, 333-340.

Markham, G., Hall, R., & Feinroth, H. (2012). RECESSION OF SILICON CARBIDE IN STEAM UNDER NUCLEAR PLANT LOCA CONDITIONS UP TO 1400 °C. (K. Fox, Y. Katoh, H.-T. Lin, I. Belharouak, M. Halbig, & S. Mathur, Eds.) *Ceramic Materials for Energy Applications II.*

McNulty, J. C., & Zok, F. W. (1997). Application of Weakest-Link Fracture Statistics to Fiber-Reinforced Ceramic-Matrix Composites. *Journal of the American Ceramic Society, 80*(6), 1535-1543.

Mieskowski, D. M., Mitchell, T. E., & Heuer, A. H. (1984). Bubble Formation in Oxide Scales on SiC. *Communications of the American Ceramic Society*, C17-C18.

Minford, E., Costello, J. A., Tsong, I. S., & Tressler, R. E. (1983). Oxidation Effects on Crack Growth and Blunting in SiC Ceramics,". (R. C. Bradt, A. G. Evans, D. P. Hasselman, & F. F. Lange, Eds.) *Fracture Mechanics of Ceramics, 6*, 511-522.

Munro (A), R. G. (1997). Material Properties of a Sintered α-SiC. *Journal of Physical and Chemical Reference Data, 26*(5), 1195-1203.

Munro (B), R. G. (1997). Evaluated Material Properties for a Sintered α-Alumina. *Journal of the American Ceramic Society, 80*(8), 1919-1928.

Narushima, T., Goto, T., & Hirai, T. (1989). High-Temperature Passive Oxidation of Chemically Vapor Deposited Silicon Carbide. *Journal of the American Ceramic Society, 72*(8), 1386-1390.

Narushima, T., Goto, T., Iguchi, Y., & Hirai, T. (1990). High-Temperature Oxidation of Chemically Vapor-Deposited Silicon Carbide in Wet Oxygen at 1823 to 1923 K. *Journal of the American Ceramic Society, 73*(12), 3580-3584.

NEA. (2006). *Very High Burn-ups in Light Water Reactors.* Paris: Nuclear Energy Agency (NEA), Organization for Economic Co-Operation and Development (OECD).

Newsome, G., Snead, L. L., Hinoki, T., Katoh, Y., & Peters, D. (2007). Evaluation of neutron irradiated silicon carbide and silicon carbide composites. *Journal of Nuclear Materials, 371*, 76-89.

Nishio, S., & Auracher, H. (1999). Film and Transition Boiling. In S. G. Kandlikar, M. Shoji, & V. K. Dhir, *Handbook of Phase Change* (p. 173). Philadelphia, PA: Taylor and Francis.

Nishio, S., & Ohtake, H. (1993). Vapor-film-unit model and heat transfer correlation for natural-convection film boilig with wave motion under subcooled conditions. *International Journal of Heat and Mass Transfer, 36*(10), 2541-2552.

Nozawa, T., Choi, Y., Hinoki, T., Kishimoto, H., Kohyama, A., & Tanigawa, H. (2011). Tensile, Compressive and In-Plane/Inter-Laminar Shear Failure Behavior of CVI- and NITE-SiC/SiC Composites. *IOP Conf. Series: Materials Science and Engineering . 18.* Ceramic Society of Japan.

Nozawa, T., Ozawa, K., Choi, Y.-B., Kohyama, A., & Tanigawa, H. (2012). Determination and prediction of axial/off-axial mechanical properties of SiC/SiC composites. *Fusion Engineering and Design, 87*, 803-807.

NRC. (2000). *Extended Burnup Evaluation (BAW-10186-A, Rev. 1).* Washington, D.C: U.S NRC.

NRC. (2007, 5 23). Proposed Technical Basis for the Revision to 10 CFR 50.46 LOCA Embrittlement Criteria for Fuel Cladding Materials. Washington, DC, United States of America: U.S NRC.

NRC. (2008, 12 18). Technical Basis and Rulemaking Strategy for the Revision of 10 CFR 50.46(b) Loss-of-Coolant Accident Embrittlement Criteria for Fuel Cladding Materials. Washington, DC: U.S NRC.

NRC. (2011). *Recommendations for Enhancing Reactor Safety in the 21st Century, the Near-Term Task Force, Review of Insights from the Fukushima Dai-Ichi Accident.* U.S NRC.

NRC. (2013, 3 20). Code of Federal Regulation 10 CFR 50.46. U.S NRC. Retrieved from U.S NRC Regulations (10 CFR): http://www.nrc.gov/reading-rm/doc-collections/cfr/part050/part050-0046.html&hl=en&strip=1

OECD/NEA. (2009). *Nuclear Fuel Behaviour in Loss-of-coolant Accident (LOCA) Conditions.* NUCLEAR ENERGY AGENCY ORGANISATION FOR ECONOMIC CO-OPERATION AND DEVELOPMENT.

Ogbuji, L. U. (1981). Development of oxide scale microstructure on single-crystal SiC. *Journal of Materials Science*, 2753-2759.

Ogbuji, L. U. (1998). A Pervasive Mode of Oxidative Degradation in a SiC-SiC Composite. *Journal of the American Ceramic Society, 81*(11), 2777-2784.

Olander, D. R. (2001). Light Water Reactor Fuel Design and Performance. In *Encyclopedia of Materials: Science and Technology* (pp. 4490-4504). Elsevier Science Ltd.

Opila, E. (2004). Volatility of Common Protective Oxides in High-Temperature Water Vapor: Current Understanding and Unanswered Questions. *Materials Science Forum*, 765-774.

Opila, E. J. (1994). Oxidation Kinetics of Chemically Vapor-Deposited Silicon Carbide in Wet Oxygen. *Journal of the American Ceramic Society, 77*(3), 730-736.

Opila, E. J. (1999). Variation of the Oxidation Rate of Silicon Carbide with Water-Vapor Pressure . *Journal of the American Ceramic Society, 82*(3), 625-636.

Opila, E. J. (2003). Oxidation and Volatilization of Silica Formers in Water Vapor. *Journal of the American Ceramic Society*, 1238-1248.

Opila, E. J., & Hann Jr, R. E. (1997). Paralinear Oxidation of CVD SiC in Water Vapor. *Journal of the American Ceramic Society, 80*(1), 197-205.

Opila, E. J., & Jacobson, N. S. (1995). SiO(g) Formation from SiC in Mixed Oxidizing-Reducing Gases. *Oxidation of Metals, 44*, 527-544.

Opila, E. J., Smialek, J. L., Robinson, R. C., Fox, D. S., & Jacobson, N. S. (1999). SiC Recession Caused by SiO2 Conditions: II, Thermodynamics and Gaseous-Diffusion Model. *Journal of the American Ceramic Society, 82*(7), 1826-1834.

Osman, A. M., & Beck, J. V. (1990). Investigation of Transient Heat Transfer Coefficient in Quenching Experiments. *Journal of Heat Transfer, 112*, 843-848.

Pacific Northwest National Laboratory (A). (2011). *FRAPCON-3.4: A Computer Code for the Calculation of Steady-State, Thermal-Mechanical Behavior of Oxide Fuel Rods for High Burnup (NUREG/CR-7022, Vol. 1).* Richland, WA: U.S NRC.

Pacific Northwest National Laboratory (B). (2011). *Material Property Correlations: Comparisons between FRAPCON-3.4, FRAPTRAN 1.4, and MATPRO (NUREG/CR-7024).* Richland, WA: U.S. NRC.

Pacific Northwest National Laboratory (C). (2011). *FRAPTRAN 1.4: A Computer Code for the Transient Analysis of Oxide Fuel Rods (NUREG/CR-7023, Vol. 1).* Richland, WA: U.S NRC.

Parker, G. W., Lorenz, R. A., & Wilhelm, J. G. (1965). Release of Fission Products from Reactor Fuels During Transient Accidents Simulated in Treat. *Proc. Intl. Symp. Fission Product Release and Transport under Accident Conditions.* Tennesse : Oak Ridge National Laboratory .

Petrovic, J. J. (1987). Weibull statistical fracture theory for the fracture of ceramics. *Metallurgical Transactions A, 18*(11), 1829-1834.

Pitts, D. R., Yen, H. H., & Jackson, T. W. (1968). Transient Film Boiling of Water on a Horizontal Wire. *Journal of Heat Transfer*, 476-481.

Rice, R. W. (2000). *Mechanical Properties of Ceramics and Composites - Grain and Particle Effects.* New York: Marcel Dekker, Inc.

Robinson, R. C., & Smialek, J. L. (1999). SiC Recession Caused by SiO2 Scale Volatility under Combustion Conditions: I, Experimental Results and Empirical Model. *Journal of the American Ceramic Society, 82*(7), 1817-1825.

Sakurai, A., & Shiotsu, M. (1977). Transient Pool Boiling Heat Transfer. *Journal of Heat Transfer, 99*, 547-553.

Schanz, G., Adroguer, B., & Volchek, A. (2004). Advanced treatment of zircaloy cladding high-temperature oxidation in severe accident code calculations Part I. Experimental database and basic modeling. *Nuclear Engineering and Design*, 75-84.

Schlichting, H., & Gersten, K. (2000). *Bound Layer Theory* (8th ed.). New York: Springer.

Shah, R. C., & Koboyashi, A. S. (1971). STRESS INTENSITY FACTOR FOR AN ELLIPTICAL CRACK UNDER ARBITRARY NORMAL LOADINGt. *Engineering Fracture Mechanics, 3*, 71-96.

Sih, G. C., Paris, P. C., & Erdogan, F. (1962). Crack-Tip, Stress-Intensity Factors for Plane Extension and Plate Bending Problems. *Journal of Applied Mechanics*, 306-312.

Singhal (B), S. C. (1976). Oxidation kinetics of hot-pressed silicon carbide. *Journal of Materials Science*, 1246-1253.

Singhal(A), S. C. (1976). Thermodynamic analysis of the high-temperature stability of silicon nitride and silicon carbide. *Ceramurgia International, 2*(3), 123-130.

Snead , L. L. (2004). Ceramic Structural Composites The Most Advanced Structural Material. Erice, Italy: Oak Ridge National Laboratory .

Snead, L. L. (2004). Ceramic Structural Composites The Most Advanced Structural Materials. Erice, Italy.

Snead, L. L. (2013, May 1). Issues and Overview of SiC-based Fuel and Clad Technologies in Support of Accident Tolerant Fuel Development. *SiC/Accident Tolerant Fuel (ATF) Meeting, NSE Department Seminar*. Cambridge, Massachusetts, US: MIT Department of Nuclear Science and Engineering.

Snead, L. L., Nozawa, T., Katoh, Y., Byun, T.-S., Kondo, S., & Petti, D. A. (2007). Handbook of SiC properties for fuel performance modeling. *Journal of Nuclear Materials, 371*, 329-377.

Snead, L. L., Terrani, K., Gehin, J., & Kiggans, J. (2012, March). Fully Ceramic Microencapsulated fuels for LWRs. *MIT Symposium on Advanced LWR Fuels*. Cambridge.

Song, Y., Dhar, S., Feldman, L. C., Chung, G., & Williams, J. R. (2004). Modified Deal Grove model for the thermal oxidation of silicon carbide. *Journal of Applied Physics, 95*(9), 4953-4957.

Stempien, J. D., Carpenter , D. M., Kohse, G., & Kazimi, M. S. (2011). *Behavior of Triplex Silicon Carbide Fuel Cladding Designs Tested Under Simulated PWR Conditions.* Cambridge: MIT Center for Advanced Nuclear Energy Systems.

Strumpell, J. H. (2012, March). Material Development Supporting Customer Needs. *MIT Symposium on Advanced LWR Fuels*. Cambridge: MIT.

Sudhir, B., & Raj, R. (2006). Effect of Steam Velocity on the Hydrothermal Oxidation/Volatilization of Silicon Nitride. *Journal of the American Ceramic Society, 89*(4), 1380-1387.

T Nozawa, Y. C. (2011). Tensile, Compressive and In-Plane/Inter-Laminar Shear Failure Behavior of CVI- and NITE-SiC/SiC Composites. *18.* Ceramic Society of Japan.

T.S. Byun, E. L.-C. (2007). Miniaturized fracture stress tests for thin-walled tubular SiC Specimens. *Journal of Nuclear Materials, 367-370*, 653-658.

Takashi Nozawa, K. O.-B. (2012). Determination and prediction of axial/off-axial mechanical properties of SiC/SiC composites. *Fusion Engineering and Design*.

Tedmon, Jr, C. S. (1966). The Effect of Oxide Volatilization on the Oxidation Kinetics of Cr and Fe-Cr Alloys. *Journal of the Electrochemical Society, 113*(8), 766-768.

Terrani, K. A., Pint, B. A., Katoh, Y., & Snead , L. L. (2013, May 1). SiC Steam oxidation Testing at ORNL. *SiC/Accident Tolerant Fuel (ATF) Meeting*. Cambridge, Massachusetts, US: MIT Department of Nuclear Science and Engineering.

Terrani, K. A., Snead, L. L., Zinkle, S. J., Pint, B. A., Yamamoto, Y., Robb, K. R., . . . Kim, Y.-J. (2013, May 1). Materials Development in Support of Accident Tolerant Fuel Technologies. *SiC/Accident Tolerant Fuel (ATF) Meeting, NSE Department Seminar*. Cambridge, Massachusetts, US: MIT Department Nuclear Science and Engineering.

Terrani, K., Pint, B., & Snead, L. L. (2012, March). Cladding Steam Corrosion Studies. *MIT Symposium on Advanced LWR Fuels*. Cambridge: MIT Center for Advanced Nuclear Energy Systems.

Thiemeier, T., Bruckner-Foit, A., & Kolker, H. (1991). Influence of the Fracture Criterion on the Failure Prediction of Ceramics loaded in Biaxial Flexure. *Journal of the American Ceramic Society, 74*(1), 48-52.

Todreas, N. E., & Kazimi, M. S. (2012). *Nuclear Systems I* (2nd ed.). New York: CRC Press Taylor & Francis Group.

Tortorelli, P. F., & More, K. L. (2003). Effects of High Water-Vapor Pressure on Oxidation of Silicon Carbide at 1200°C. *Journal of the American Ceramic Society, 86*(8), 1240-1255.

Tressler, R. E. (1990). Environmental Effects on Long Term Reliability of SiC and Si3N4Ceramics. (R. E. Tressler, & M. McNallan, Eds.) *CeramicTransacions, 10: Corrosion and Corrosive Degradation of Ceramics*, 99-124.

Ugural, A. C., & Fenster, S. K. (2003). *Advanced strength and applied elasticity* (4th edition ed.). New Jersey: Prentice Hall PTR.

Wachtman, J. B., Cannon, W. R., & Matthewson, M. J. (2009). *Mechanical properties of ceramics* (2nd Edition ed.). New Jersey: Wiley.

Wagner, C. (1958). Passivity during the Oxidation of Silicon at Elevated Temperatures. *Journal of Applied Physics, 29*(9), 1295-1297.

Wagstaff, F. E., & Richards, K. J. (1966). Kinetics of Crystallization of Stoichiometric SiO2 Glass in H20 Atmospheres. *Journal of the American Ceramic Society, 49*(3), 118-121.

Wang, H., & Singh, R. N. (1994). Thermal shock behaviour of ceramics and ceramic composites. *International Materials Reviews, 39*(6), 228-244.

Whitmarsh, C. L. (1962). *REVIEW OF ZIRCALOY-2 AND ZIRCALOY-4 PROPERTIES RELEVANT TO N.S. SAVANNAH REACTOR DESIGN (ORNL-3281, UC-80-Reactor Technology).* Tennesse: Oak Ridge National Laboratory (ORNL).

Wiebe, J. R., & Judd, R. L. (1971). Superheat Layer Thickness Measurements in Saturated and Subcooled Nucleate Boiling. *Journal of Heat Transfer*, 455-461.

Yang, R., Cheng, B., Deshon, J., Edsinger, K., & Ozer, O. (2006). Fuel R & D to Improve Fuel Reliability. *Journal of Nuclear Science and Technology, 43*(9), 951-959.

Yin, X., Cheng, L., Zhang, L., Xu, Y., & Luan, X. (2001). Oxidation Behavior of Three-Dimensional Woven C/SiC Composite. *Materials Science and Technology, 17*, 727-30.

Yvon, P., & Carre, F. (2009). Structural Materials Challenges for Advanced Reactor Systems. *Journal of Nuclear Materials, 385*, 217-222.

Zweben, C., & Rosen, B. W. (1970). A Statistical Theory of Material Strength with Application to Composite Materials. *Journal of the Mechanics and Physics of Solids, 18*, 189-206.

APPENDIX:

Experimental Facility

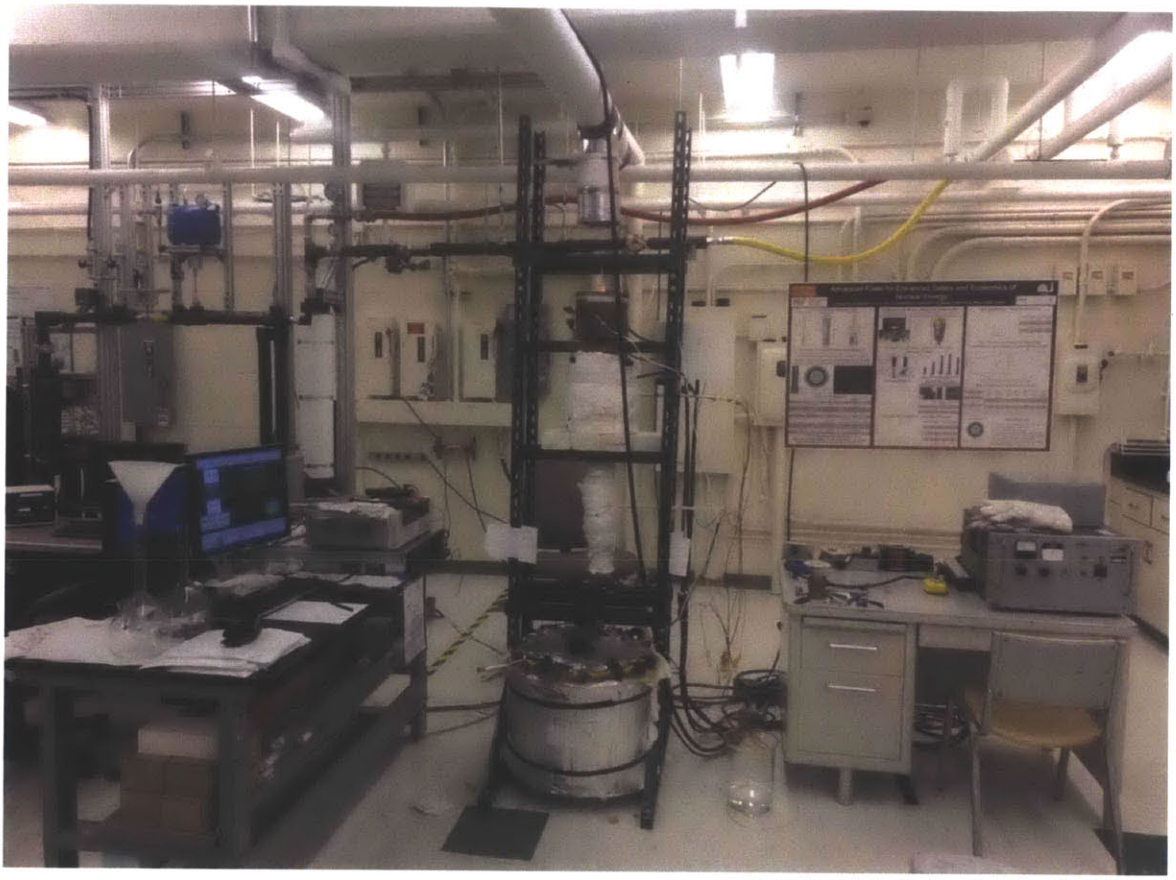

A1: Oxidation Experiment Facility

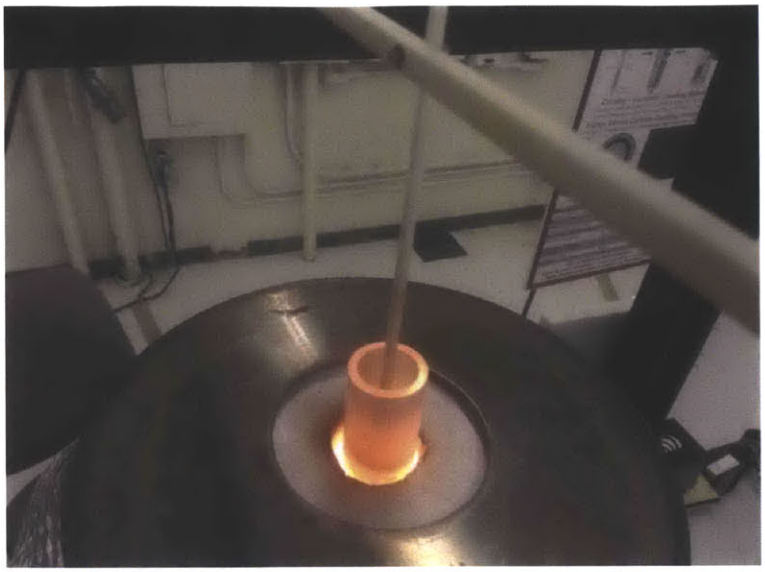

A2: Sample Holder of the Oxidation Facility

A3: Power Supplier of the Sample Furnace of the Oxidation Facility

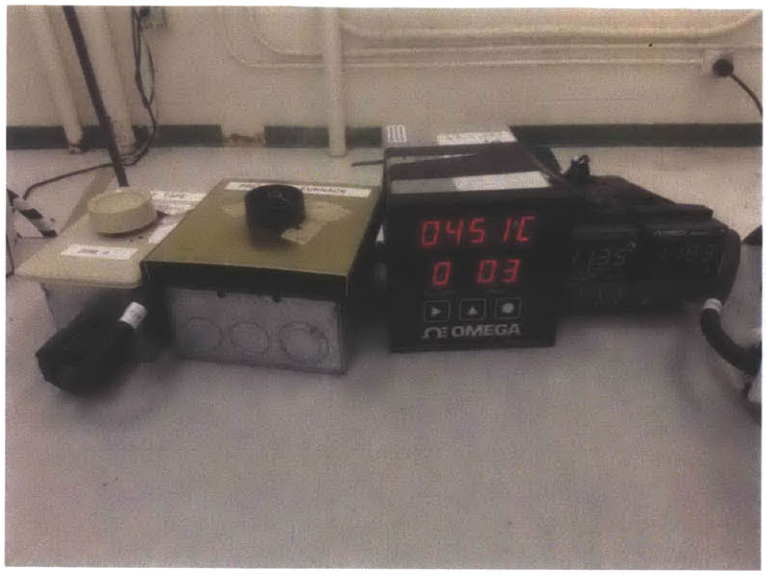

A4: Temperature Monitors and Controllers of the Oxidation Facility

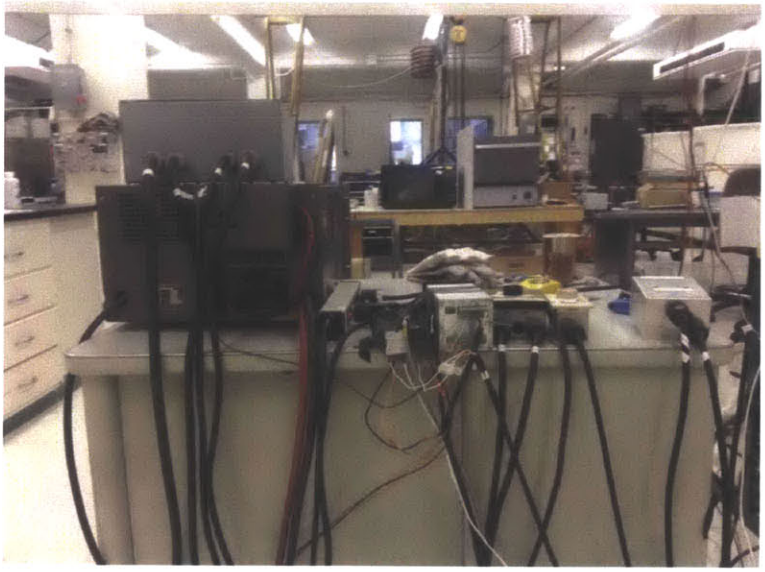

A5: Electric Wire Connections of the Temperature Monitors and Controllers

A6: Quenching Experiment Area

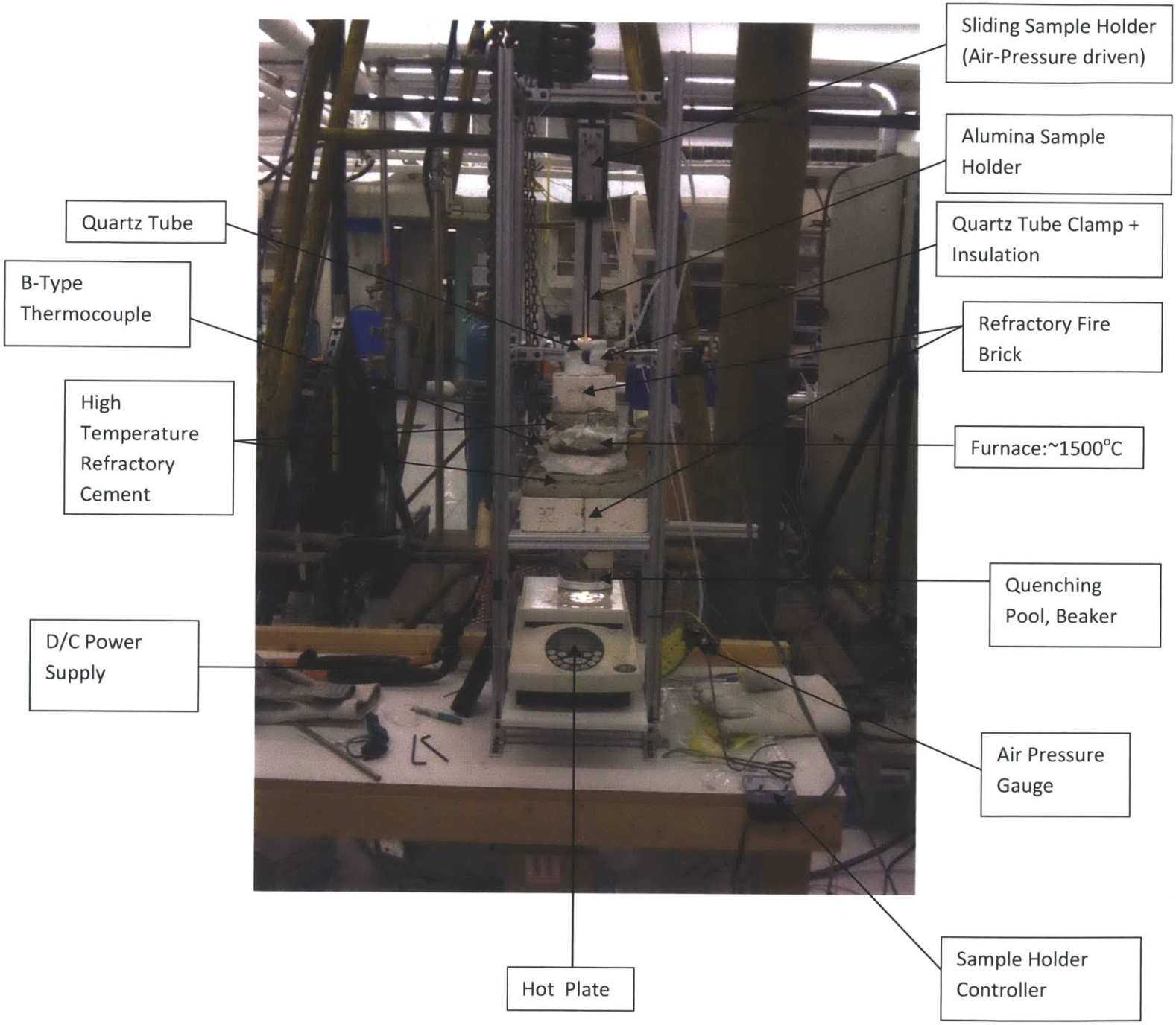

A7: Quenching Experiment Facility